APR 1 1983

COMPLETED

NAS 1.55:2264

NASA Conference Publication 2264

ORIGINAL

Tire Modeling

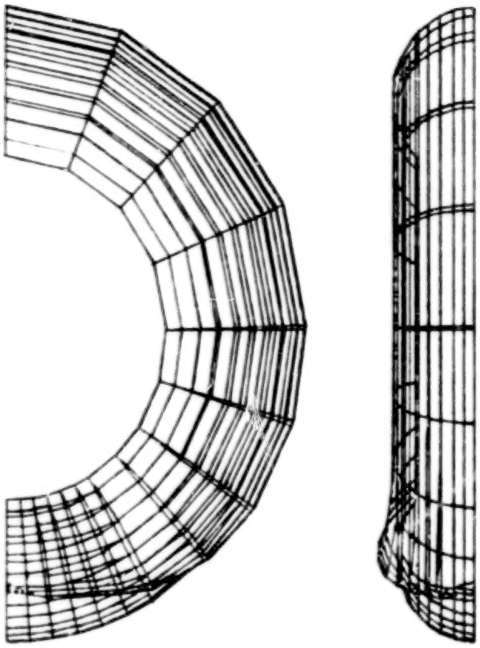

Proceedings of a workshop held at
Langley Research Center
Hampton, Virginia
September 7-9, 1982

NASA

NASA Conference Publication 2264

Tire Modeling

Compiled by
John A. Tanner
Langley Research Center
Hampton, Virginia

Proceedings of a workshop held at
Langley Research Center
Hampton, Virginia
September 7-9, 1982

National Aeronautics
and Space Administration

Scientific and Technical
Information Branch

1983

I

PREFACE

The papers included herein were presented at the NASA Tire Modeling Workshop held at Langley Research Center, September 7-9, 1982. The workshop was organized into six sessions dealing with finite element developments, applications to tire dynamic problems, solution techniques for tire contact problems, experimental data, tire thermal studies, and current design practices. Discussion periods at the end of each session allowed the participants to describe their own work or problem areas and to make recommendations for future directions of tire modeling research.

The objective of the workshop was to provide a forum for the interchange of information among tire analysts and to establish goals and objectives for future research programs in this area. Hence the various conclusions and recommendations suggested by the workshop participants are expected to provide guidance for tire modeling studies within NASA and, to some extent, the tire industry for the next several years.

Special recognition is due Ms. Connie O. Featherston for her planning, coordination, and execution of the various administrative tasks associated with the workshop.

The use of trade names or names of manufacturers in this report does not constitute an official endorsement of such products or manufacturers, either expressed or implied, by the National Aeronautics and Space Administration.

John A. Tanner
Langley Research Center

CONTENTS

PREFACE iii

ATTENDEES vii

FINITE ELEMENT MODELING AND ANALYSIS OF TIRES 1
Ahmed K. Noor and C. M. Andersen

FINITE ELEMENT METHODS FOR NONLINEAR ELASTOSTATIC PROBLEMS IN RUBBER ELASTICITY 39
J. T. Oden, E. B. Becker, T. H. Miller, T. Endo, and E. B. Pires

APPLICATION OF TIRE DYNAMICS TO AIRCRAFT LANDING GEAR DESIGN ANALYSIS 71
Raymond J. Black

A TIRE CONTACT SOLUTION TECHNIQUE 95
John T. Tielking

ANALYTICAL AND EXPERIMENTAL STUDY OF A STANDING TORUS WITH NORMAL LOADS 123
Michael J. Mack, Jr., Daniel E. Hill, and Joseph R. Baumgarten

EXPERIMENTAL AND FINITE ELEMENT STUDY OF A STANDING TORUS UNDER NORMAL AND TANGENTIAL LOADS 141
Donald R. Flugrad and Bruce A. Miller

OVERVIEW OF NASA TIRE EXPERIMENTAL PROGRAMS 163
John A. Tanner

ADHESION TESTING OF AIRCRAFT TIRES 175
Stephen N. Bobo

HEAT GENERATION IN AIRCRAFT TIRES 193
Samuel K. Clark

RESULTS FROM RECENT NASA TIRE THERMAL STUDIES 211
John L. McCarty

SUMMARY OF SESSION DISCUSSIONS 223
John A. Tanner

BIBLIOGRAPHY 225

ATTENDEES

Carl M. Andersen
Senior Research Associate in Math
and Computer Science
College of William and Mary
Williamsburg, VA 23185

Joseph R. Baumgarten
Iowa State University
Department of Mechanical Engineering
209 Mechanical Engineering
Ames, IA 50011

Ian Beaty
Cranfield Institute of Technology
Cranfield, Bedford
United Kingdom MK43 OAL

Raymond J. Black
Bendix Aircraft Brake and Strut
Division
3520 W. Westmoor Street
P.O. Box 10
South Bend, IN 46624

Stephen N. Bobo
Department of Transportation
Transportation Systems Center
Kendall Square
Cambridge, MA 02142

Michael F. Card
NASA Langley Research Center
Mail Stop 244
Hampton, VA 23665

Mathew K. Chakko
B. F. Goodrich Company
Research and Development Center
9921 Brecksville Road
Brecksville, OH 44141

Samuel K. Clark
Department of Applied Mechanics and
Engineering Science
1121 G. G. Brown Lab
Beal and Hayward Streets
University of Michigan
Ann Arbor, MI, 48109

William F. Conley
Goodyear Aerospace Corporation
Wheel and Brake Engineering
D693 B-2
1210 Massillon Road
Akron, OH 44315

Robert H. Daugherty
NASA Langley Research Center
Mail Stop 497
Hampton, VA 23665

Jozef DeEskinazi
The General Tire and Rubber Company
One General Street
Akron, OH 44329

James E. Evans
General Dynamics/Fort Worth
Division
Mail Zone 2646
P.O. Box 748
Fort Worth, TX 76013

Edwin L. Fasanella
Kentron International Incorporated
NASA Langley Research Center
Mail Stop 495
Hampton, VA 23665

Connie O. Featherston
NASA Langley Research Center
Mail Stop 497
Hampton, VA 23665

Denis J. Feld
Goodyear Aerospace Corporation
Research and Development -
Operations
1210 Massillon Road
Department 150-G2
Akron, OH 44315

Donald R. Flugrad
Iowa State University
Department of Mechanical Engineering
209 Mechanical Engineering
Ames, IA 50011

Jerry B. Gehringer
The Goodyear Tire and Rubber Company
1144 E. Market Street
Department 461B
Akron, OH 44316

Robert C. Goetz
NASA Langley Research Center
Mail Stop 118
Hampton, VA 23665

Robert J. Hayduk
NASA Langley Research Center
Mail Stop 495
Hampton, VA 23665

Etienne Jankovich
Battelle Columbus Laboratories
505 King Avenue
Columbus, OH 43201

Ben-Gang Kao
Ford Motor Company
Structural Analysis Department
ECC 218
20000 Rotunda Drive
Dearborn, MI 48121

Subhotosh Khan
E. I. Du Pont De Nemours Incorporated
Textile Research Laboratory
Chestnut Run
Wilmington, DE 19898

Richard L. Kirk
Goodyear Aerospace Corporation
Wheel and Brake Engineering
D693 B-2
1210 Massillon Road
Akron, OH 44315

Werner W. Klingbeil
Corporate Research Center
Uniroyal Incorporated
World Headquarters R-1-2
Middlebury, CT 06749

Lin-E. Kung
Purdue University
Ray W. Herrick Laboratories
West Lafayette, IN 47907

Trafford J. W. Leland
NASA Langley Research Center
Mail Stop 497
Hampton, VA 23665

Daniel I. Livingston
Goodyear Aerospace
142 Goodyear Boulevard
Akron, OH 44316

Spencer D. Lucas
Dunlop Tire and Rubber Corporation
P.O. Box 1109
Buffalo, NY 14240

John R. Luchini
Cooper Tire and Rubber Company
Lima and Western Avenues
Findlay, OH 45840

Bill Macy
McDonnell Aircraft Company
P.O. Box 516
St. Louis, MO 63166

Stan Mays
B. F. Goodrich Tire Company
500 South Main Street
Department 6143
Building 10E
Akron, OH 44318

John L. McCarty
NASA Langley Research Center
Mail Stop 497
Hampton, VA 23665

Marc C. McReynolds
McDonnell-Douglas Corporation
Douglas Aircraft Company
3855 Lakewood Boulevard
Long Beach, CA 90846

Chet Miller
E. I. Du Pont De Nemours Incorporated
Du Pont Experimental Station
Building 304 Room C217
Wilmington, DE 19898

Ahmed K. Noor
George Washington University
Joint Institute for Advancement
of Flight Sciences
Mail Stop 246
Langley Research Center
Hampton, VA 23665

J. Tinsley Oden
The University of Texas
TICOM - ASE-EM Department
Austin, TX 78712

John J. Parker
Cooper Tire and Rubber Company
Lima and Western Avenues
Findlay, OH 45840

Peter Popper
E. I. Du Pont De Nemours Incorporated
Du Pont Experimental Station
Building 304 Room C217
Wilmington, DE 19898

Marion G. Pottinger
B. F. Goodrich
Research and Development Center
9921 Brecksville Road
Brecksville, OH 44141

Gerald R. Potts
GMI Engineering and Management
Institute
1700 W. Third Avenue
Flint, MI 48502

Wim J. Schaffers
E. I. Du Pont De Nemours Incorporated
Du Pont Experimental Station
Building 304 Room C217
Wilmington, DE 19898

Leonard Segel
Highway Safety Research Institute
University of Michigan
Huron Parkway and Baxter Road
Ann Arbor, MI 48109

Kevin L. Smith
AFWAL/FIEMA
Wright-Patterson AFB, OH 45433

Shimoga K. Srinath
Boeing Commercial Airplane Company
P.O. Box 3707
Mail Stop 47-03
Seattle, WA 98124

James A. Susko
Cooper Tire and Rubber Company
Box 550
Findlay, OH 45840

Farhad Tabaddor
B. F. Goodrich Company
500 South Main Street
Akron, OH 44318

John A. Tanner
NASA Langley Research Center
Mail Stop 497
Hampton, VA 23665

Robert L. Taylor
721 Davis Hall
University of California
Department of Civil Engineering
Berkley, CA 94720

Robert G. Thomson
NASA Langley Research Center
Mail Stop 495
Hampton, VA 23665

John T. Tielking
Texas A&M University
Civil Engineering Department
College Station, TX 77843

M. J. Trinko
Department 460G
Goodyear Tire and Rubber Company
Akron, OH 44316

William A. Vogler
Kentron International Incorporated
NASA Langley Research Center
Mail Stop 497
Hampton, VA 23665

M. Susan Williams
NASA Langley Research Center
Mail Stop 495
Hampton, VA 23665

Doug L. Wilson S2105
Scientific Research Laboratory
Ford Motor Company
20000 Rotunda Drive
Dearborn, MI 48121

Christopher Winkler
Highway Safety Research Institute
University of Michigan
Huron Parkway and Baxter Road
Ann Arbor, MI 48109

Thomas J. Yager
NASA Langley Research Center
Mail Stop 497
Hampton, VA 23665

FINITE ELEMENT MODELING AND ANALYSIS OF TIRES

Ahmed K. Noor
Joint Institute for Advancement of Flight Sciences
George Washington University

and

C. M. Andersen
College of William and Mary

Abstract

Although the problem of tire modeling and analysis has been a subject of continuing concern for the tire industry, to date no simple and general tire model exists for predicting the response of the tire under various loading conditions. Much of the recent progress in finite element technology has not been exploited for tire modeling and analysis. The present paper focuses on this issue. Specifically, the paper reviews some of the recent advances in finite element technology which have high potential for application to tire modeling problems. It also identifies the analysis and modeling needs for tires.

The topics covered include: 1) reduction methods for large-scale nonlinear analysis, with particular emphasis on treatment of combined loads, displacement-dependent and nonconservative loadings; 2) development of simple and efficient mixed finite element models for shell analysis, identification of equivalent mixed and purely displacement models, and determination of the advantages of using mixed models; and 3) effective computational models for large-rotation nonlinear problems, based on a total Lagrangian description of the deformation.

INTRODUCTION

The problem of tire modeling and analysis has long been an area of major concern to the tire and aircraft industries. A hierarchy of models varying in the degree of sophistication has been proposed. Some of these models are listed in Fig. 1 and are sketched in Fig. 2. For a detailed description of the models see Ref. 1. The models are grouped into six groups as follows:

The first group consists of the early tire models which are characterized by their simplicity. Among these models are the *string, beam, and ring on elastic (or viscoelastic) foundations*. These models were used by Clark and co-workers (Ref. 2). Their major drawbacks are: 1) they require extensive experiments to evaluate the equivalent properties, and 2) their accuracy and range of validity are not known in advance.

The second group consists of the *cord-network models*, which are sometimes referred to as *netting analysis*, wherein the inflation pressure is assumed to be carried exclusively by the cords (see Ref. 3). These models have the drawback of neglecting both the bending in the tire and the stiffening effect of the rubber.

The third group of models are the *membrane models*, which are based on the use of a linear or nonlinear momentless theory of shells (Refs. 4, 5 and 6). Their major drawback is that they cannot handle discontinuities in loading, geometry or material properties.

The fourth group is the *two-dimensional axisymmetric models* (Ref. 7), which are limited to axisymmetric loadings.

The fifth group is the *three-dimensional continuum models*. Two approaches have been proposed for the analysis of these models. The first approach is based on using semi-analytic techniques to reduce the dimensionality of the problem (e.g., Fourier expansions in the circumferential direction). The second approach is based on using three-dimensional isoparametric solid elements.

The sixth group of models includes a variety of *two-dimensional thin and thick shell models* (see, for example, Refs. 8 and 9). Thin shell models neglect transverse shear deformation, and their use for modeling tires is therefore questionable. Anisotropy results in increasing the size of the analysis model, and consequently many investigators neglect its effects by using an orthotropic model.

The present paper focuses on the use of two-dimensional thick shell models.

DIFFERENT TIRE MODELS

MODEL	DRAWBACKS
• SIMPLE MODELS STRING BEAM } ON { ELASTIC OR VISCO-ELASTIC } FOUNDATION RING	• REQUIRE EXTENSIVE EXPERIMENTS TO EVALUATE EQUIVALENT PROPERTIES • ACCURACY AND RANGE OF VALIDITY NOT KNOWN IN ADVANCE
• CORD-NETWORK MODELS	• NEGLECT BENDING IN TIRE AND STIFFENING EFFECTS OF RUBBER
• MEMBRANE MODELS (BASED ON MOMENTLESS THEORY OF SHELLS)	• CANNOT HANDLE DISCONTINUITIES (OR SHARP CHANGES) IN LOADING, GEOMETRY (CURVATURE) OR MATERIAL PROPERTIES
• TWO-DIMENSIONAL AXISYMMETRIC MODELS	• LIMITED TO AXISYMMETRIC LOADING
• THREE-DIMENSIONAL MODELS • SEMI-ANALYTIC SOLUTIONS • THREE-DIMENSIONAL SOLID ELEMENTS	• COMPUTATIONALLY EXPENSIVE
• LAMINATED ANISOTROPIC SHELL MODELS (THIN AND THICK)	• THIN SHELL MODELS NOT ADEQUATE • EFFECT OF ANISOTROPY CAN BE SIGNIFICANT

Figure 1

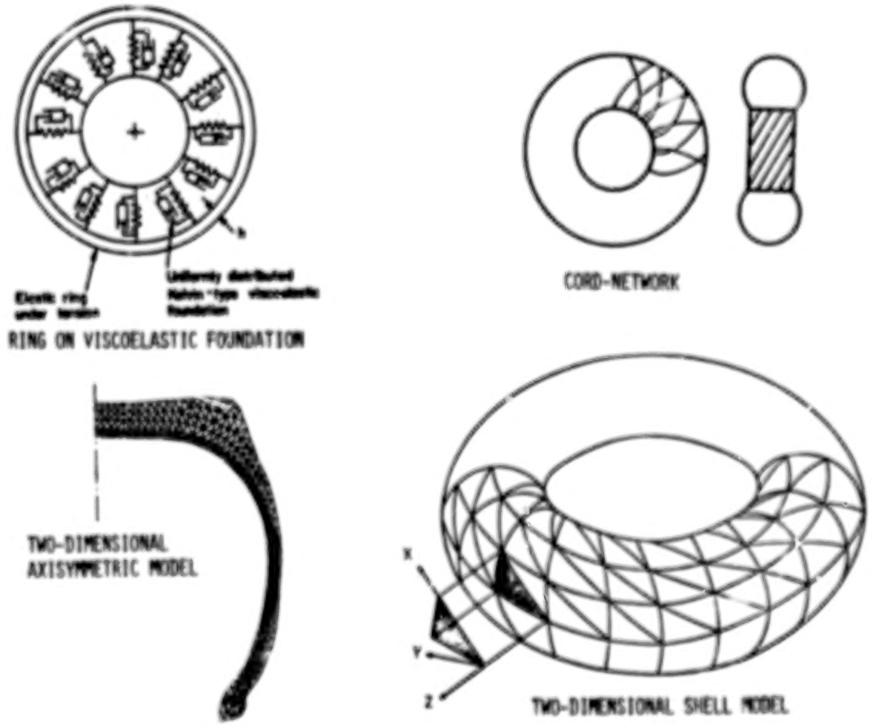
b
Elastic ring under tension
Uniformly distributed Kelvin-type viscoelastic foundation
RING ON VISCOELASTIC FOUNDATION
CORD-NETWORK
TWO-DIMENSIONAL AXISYMMETRIC MODEL
X
Y
Z
TWO-DIMENSIONAL SHELL MODEL

Figure 2

BEST DOCUMENT AVAILABLE

BEST DOCUMENT AVAILABLE

TIRE CONFIGURATION AND COMPONENTS

Typical configurations and components of modern tires are shown in Fig. 3 (see Ref. 10). Commercially successful tires are now built as a series of layers of flexible high-modulus cords encased in a low-modulus rubber or rubber-like material. Hence, a laminated (or layered) model is needed.

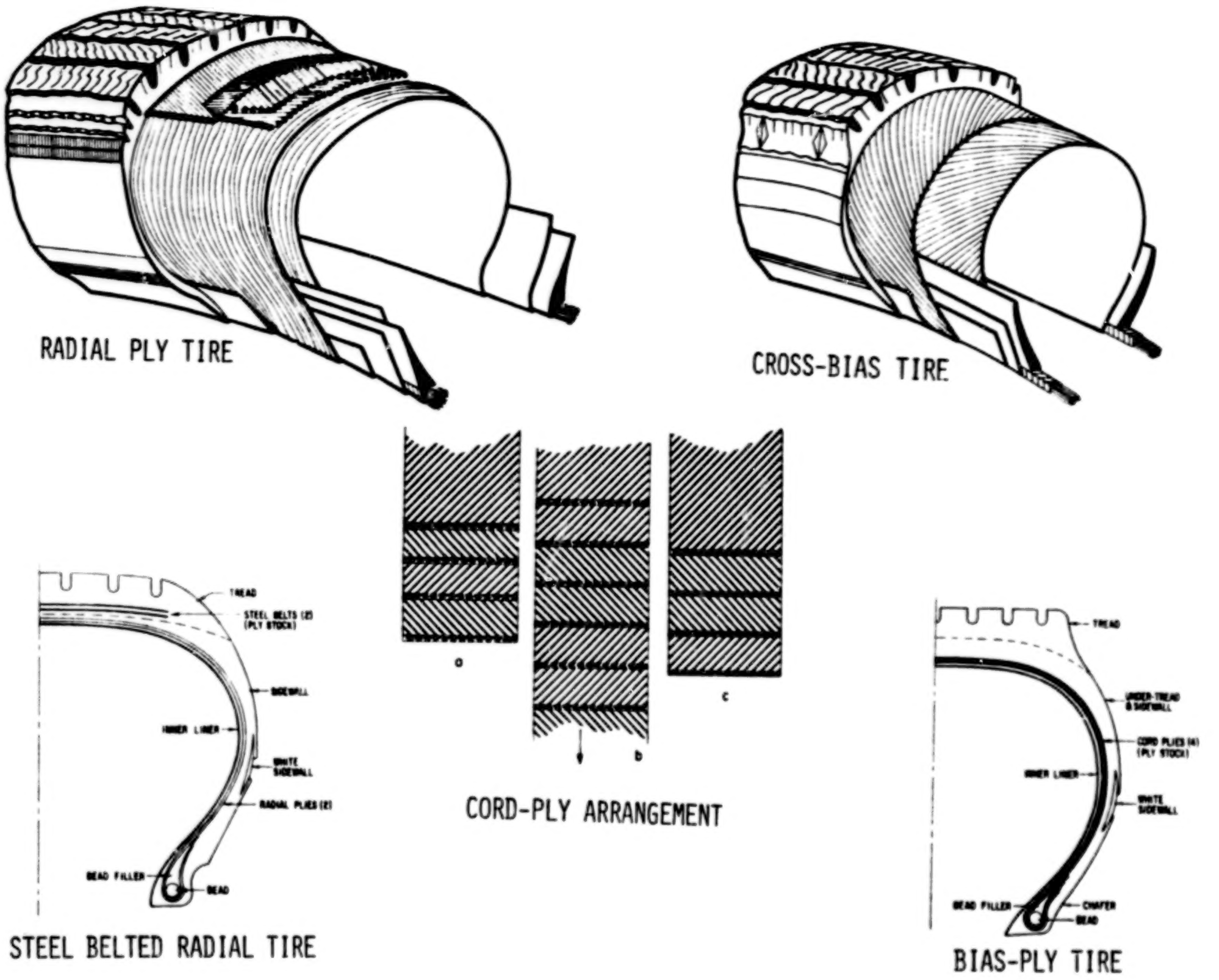
RADIAL PLY TIRE
CROSS-BIAS TIRE
a
b
c
CORD-PLY ARRANGEMENT
TREAD
STEEL BELTS (2) (PLY STOCK)
SIDEWALL
INNER LINER
WHITE SIDEWALL
RADIAL PLIES (2)
BEAD FILLER
BEAD
STEEL BELTED RADIAL TIRE
TREAD
UNDER-TREAD & SIDEWALL
CORD PLIES (4) (PLY STOCK)
INNER LINER
WHITE SIDEWALL
BEAD FILLER
CHAFER
BEAD
BIAS-PLY TIRE

Figure 3

TIRE LOADS

The three types of loads applied to the tire and their major characteristics are listed in Fig. 4. The three load types are:

1) *Inflation pressure*, which is axisymmetric but is displacement dependent

2) *Mechanical loads* which include centrifugal force, impact loading, contact forces, and frictional forces; except for the centrifugal force, which is axisymmetric (and displacement dependent), all the other loads are symmetric

3) *Thermal loads*, which arise due to various manufacturing and operating conditions, such as unequal expansion and contraction of rubber and cord, hysteretic heating, sliding of the tread on a rough surface, and cord shrinking after molding

LOADS	CHARACTERISTICS
• INFLATION PRESSURE	• AXISYMMETRIC BUT DISPLACEMENT-DEPENDENT
• MECHANICAL LOADS	
• CENTRIFUGAL FORCE	• AXISYMMETRIC BUT DISPLACEMENT-DEPENDENT
• IMPACT LOADING	• ASYMMETRIC
• CONTACT FORCES	⋮
• FRICTIONAL FORCES	⋮
• THERMAL LOADS	• ASYMMETRIC
• UNEQUAL EXPANSION AND CONTRACTION OF RUBBER AND CHORD	⋮
• HYSTERETIC HEATING	⋮
• CHORD SHRINKING AFTER MOLDING	⋮

Figure 4

CHARACTERISTICS OF EFFECTIVE SHELL ELEMENTS FOR ANALYZING TIRES

The characteristics of an effective shell finite element model for analyzing tires are listed in Fig. 5. The shell element is developed using either a consistent two-dimensional shell theory or a three-dimensional continuum theory with proper interpolation functions in the thickness direction. The elements obtained by using the latter approach are referred to as *degenerate shell elements*. If a two-dimensional shell theory is used, the elements need to be deep and curved and must account for each of the following effects:

1) Laminated construction and anisotropic material behavior
2) Variation in geometry (e.g., curvature and thickness) as well as of other lamination parameters
3) Transverse shear deformation
4) Large rotations
5) Pressure stiffness (for displacement-dependent loadings such as inflation pressure)
6) Thermoviscoelastic material response

- BASED ON EITHER
  - CONSISTENT TWO-DIMENSIONAL SHELL THEORY, OR
  - THREE-DIMENSIONAL CONTINUUM THEORY WITH PROPER INTERPOLATION FUNCTIONS IN THE THICKNESS DIRECTION (DEGENERATE SHELL ELEMENTS)
- DEEP, CURVED ELEMENTS
- INCLUDE EFFECTS OF:
  - LAMINATED CONSTRUCTION AND ANISOTROPIC MATERIAL BEHAVIOR
  - VARIATION IN GEOMETRY (E.G., CURVATURE AND THICKNESS), LAMINATION PARAMETERS
  - TRANSVERSE SHEAR DEFORMATION
  - LARGE ROTATIONS
  - PRESSURE STIFFNESS (FOR DISPLACEMENT-DEPENDENT LOADING; E.G., INFLATION PRESSURE)
  - THERMOVISCOELASTIC MATERIAL RESPONSE

Figure 5

OBJECTIVES AND SCOPE

The objectives of this paper are listed in Fig. 6. They are:

1) To review some recent developments in finite element technology which are applicable to the analysis and modeling of tires

2) To identify some of the analysis and modeling needs for tires

The paper is divided into four parts. The first part deals with new developments in reduction methods for nonlinear problems. These include computational procedures for handling combined, displacement-dependent, and nonconservative loads. The second part of the paper deals with mixed finite element models for tires in which the fundamental unknowns consist of both force and displacement parameters. The equivalence of some of these models with some of the purely displacement models is discussed.

The third part of the paper deals with large-rotation nonlinear problems. Two formulations are presented; namely, a mixed formulation and a penalty formulation. Both formulations are based on the total Lagrangian description of the deformation. The fourth and last part of the paper deals with analysis and modeling needs for tires.

OBJECTIVES

- REVIEW SOME RECENT DEVELOPMENTS IN FINITE ELEMENT TECHNOLOGY WHICH ARE APPLICABLE TO ANALYSIS AND MODELING OF TIRES
- IDENTIFY ANALYSIS AND MODELING NEEDS FOR TIRES

SCOPE

- REDUCTION METHODS FOR NONLINEAR PROBLEMS
  - COMBINED LOADING PROBLEMS
  - DISPLACEMENT-DEPENDENT AND NONCONSERVATIVE LOADING PROBLEMS
  - DYNAMIC PROBLEMS
- MIXED FINITE ELEMENT MODELS
  - EFFICIENT AND ACCURATE MIXED MODELS
  - EQUIVALENT CLASSES OF MIXED MODELS AND REDUCED/SELECTIVE INTEGRATION DISPLACEMENT MODELS
  - MERITS OF MIXED MODELS OVER EQUIVALENT DISPLACEMENT MODELS
- LARGE-ROTATION NONLINEAR PROBLEMS
  - MIXED FORMULATION
  - PENALTY FORMULATION

Figure 6

REDUCTION METHODS FOR NONLINEAR TIRE PROBLEMS

The first topic considered in this paper is reduction methods for nonlinear analysis. The basic features of reduction methods are outlined in Fig. 7. They are techniques for reducing the number of degrees of freedom through the transformation shown in the figure. The vector $\{X\}$ represents the original displacement degrees of freedom. The vector $\{\psi\}$ refers to amplitudes of displacement modes and $[\Gamma]$ is a transformation matrix whose columns represent a priori chosen global displacement modes.

As is to be expected, the effectiveness of reduction methods depends to a great extent on the proper selection of the displacement modes. In a number of studies it was shown that an effective choice of the displacement modes includes the various-order derivatives of the displacement vector with respect to the load parameter (see Refs. 11 and 12). These vectors are *generated by using the finite element model of the tire*. The recursion formulas for evaluating the derivatives $\{\frac{\partial X}{\partial p}\}$, $\{\frac{\partial^2 X}{\partial p^2}\}$, ... are obtained by successive differentiation of the original finite element equations. The left-hand sides of the recursion formulas are the same (see Ref. 12). Therefore, *only one matrix factorization is required for the generation of all the global approximation vectors*. Several numerical experiments have demonstrated the effectiveness of this choice (see Refs. 12 and 13).

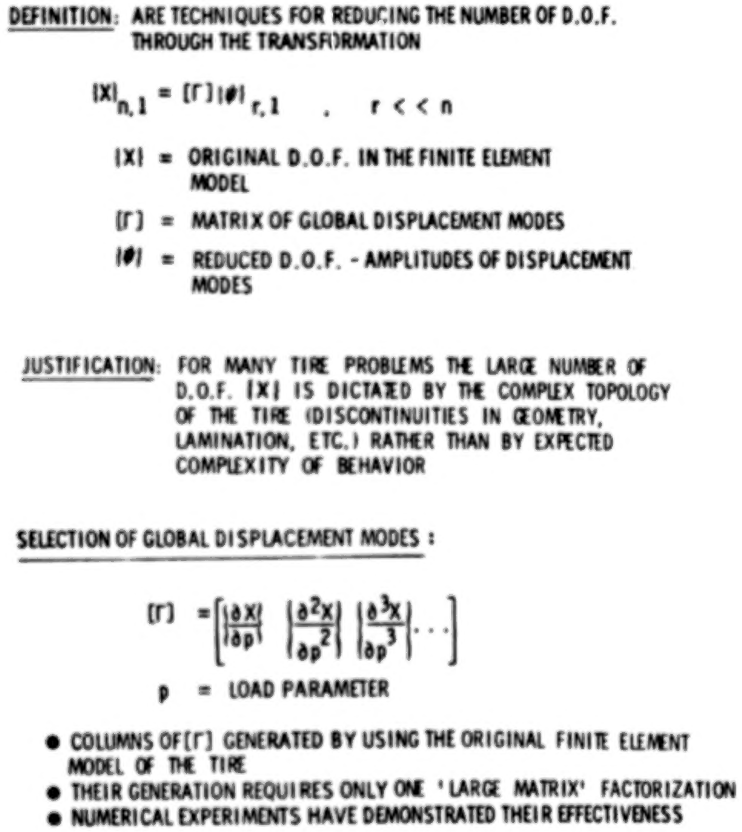

DEFINITION: ARE TECHNIQUES FOR REDUCING THE NUMBER OF D.O.F. THROUGH THE TRANSFORMATION

$$\{X\}_{n,1} = [\Gamma]\{\psi\}_{r,1} \quad , \quad r << n$$

$\{X\}$ = ORIGINAL D.O.F. IN THE FINITE ELEMENT MODEL

$[\Gamma]$ = MATRIX OF GLOBAL DISPLACEMENT MODES

$\{\psi\}$ = REDUCED D.O.F. - AMPLITUDES OF DISPLACEMENT MODES

JUSTIFICATION: FOR MANY TIRE PROBLEMS THE LARGE NUMBER OF D.O.F. $\{X\}$ IS DICTATED BY THE COMPLEX TOPOLOGY OF THE TIRE (DISCONTINUITIES IN GEOMETRY, LAMINATION, ETC.) RATHER THAN BY EXPECTED COMPLEXITY OF BEHAVIOR

SELECTION OF GLOBAL DISPLACEMENT MODES :

$$[\Gamma] = \left[\left\{\frac{\partial X}{\partial p}\right\} \left\{\frac{\partial^2 X}{\partial p^2}\right\} \left\{\frac{\partial^3 X}{\partial p^3}\right\} \ldots \right]$$

p = LOAD PARAMETER

- COLUMNS OF $[\Gamma]$ GENERATED BY USING THE ORIGINAL FINITE ELEMENT MODEL OF THE TIRE
- THEIR GENERATION REQUIRES ONLY ONE 'LARGE MATRIX' FACTORIZATION
- NUMERICAL EXPERIMENTS HAVE DEMONSTRATED THEIR EFFECTIVENESS

Figure 7

BASIC EQUATIONS USED IN REDUCTION METHODS FOR NONLINEAR TIRE PROBLEMS

The basic equations used in the reduction methods for geometrically nonlinear tire problems are given in Fig. 8. It is worth noting that the original displacement unknowns $\{X\}$ can be on the order of thousands whereas the reduced unknowns $\{\psi\}$ are typically 20 or less. This is true regardless of the complexity of the structure and/or loading. The details of the computational procedure for tracing the load-deflection paths in geometrically nonlinear static analysis are given in Refs. 11 and 12.

	ACTUAL (LARGE) PROBLEM	REDUCED (SMALL) PROBLEM
FUNDAMENTAL UNKNOWNS	$\{X\}$ = INDIVIDUAL DISPLACEMENTS $\rightarrow \boxed{\{X\} = [\Gamma]\{\psi\}}$ ● THOUSANDS OF UNKNOWNS	$\rightarrow$ AMPLITUDES OF DISPLACEMENT MODES ● TWENTY OR LESS
GOVERNING EQUATIONS	$[K]\{X\} + \{G(X)\} - p\{P\} = 0$ ~ 1000 EQUATIONS	$[\tilde{K}]\{\psi\} + \{\tilde{G}(\psi)\} - p\{\tilde{P}\} = 0$ ~ 20 EQUATIONS
HOW TO TRACE LOAD-DEFLECTION PATH	● REPEATED SOLUTION OF LARGE SYSTEMS OF SIMULTANEOUS NONLINEAR ALGEBRAIC EQUATIONS	● GENERATION OF $[\Gamma]$ ● MARCHING WITH SMALL SYSTEM OF EQUATIONS ● ERROR SENSING AND CONTROL (UPDATING $[\Gamma]$ WHENEVER NEEDED)

$$[\tilde{K}] = [\Gamma]^T[K][\Gamma] \quad , \quad \{\tilde{G}(\psi)\} = [\Gamma]^T\{G(X)\} \quad , \quad \{\tilde{P}\} = [\Gamma]^T\{P\}$$

Figure 8

APPLICATION OF REDUCTION METHODS TO GEOMETRICALLY NONLINEAR ANALYSIS OF A TIRE SUBJECTED TO UNIFORM INTERNAL PRESSURE

As a simple application of reduction methods to the geometrically nonlinear analysis of tires, consider the laminated anisotropic elliptic toroidal shell shown in Fig. 9. Due to axial symmetry, only one meridian was modeled using four-noded elements with cubic Lagrangian interpolation functions for all the displacement and rotation degrees of freedom. The high accuracy of the total strain energy obtained by using six basis vectors is demonstrated in Fig. 9.

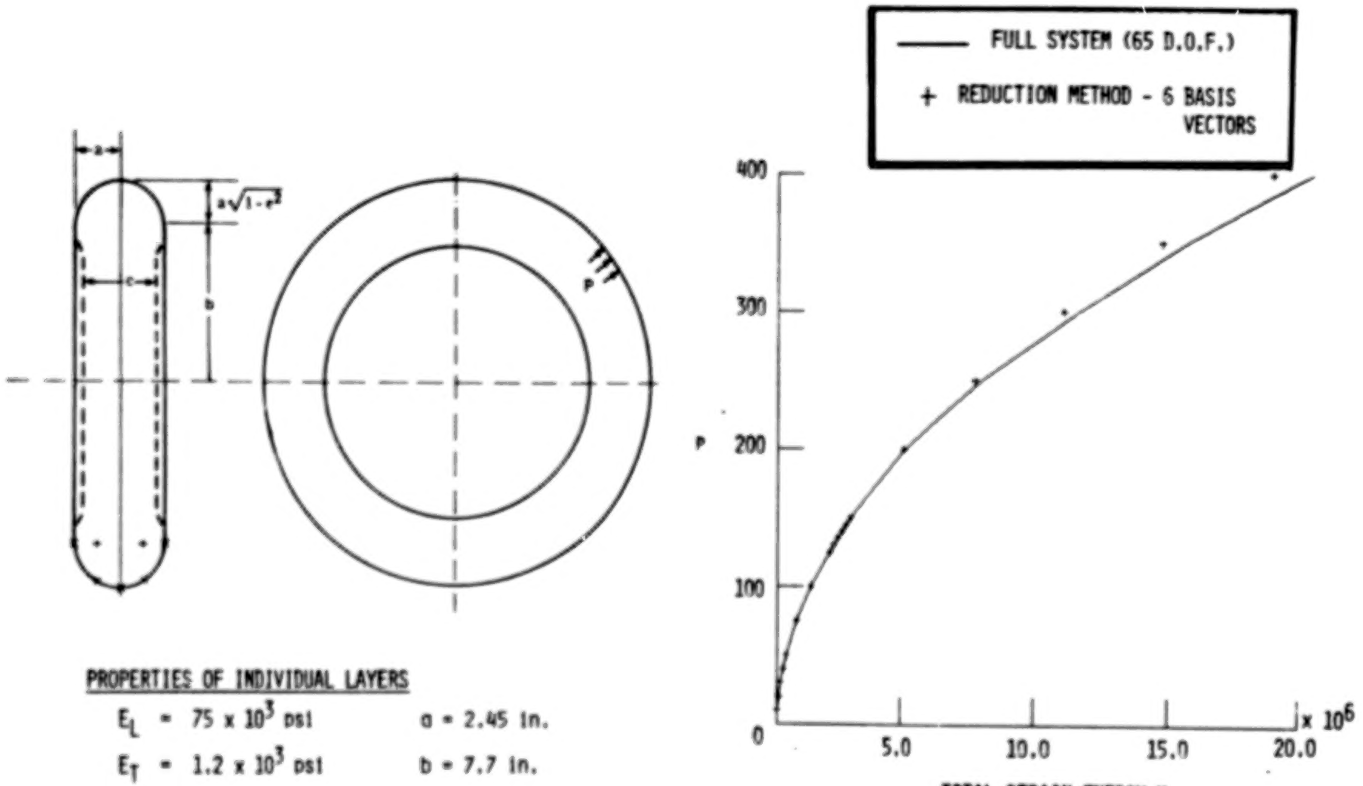

PROPERTIES OF INDIVIDUAL LAYERS

E_L = 75 x 10^3 psi a = 2.45 in.
E_T = 1.2 x 10^3 psi b = 7.7 in.
G_{LT} = 450 psi c = 4.0 in.
G_{TT} = 270 psi h = 0.42 in.
ν_{LT} = 0.4 e = 0.5

CORD ORIENTATION + 45/- 45/ + 45/ - 45 ....
NL = 10

Figure 9

TREATMENT OF COMBINED LOADS

The basic equations and the computational procedure used in applying reduction methods to the analysis of tires subjected to combined loads are highlighted in Figs. 10 and 11. For simplicity, only two independent loads are considered.

First, the original finite element equations are given. The external loading is normalized with respect to two independent load parameters p_1 and p_2. The basis reduction is done as before, via the transformation shown in Fig. 10. Then the Rayleigh-Ritz technique is used to approximate the original set of finite element equations by a reduced system of equations in the new unknown parameters $\{\psi\}$. The number of these equations is considerably less than that of the original equations.

As previously noted, the crux of reduction methods is the proper selection of the transformation matrix $[\Gamma]$. In the case of combined loading, the columns of the matrix $[\Gamma]$ are selected to be the various-order derivatives of the displacement vector $\{X\}$ with respect to the two independent parameters p_1 and p_2.

To trace the different nonlinear paths, corresponding to different combinations of the independent load parameters, the basis vectors are evaluated for the unloaded structure ($p_1 = p_2 = 0$), and the corresponding reduced equations are generated. The different nonlinear paths of the tire are obtained by fixing one of the load parameters, varying the other, and repeating the process with different values of the first load parameter. This is all done using the *same set of reduced equations*. The total cost of the analysis, to a first approximation, is little more than the cost of one linear solution of the original, full system of finite element equations. The procedure is described in detail in Ref. 14.

As a by-product of this technique, a considerable reduction can be made in the size of the analysis model used in studying the nonlinear response of tires subjected to asymmetric loading. This can be accomplished by decomposing the loading into symmetric and antisymmetric components and treating each as an independent loading.

REDUCTION METHODS FOR NONLINEAR PROBLEMS
TREATMENT OF COMBINED LOADS

GOVERNING FINITE ELEMENT EQUATIONS

$$[K]\{X\} + \{G(X)\} - p_1\{P^{(1)}\} - p_2\{P^{(2)}\} = 0$$

$[K]$ = LINEAR GLOBAL STIFFNESS MATRIX

$\{X\}$ = VECTOR OF NODAL DISPLACEMENTS

$\{G(X)\}$ = VECTOR OF NONLINEAR TERMS

$\{P^{(1)}\}$, $\{P^{(2)}\}$ = NORMALIZED LOAD VECTORS

p_1, p_2 = INDEPENDENT LOAD PARAMETERS

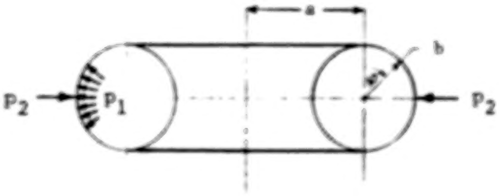

BASIS REDUCTION

$$\{X\}_{n,1} = [\Gamma]_{n,r}\{\psi\}_{r,1} \quad , \quad r << n$$

REDUCED SYSTEM OF EQUATIONS

$$[\tilde{K}]\{\psi\} + \{\tilde{G}(\psi)\} - p_1\{\tilde{P}^{(1)}\} - p_2\{\tilde{P}^{(2)}\} = 0$$

Figure 10

TREATMENT OF COMBINED LOADS

SELECTION OF BASIS VECTORS

$$\{X\} = [\Gamma]\{\psi\}$$

$$[\Gamma] = \left[\{\frac{\partial X}{\partial p_1}\} \quad \{\frac{\partial X}{\partial p_2}\} \quad \{\frac{\partial^2 X}{\partial p_1^2}\} \quad \{\frac{\partial^2 X}{\partial p_1 \partial p_2}\} \quad \{\frac{\partial^2 X}{\partial p_2^2}\} \quad \cdots \right]$$

COMPUTATIONAL PROCEDURE

- EVALUATE BASIS VECTORS AT $p_1 = p_2 = 0$ (UNLOADED TIRE) AND GENERATE REDUCED EQUATIONS
- TRACE DIFFERENT EQUILIBRIUM PATH BY FIXING ONE OF THE LOAD PARAMETERS AND VARYING THE OTHER (USING THE SAME SET OF REDUCED EQUATIONS)

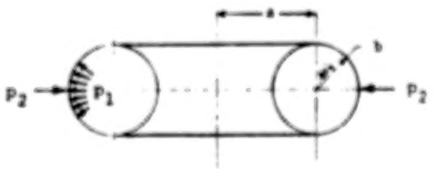

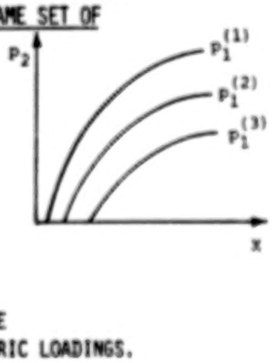

NOTE: THIS APPROACH CAN BE USED TO REDUCE THE SIZE OF ANALYSIS MODELS FOR THE CASE OF UNSYMMETRIC LOADINGS.

Figure 11

TREATMENT OF DISPLACEMENT-DEPENDENT AND NONCONSERVATIVE LOADING

The basic equations used in applying reduction methods to the nonlinear analysis of tires subjected to displacement-dependent loading are given in Fig. 12.

First, the governing finite element equations for the total Lagrangian formulation are shown. The only new term in these equations is the pressure stiffness matrix which represents the follower-load effect and is unsymmetric for nonconservative loadings. The basis reduction is done and the reduced equations are obtained in the manner outlined previously. The following two important facts are to be noted:

1. The basis vectors are evaluated for the unloaded structure. Hence, the pressure stiffness matrix does not enter into the left-hand side and *only the linear symmetric global stiffness matrix needs to be decomposed.*

2. Since the reduced equations are small in number (on the order of ten or less) no symmetrization is needed in the case of nonconservative loadings.

GOVERNING FINITE ELEMENT EQUATIONS

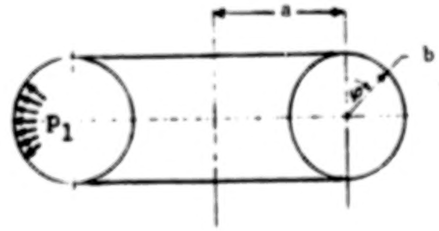

FOR A TOTAL LAGRANGIAN FORMULATION

$$\left[[K] - p[K^{(p)}]\right]\{X\} + \{G(X)\} - p\{P\} = 0$$

$[K^{(p)}]$ = PRESSURE STIFFNESS MATRIX (UNSYMMETRIC FOR NONCONSERVATIVE LOADING)

BASIS REDUCTION

$$\{X\} = [\Gamma]\{\psi\}$$

REDUCED SYSTEM OF EQUATIONS

$$\left[[\tilde{K}] - p[\tilde{K}^{(p)}]\right]\{\psi\} + \{\tilde{G}(\psi)\} - p\{\tilde{P}\} = 0$$

NOTES:

- BASIS VECTORS ARE EVALUATED AT $p = 0$. THEREFORE, ONLY THE SYMMETRIC $[K]$ MATRIX NEEDS TO BE DECOMPOSED.
- REDUCED EQUATIONS ARE SMALL IN NUMBER (~10). THEREFORE, NO SYMMETRIZATION IS NEEDED.

Figure 12

APPLICATION OF REDUCTION METHODS TO THE BIFURCATION BUCKLING ANALYSIS OF A RING SUBJECTED TO HYDROSTATIC PRESSURE

As a simple application of reduction methods to structures subjected to displacement-dependent loadings, consider the circular ring subjected to hydrostatic pressure shown in Fig. 13.

Doubly-symmetric buckling modes are considered; hence, only one quadrant of the ring was analyzed using higher-order shear-flexible elements with a total of 59 nonzero degrees of freedom. The lowest three buckling loads obtained using three, four and five vectors are listed in Fig. 13. The lowest buckling load obtained by using four vectors agrees, to five significant digits, with that obtained using the full system of equations. With five vectors, the error in the third buckling load is less than 3%.

NUMBER OF BASIS VECTORS	EIGENVALUES $\hat{p} = \frac{p_o R^3}{EI}$		
	$\hat{p}_1$	$\hat{p}_2$	$\hat{p}_3$
3	2.9998	15.1888	
4	2.9997	14.9964	36.5126
5	2.9997	14.9957	35.9668
FULL SYSTEM (59 D.O.F.)	2.9997	14.9947	34.9751

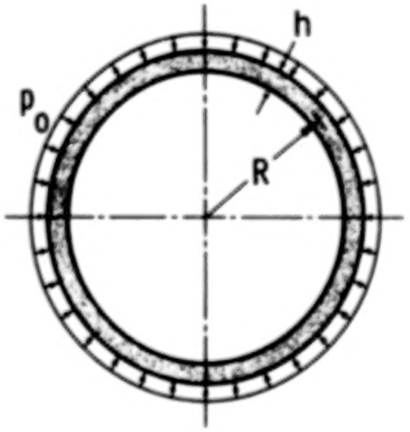

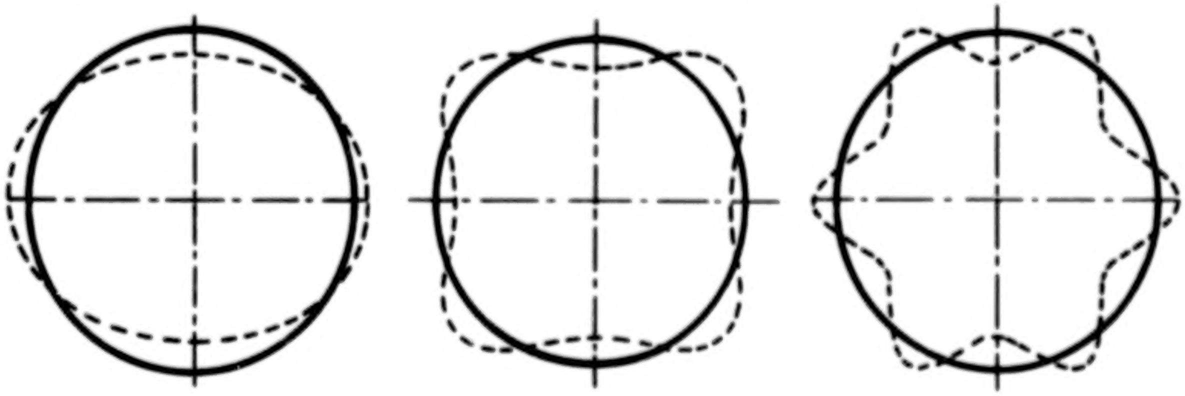

Figure 13

REDUCTION METHODS FOR NONLINEAR DYNAMIC PROBLEMS

The application of reduction methods to transient tire problem is highlighted in Fig. 14. First, the governing semi-discrete finite element equations are given for the case of no damping. Then the key elements for an effective reduction method are listed (see Ref. 13). They include:

1) The proper selection of basis vectors (the columns of the matrix $[\Gamma]$)

2) Characterization of nonlinear dynamic response by means of one or few scalars

3) Sensing and controlling the error in the reduced system of equations

GOVERNING SEMI-DISCRETE FINITE ELEMENT EQUATIONS

$$[M]\{\ddot{X}\} = \{P\}_t - [K]\{X\} - \{G(X)\}$$

KEY ELEMENTS FOR EFFECTIVE REDUCTION METHOD

- **PROPER SELECTION OF BASIS VECTORS**

$$\{X\}_{n,1} = [\Gamma]_{n,r}\{\psi\}_{r,1}, \quad r << n$$

- CHARACTERIZATION OF NONLINEAR DYNAMIC RESPONSE BY MEANS OF ONE OR FEW SCALARS

- SENSING AND CONTROLLING THE ERROR IN THE REDUCED SYSTEM OF EQUATIONS

Figure 14

SELECTION OF BASIS VECTORS FOR THE CASE OF STEP LOADING

A particular choice of basis vectors which was found to work well for the case of step loading is shown in Fig. 15. The vectors consist of a few eigenvectors of the linear problem and a few eigenvectors of the steady-state (static) nonlinear problem. The matrix $[\frac{\partial G_i}{\partial X_j}]$ is obtained by using the steady-state (static) nonlinear solution. Reduction methods can be used to reduce the computational effort required for generating the steady-state nonlinear solution.

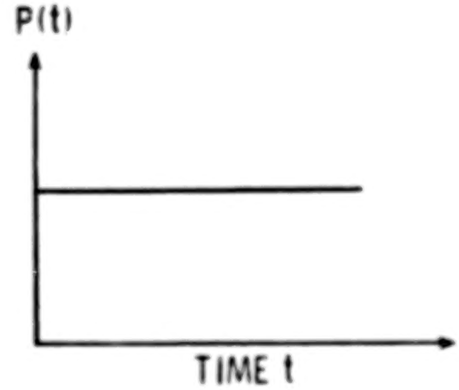

BASIS VECTORS CONSIST OF:

- FEW EIGENVECTORS OF LINEAR PROBLEM

$$[K]\{X\} = \lambda [M]\{X\}$$

- FEW EIGENVECTORS OF STEADY-STATE (STATIC) NONLINEAR PROBLEM

$$\left[[K] + \left[\frac{\partial G_j}{\partial X_j}\right] \right] \{X\} = \lambda [M]\{X\}$$

Figure 15

APPLICATION TO CLAMPED SHALLOW SPHERICAL CAP SUBJECTED TO A CONCENTRATED LOAD AT THE APEX

As a simple application of reduction methods to nonlinear dynamic problems, consider the clamped spherical cap subjected to a concentrated load which has a step variation in time (see Fig. 16). The displacement time history obtained using the full system of finite element equations, the reduced system with ten linear vibration modes, and the reduced system with the proposed set of modes are shown in Fig. 16. *The basis vectors (eigenmodes) were not updated throughout the analysis.* As can be seen from Fig. 16, the proposed set of basis vectors predicts qualitatively the correct response. The phase shift was almost eliminated by increasing the number of basis vectors to 14.

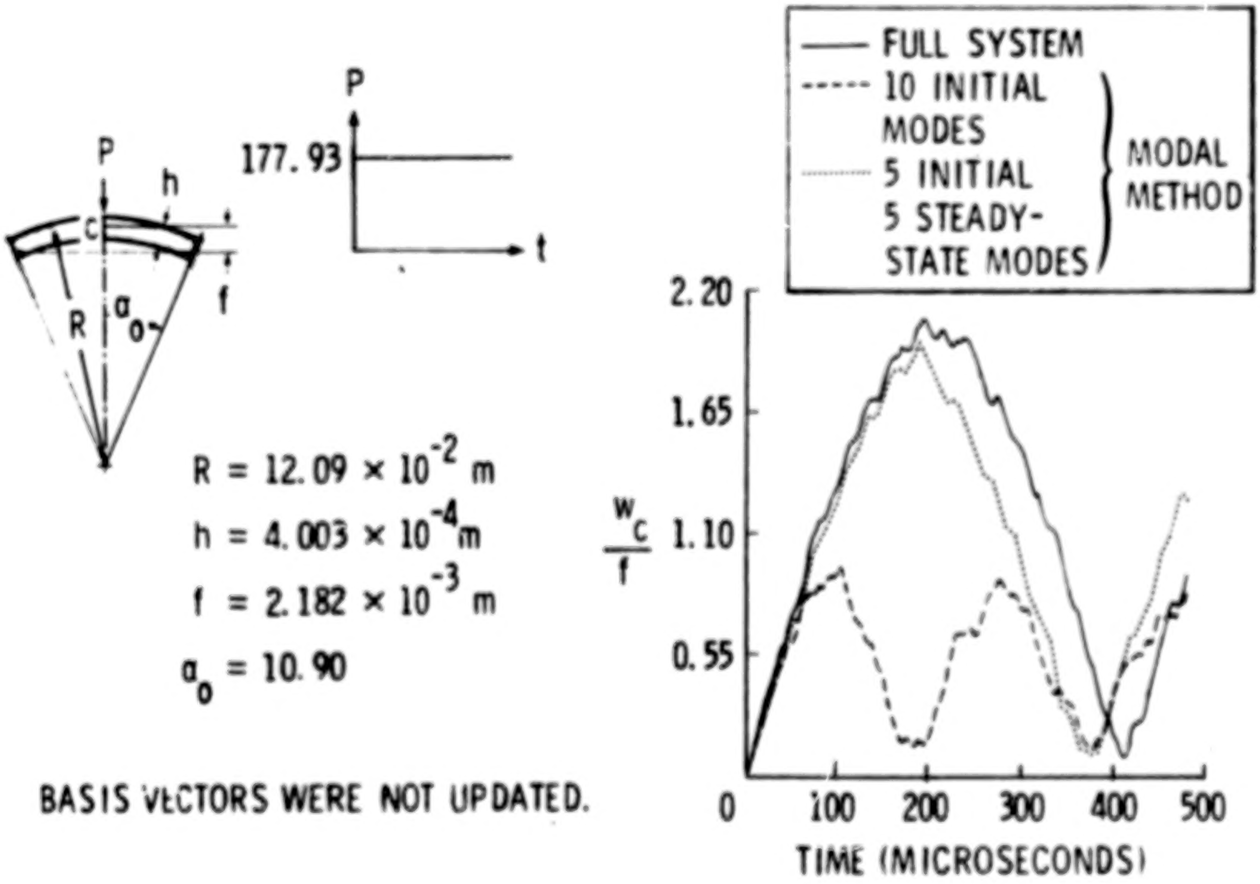

Figure 16

MIXED FINITE ELEMENT MODELS FOR TIRES

The second topic considered in this paper is mixed finite element models for tires. The basic features of the mixed models are outlined in Fig. 17. The finite element models include the effects of both laminated anisotropic construction and transverse shear deformation, and allow the geometric and material properties to vary within individual elements. The fundamental unknowns consist of the eight stress resultants and the five generalized displacements. The stress resultants are discontinuous at element interfaces, and therefore can be eliminated on the element level.

- TIRE MODELED USING LAMINATED ANISOTROPIC, SHEAR-FLEXIBLE, DEEP SHELL ELEMENTS WITH VARIABLE GEOMETRIC AND MATERIAL PROPERTIES
- FUNDAMENTAL UNKNOWNS ARE:

STRESS RESULTANTS	$N_{\alpha\beta}$, $M_{\alpha\beta}$, Q_α
GENERALIZED DISPLACEMENTS	u_α , w , ϕ_α

- STRESS RESULTANTS ARE DISCONTINUOUS AT ELEMENT INTERFACES - ELIMINATED ON ELEMENT LEVEL

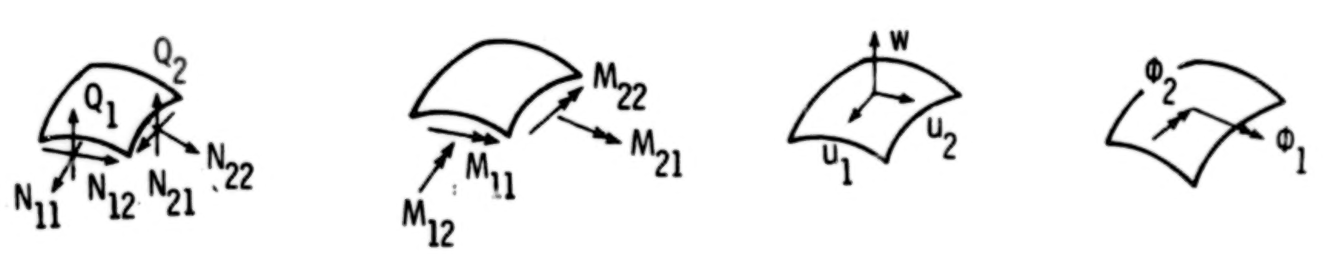

Figure 17

MATHEMATICAL FORMULATION FOR THE MIXED MODEL

The mathematical formulation for the two-field mixed model is based on the use of a moderate-rotation nonlinear shell theory in conjunction with the Hellinger-Reissner mixed variational principle. The basic features of this formulation are outlined in Fig. 18. Different approximation functions are used for each of the stress-resultant fields and the generalized displacement field. The governing finite element equations for individual elements can be partitioned as shown in Fig. 18. The vector $\{M\}$ is quadratic in $\{X\}$ and the vector $\{G\}$ is bilinear in $\{H\}$ and $\{X\}$.

For mixed models with discontinuous stress resultants at element interfaces, the stress resultants can be eliminated on the element level and the governing finite element equations reduce to cubic equations in $\{X\}$ (see Ref. 15).

APPROXIMATION FUNCTIONS

STRESS RESULTANTS

$$\begin{Bmatrix} N_{\alpha\beta} \\ M_{\alpha\beta} \\ Q_{\alpha} \end{Bmatrix} = [\bar{N}]\{H\} \quad . \quad \{H\} = \text{VECTOR OF STRESS RESULTANT PARAMETERS}$$

DISPLACEMENTS

$$\begin{Bmatrix} u_{\alpha} \\ w \\ \phi_{\alpha} \end{Bmatrix} = [N]\{X\} \quad . \quad \{X\} = \text{VECTOR OF NODAL DISPLACEMENTS}$$

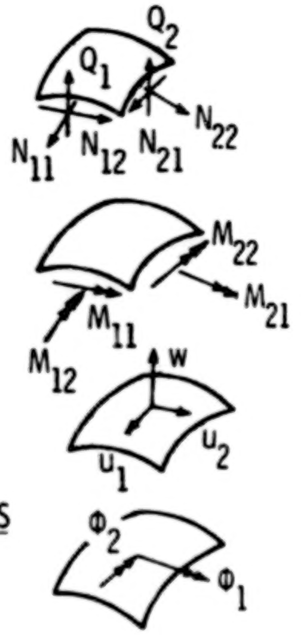

GOVERNING FINITE ELEMENT EQUATIONS FOR INDIVIDUAL ELEMENTS

$$\begin{bmatrix} -[F] & [S] \\ [S]^T & [0] \end{bmatrix} \begin{Bmatrix} H \\ X \end{Bmatrix} + \begin{Bmatrix} \{M(X)\} \\ \{G(H,X)\} \end{Bmatrix} = \begin{Bmatrix} 0 \\ P \end{Bmatrix}$$

WHERE $\{M(X)\}$ AND $\{G(H,X)\}$ ARE VECTORS OF NONLINEAR TERMS (QUADRATIC AND BILINEAR IN $\{H\}$ AND $\{X\}$).

DISCONTINUOUS STRESS RESULTANTS AT ELEMENT INTERFACES

$$\{H\} = [F]^{-1}[S]\{X\} + [F]^{-1}\{M(X)\}$$

AND GOVERNING FINITE ELEMENT EQUATIONS REDUCE TO

$$[S]^T[F]^{-1}[S]\{X\} + \{\bar{G}(X)\} = \{P\}$$

WHERE $\{\bar{G}(X)\}$ = VECTOR OF NONLINEAR TERMS (CUBIC IN $\{X\}$).

Figure 18

REDUCED/SELECTIVE INTEGRATION DISPLACEMENT MODELS

In recent years a class of displacement models with a performance comparable to that of the mixed model has been developed. These are referred to as reduced/selective integration displacement models (see, for example, Refs. 15 and 16). The major features of these models are outlined in Fig. 19. The governing finite element equations for the individual elements are cubic in $\{X\}$. The definitions of full, reduced, and selective integration are given in Fig. 19. If an $n \times n$ Gauss-Legendre formula is used to integrate the linear stiffness matrix $[K]$ exactly for parallelogram elements, then in full integration $n \times n$ quadrature points are used. In reduced integration $(n-1) \times (n-1)$ quadrature points are used, and in selective integration $n \times n$ quadrature points are used for some terms of $[K]$ and $(n-1) \times (n-1)$ points for other terms.

GOVERNING FINITE ELEMENT EQUATIONS FOR INDIVIDUAL ELEMENTS

$$[K]\{X\} + \{G(X)\} = \{P\}$$

$\{X\}$ = VECTOR OF NODAL DISPLACEMENTS

$\{G(X)\}$ = VECTOR OF NONLINEAR TERMS (CUBIC IN $\{X\}$)

FULL (NORMAL), REDUCED AND SELECTIVE INTEGRATION

- IF nxn GAUSS-LEGENDRE FORMULA IS USED TO INTEGRATE [K] EXACTLY FOR RECTANGULAR (OR PARALLELOGRAM) ELEMENTS
    - ***FULL (NORMAL) INTEGRATION*** USES nxn QUADRATURE POINTS
    - ***REDUCED INTEGRATION*** USES (n-1) × (n-1) QUADRATURE POINTS
    - ***SELECTIVE INTEGRATION*** USES nxn POINTS FOR SOME TERMS AND (n-1) × (n-1) POINTS FOR OTHER TERMS OF [K]

Figure 19

EQUIVALENT FINITE ELEMENT MODELS

The equivalence between finite element models is defined in Fig. 20. Finite elements are equivalent if their individual governing equations, when expressed in terms of a common set of nodal variables and/or parameters, are identical (see Ref. 16). It is important to note that the other parameters not contained in the common set are local to the individual elements. For nearly equivalent models, the finite element equations are almost identical.

DEFINITION OF EQUIVALENCE

- TWO FINITE ELEMENT MODELS ARE EQUIVALENT IF THEIR GOVERNING FINITE ELEMENT EQUATIONS, WHEN EXPRESSED IN TERMS OF A COMMON SET OF NODAL VARIABLES AND/OR PARAMETERS, ARE IDENTICAL.

  THE OTHER NODAL VARIABLES AND/OR PARAMETERS NOT CONTAINED IN THE COMMON SET MUST BE LOCAL TO THE INDIVIDUAL ELEMENTS (I.E., DO NOT AFFECT THE ASSEMBLY PROCESS).

- NEARLY EQUIVALENT MODELS ARE ONES FOR WHICH THE GOVERNING FINITE ELEMENT EQUATIONS ARE ALMOST IDENTICAL.

Figure 20

EQUIVALENT MIXED AND DISPLACEMENT MODELS

The governing finite element equations of both mixed and displacement models are shown in Fig. 21 and the mathematical requirements for the equivalence of the two models are listed. The table given in Fig. 21 lists examples of equivalent quadrilateral (in planform) mixed and displacement models. The following can be noted:

1) Equivalent mixed and displacement models have the same number of displacement nodes, use the same approximation functions for the generalized displacements, and use the same number of numerical quadrature points.

2) The symbol (F) refers to full integration and (R) refers to reduced integration.

3) If the geometric and material characteristics within the individual elements are constants, the number of quadrature points listed in the table generates exact integrals for the mixed models and only approximate integrals for the displacement models.

EQUIVALENCE

MIXED MODEL WITH DISCONTINUOUS STRESS RESULTANTS	DISPLACEMENT MODEL
GOVERNING FINITE ELEMENT EQUATIONS	
$[S]^T[F]^{-1}[S]\{X\}+\{\bar{G}(X)\} = \{P\}$	$[K]\{X\} + \{G(X)\} = \{P\}$
FROM WHICH	
$[S]^T[F]^{-1}[S] =$	$[K]$
$\{\bar{G}(X)\} =$	$\{G(X)\}$

NEAR EQUIVALENCE = IS REPLACED BY ≃

EXAMPLES OF EQUIVALENT QUADRILATERAL ELEMENTS

NUMBER OF DISPLACEMENT NODES	QUADRATURE POINTS	NUMBER OF STRESS RESULTANT PARAMETERS	
4	2 × 2 (F) 1 (R)	4 1	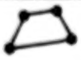
9	3 × 3 (F) 2 × 2 (R)	9 4	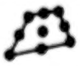
16	4 × 4 (F) 3 × 3 (R)	16 9	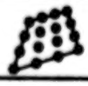

Figure 21

NONLINEAR RESPONSE OF CIRCULAR TOROIDAL SHELL SUBJECTED TO UNIFORM EXTERNAL PRESSURE

To assess the accuracy of the mixed models with discontinuous stress resultants at interelement boundaries, the nonlinear response of the circular toroidal shell shown in Fig. 22 is analyzed using these models. The solutions obtained using six and eight finite elements with nine displacement nodes and four stress nodes are compared with the converged solution in Fig. 22.

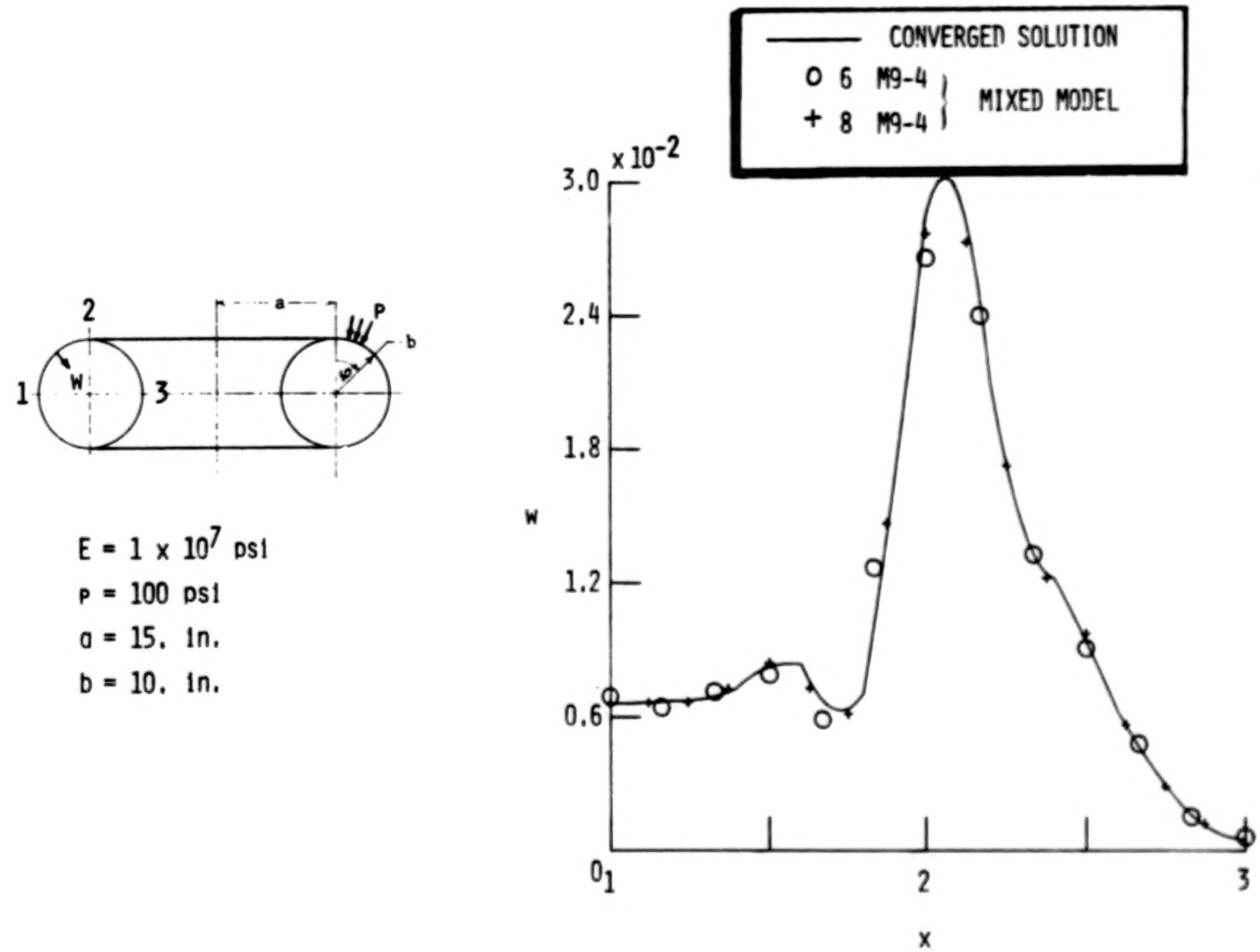

Figure 22

CLAMPED CYLINDRICAL SHELLS SUBJECTED TO UNIFORM PRESSURE LOADING

To assess the accuracy of the different displacement and mixed models, the large-deflection nonlinear response of the clamped cylindrical panel shown in Fig. 23 is analyzed using these models. The solutions obtained using a 4 x 4 grid of four-noded quadrilateral elements are shown in Fig. 23. The solutions obtained using a 2 x 2 grid of nine-noded quadrilateral elements are shown in Fig. 24.

As is to be expected, the full-integration four-noded displacement model is too stiff. The full-integration nine-noded displacement model (with the same total number of degrees of freedom), though less stiff than the four-noded model, overestimates the stiffness, particularly at higher loads. The mixed model with discontinuous stress resultants is more accurate than the mixed models with continuous stress resultants developed in Refs. 17 and 18.

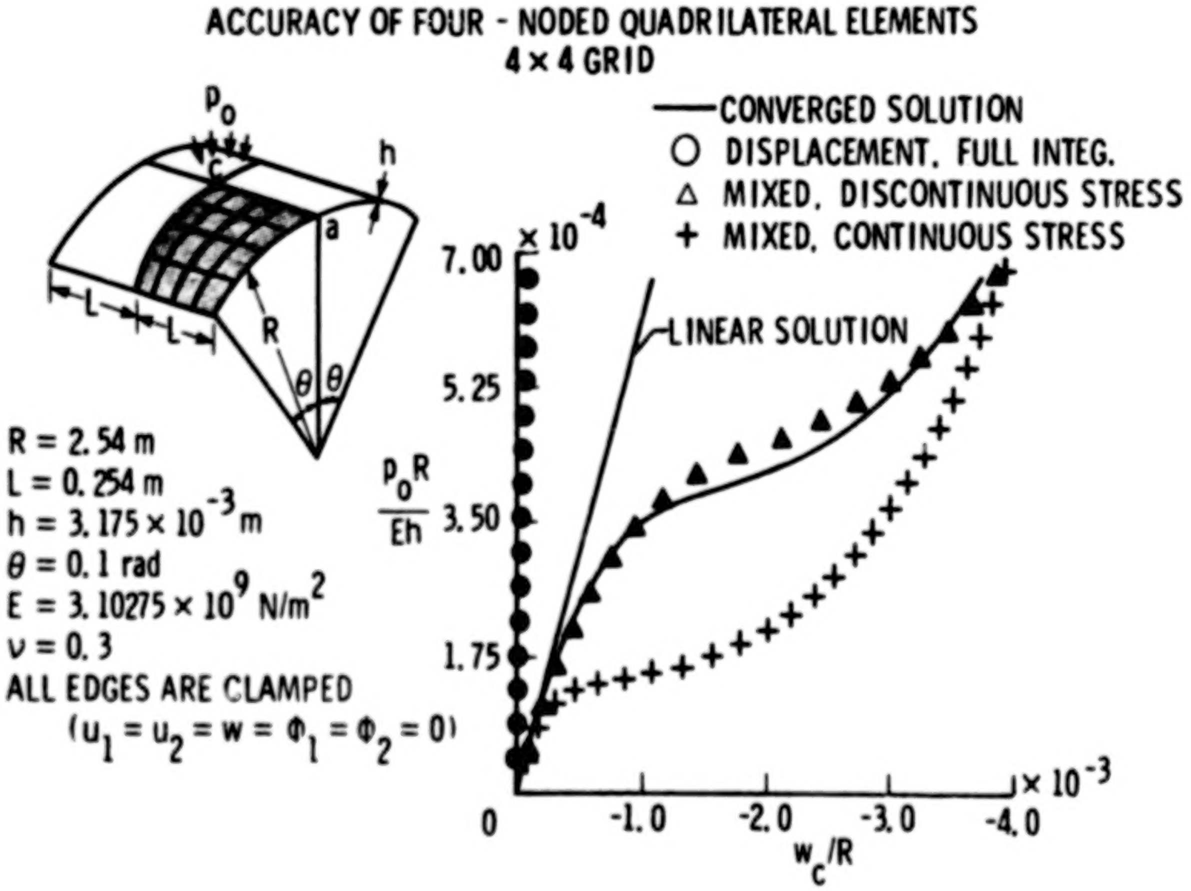

Figure 23

CLAMPED CYLINDRICAL PANEL

ACCURACY OF NINE - NODED QUADRILATERAL ELEMENTS

2 × 2 GRID

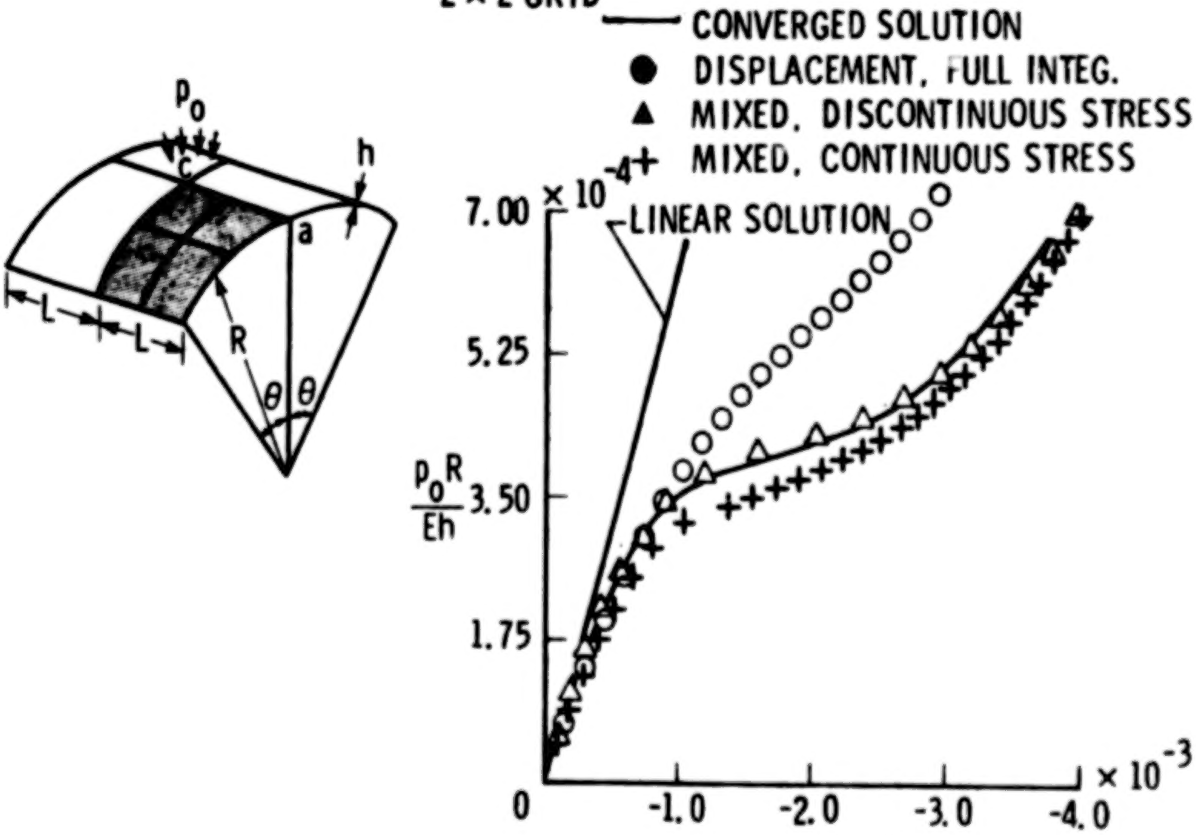

Figure 24

USE OF REDUCTION METHODS IN CONJUNCTION WITH MIXED MODELS

The use of reduction methods in conjunction with mixed models is outlined in Fig. 25. First, the governing finite element equations for the individual elements are given. Then, the vectors of fundamental unknowns (stress resultants and displacements) are expressed as linear combinations of a small number of vectors. The basis reduction and reduced system of equations are obtained in the manner outlined previously. It is important to note that *the reduced equations are quadratic in the reduced unknowns* $\{\phi\}$.

GOVERNING FINITE ELEMENT EQUATIONS FOR INDIVIDUAL ELEMENTS

$$\begin{bmatrix} -[F] & [S] \\ [S]^T & [0] \end{bmatrix} \begin{Bmatrix} H \\ X \end{Bmatrix} + \begin{Bmatrix} M(X) \\ G(H,X) \end{Bmatrix} = \begin{Bmatrix} 0 \\ P \end{Bmatrix}$$

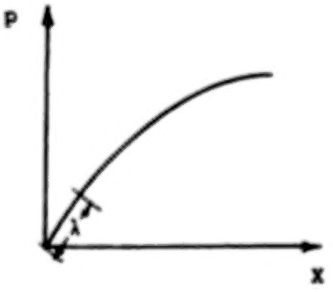

BASIS REDUCTION

$$\begin{Bmatrix} H \\ X \end{Bmatrix}_{n,1} = \begin{bmatrix} \Gamma_H \\ \Gamma_X \end{bmatrix}_{n,r} \{\phi\}_{r,1} \quad , \qquad r << n$$

WHERE

$$\begin{bmatrix} \Gamma_H \\ \Gamma_X \end{bmatrix} = \left[\begin{Bmatrix} H \\ X \end{Bmatrix} \quad \frac{\partial}{\partial p} \begin{Bmatrix} H \\ X \end{Bmatrix} \quad \cdots\cdot \quad \frac{\partial^{r-1}}{\partial p^{r-1}} \begin{Bmatrix} H \\ X \end{Bmatrix} \right]$$

$\{\phi\}$ = VECTOR OF UNDETERMINED COEFFICIENTS

P = LOAD PARAMETER

REDUCED SYSTEM OF EQUATIONS

$$[\tilde{F}]\{\phi\} + \{\tilde{M}(\phi)\} = p\{\tilde{P}\}$$

WHERE

$$[\tilde{F}] = \sum_{\text{elements}} -[\Gamma_H]^T[F][\Gamma_H] + [\Gamma_H]^T[S][\Gamma_X] + [\Gamma_X]^T[S]^T[\Gamma_H]$$

$$\{\tilde{M}\} = \sum_{\text{elements}} [\Gamma_H]^T\{M(X)\} + [\Gamma_\psi]^T\{G(H,X)\}$$

$\{\phi\}$ = VECTOR OF UNDETERMINED COEFFICIENTS OR PARAMETERS

Figure 25

USE OF REDUCTION METHODS IN CONJUNCTION WITH DISPLACEMENT MODELS

The use of reduction methods in conjunction with displacement models, which are equivalent to the proposed mixed models, is outlined in Fig. 26. Note that the resulting reduced system of equations is cubic in the reduced unknowns $\{\phi\}$. The implication of this is that *even if the mixed model and the displacement model are equivalent their reduced systems are not equivalent.*

GOVERNING FINITE ELEMENT EQUATIONS FOR INDIVIDUAL ELEMENTS

$$[K]\{X\} + \{G(X)\} = p\{P\}$$

BASIS REDUCTION

$$\{X\}_{n,1} = \left[\Gamma_X\right]_{n,r} \{\Phi\}_{r,1} \quad , \qquad r << n$$

$$\left[\Gamma_X\right] = \left[\{X\} \quad \frac{\partial}{\partial p}\{X\} \ . \ . \ . \ . \quad \frac{\partial^{r-1}}{\partial p^{r-1}}\{X\}\right]$$

$\{\Phi\}$ = VECTOR OF UNDETERMINED COEFFICIENTS OR PARAMETERS

p = LOAD PARAMETER

REDUCED SYSTEM OF EQUATIONS

$$[\tilde{K}]\{\Phi\} + \{\tilde{G}(\Phi)\} = p\{\tilde{P}\}$$

WHERE $[\tilde{K}] = \left[\Gamma_X\right]^T [K] \left[\Gamma_X\right]$

$\{\tilde{G}(\Phi)\} = \left[\Gamma_X\right]^T \{G(\Phi)\}$

= VECTOR OF NONLINEAR TERMS (CUBIC IN (Φ))

NOTE: EVEN IF MIXED MODEL AND DISPLACEMENT MODEL ARE EQUIVALENT, THEIR REDUCED SYSTEMS ARE NOT EQUIVALENT.

Figure 26

ACCURACY OF REDUCTION METHOD - MIXED AND DISPLACEMENT MODELS

The nonlinear solutions obtained using the reduction method in conjunction with the equivalent mixed and reduced-integration displacement models are compared in Fig. 27 for the case of a clamped cylindrical shell subjected to uniform pressure loading. Seven basis vectors were generated for the unloaded shell. The variations of the strain energy with the loading, as predicted by the reduction method mixed and displacement models, are shown in Fig. 27. The high accuracy of the predictions of the mixed model is clearly seen in this figure.

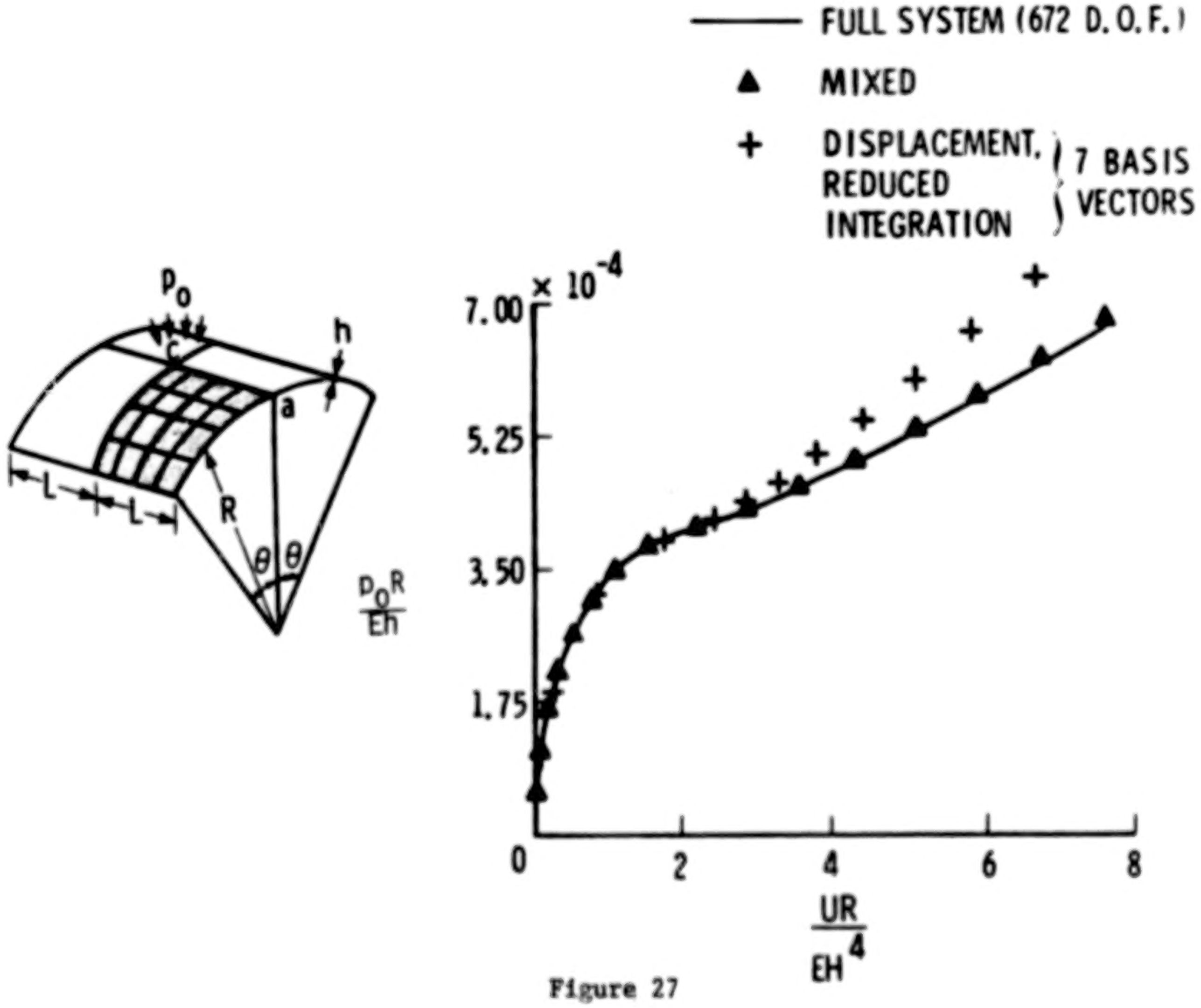

Figure 27

ADVANTAGES OF MIXED MODELS OVER EQUIVALENT DISPLACEMENT MODELS

The advantages of mixed models over the equivalent displacement models are listed in Fig. 28. These include:

1) *Simplicity of formulation.* Only quadratic and bilinear terms appear in the governing finite element equations. By contrast, the governing equations of the displacement model include cubic terms.

2) If the geometric and material characteristics are constants within each element, then *most of the integrals can be evaluated exactly* for the mixed elements (even when the element has curved faces and edges).

3) The mixed models are *better suited for use with reduction methods* in nonlinear problems, in the sense that:

a) The basis vectors are simpler to generate.

b) The mixed models lead to higher accuracy of the solutions obtained by the reduced system. This is especially true for stress resultants.

- SIMPLICITY OF FORMULATION (ONLY QUADRATIC AND BILINEAR TERMS APPEAR IN GOVERNING FINITE ELEMENT EQUATIONS)
- MOST OF THE INTEGRALS CAN BE EVALUATED EXACTLY (EVEN FOR ELEMENTS WITH CURVED FACES AND EDGES)
- BETTER SUITED FOR USE WITH REDUCTION METHODS
  - BASIS VECTORS ARE SIMPLER TO GENERATE
  - BETTER APPROXIMATION PROPERTIES (HIGHER ACCURACY OF REDUCED SYSTEM, ESPECIALLY FOR STRESS RESULTANTS)

Figure 28

LARGE ROTATION NONLINEAR PROBLEMS

The third topic considered in this paper is the large rotation nonlinear problems. The basic features of two effective computational models are outlined in Fig. 29. In both models a *total Lagrangian* description of the deformation is used. Consequently, the strain-displacement relations contain *trigonometric functions of the rotation components.*

The first computational model is a two-field mixed model with discontinuous stress-resultant fields at interelement boundaries. The second model is based on the use of the penalty method for handling the trigonometric functions, thereby simplifying the analysis.

FORMULATION

- TOTAL LAGRANGIAN DESCRIPTION OF DEFORMATION
- STRAIN - DISPLACEMENT RELATIONS CONTAIN TRIGONOMETRIC FUNCTIONS OF ROTATION COMPONENTS

FINITE ELEMENT MODELING

- MIXED MODELS WITH DISCONTINUOUS STRESS RESULTANTS
- PENALTY METHOD FOR HANDLING TRIGONOMETRIC FUNCTIONS

Figure 29

ELASTICA PROBLEM - FORMULATION

As an application of the proposed computational models, consider the elastica problem shown in Fig. 30. In the mixed formulation, the Hellinger-Reissner two-field mixed variational principle is used. Transverse shear deformation, though small, is included to simplify the formulation. The extensional strain ε and the transverse shear strain γ are trigonometric functions of the rotation ϕ.

The penalty formulation, on the other hand, is based on the Euler-Bernoulli type beam theory with both the extensional and transverse shearing strains neglected. The axial and transverse displacements u and w are incorporated into the functional through the use of constraints and penalty numbers.

MIXED FORMULATION

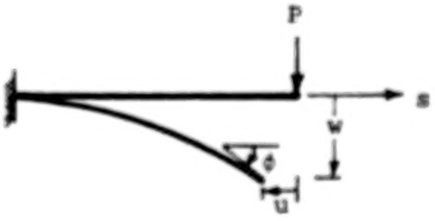

$$\pi = \int [(N\,\varepsilon + M\,\kappa + Q\,\gamma) - \frac{1}{2}\left(\frac{N^2}{EA} + \frac{M^2}{EI} + \frac{Q^2}{GA}\right)]\,ds$$

ε, γ INCLUDE TRIGONOMETRIC FUNCTIONS OF ϕ

$$\kappa = \frac{d\phi}{ds}$$

N, M, Q ARE DISCONTINUOUS AT INTERELEMENT BOUNDARIES

PENALTY FORMULATION

$$\pi = \int [\frac{1}{2}\,EI\left(\frac{d\phi}{ds}\right)^2 + \lambda_1\left(\frac{dw}{ds} - \sin\phi\right)^2 + \lambda_2\left(\frac{du}{ds} - 1 + \cos\phi\right)^2]\,ds$$

WHERE λ_1, λ_2 ARE PENALTY NUMBERS

THE RESULTING STIFFNESS MATRIX IS POSITIVE DEFINITE.

Figure 30

ELASTICA PROBLEM - NUMERICAL RESULTS

The displacements, rotations and total strain energy obtained by using *four two-noded elements and two three-noded elements* are depicted in Figs. 31 and 32. Also, the deformed configurations of the beam for various values of the transverse load P are shown in Fig. 31. Both exact-integration displacement models (DE models) and mixed models with discontinuous forces (MD models) are used. As to be expected, the displacement models are too stiff. This is particularly true for the two-noded elements. By contrast, the predictions of the mixed models are highly accurate.

LARGE-ROTATION ELASTICA PROBLEM

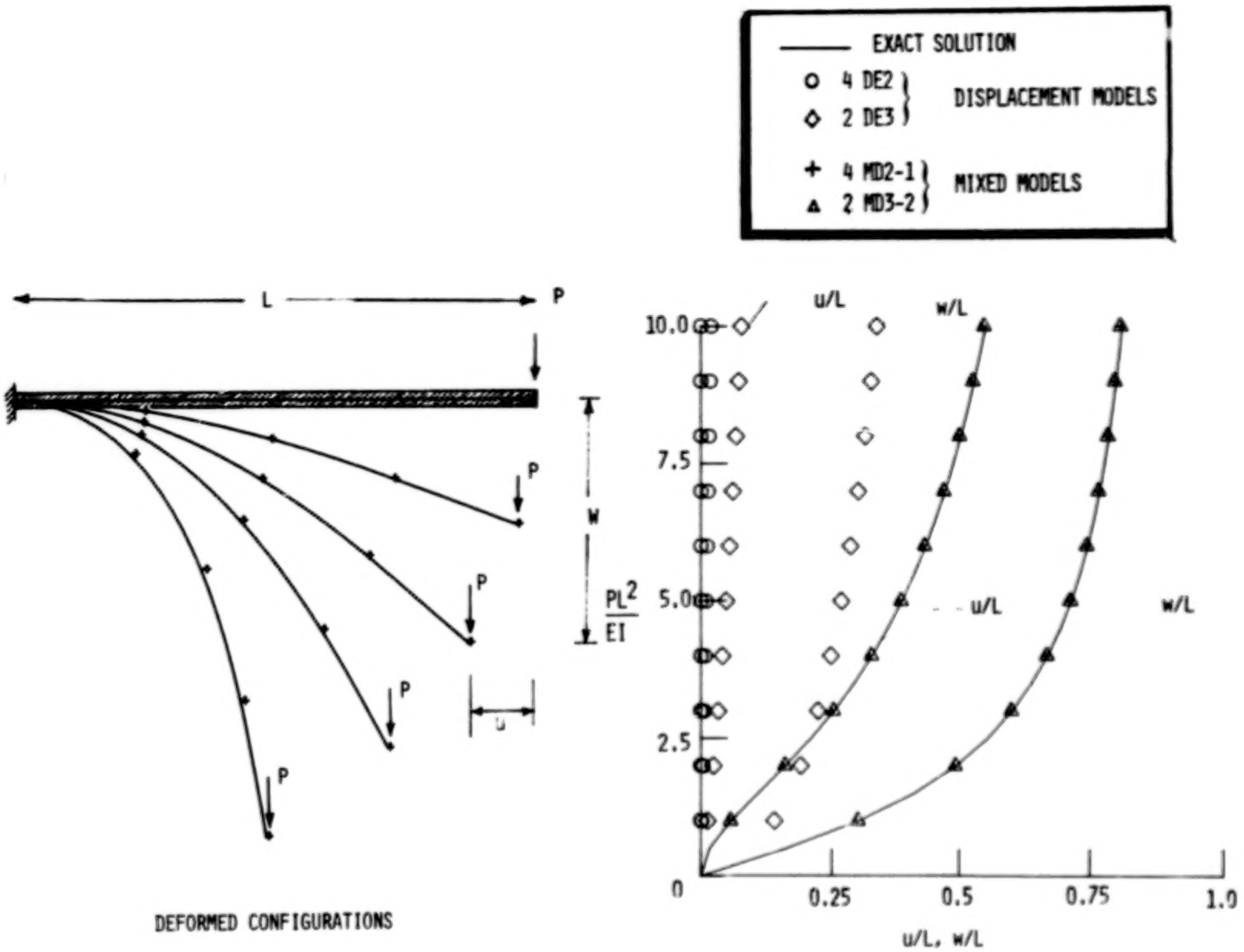

Figure 31

LARGE-ROTATION ELASTICA PROBLEM (Cont'd.)

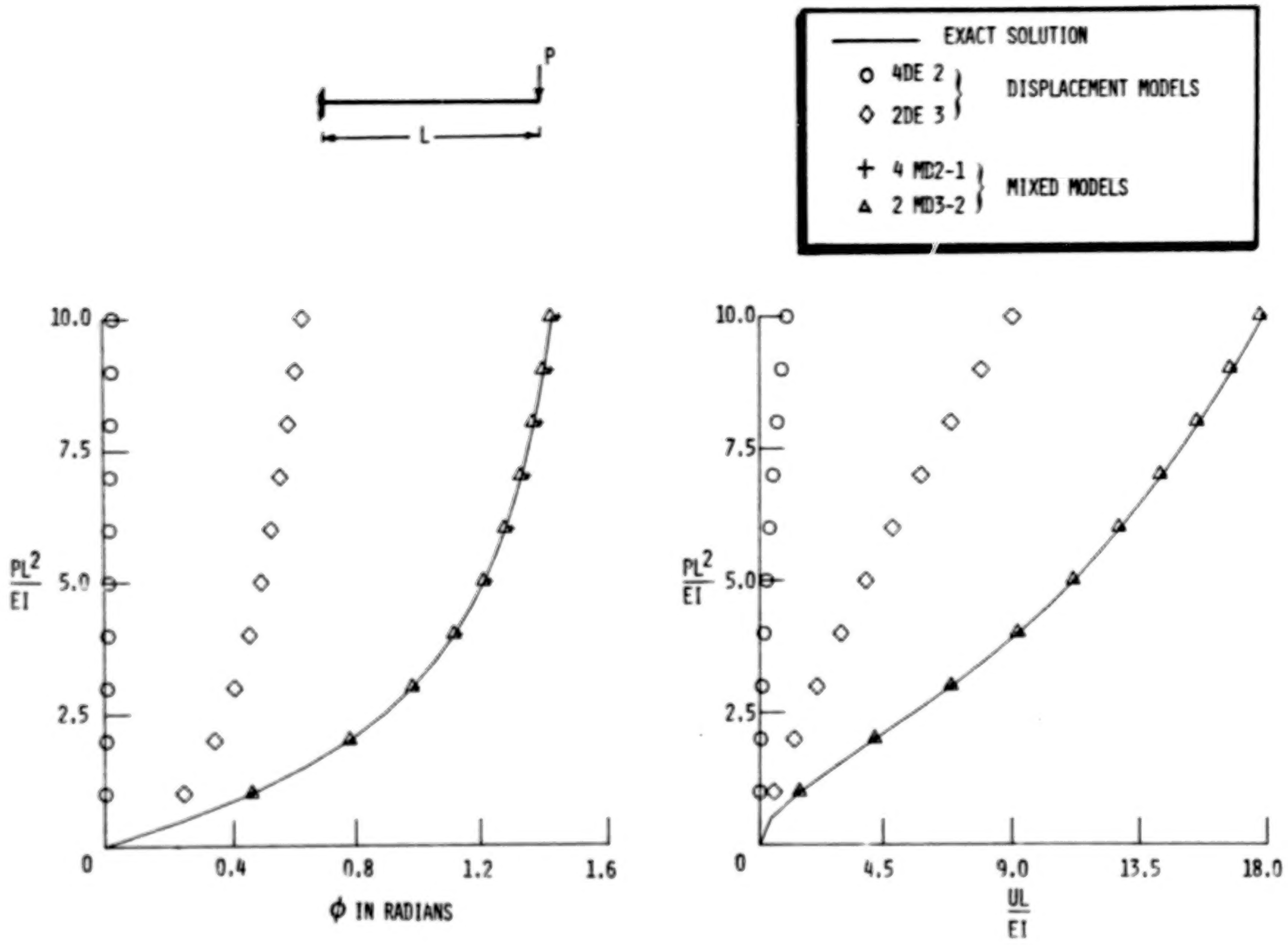

Figure 32

ANALYSIS AND MODELING NEEDS FOR TIRES

The fourth part of the paper deals with future analysis and modeling needs for tires. The overall goal is to develop a general tire analysis capability which includes (see Fig. 33):

1) Accurate representation of the tire configuration and construction

2) Reliable material characterization including thermo-viscoelastic response

3) Capability for predicting the stresses and deformations due to footprint loading; this also includes the prediction of the contact area

Since there is a certain degree of uncertainty in the accuracy of the various elements of the tire model, considerable work should be directed towards assessing the sensitivity of the tire response to various modeling details such as material characteristics, surface inaccuracies, and variations in the tire design variables. The result of such sensitivity study would allow the identification of the minimum degree of sophistication of the model required to achieve a prescibed level of accuracy.

There is also a need for identifying failure mechanisms and developing a verifiable failure analysis capability for tires. Use can be made of the considerable experience gained in damage tolerance design concepts for fibrous composite structures.

- GENERAL TIRE ANALYSIS CAPABILITY
  - ACCURATE REPRESENTATION OF TIRE CONFIGURATION AND CONSTRUCTION
  - RELIABLE MATERIAL CHARACTERIZATION INCLUDING THERMO-VISCOELASTIC RESPONSE
  - PREDICTION OF STRESSES AND DEFORMATIONS DUE TO FOOTPRINT LOADING (CONTACT AREA, STRESSES AND SLIP)
- SENSITIVITY ANALYSIS - SENSITIVITY OF RESPONSE TO:
  - MATERIAL CHARACTERISTICS
  - SURFACE INACCURACIES
  - VARIATIONS IN DESIGN VARIABLES (REQUIRED FOR EVALUATION OF STRUCTURAL CONCEPTS AND FOR OPTIMIZATION)
  - MODELING DETAILS (IN ORDER TO DEVELOP SIMPLE TIRE MODELS)
- FAILURE MECHANISMS AND FAILURE ANALYSIS OF TIRES
  - DAMAGE TOLERANCE

Figure 33

SUMMARY

In summary, four topics are covered in this paper; namely, recent advances in reduction methods for nonlinear problems, mixed models for tires, computational models for large-rotation nonlinear problems, and analysis and modeling needs for tires. (See Fig. 34.)

Reduction methods have proven to be very effective for the nonlinear static analysis of structures subjected to either combined loads or displacement-dependent loads. However, more work is needed to realize their full potential for nonlinear dynamic and time-dependent problems.

Mixed shell models with discontinuous stress resultants at element interfaces have high potential for nonlinear analysis of tires. These models can be easily incorporated into existing general-purpose finite element programs based on the displacement formulation.

Two computational models are presented for the large-rotation nonlinear problems. Both models use a total Lagrangian description of the deformation. The first model uses a mixed formulation, and the second model uses a penalty formulation. Both models appear to have high potential.

As far as analysis and modeling needs are concerned, three areas have been identified. As is to be expected, the modeling and analysis of tires will be strongly impacted by new advances in materials technology, computer hardware, software, integrated analysis, and CAD/CAM systems.

- REDUCTION METHODS
  - VERIFIED FOR STATIC NONLINEAR PROBLEMS INCLUDING CASES OF COMBINED LOADS AND DISPLACEMENT-DEPENDENT LOADS
  - FURTHER DEVELOPMENT NEEDED FOR NONLINEAR DYNAMIC PROBLEMS
- MIXED MODELS WITH DISCONTINUOUS STRESS RESULTANTS
  - HAVE HIGH POTENTIAL FOR ANALYZING TIRES
  - CAN BE EASILY INCORPORATED INTO EXISTING GENERAL-PURPOSE FINITE ELEMENT PROGRAMS
- LARGE ROTATION NONLINEAR PROBLEMS
  - BOTH MIXED AND PENALTY FORMULATIONS PROVIDE EFFECTIVE ANALYSIS TECHNIQUES
- ANALYSIS AND MODELING NEEDS
  - GENERAL ANALYSIS CAPABILITY FOR TIRES
  - SENSITIVITY ANALYSIS
  - FAILURE MECHANISMS AND FAILURE ANALYSIS

Figure 34

REFERENCES

1. Ridha, R. A.; and Clark, S. K.: Tire Stresses and Deformation. Mechanics of Pneumatic Tires, edited by S. K. Clark, National Highway Traffic Safety Administration, U.S. Department of Transportation, Washington, D.C., 1981, pp. 475-540.

2. Clark, S. K. (Ed.): Mechanics of Pneumatic Tires. National Bureau of Standards, Monograph 122, Washington, D.C., 1971.

3. Frank, F.; and Hofferberth, W.: Mechanics of the Pneumatic Tire. Rubber Chemistry and Technology, Vol. 40, 1967, pp. 271-322.

4. Lou, A. Y. C.: Modification of Linear Membrane Theory for Predicting Inflated Tire Shapes. Developments in Mechanics, Vol. 7, Proceedings of the 13th Midwestern Mechanics Conference, University of Pittsburgh, 1973, pp. 637-656.

5. Tielking, J. T.; and Feng, W. W.: The Application of the Maximum Potential Energy Principle to Nonlinear Axisymmetric Membrane Problems. Journal of Applied Mechanics, Vol. 73, 1974, pp. 491-496.

6. DeEskinazi, J.; Werner, S.; and Yang, T. Y.: Contact of an Inflated Toroidal Membrane with a Flat Surface as an Approach to the Tire Deflection Problem. Tire Science and Technology, Vol. 3, 1975, pp. 43-61.

7. Ridha, R. A.: Analysis for Tire Mold Design. Tire Science and Technology, Vol. 1, 1974, pp. 195-210.

8. Brewer, H. K.: Stresses and Deformations in Multi-Ply Aircraft Tires Subject to Inflation Pressure Loading. Technical Report AFFDL-TR-70-62, Wright-Patterson Air Force Base, Ohio, June 1970.

9. Patel, H. P.: Mathematical Analysis of Statically Loaded Pneumatic Tires. Ph.D. Thesis, North Carolina State University, Raleigh, 1975.

10. Gough, V. E.: Structure of the Pneumatic Tire. Mechanics of Pneumatic Tires, edited by S. K. Clark, National Highway Traffic Safety Administration, U.S. Department of Transportation, Washington, D.C., 1981, pp. 203-248.

11. Noor, A. K.; and Peters, J. M.: Reduced Basis Technique for Nonlinear Analysis of Structures. AIAA Journal, Vol. 18, No. 4, 1980, pp. 455-462.

12. Noor, A. K.; Andersen, C. M.; and Peters, J. M.: Global-Local Approach for Nonlinear Shell Analysis. Proceedings of the Seventh ASCE Conference on Electronic Computation, American Society of Civil Engineers, pp. 634-657.

13. Noor, A. K.: Recent Advances in Reduction Methods for Nonlinear Problems. Computers and Structures, Vol. 13, No. 1/2, 1981, pp. 31-44.

14. Noor, A. K.; and Peters, J. M.: Recent Advances in Reduction Methods for Instability Analysis of Structures. Computers and Structures, Vol. 16, No. 1, Jan. 1983.

15. Noor, A. K.; and Andersen, C. M.: Mixed Models and Reduced/Selective Integration Displacement Models for Nonlinear Shell Analysis. International Journal for Numerical Methods in Engineering, Vol. 18, 1982, pp. 1429-1454.

16. Malkus, D. S.; and Hughes, T. J. R.: Mixed Finite Element Models - Reduced and Selective Integration Techniques: A Unification of Concepts. Computer Methods in Applied Mechanics and Engineering, Vol. 15, No. 1, 1978, pp. 63-81.

17. Noor, A. K.; and Andersen, C. M.: Mixed Isoparametric Finite Element Models of Laminated Composite Shells. Computer Methods in Applied Mechanics and Engineering, Vol. 11, 1977, pp. 255-280.

18. Noor, A. K.; and Hartley, S. J.: Nonlinear Shell Analysis Via Mixed Isoparametric Elements. Computers and Structures, Vol. 7, No. 5, Oct. 1977, pp. 615-626.

FINITE ELEMENT METHODS FOR NONLINEAR ELASTOSTATIC PROBLEMS IN RUBBER ELASTICITY

J. T. Oden, E. B. Becker, T. H. Miller, T. Endo, and E. B. Pires
The University of Texas at Austin

ABSTRACT

This paper outlines a number of finite element methods for the analysis of nonlinear problems in rubber elasticity. Several different finite element schemes are discussed. These include the augmented Lagrangian method, continuation or incremental loading methods, and associated Riks-type methods which have the capability of incorporating limit point behavior and bifurcations. Algorithms for the analysis of limit point behavior and bifurcations are described and the results of several numerical experiments are presented. In addition, a brief survey of some recent work on modelling contact and friction in elasticity problems is given. These results pertain to the use of new nonlocal and nonlinear friction laws.

OUTLINE

1. PRELIMINARIES AND NOTATION
2. FINITE ELEMENT MODELS
3. ALGORITHMS
4. NUMERICAL EXPERIMENTS
5. FRICTION MODELS
6. NUMERICAL RESULTS

PRELIMINARIES AND NOTATIONS

KINEMATICS

The usual notation in finite elasticity is employed: $\underset{\sim}{u}$ is the displacement vector, $\underset{\sim}{x}$ is the position of a particle in the current configuration whose position was $\underset{\sim}{X}$ in the reference configuration, $\underset{\approx}{F}$ is the deformation gradient. These quantities are illustrated in the figure below.

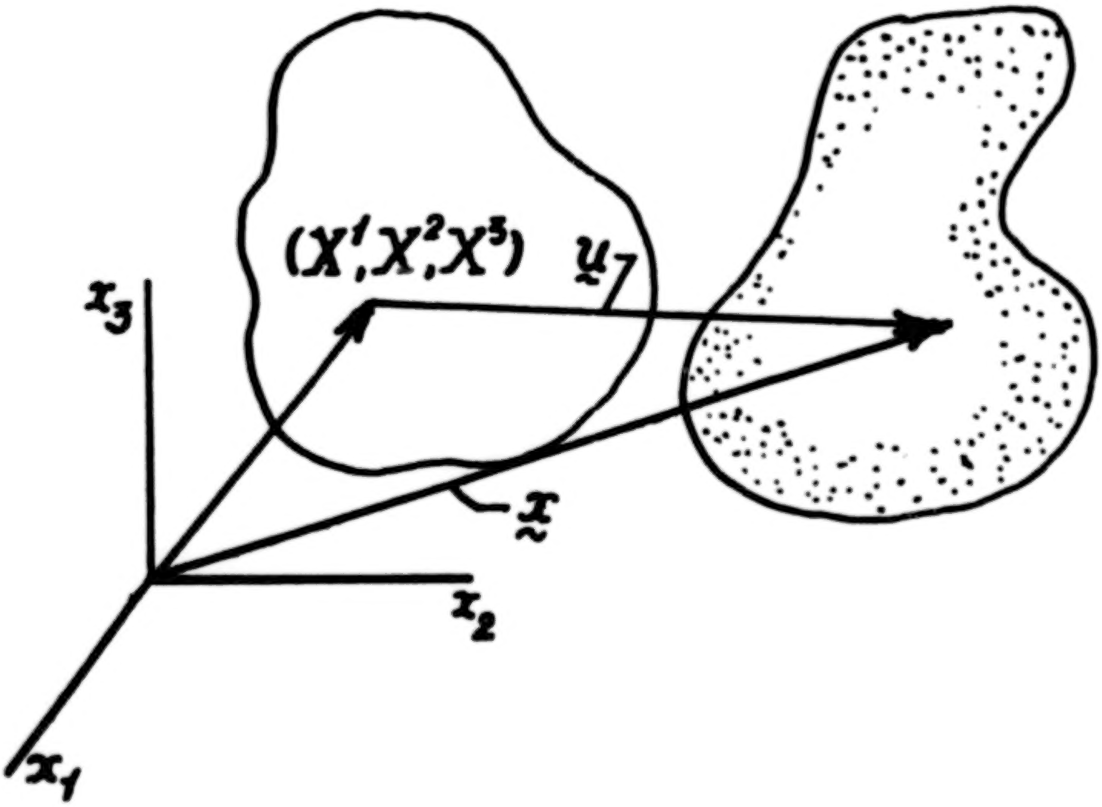

$\underset{\sim}{u}$ = DISPLACEMENT VECTOR

$= \underset{\sim}{x} - \underset{\sim}{X}$

$\underset{\approx}{F}$ = DEFORMATION GRADIENT

$= \nabla(\underset{\sim}{X} + \underset{\sim}{u})$; $F_{\alpha i} = \frac{\partial}{\partial X^\alpha} (X^i + u^i)$

HOMOGENEOUS, ISOTROPIC HYPERELASTIC MATERIAL

We begin with a study of equilibrium problems in finite elasticity. It is assumed that the materials involved are hyperelastic, isotropic, and homogeneous. Therefore, they are characterized by a strain energy function W which is given as a function of invariants of the deformation tensor $\underset{\approx}{C}$. These problems are complicated by the fact that nonconvex constraints must be enforced. For compressible materials the constraint manifests itself in the condition that $J(\underset{\sim}{u}) = \det \underset{\approx}{F} > 0$ while for incompressible materials $J(\underset{\sim}{u}) = 1$.

$$W = \hat{W}(I_1, I_2, J) = \text{STRAIN ENERGY PER UNIT VOLUME}$$

$$I_1 = \text{TRACE } \underset{\approx}{C}$$

$$I_2 = \frac{1}{2}(\text{TRACE } \underset{\approx}{C})^2 - \frac{1}{2}\text{ TRACE } \underset{\approx}{C}^2$$

$$J = \sqrt{I_3} = \det \underset{\approx}{F} \qquad \underset{\approx}{C} = \underset{\approx}{F}^T \underset{\approx}{F}$$

COMPRESSIBLE MATERIALS

$$J(\underset{\sim}{u}) = \det \underset{\approx}{F} > 0$$

INCOMPRESSIBLE MATERIALS

$$J(\underset{\sim}{u}) = 1$$

SOME CONDITIONS ON THE FORM OF W

Some conditions on the form of the energy W are presented below. In addition to the fact that the energy must be form invariant under changes of the spatial frame of reference, other conditions must be enforced if one expects a well-behaved solution. Three of these are listed below:

1. COERCIVITY:

$$W(\underset{\sim}{u}) = \hat{W}(I_1(\underset{\sim}{u}), I_2(\underset{\sim}{u}), J(\underset{\sim}{u}))$$

$$W(\underset{\sim}{u}) \to +\infty \text{ as } ||\nabla \underset{\sim}{u}|| \to +\infty$$

2. SINGULAR BEHAVIOR:

$$\begin{array}{ll} W(\underset{\sim}{u}) \to +\infty & \\ & \text{as } \det \underset{\approx}{F} \to 0^+ \\ \left|\frac{\partial W}{\partial \underset{\approx}{F}}\right| \to +\infty & \end{array}$$

3. QUASICONVEXITY:

$$\leftarrow \frac{\partial^2 W(\underset{\sim}{u})}{\partial F_{i\alpha} \partial_{j\infty}} \lambda_i \lambda_j \mu_\alpha \mu_\beta \geq 0$$

$$\forall \underset{\sim}{\lambda}, \underset{\sim}{\mu} \quad \mathbb{R}^3$$

INCOMPRESSIBLE AND NEARLY INCOMPRESSIBLE MATERIALS

Two basic classes of methods are employed here to handle compressible and nearly incompressible materials: Lagrange-multiplier methods (mixed methods), in which the incompressibility constraint $h(J) = 0$ is accounted for using Lagrange multipliers and penalty methods in which the total potential energy functional Π is penalized by the addition of a positive semi-definite, generally convex penalty functional.

INCOMPRESSIBILITY CONSTRAINT

$$h(J) = 0$$

$$h(J) = J - 1 \ , \ J^2 - 1 \ , \ (J - 1)^2, \ -\ln J \ , \text{ etc.}$$

$$W = \tilde{W}(I_1, I_2) - p\, h(J)$$

p = Lagrange Mult. ≈ Hydrostatic Pressure

PENALTY TERMS

$$\Pi(\underset{\sim}{u}) = \int_\Omega W(\underset{\sim}{u})dX - f(\underset{\sim}{u},\underset{\sim}{v})$$

$$+ \varepsilon^{-1} \int_\Omega g(J(\underset{\sim}{u}))dX$$

$$g(J) \geq 0 \quad g(J) = 0 \leftrightarrow J = 1$$

EQUILIBRIUM CONDITIONS

The finite elements employed are based on various alternative statements of equilibrium conditions for elastic bodies:

1) ENERGY FORMULATION

$$\Pi(\boldsymbol{u}) = \text{TOTAL POTENTIAL ENERGY}$$

$$= \int_\Omega W(\boldsymbol{u})dX - f(\boldsymbol{u},\boldsymbol{u})$$

$$f(\boldsymbol{u},\boldsymbol{v}) = \int_\Omega \boldsymbol{f}(\boldsymbol{u})\cdot\boldsymbol{v}dX + \int_{\Gamma_2} \boldsymbol{t}(\boldsymbol{u})\cdot\boldsymbol{v}ds$$

$$\Pi(\boldsymbol{u}) \le \Pi(\boldsymbol{v}) \text{ for all } \boldsymbol{v} \text{ in}$$

$$K = \{\boldsymbol{v} : |\int_\Omega W(\boldsymbol{v})dX| < \infty ;$$

$$\boldsymbol{v} = \boldsymbol{0} \text{ on } \Gamma_1 ; \det \nabla\boldsymbol{v} \ge 0 \text{ or } = 1\}$$

---

2) AUGUMENTED LAGRANGE

$$L(\boldsymbol{u},\boldsymbol{F},\boldsymbol{\lambda}) = \Pi(\boldsymbol{u}) + \frac{c}{2}\int_\Omega |\nabla\boldsymbol{u} - \boldsymbol{F}|^2 dX$$

$$+ \int_\Omega \boldsymbol{\lambda} : (\nabla\boldsymbol{u} - \boldsymbol{F})dX$$

$$L: \ \boldsymbol{V} \times \{\boldsymbol{G}: \ \det \boldsymbol{G} = 1\} \times \{\cdot\cdot\}^*$$

The augmented Lagrange method combines features of both penalty and Lagrange-multiplier schemes. The incompressibility constraint can be satisfied a priori in a straightforward manner for Mooney-Rivlin **materials, with the** result that the method is extremely fast and efficient when used in conjunction with, e.g., Uzawa's method (ref 1). (See equation.)

3. VIRTUAL WORK I

$$\int_\Omega v_{i,\alpha} \frac{\partial W(\boldsymbol{u})}{\partial u_{i,\alpha}} dX - \int_\Omega p \frac{\partial h}{\partial J} \frac{\partial J}{\partial u_{i,\alpha}} v_{i,\alpha} dX$$

$$= f(\boldsymbol{u},\boldsymbol{v}) \text{ for all } \boldsymbol{v} \text{ in } \boldsymbol{V}$$

$$\int_\Omega q h(J(\boldsymbol{u}))dX = 0 \text{ for all } q \text{ in } Q$$

4. VIRTUAL WORK II

$$\int_\Omega \frac{\partial W(\boldsymbol{u}_\epsilon)}{\partial u_{i,\alpha}} v_{i,\alpha} dX + \epsilon^{-1} \int_\Omega \frac{\partial g}{\partial J} \cdot \frac{\partial J}{\partial u_{i,\alpha}} v_{i,\alpha} dX$$

$$= f(\boldsymbol{u}_\epsilon, X) \text{ for all } \boldsymbol{v} \text{ in } \boldsymbol{V}$$

$$\boxed{p_\epsilon = -\epsilon^{-1} \frac{\partial g(J(\boldsymbol{u}_\epsilon))}{\partial J}}$$

FINITE ELEMENT METHODS

SOME ELEMENT FAMILIES

The figure below illustrates some of the standard finite element methods employed. Unfortunately, not all of these methods are numerically stable since some may not satisty the generalized LBB condition of Oden and LeTallec (refs. 2 and 3). This condition is given in the equation on the following page, where Q is the space of Lagrange multipliers, V_h is the space of finite element approximations of displacement, p is the hydrostatic pressure and $||\nabla \underset{\sim}{v}^h||_{o,p}$ is an appropriate energy norm on $\underset{\sim}{v}^h$. The existence of a $\beta_h > 0$ independent of mesh size h is necessary for the stability of the mixed and penalty methods, particularly for pressure approximations.

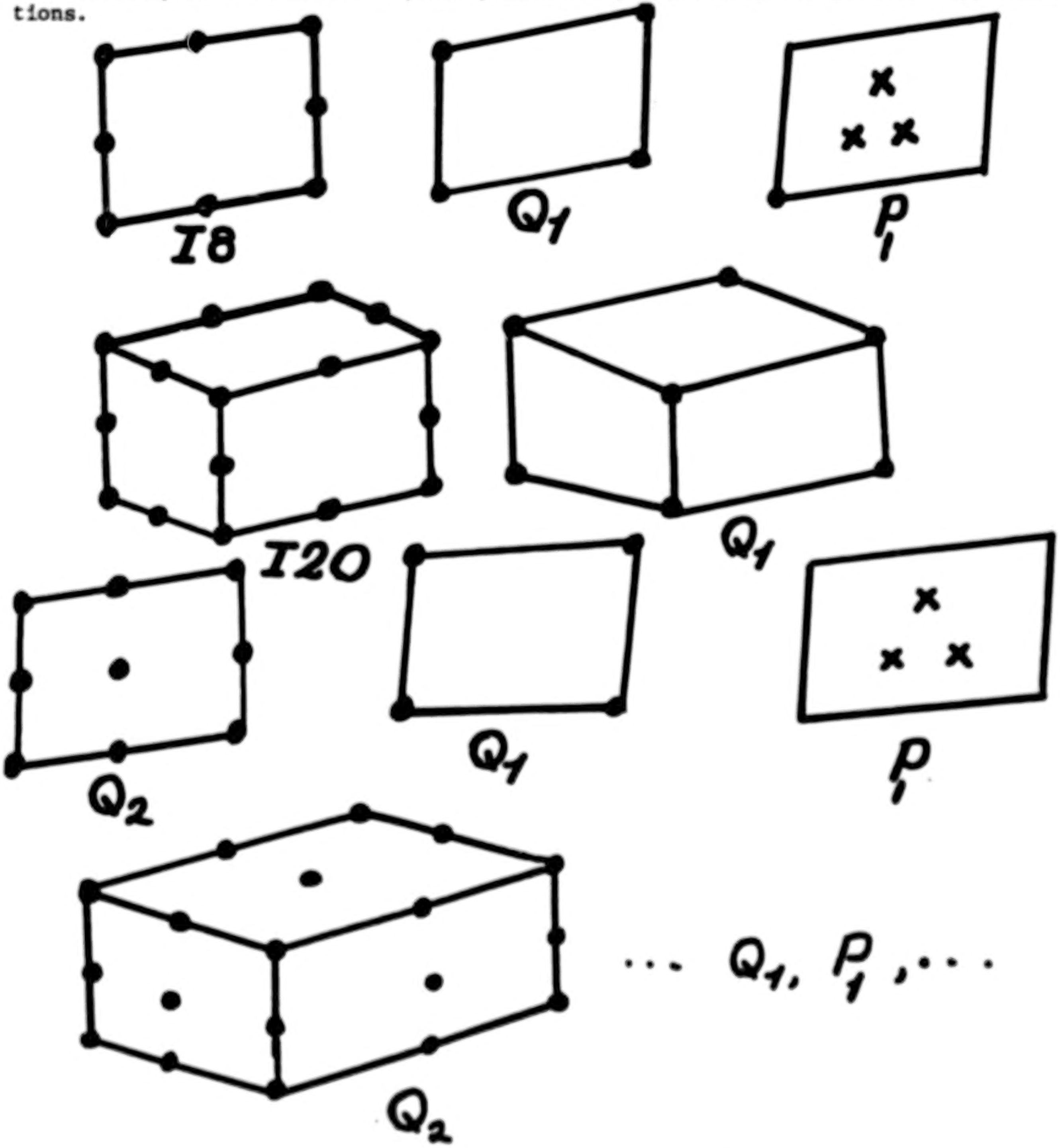

THE GENERALIZED LBB CONDITION

(REFS. 2 AND 3)

$\beta_h(\underset{\sim}{u}) > 0$ such that

$$\beta_h \|p\|_{Q/\ker \nabla J(\underset{\sim}{u})} \leq \max_{V_h} \frac{\int_\Omega p \frac{\partial J(\underset{\sim}{u})}{\partial u_{i,\alpha}} v^h_{i,\alpha} \, dX}{\|\nabla \underset{\sim}{v}^h\|_{o,p}}$$

for all p in Q

The numerical stability of mixed- and penalty finite element methods depends upon this condition, and particularly on the behavior of the parameter β_h with the mesh size h.

STABILITY RESULTS

Oden and Jacquotte (ref. 4) have recently completed a mathematical analysis of the LBB condition for incompressible viscous flows. Some of these results appear to be directly applicable to the finite elasticity problem. The following table summarizes the behavior of certain finite element methods for these constrained problems. The results generally fall into three categories: the stability parameter β_h is independent of h and the method is stable, β_h is dependent on h and the method is unstable having spurious pressure modes, or the element is "locked", meaning that the penalty parameter ε depends on the mesh size and that the displacements approach 0 as ε tends to zero for a fixed mesh size h .

VELOCITY APPROX.	QUADRATURE RULE (PRESSURE APPROX. Q)		CONVERGENCE RATE
1 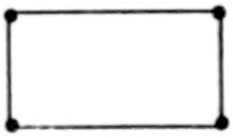 Q_1	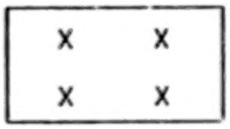 Q_2	O(1)	LOCKS
2 Q_1	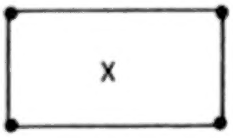 Q_0	O(h)	UNSTABLE
3 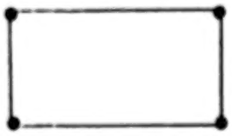 1B	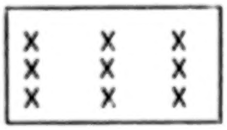 Q_2	O(1)	LOCKS

VELOCITY APPROX.	PRESSURE		RATE OF CONVERGENCE
4 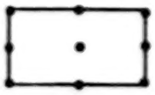 I8	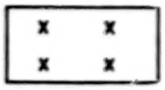 Q_1	$O(h)$	UNSTABLE PRESSURE
5 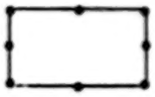 I8	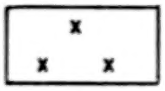 P_1	$O(h)$	UNSTABLE PRESSURE
6 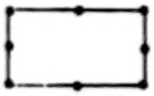 I8	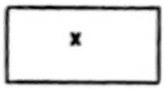 Q_0	$O(1)$	SUBOPTIMAL ($O(h)$) IN VELOCITY ERROR IN ENERGY NORM
7 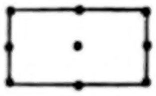 Q_2	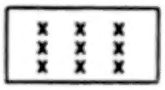 Q_2	$O(1)$	LOCKS FOR SMALL ε ; ε MUST BE TAKEN AS DEPENDENT ON h

VELOCITY APPROX.	PRESSURE		RATE OF CONVERGENCE
8 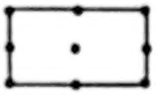 Q_2	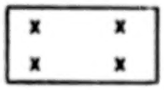 Q_1	$O(h)$	UNSTABLE PRESSURE
9 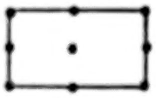 Q_2	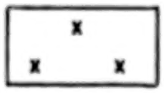 P_1	$O(1)$	OPTIMAL :
10 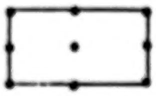 Q_2	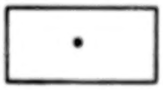 Q_0	$O(1)$	SUBOPTIMAL ($O(h)$) IN VELOCITY ERROR IN ENERGY NORM
11 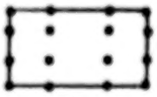 Q_3	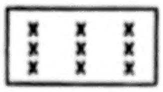 Q_2	$O(h)$	UNSTABLE PRESSURE*

VELOCITY APPROX.	PRESSURE		RATE OF CONVERGENCE
12 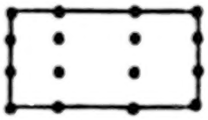 Q_3	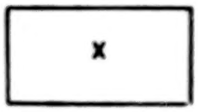 Q_0	$O(1)$	SUBOPTIMAL ($O(h)$) IN VELOCITY ERROR IN ENERGY NORM*
13 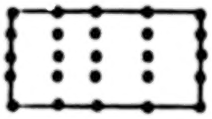 COMPOSITE $Q_2/I8$	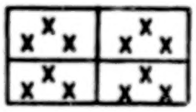 COMPOSITE 4 P_1	$O(1)$	OPTIMAL
14 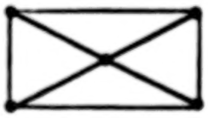 COMPOSITE 4 P_1	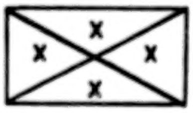 COMPOSITE $4P_0$	$O(h)$	UNSTABLE PRESSURE
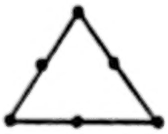 P_2	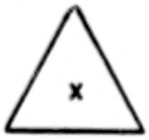 P_0 P_0	$O(1)$	SUBOPTIMAL ($O(h)$) IN VELOCITY ERROR IN ENERGY NORM

ALGORITHMS

Several different algorithms are employed for the analysis of finite elasticity problems. These include the augumented Lagrange/Uzawa methods, continuation (incremental loading) methods, and homotopy methods. In the present paper, augmented Lagrange methods are discussed briefly, but the focus is on the continuation-type methods of, for example, Riks (ref. 5), Keller (ref. 6), Crisfield (ref. 7), and Padovan (ref. 8).

1. AUGUMENTED LAGRANGE/UZAWA

1. EXTREMELY SIMPLE & FAST
2. FOLLOWS STABLE BRANCHES
3. NOT EASILY ADAPTED TO GENERAL MAT'LS

2. CONTINUATION (INCREMENTAL LD'G)

1. RIKS (REF. 5), WEMPNER (REF. 9)
2. KELLER (REF. 6), RHEINBOLT (REF. 10)
3. CRISFIELD (REF. 7), PADOVAN (REF. 8)

3. HOMOTOPY METHODS

$$\underset{\sim}{f}(\underset{\sim}{x},p) = 0$$

$$\frac{\partial f(\underset{\sim}{x}(s),p(s))}{\partial x}\dot{\underset{\sim}{x}} + \frac{\partial f(\underset{\sim}{x}(s),p(s))}{\partial p}\dot{p} = 0$$

$$N(\dot{\underset{\sim}{x}}(s),\dot{p}(s)) = 0$$

+ ODE SOLVER

The augumented Lagrange is a super-fast method.

AUGUMENTED LAGRANGE $\Rightarrow$ BLOCK RELAXATION

1. $\underset{\approx}{\lambda}^{n+1} = \underset{\approx}{\lambda}^{n} - p\,(\nabla \underset{\sim}{u}^{n} - \underset{\sim}{F}^{n})$

2. $L(\underset{\sim}{u}_{k}^{n}\,,\ \underset{\approx}{F}_{k+1}\,,\ \underset{\approx}{\lambda}^{n}) \le L(\underset{\sim}{u}_{k}^{n}\,,\ \underset{\approx}{G}\,,\ \underset{\approx}{\lambda}^{n})$

   |SOLVED EXPLICITLY, N + 2,3|

3. $\partial_{v} L(\underset{\sim}{u}_{k+1}^{n}\,,\ \underset{\sim}{F}_{k+1}^{n}\,,\ \underset{\approx}{\lambda}^{n}) \cdot X = 0$

CONTINUATION METHODS

$$\underset{\sim}{f}(\underset{\sim}{x}(s)\,,\ p(s)) = 0$$

$$\dot{\underset{\sim}{x}}(s) \cdot \dot{\underset{\sim}{x}}(s) + \dot{p}^{2}(s) = 1 \Leftarrow N(\dot{\underset{\sim}{x}},\dot{p}) = 0$$

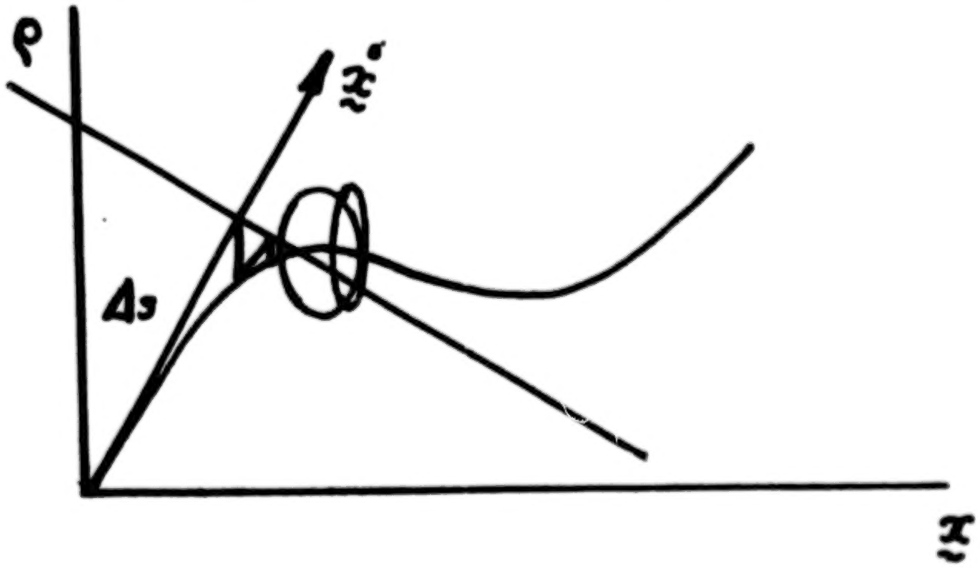

NUMERICAL EXAMPLES

Consider the inflation of a thick rubber spherical shell subjected to external loading. The shell is pressurized until it snaps through. Pressure continues to increase until the shell inflates. The material is assumed to be an incompressible Mooney-Rivlin material. The numerically stable Q2/P1 element is employed. Good results are obtained using the Riks-Crisfield method (refs. 5 and 7) with Newton-Raphson correction. Geometry of the shell is shown below and this is followed by several figures which illustrate numerical results. It is noted that the stiffness of the shell is strongly dependent on the material properties. In particular, for a fixed value of the Mooney-Rivlin constant C_1, if C_2 is chosen sufficiently small, a limit point type behavior occurs in the inflated shell. This represents the phenomenon of a large decrease in pressure in an inflated balloon with a large increase in strain at the crown. This limit point behavior disappears for larger values of C_2. (See ref. 11.)

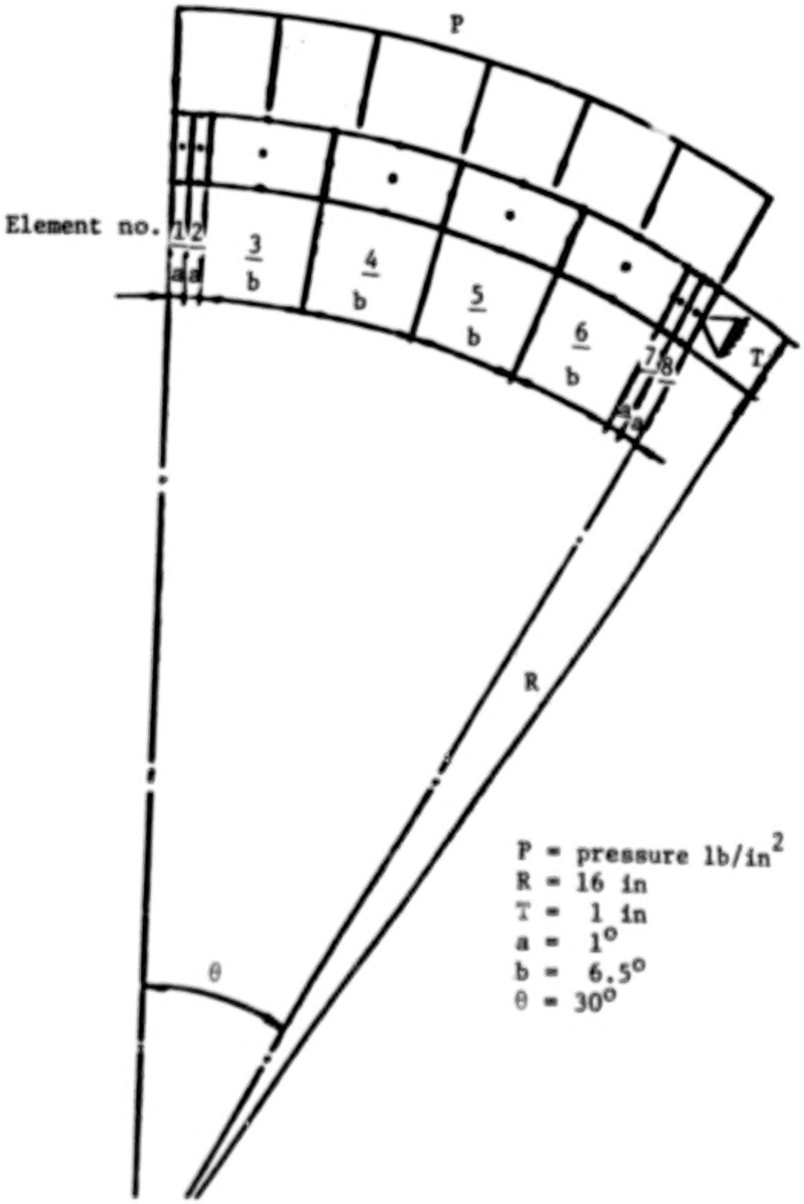

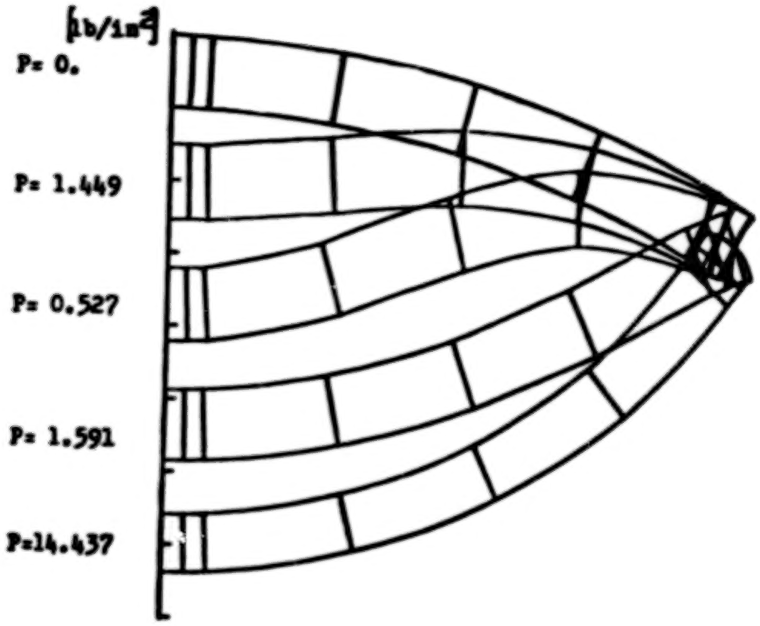
[lb/in^2]
P= 0.
P= 1.449
P= 0.527
P= 1.591
P=14.437

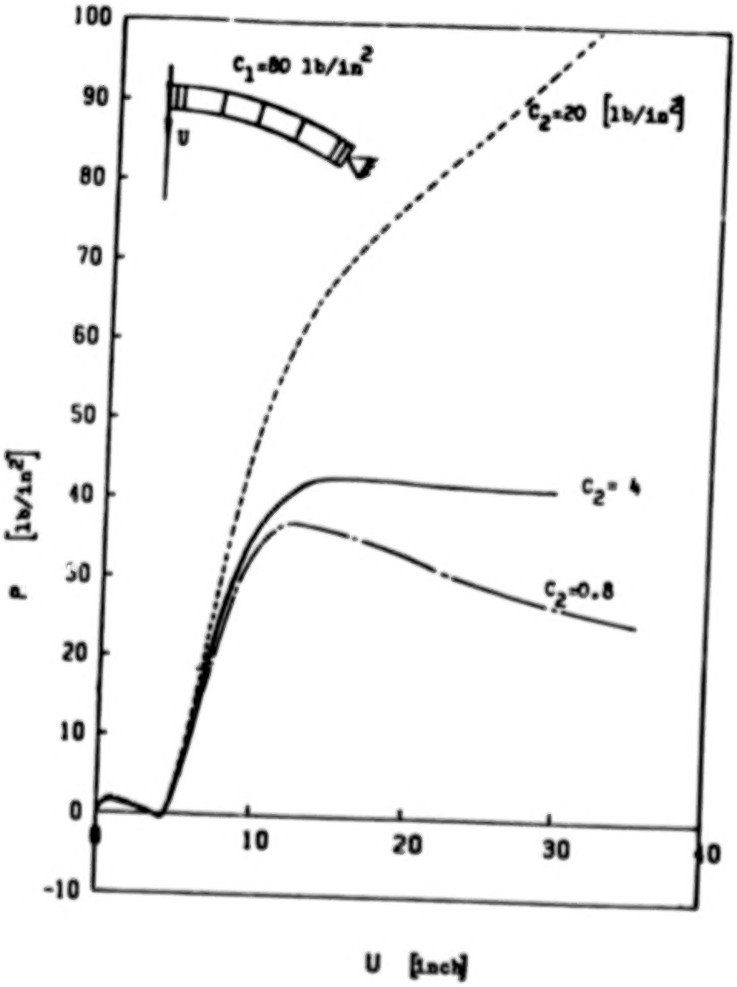
C_1=80 lb/in^2
U
C_2=20 [lb/in^2]
C_2= 4
C_2=0.8
100
90
80
70
60
50
40
30
20
10
0
-10
0
10
20
30
40
P [lb/in^2]
U [inch]

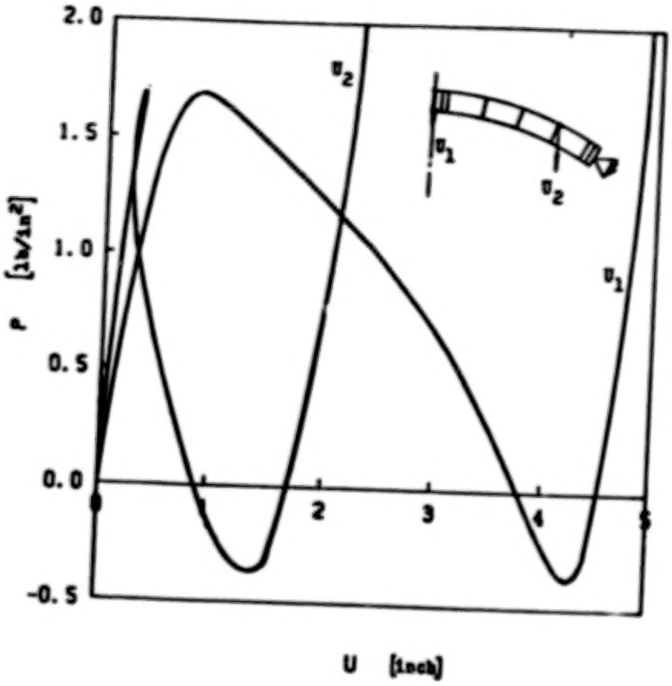
2.0
1.5
1.0
0.5
0.0
-0.5
P [lb/in²]
0
1
2
3
4
5
U [inch]
U_2
U_1
U_1
U_2
U_1

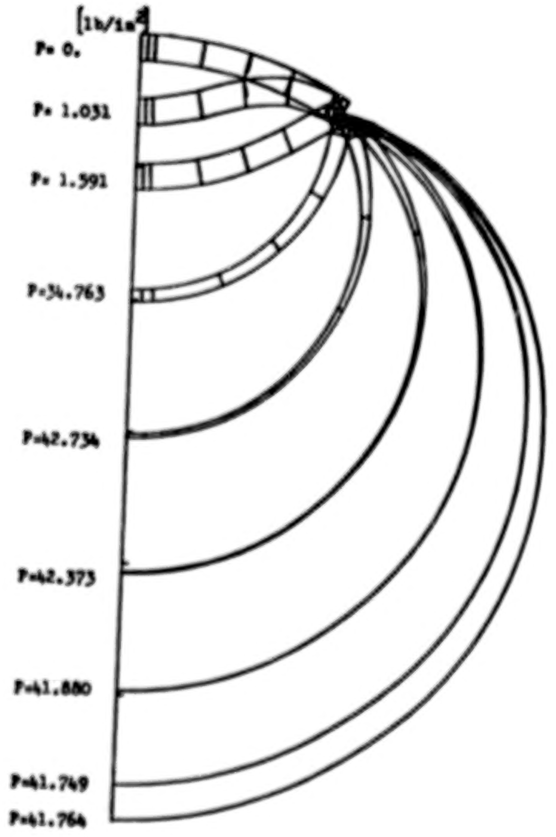
[lb/in²]
P= 0.
P= 1.031
P= 1.591
P=34.763
P=42.734
P=42.373
P=41.880
P=41.749
P=41.764

CALCULATION OF BIFURCATION PATHS

The Riks method (ref. 5) makes it possible to calculate bifurcation paths as well. A second example involves the buckling of a thick rubber plate under end thrust. This problem was analyzed by Sawyers and Rivlin (ref. 12), and provides a good example to test the bifurcation capabilities of the code. For low initial aspect ratios, a barreling mode of bifurcation is obtained, whereas for thinner slabs a flexural mode is obtained. The following figures show computed numerical results for these elements. Bifurcation branches were calculated for this problem as well. The following figures show the results of these calculations. After checking the energy of the system on each branch, the branch of lower energy is then calculated. In the first figure, branch one has lowest energy and branch two indicates a secondary bifurcation. The lower branches in each of the subsequent figures also represent lower energy equilibrium states. (See ref. 13.)

PLATE UNDER END THRUST

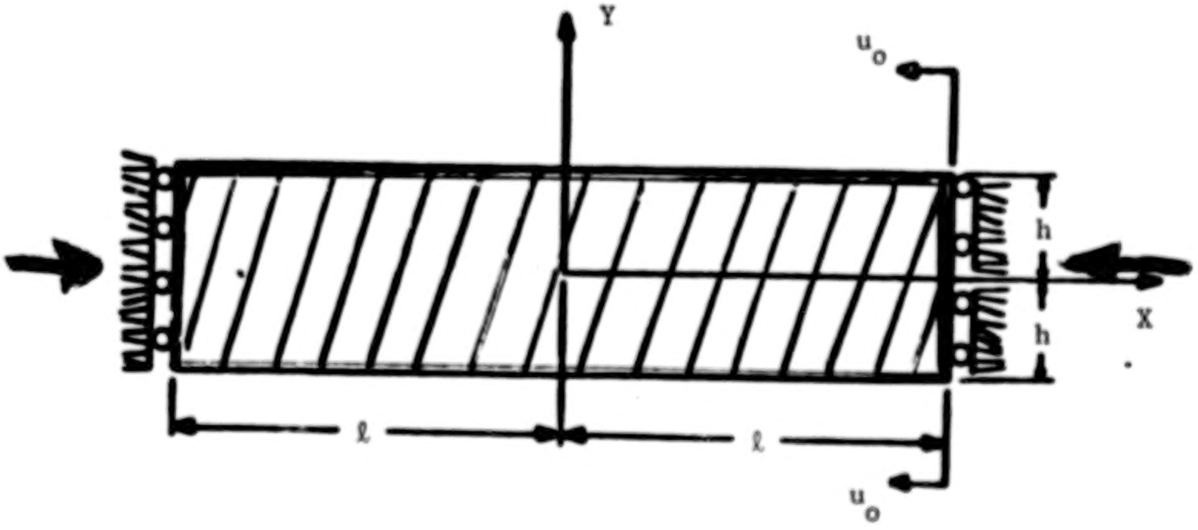

FIRST THREE BUCKLING MODES FOR A PLATE UNDER END THRUST

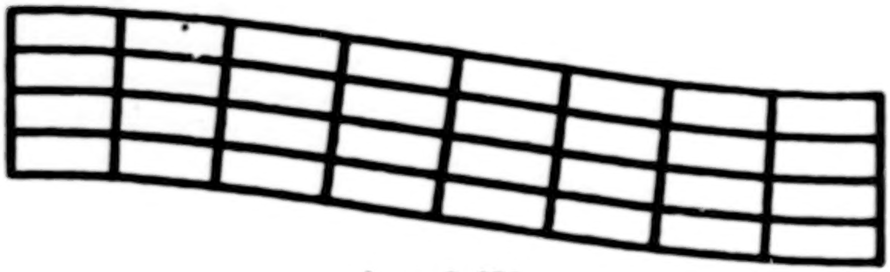

$\lambda_x = 0.973$

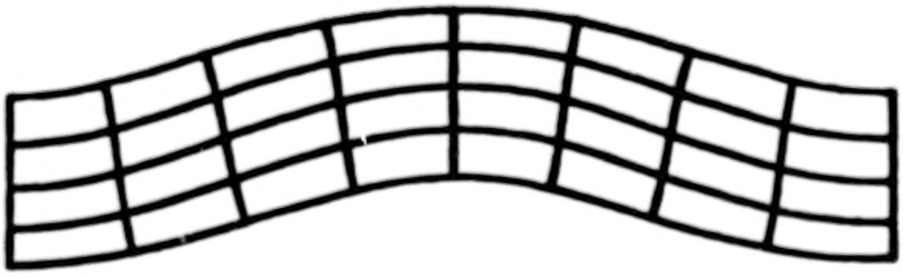

$\lambda_x = 0.892$

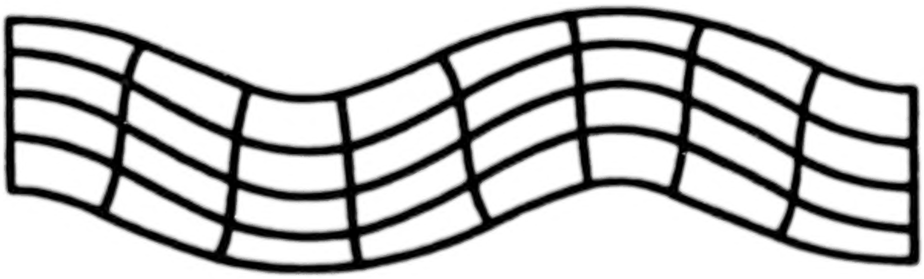

$\lambda_x = 0.762$

BUCKLED CONFIGURATIONS OF A PLATE FOR FIRST MODE BUCKLING

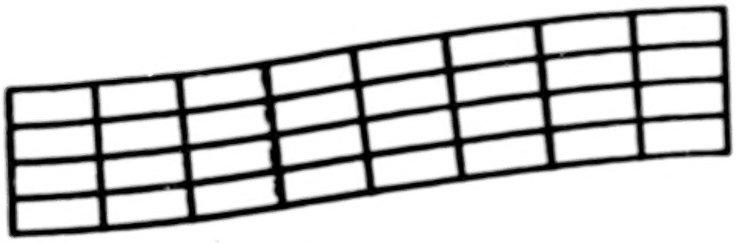

$\Delta L/L = 0.30$

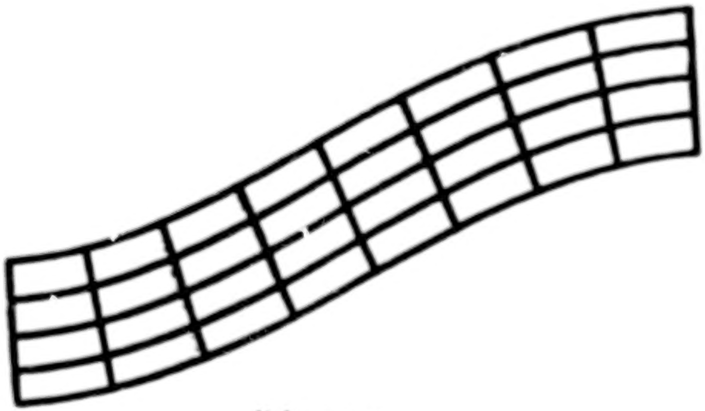

$\Delta L/L = 0.32$

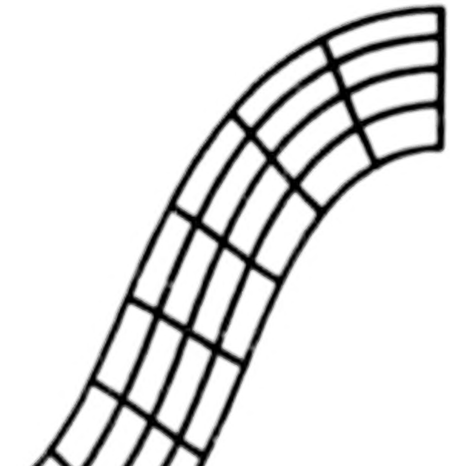

$\Delta L/L = 0.67$

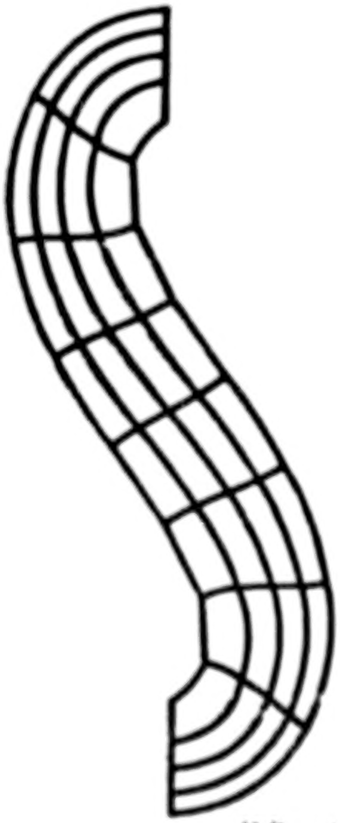

$\Delta L/L = 1.02$

LOAD-DEFLECTION CURVE FOR A PLATE
ASPECT RATIO OF 0.18

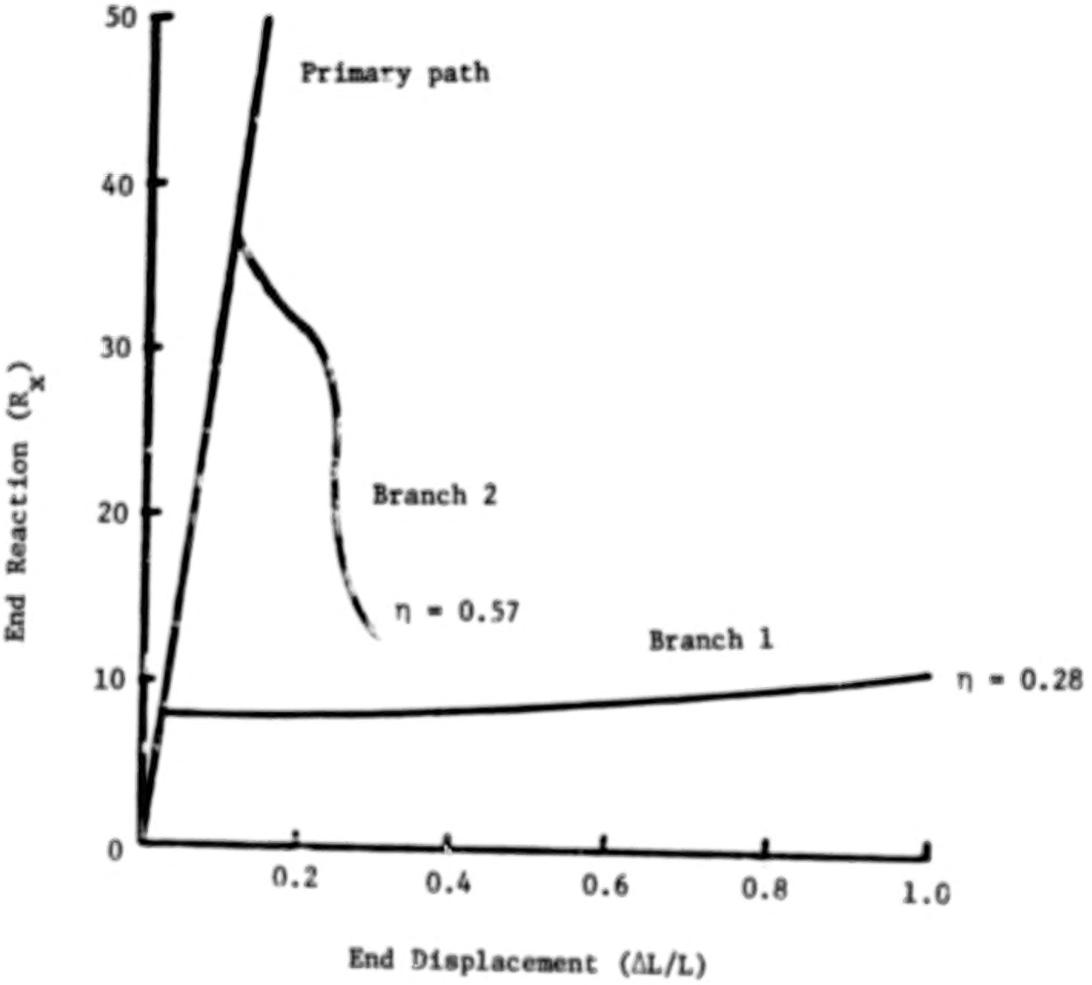

COMPUTATIONAL PROBLEMS DURING HIGH COMPRESSION

The augumented Lagrange method failed for problems with high compression as indicated in the figure below. An oscillatory mode was obtained at compressions of 30%. Here the Q1/P0 element was employed. In view of this, the continuation techniques with Q2/P1 elements were attempted in the following examples.

30% COMPRESSION

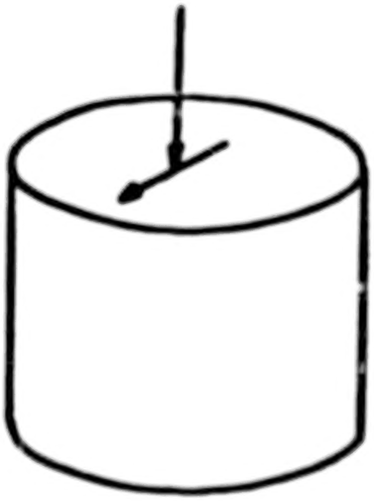

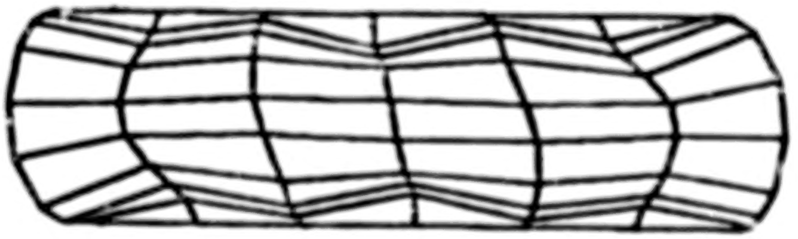

FIXED END CYLINDER

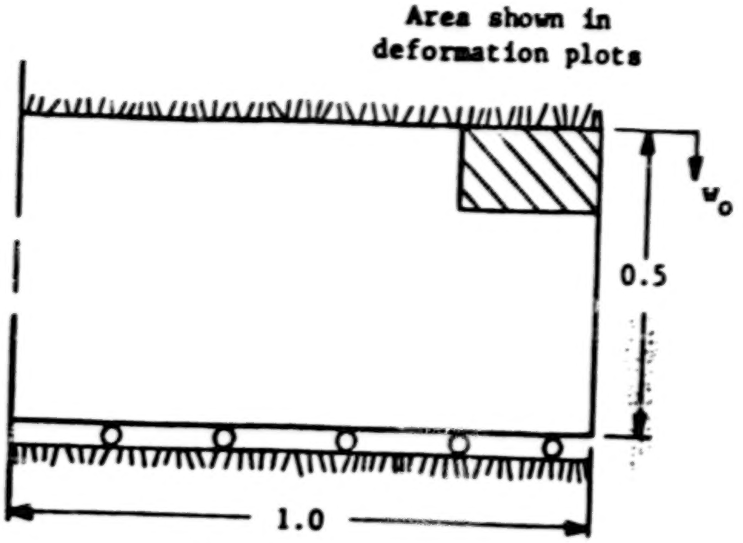
Area shown in deformation plots
w_o
0.5
1.0

Physical problem

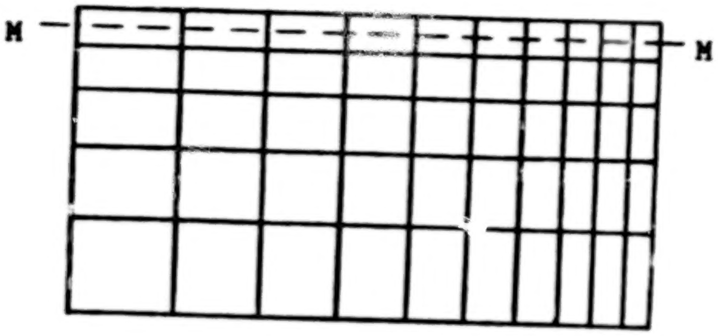

50-element mesh

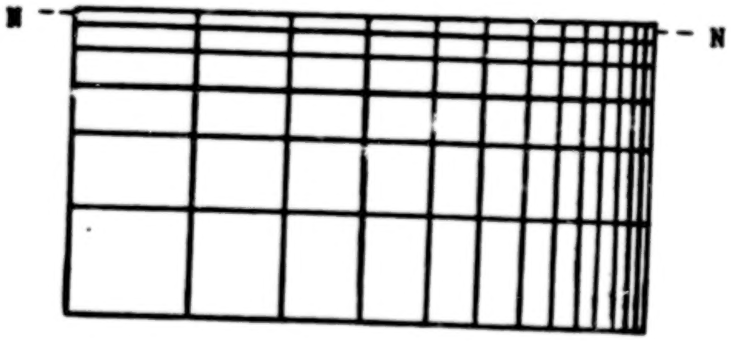

78-element mesh

DISPLACED CONFIGURATION OF FIXED END CYLINDER: EIGHT-NODE ELEMENTS

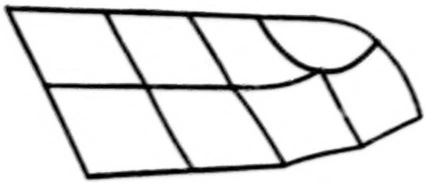

Q8DP, 50-element model, $w_o = 0.1$

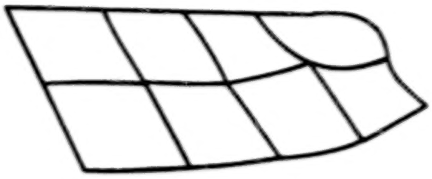

Q8CP, 50-element model, $w_o = 0.1$

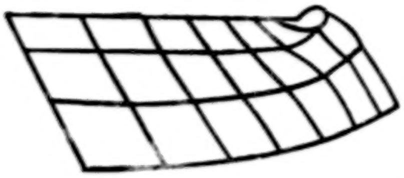

Q8DP, 78-element model, $w_o = 0.1$

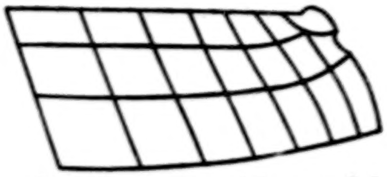

Q8CP, 78-element model, $w_o = 0.1$

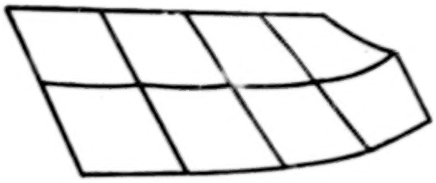

Q8D, 50-element model, $w_o = 0.1$

DISPLACED CONFIGURATION OF FIXED END CYLINDER: NINE-NODE ELEMENTS

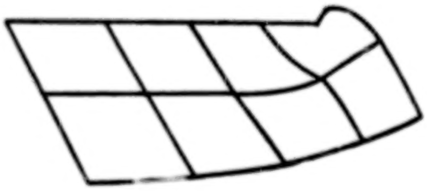

Q9DP, 50-element model, $w_o = 0.1$

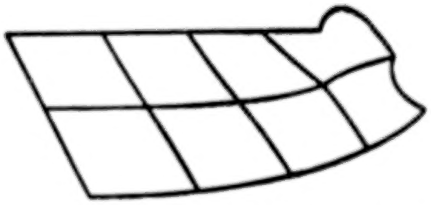

Q9CP, 50-element model, $w_o = 0.1$

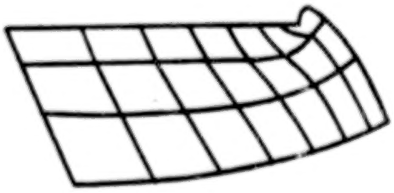

Q9DP, 78-element model, $w_o = 0.1$

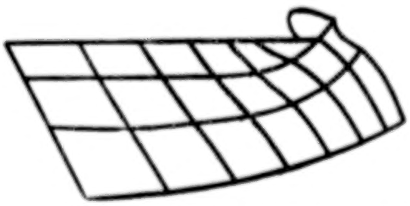

Q9CP, 78-element model, $w_o = 0.1$

COMPRESSION OF A RUBBER BLOCK

Here a rubber block of revolution is one-quarter of the cross section of a block of revolution is shown. The block is subject to compression by uniformed displacement of the edges. A strong singularity is developed in the free edge leading to a cusp as indicated in the calculated deformed configurations. Ultimately, contact of these surrounding regions occurs. This is a very difficult class of elastostatic problems and contact conditions must be incorporated in the analysis procedure to handle these problems.

PLANE STRAIN BLOCK

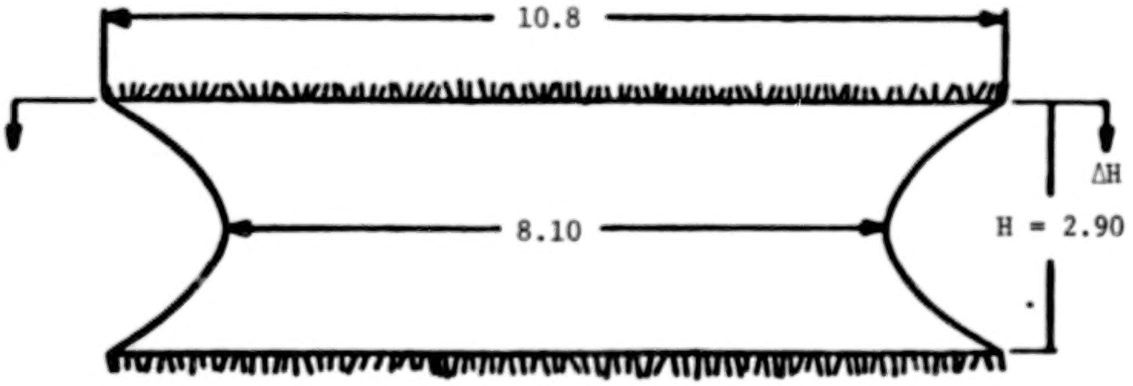

SYMMETRIC MODEL OF PLANE STRAIN BLOCK

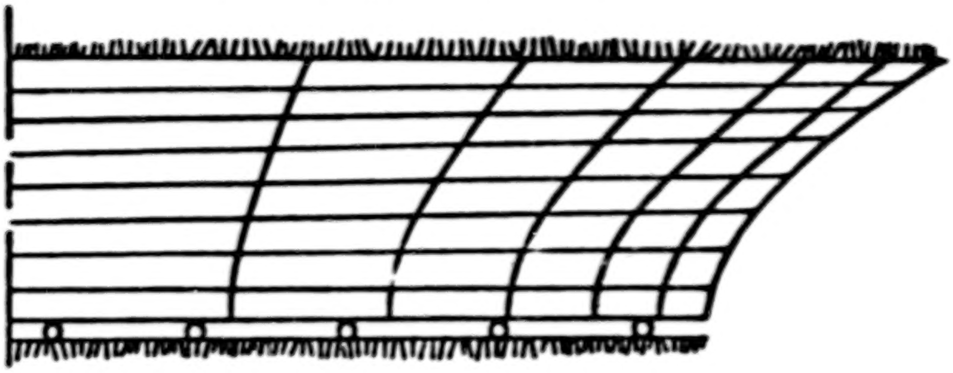

DEFORMATION BEFORE LIMIT POINT

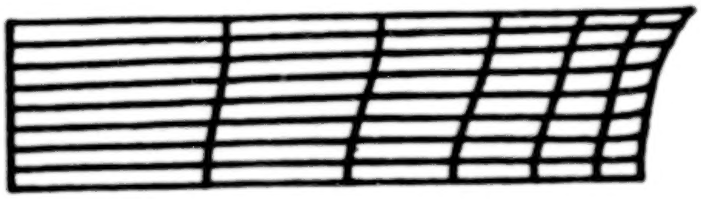

$\Delta H/H = 0.1175$

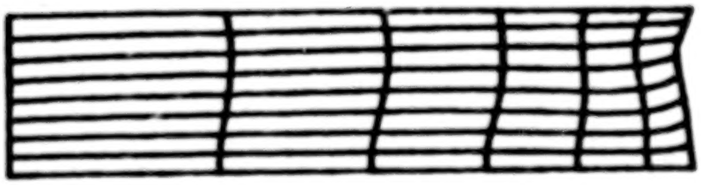

$\Delta H/H = 0.1564$

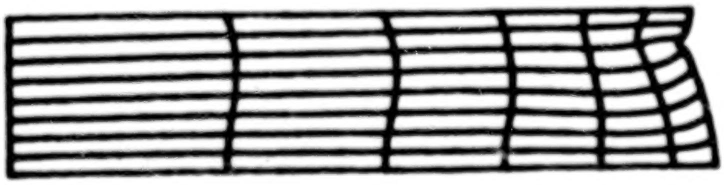

$\Delta H/H = 0.1743$

DEFORMATION AFTER THE LIMIT POINT

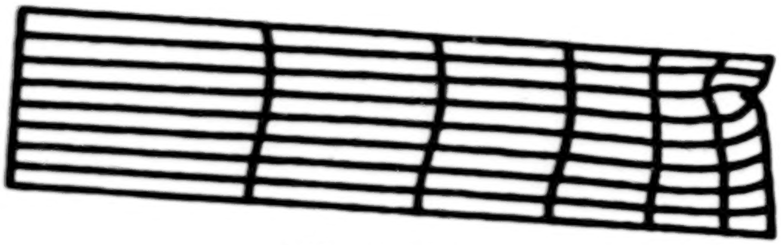

ΔH/H = 0.164

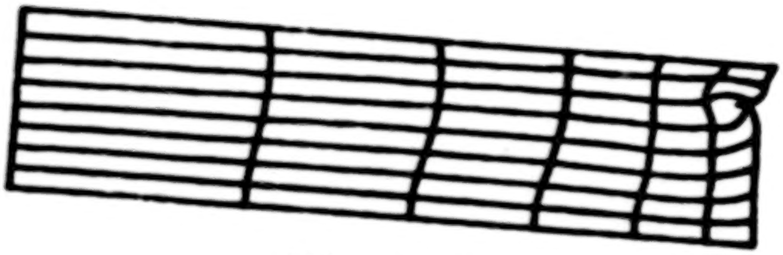

ΔH/H = 0.151

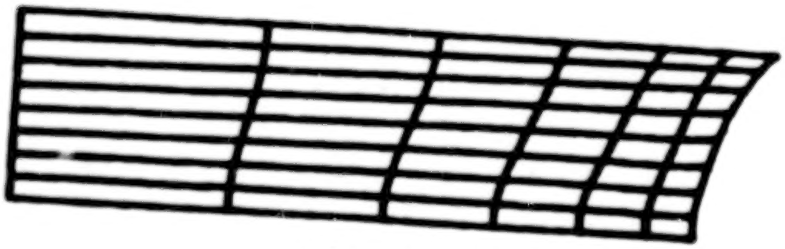

ΔH/H = 0.104

ENLARGED VIEW OF DEFORMED CONFIGURATION

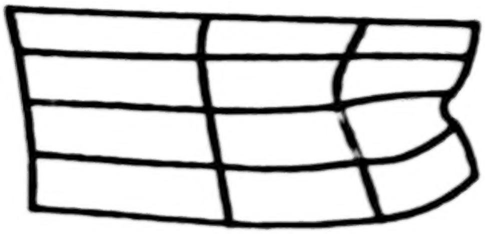

At limit point

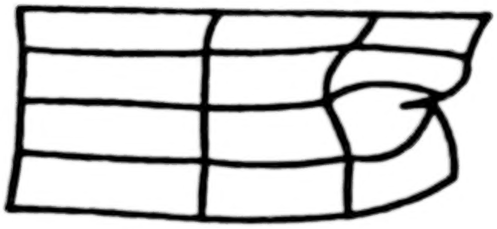

After limit point

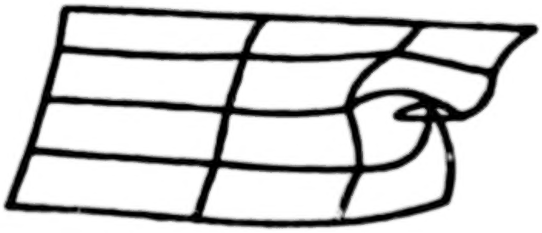

Element boundary overlap at the cusp

LOAD-DEFLECTION CURVE FOR THE PLANE STRAIN BLOCK

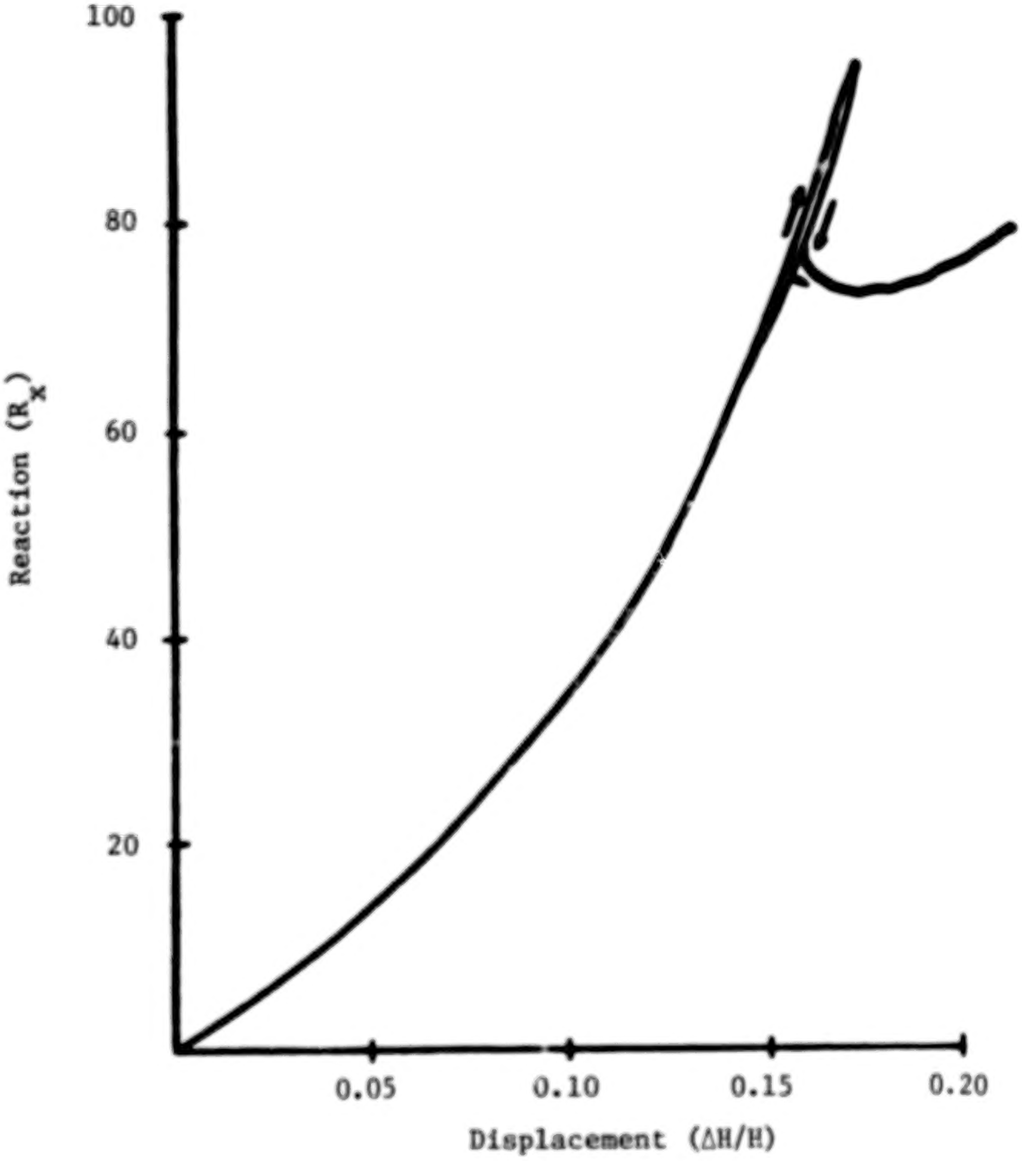

NEW FRICTION MODELS

It is now the generally held view that the classical Mohr-Coloumb law of friction is inadequate on both physical and mathematical grounds when modelling friction effects in real materials. For this reason, a preliminary study of several new non-classical friction laws have been undertaken. These friction laws include nonlocal effects to approximate deformed asperities, adhesion effects, and elastic junction effects, and ultimately will include fracture and damage models of the junctions on the contact surface. The general form of these contact laws is given below, where σ_T is the tangential frictional stress, ν is the coefficient of friction, which may depend upon the number of loading cycles and the stress state on the contact surface, gradients of deformation, etc., S_ρ is a smoothing operator with ρ representing a characteristic dimension of deformed asperities on the contact surface, σ_n is the normal contact pressure, and ϕ_ε represents a compliance function which models the elasticity and elastoplasticity of interface junctions. This compliance reaction is given as an anti-symmetric function of the value of the tangential velocity vector $\dot{u}_T$ on the contact surface. An algorithm has been developed for implementing this new friction law. Some preliminary results are indicated in the final two figures of this paper. (See also refs. 14 through 16.)

4. NEW FRICTION MODELS

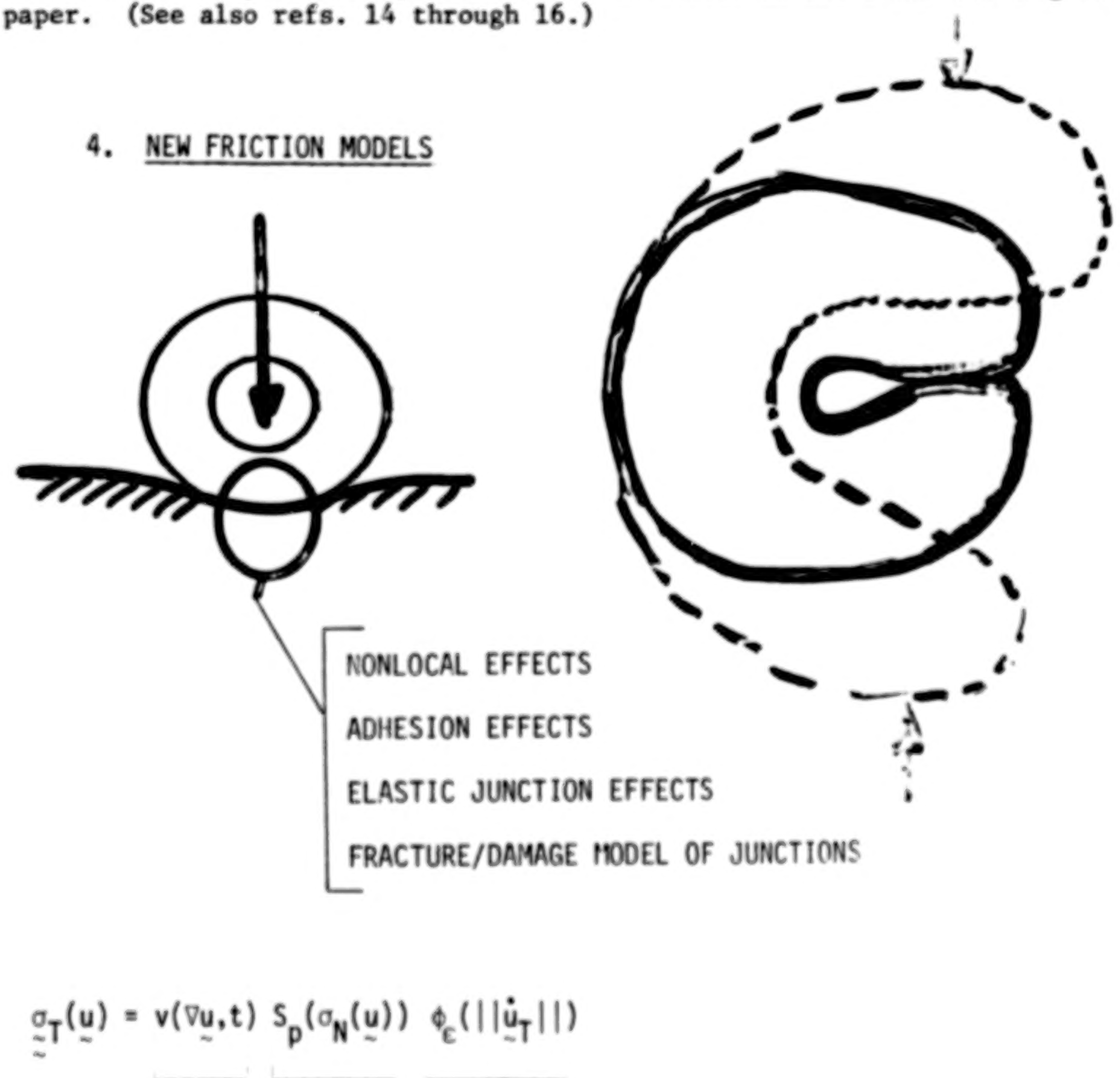

NONLOCAL EFFECTS

ADHESION EFFECTS

ELASTIC JUNCTION EFFECTS

FRACTURE/DAMAGE MODEL OF JUNCTIONS

$$\underset{\sim}{\sigma}_T(\underset{\sim}{u}) = \underbrace{\nu(\nabla \underset{\sim}{u},t)}_{\text{CYCLIC/DAMAGE}}\ \underbrace{S_p(\sigma_N(\underset{\sim}{u}))}_{\text{NONLOCAL}}\ \underbrace{\phi_\varepsilon(||\dot{\underset{\sim}{u}}_T||)}_{\text{JUNCTION ELASTICITY \& PLASTICITY}}$$

NEW FRICTION MODEL APPLICATIONS

An example of the indentation of a rigid cylindrical stamp into an elastic slab is considered. A non-classical friction law is used, with $\rho = -0.1$, $\varepsilon = 10^{-4}$, $E = 1000$, $\mu = 0.6$. Nine-node bi-quadratic elements were used. Deformed shape and stresses on the contact surface are shown.

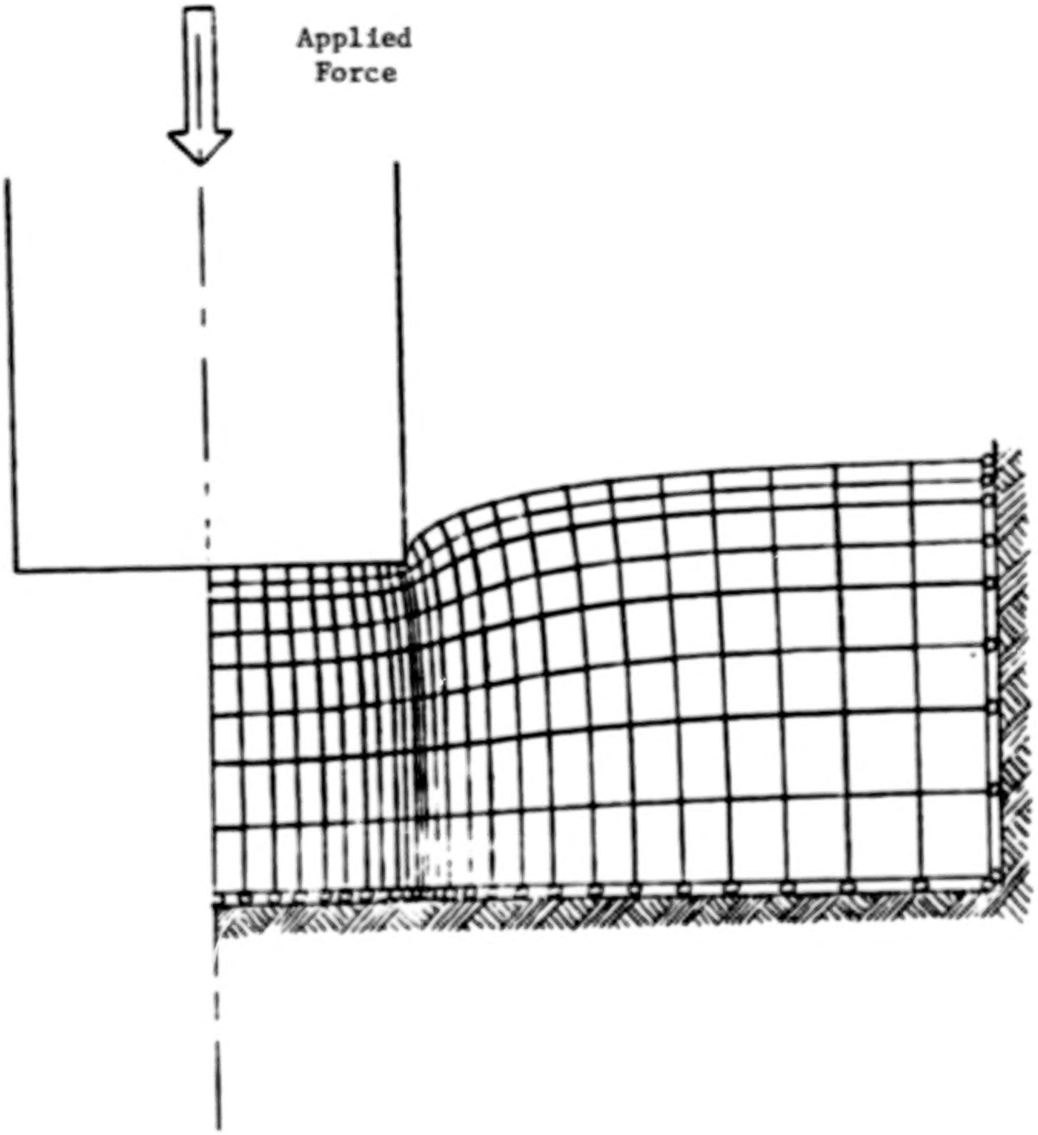

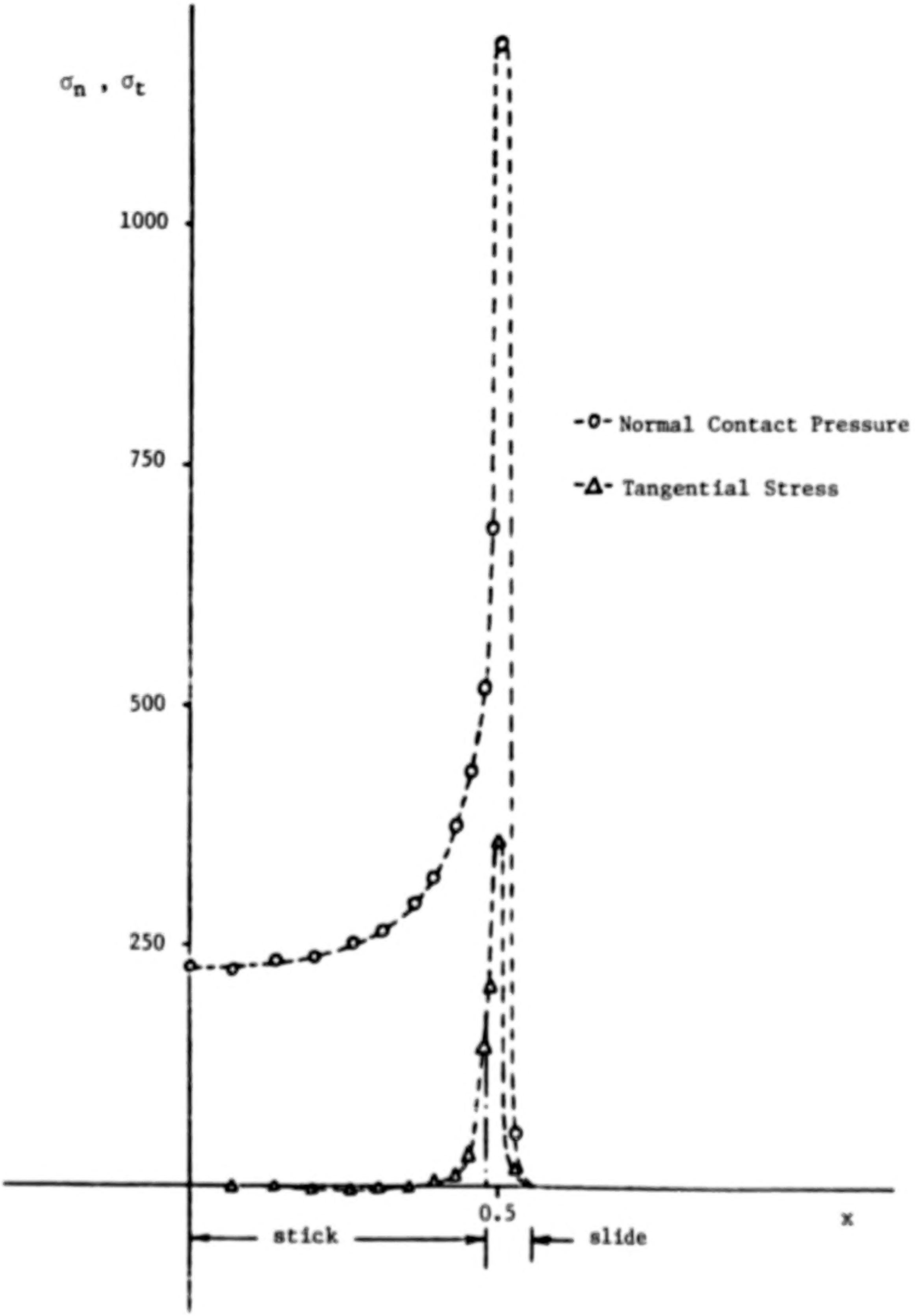
σ_n , σ_t
1000
750
500
250
0.5
x
stick
slide
-o- Normal Contact Pressure
-Δ- Tangential Stress

REFERENCES

1. Glowinski, R.; Lions, J. L.; and Tremolieres, R.: Analyse Numerique des Inequations Variationelles. Dunod-Bordas: Paris, 1976.

2. Oden, J. T.: Penalty Methods for Constrained Oroblems in Nonlinear Elasticity. IUTAM Symposium on Finite Elasticity, Martinum-Nijhoff Publ.: The Hague, 1982, pp. 281-300.

3. LeTallec, P.; and Oden, J. T.: Existence and Characterization of Hydrostatic Pressure in Finite Deformations of Incompressible Elastic Bodies. J. Elast., vol. 11, no. 4, 1981, pp. 341-357.

4. Oden, J. T.; and Jacquotte, O.: Stability of RIP Methods for Stokesian Flows. TICOM Report No. 82-2, Texas Institute for Computational Mechanics, Austin, 1982.

5. Riks, E.: The Application of Newton's Method to the Problems of Elastic Stability. J. Appl. Mech., vol. 39, 1972, pp. 1060-1066.

6. Keller, H. B.: Practical Procedures in Path Following Near Limit Point. Computational Methods in Applied Sciences and Engineering, R. Glowinski and J. L. Lions, eds., North-Holland, 1982.

7. Crisfield, M. A.: A First Incremental/Iterative Solution Procedure That Handles 'Snap-Through'. Computers and Structures, vol. 13, 1981, pp. 55-62.

8. Padovan, J.; and Arechaga, T.: Formal Convergence Characteristics of Elliptically Constrained Incremental Newton-Raphson Algorithms. Int. J. Engn. Sci., vol. 20, no. 10, 1982, pp. 1077-1097.

9. Wempner, G. A.: Discrete Approximations Related to Nonlinear Theories of Solids. Int. J. Solids Structures, vol. 7, 1971, pp. 1581-1599.

10. Rheinboldt, W. C.: Numerical Analysis of Continuation Methods for Nonlinear Structural Problems. Computers and Structures, vol. 13, 1981, pp. 103-113.

11. Oden, J. T.: Finite Elements of Nonlinear Continua. McGraw-Hill, 1972.

12. Sawyers, K. N.; and Rivlin, R. S.: Stability of a Thick Elastic Plate Under Thrust. J. Elast., vol. 12, 1980, pp. 101-125.

13. Miller, T. H.: A Finite Element Study of Instabilities in Rubber Elasticity. Ph.D. Dissertation, Univ. of Texas, Austin, 1982.

14. Pires, E. B.: Analysis of Nonclassical Friction Laws for Contact Problems in Elastostatics. Ph.D. Dissertation, Univ. of Texas, Austin, 1982.

15. Oden, J. T.; and Pires, E. B.: Nonlocal and Nonlinear Friction Laws and Variational Principles for Contact Problems in Elasticity. J. Appl. Mech., 1983, in press.

16. Oden, J. T.; and Pires, E. B.: Numerical Analysis of Certain Contact Problems in Elasticity With Nonclassical Friction Laws. Computers and Structures, vol. 16, no. 1-4, 1982, pp. 481-485.

APPLICATION OF TIRE DYNAMICS TO AIRCRAFT LANDING GEAR DESIGN ANALYSIS

Raymond J. Black
Bendix Aircraft Brake and Strut Division

ABSTRACT

The tire plays a key part in many analyses used for design of aircraft landing gear. Examples include structural design of wheels, landing gear shimmy, brake whirl, chatter and squeal, complex combination of chatter and shimmy on main landing gear (MLG) systems, anti-skid performance, gear walk, and rough terrain loads and performance. This paper discusses which tire parameters are needed in the various analyses.

Two tire models are discussed for shimmy analysis, the modified Moreland approach (ref. 1) and the Von Schlippe-Dietrich approach (ref. 2). It is shown that the Moreland model can be derived from the Von Schlippe-Dietrich model by certain approximations.

The remaining analysis areas are discussed in general terms and the tire parameters needed for each are identified. The conclusion of the paper is that accurate tire data allows more accurate design analysis and the correct prediction of dynamic performance of aircraft landing gear.

INTRODUCTION

A number of important design analysis areas of aircraft landing gear require accurate data on tire dynamic parameters. One of the more obvious examples is wheel design. The primary loads acting on the wheel act through the tire onto the wheel bead seat area. The wheel cannot be efficiently designed without accurate data on tire to wheel contact loads for the entire spectrum of operating conditions to which the landing gear system is subjected. This includes landing impact, braked roll, taxiing, turning, cross wind landing, and in some cases obstacle impact. The latter is particularly true for carrier based airplanes. The wheels of such aircraft must accommodate running over arresting cables when the tire is in the near bottomed condition. Modern aircraft wheel design makes use of experimentally and analytically determined bead contact forces to arrive at optimized designs of the wheel cross sections. In spite of increased demands for more durable wheels having longer fatigue life and increased capabilities, wheel weight per unit load has decreased in recent years.

Other design analysis areas involving the entire landing gear system include:

- Landing gear shimmy (both nose and main landing gear)
- Brake-landing gear whirl stability
- Brake chatter and squeal
- Complex combinations of chatter and shimmy
- Anti-skid performance
- Gear walk
- Rough terrain operations

This paper will concentrate primarily on the tire parameters needed in the first four of the above problem areas.

LANDING GEAR SHIMMY

There are two tire models commonly used for aircraft landing gear shimmy analysis: the modified Moreland model (refs. 1, 3, and 4) and the Von Schlippe-Dietrich model (refs. 2, 5, and 6). The equations for the forces and moments at the tire footprint are similar for the currently used versions of the two models and as a result there are a large number of parameters which are common to both models. Both models require that the vertical load deflection characteristics of the tire be known along with the general load, inflation pressure and speed envelope of operation of the aircraft. In addition the following parameters must be known for the operational envelope:

m_t = mass of tire (kg)

I_{pt} = polar moment of inertia of inflated tire ($kg \cdot m^2$)

I_{dt} = diametral moment of inertia of inflated tire ($kg \cdot m^2$)

K_1 = lateral spring rate of tire (N/m)

C_L = lateral equivalent viscous damping coefficient (N·sec/m)

μ_1 = rolling tire torsional spring rate (N-m/m)

μ_D = rolling tire torsional damping coefficient (N·m/sec)

R_g = loaded radius of the tire (m)

C_w = slope of drag force versus slip ratio for small slip ratios (N)

R_r = tire rolling radius (m)

For the modified Moreland model, two additional parameters are required:

C = coefficient of yaw (rad/N)

C_1 = yaw time constant (sec)

These parameters are used in Moreland's cornering relationship:

$$CF_{nj} = \psi_{tj} + C_1 \dot{\psi}_{tj} \qquad (1)$$

where

j = index indicating the jth wheel of a multi-wheel landing gear

F_{nj} = lateral force acting on tire footprint (N)

ψ_{tj} = yaw angle or sideslip angle of tire footprint with respect to the tire (rad)

Dots over a variable are used to indicate differentiation with respect to time.

In the Von Schlippe-Dietrich model it is shown that the cornering characteristics come about due to continuity between the tire distortion in the footprint's most forward position and the lateral distortion of the tire as a function of peripheral distance, combined with adhesion of the tire footprint centerline to the ground surface. Denoting the lateral displacement of the tire outside the footprint as λ and the peripheral distance around the tire as s ($s = 0$ corresponds to the forward tip of the footprint and $s > 0$ corresponds to moving upward around the tire center) it is found from experiments that when a pure lateral load is applied to the tire λ is given by

$$\lambda = \lambda_p \left(a_1 e^{-s/L} + (1-a_1)\right) \qquad (2)$$

where λ_p = lateral deflection of footprint (constant within footprint) (m)

s = peripheral distance (m)

a_1 = experimental constant between zero and 1 (dimensionless)

L = experimentally determined "relaxation" length (m)

For type VII tires, a_1 is very close to 1. However, for many new design tires with a relatively small aspect ratio and a relatively small width between wheel flanges, a_1 is significantly less than unity. For example, on a H45 x 17-20, PR22 tire, typical values of a_1 range from 0.80 to 0.92, depending on the vertical load and the tire pressure.

As a consequence of Equation (2), it can be shown that when the wheel moves forward an amount ds the most forward position of the tire footprint will move an amount

$$d\lambda_1 = \lambda_p \frac{a_1}{L} ds \qquad (3)$$

relative to its position prior to rolling forward. The quantity a_1/L is denoted by

$$C_\lambda = a_1/L \tag{4}$$

It can be shown that as a consequence of Equation (2) the steady state "cornering power" or cornering coefficient is given by

$$N = \tfrac{1}{2} \frac{K_1}{C_\lambda} \left(1 + e^{2C_\lambda h}\right) \tag{5}$$

where

N = cornering coefficient (N/rad)

C_λ = tire coefficient defined by Equation (4), (1/m)

h = half length of the tire footprint (m)

For transient conditions the general kinematic situation is illustrated in Figure 1. Due to strut deflection, the wheel is tilted at an angle ϕ_B' and twisted in the yaw direction at an angle ψ_S'. The coordinate of the wheel axle center is y_a and the coordinate of the most forward position of the tire footprint is y_{fp}. The wheel is rolled forward an amount ds during which time the position variables of the tire change by amounts $d\phi_B'$, $d\psi_S'$, dy_a, $d\lambda$, and $C_\lambda \lambda ds$ as defined by Equations (3) and (4).

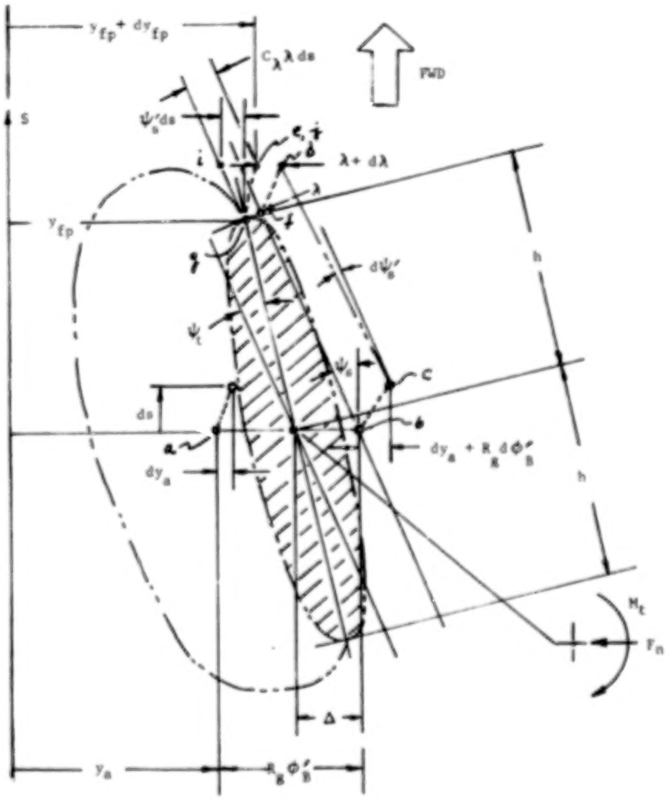
$y_{fp} + dy_{fp}$
$C_\lambda \lambda ds$
FWD
S
$\psi_s' ds$
e, f
d
$\lambda + d\lambda$
i
λ
y_{fp}
h
g
$d\psi_s'$
ψ_t
ψ_s
c
ds
b
a
$dy_a + R_B d\phi_B'$
dy_a
h
M_t
F_n
Δ
y_a
$R_B \phi_B'$

Figure 1.- Tire distortion nomenclature.

BEST DOCUMENT AVAILABLE

With this in mind we can, from Figure 1, write the quantity $y_{fp} + dy_{fp}$ in two ways. We first consider the path a to b to c to d to e which gives

$$y_{fp} + dy_{fp} = y_a + R_g\phi_B' + dy_a + R_g d\phi_B' - h(\psi_s' + d\psi_s') - (\lambda + d\lambda) \quad (6)$$

Next, we consider the path a to b to f to g to i to j which gives

$$y_{fp} + dy_{fp} = y_a + R_g\phi_B' - h\psi_s' - \lambda - \psi_s' ds + C_\lambda \lambda ds \quad (7)$$

Equating (6) to (7) gives

$$dy_a + R_g d\phi_B' - hd\psi_s' - d\lambda = -\psi_s' ds + C_\lambda \lambda ds \quad (8)$$

which can be written as

$$\frac{d\lambda}{ds} + C_\lambda \lambda = \frac{dy_a}{ds} + R_g \frac{d\phi_B'}{ds} + \psi_s' - h\frac{d\psi_s'}{ds} \quad (9)$$

We can eliminate λ from Equation (9) by defining λ in terms of y_a and y_{fp}. Again from Figure 1,

$$\lambda = y_a - y_{fp} + R_g\phi_B' - h\psi_s' \quad (10)$$

Substituting (10) into (9) gives

$$\frac{dy_{fp}}{ds} + C_\lambda y_{fp} = C_\lambda (y_a + R_g\phi_B') - (1 + C_\lambda h)\psi_s' \quad (11)$$

Or, letting $\frac{d}{ds} = D$, this substitution will yield

$$y_{fp} = \frac{1}{D + C_\lambda}\left[C_\lambda\left(y_a + R_g\phi_B'\right) - \left(1 + C_\lambda h\right)\psi_s'\right] \quad (12)$$

As a result of adhesion of the tire footprint to the ground, we can write

$$y_{fp}(s = -h) = y_a + R_g\phi_B' - \Delta \quad (13)$$

Taking the series expansion for the left hand side of Equation (13) gives

$$y_{fp}(s = -h) = y_{fp} - h \frac{dy_{fp}}{ds} + \frac{h^2}{2!} \frac{d^2 y_{fp}}{ds^2} - \ldots \tag{14}$$

Applying (14) to (12) and making the substitution $D = \frac{1}{v} D_t$ where $D_t = d/dt$ gives

$$\left(1 - \frac{h}{v} D_t + \frac{h^2}{2! v^2} D_t^2 - \frac{h^3}{3! v^3} D_t^3 + \ldots\right)\left(C_\lambda (y_a + R_g \phi_B') - (1 + C_\lambda h) \psi_s'\right) = \left(\frac{D_t}{v} + C_\lambda\right)\left(y_a + R_g \phi_B' - \Delta\right) \tag{15}$$

Equation (15) is the basic cornering relationship used in the current version of the Von-Schlippe-Dietrich tire model.

Although Equation (15) does not appear to resemble the Moreland cornering relationship, it can be shown that they are similar. If the infinite series representing the distance delay is restricted to the first two terms, $1 - (h/v)D_t$, and the following kinematic relationship is introduced:

$$V(\psi_s - \psi_t) = -D_t(y_a + R_g \phi_B' - \Delta) \tag{16}$$

where V is the forward velocity of the airplane, then Equation (15) can be rewritten as:

$$\Delta = \left(\frac{1 + hC_\lambda}{C_\lambda}\right) \psi_t + \frac{h}{V}\left(\dot{\Delta} - \frac{(1 + hC_\lambda)}{C_\lambda} \dot{\psi}_s'\right) \tag{17}$$

Since the side force is given by

$$F_n = K_1 \Delta + C_L \dot{\Delta} \tag{18}$$

Equation (17) can be written

$$\frac{C_\lambda}{K_1(1 + hC_\lambda)} F_n = \psi_t + \frac{C_L}{K_1} \dot{\psi}_t + \frac{C_\lambda h(K_1 + C_L D_t)}{VK_1(1 + hC_\lambda)} \left(\dot{\Delta} - \frac{(1 + C_\lambda h)}{C_\lambda} \dot{\psi}_s'\right) \tag{19}$$

For large values of V the far right hand term is small. Thus Equation (19) is similar to Equation (1) with

$$\frac{C_\lambda}{K_1 \left(1 + hC_\lambda\right)} \approx C \text{ or } \frac{1}{N} \text{ from Equation (5)} \tag{20}$$

$$\text{and } \frac{C_L}{K_1} \approx C_1 \tag{21}$$

From the latter it is apparent that Moreland's cornering relationship is equivalent to an approximation of the Von Schlippe-Dietrich model. This explains why the two models give similar results when used in shimmy analysis. It has been found that in many cases the Moreland model is slightly more unstable than the Von Schlippe-Dietrich model. It is often more conservative to use the Moreland model for landing gear design. Moreland's model is also more simple from a computational standpoint since one does not have to deal with the infinite series or, equivalently, the time delay function represented by Equations (14) and (13) respectively.

The forces acting at the tire footprint are only part of the shimmy problem formulation. Figure 2 illustrates the factors considered in the total problem, namely the airplane, the local structure between the airplane and the landing gear, the landing gear structure, and finally the footprint of the tire.

The fuselage is represented by the three dimensional motion of a fuselage reference point. The three motions are a lateral motion y_f, a roll motion ϕ_f, and a yaw motion ψ_f. Three input forces corresponding to these three directions act from the landing gear. The motion of the fuselage is given by solution to model equations covering the first several normal modes of the fuselage. The equation of motion of the fuselage is:

$$[M]\left\{\ddot{q}\right\} + (1 + i\eta_f)\,[K]\left\{q\right\} = [\delta]\begin{Bmatrix} Fy_a \\ T\psi_a \\ T\phi_a \end{Bmatrix} \qquad (22)$$

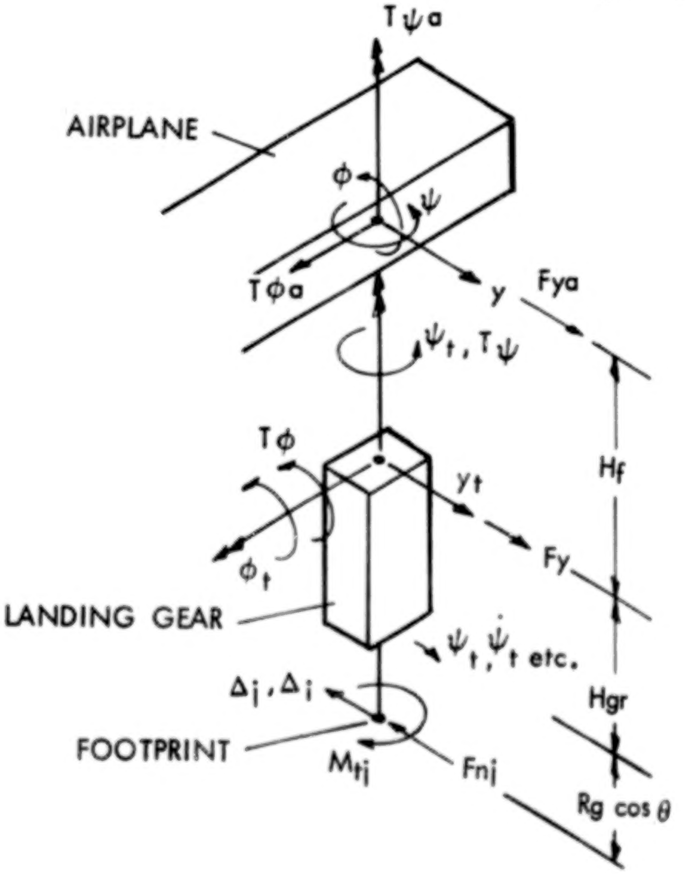

Figure 2.- Shimmy modeling considerations.

where

[M] = fuselage modal mass matrix (kg)

[K] = fuselage stiffness matrix (N/m)

n_f = loss factor for fuselage structure

[δ] = modal deflection matrix

$\left.\begin{matrix} F_{ya} \\ T_{\psi a} \\ T_{\phi a} \end{matrix}\right\}$ forces and moments in the y, ψ and ϕ directions

q = vector of n normal modes

To obtain the fuselage deflection at the reference point the q vector is multiplied by the transpose of the modal deflection matrix.

$$\begin{Bmatrix} y_f \\ \psi_f \\ \phi_f \end{Bmatrix} = [\delta]^T \begin{Bmatrix} q_1 \\ q_2 \\ \vdots \\ q_n \end{Bmatrix} \tag{23}$$

The relative deflections due to the structure from the fuselage reference point to the landing gear attach point are given by:

$$\begin{Bmatrix} y_t - y_f \\ \psi_t - \psi_f \\ \phi_t - \phi_f \end{Bmatrix} = [f] \begin{Bmatrix} F_y \\ T_\psi \\ T_\phi \end{Bmatrix} \tag{24}$$

where

$$\begin{Bmatrix} y_t - y_f \\ \psi_t - \psi_f \\ \phi_t - \phi_f \end{Bmatrix} = \text{relative deflections in the } y, \psi \text{ and } \phi \text{ directions}$$

$[f]$ = flexibility matrix

$$\begin{Bmatrix} F_y \\ T_\psi \\ T_\phi \end{Bmatrix} = \text{forces and moments in the } y, \psi, \text{ and } \phi \text{ directions}$$

The mathematical model of the landing gear is fairly straightforward. Care must be taken in properly accounting for cross coupling of flexibilities and inertial cross coupling brought on by off-center masses of the landing gear system such as torque arms, steering cylinders, lights and attachment fittings. Since each gear differs in details the equations of motion will not be given here.

The remaining equations are those of the tire forces and kinematic restraints. For both the Moreland and Von Schlippe-Dietrich models, these equations are:

$$F_{nj} = K_1 \Delta_j + C_L \dot{\Delta}_j \tag{25}$$

for the side force,

$$M_j = \mu_1 \psi_{tj} + \mu_{1D} \dot{\psi}_{tj} \tag{26}$$

for the moment, and

$$V(\psi_s' - \psi_{tj}) = -\dot{y}_a - R_g \dot{\phi}_B' + \dot{\Delta}_j \tag{27}$$

for the kinematic constraint.

For the Moreland tire model the tire equations are completed using Equation (1) as the final relationship while for the Von Schlippe-Dietrich model Equation (15) is used.

For dual wheel landing gear systems there is an additional moment acting from the ground about an axis normal to the ground plane. This moment, M_w, is governed by the following differential equation:

$$\dot{M}_w + (C_w R_r R_g / V I_p)\, M_w + 2K_w / I_p \int M_w \, dt = -(C_w l_s^2 / 2V)\, \ddot{\psi}_s' - K_w C_w l_s^2 / V I_p \, \psi_s' \qquad (28)$$

where in addition to previously defined parameters

I_p = polar moment of inertia of one wheel and tire ($\mathrm{kg \cdot m^2}$)

l_s = distance between wheel centerlines (m)

K_w = torsional spring rate of corotational axle (N·m)

If $K_w = 0$ then Equation (28) still may be used by simply setting $K_w = 0$ and retaining the remaining terms. It can be noted that an additional tire parameter, C_w, is needed to deal with dual wheel landing gear systems. This parameter defines the tire drag forces in terms of the percent tire slip for small slip ratios.

Figure 3 shows the Space Shuttle nose landing gear (NLG), which was analyzed extensively for shimmy stability using computerized solutions of the equations of motion previously described, dynamometer testing, and "runway" tests on the Langley Landing Loads Track. This work was extremely important since there were no high-speed taxi tests in the Space Shuttle development program. The first "test" of the landing gear was an actual landing at over 200 mph.

The computer study was used to select the optimum damping for the steer damp unit, to determine sensitivity to wear, friction, and tire parameters, and generally to establish what the margin of stability was for the landing gear system. This was then verified and improved upon by the dynamometer test. Application to a flat runway was verified by comparison of dynamometer and Langley Landing Loads Track test results. The Langley Landing Loads Track could not be used for the full range of speeds and vertical loads because of limitations on track capacity. The dynamometer tests covered the full range of speeds and loads.

Figure 4 demonstrates, for a typical case, the correlation between the computer analysis and the dynamometer (120" flywheel) results. Figure 5 shows the correlation between the dynamometer tests and the NASA dry concrete runway data from the Langley Landing Loads Track. Both sets of results correlate closely, showing that the analytical model can be used with confidence for prediction of the Space Shuttle NLG's stability over a wide range of landing and roll-out conditions.

The process of test and analysis for shimmy stability is described in Reference 7.

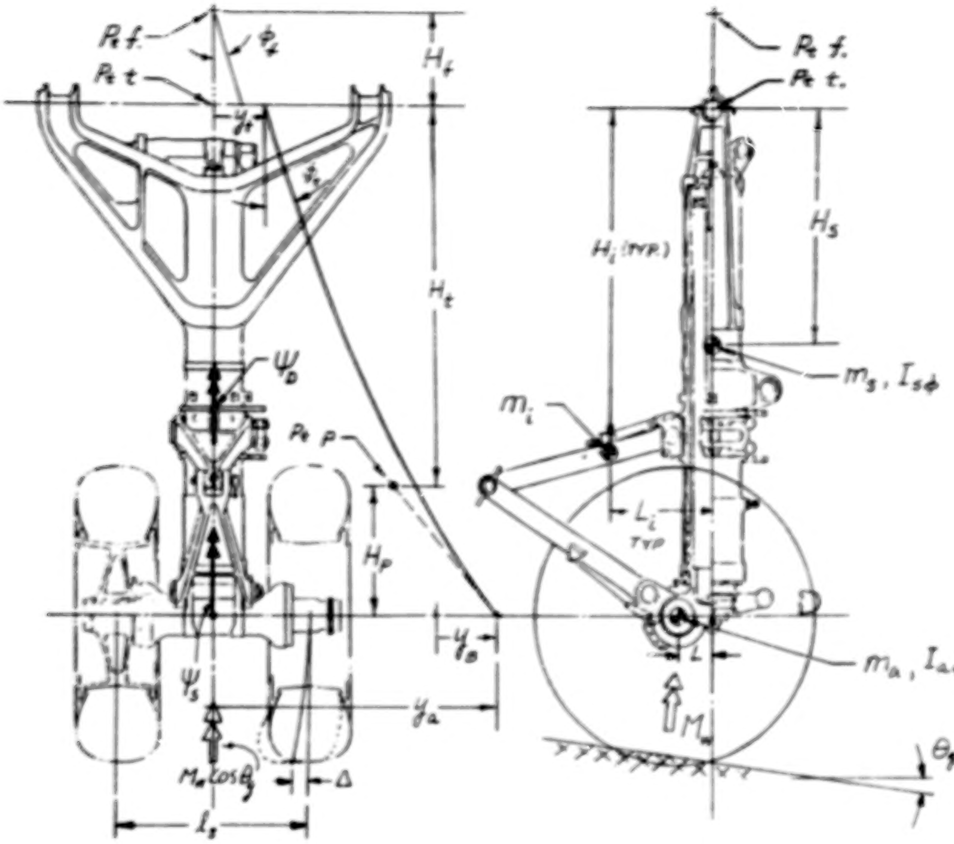
Rf.
ψf
Rt
Hf
yt
ψt
Ht
ψD
Rp
Hp
ψs
yB
ya
Ma cos θg
Δ
ls
Rf.
Rt.
Hs
Hi (TYP.)
ms, Isφ
mi
Li TYP
L
ma, Iaφ
Ma
θg

Figure 3.- Space Shuttle NLG.

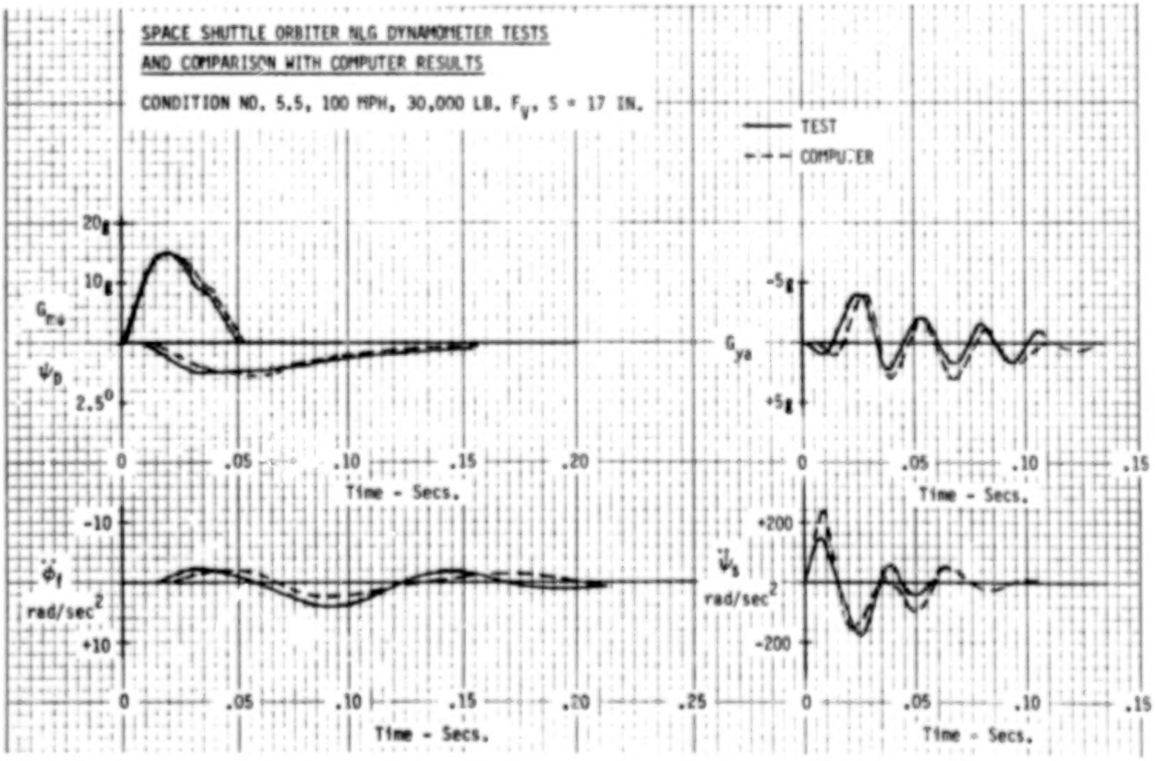

Figure 4.- Correlation between dynamometer and analytical results.

BEST DOCUMENT AVAILABLE

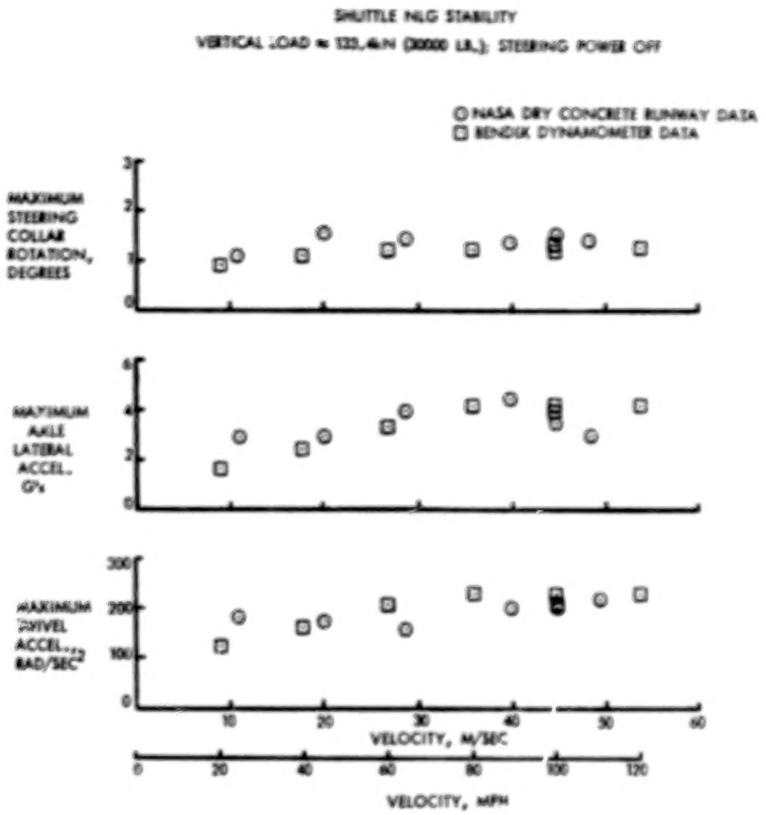

Figure 5.- Correlation between dynamometer and dry concrete runway data.

MAIN LANDING GEAR SHIMMY

In addition to NLG's, shimmy can be encountered on main landing gear systems (MLG's). Three very popular commercial jet aircraft having dual wheel main landing gears experienced similar MLG shimmy problems when they were first introduced. The problem was traced to a side brace configuration which caused twist in the landing gear due to application of a side load. The side braces were all connected to the forward part of the shock strut for the three different aircraft. Modifications were made to the MLG's to stabilize the systems. In two cases a torque arm damper was introduced while in the third case a negative (forward) mechanical trail was used to stabilize the shimmy.

In general MLG's are more complex than NLG's; however, the same tire parameters are needed for MLG stability studies as are used for NLG's. The complexity is associated with the landing gear structure itself. This is illustrated in Figure 6 which is a drawing of the six wheeled C5A MLG. The analysis of this system used a 48 degree of freedom analysis reduced to a twelve degree of freedom system for non-linear simulation studies. The 48 degrees of freedom were necessary to develop an accurate mass and stiffness matrix for the reduced system.

Sample stability results are given in Figure 7 and illustrate the importance of accurate tire parameters. Here the only difference between the two runs is the yaw time constant. The solid curve corresponds to a yaw time constant (C_1) of 0.06 seconds while the dotted curve applies to a C_1 value of 0.03 seconds. The actual yaw time constant for the 49 x 17 tires is considerably lower than both of these values but the comparison served to show the sensitivity of shimmy stability to tire parameters.

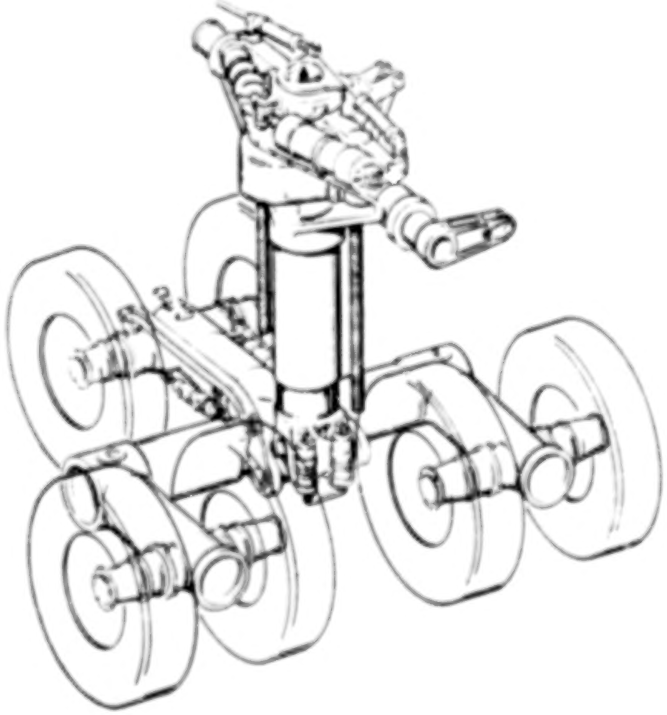

Figure 6.- C5A main landing gear.

BEST DOCUMENT AVAILABLE

The net result of the shimmy stability study showed the C5A MLG to be stable, a result which was later verified by in-service experience. The analysis was important since this was the first time that this six wheeled landing gear configuration was used on an aircraft.

The diversity of MLG designs is illustrated by the complex single wheel MLG shown in Figure 8. This was a preliminary design for the gear which was complicated by the fact that it had to retract around a wing mounted rocket. Needless to say no single set of equations of motion suffice to cover all landing gear systems. Fortunately, however, the tire parameters previously given apply to all landing gears.

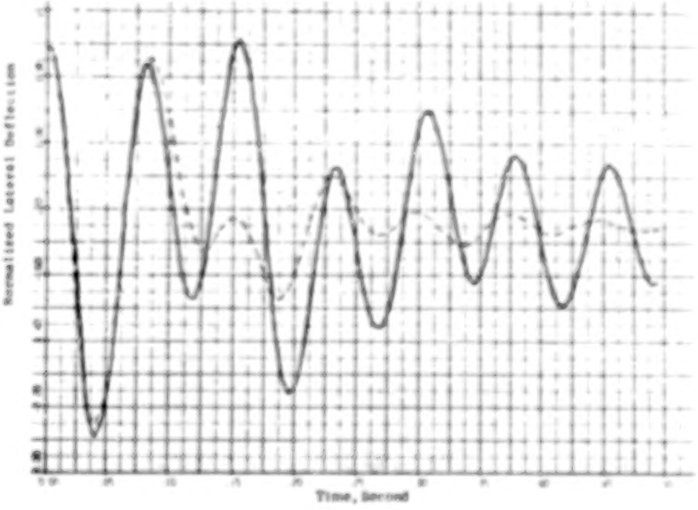

Figure 7.- Comparison of transient motion for two values of the yaw time constant (C5A MLG).

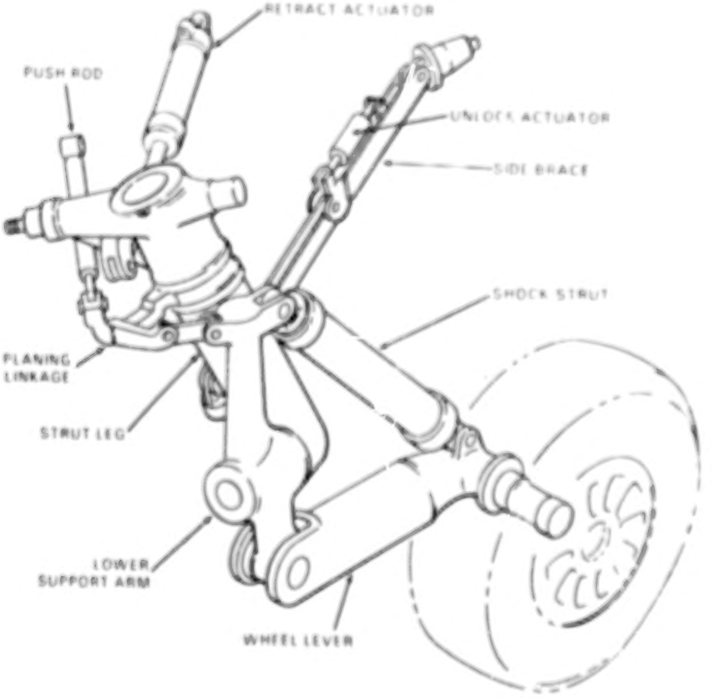
RETRACT ACTUATOR
PUSH ROD
UNLOCK ACTUATOR
SIDE BRACE
SHOCK STRUT
PLANING LINKAGE
STRUT LEG
LOWER SUPPORT ARM
WHEEL LEVER

Figure 8.- Single wheel MLG design for a fighter aircraft.

BEST DOCUMENT AVAILABLE

BRAKE WHIRL

Brake whirl is a highly destructive self excited vibration of the wheel, tire, brake and landing gear structure. It is caused by a localized high pressure region in the brake stack that brings about out of plane bending of the axle. The resulting motion is characterized by a sinusoidal bending of the axle which takes place in two planes, the z-y plane and the x-y plane, as shown in Figure 9. The two motions are 90° out of phase which makes it appear that the bending motion is whirling about the axle centerline at a speed corresponding to the radial natural frequency.

The mathematical analysis of the brake whirl problem requires that a number of tire properties be known. Since the frequency of the whirl motion is generally in the range of 200 to 400 Hz for most landing gears the tire does not respond as it does for low frequency motions. The tire tread remains fixed in the x-z plane except for its steady forward motion and rotation. The heavy bead area of the tire moves with the wheel adding to its effective mass and its moments of inertia. The region between the tread and the wheel is treated as a spring with radial and angular spring constants and associated loss factors.

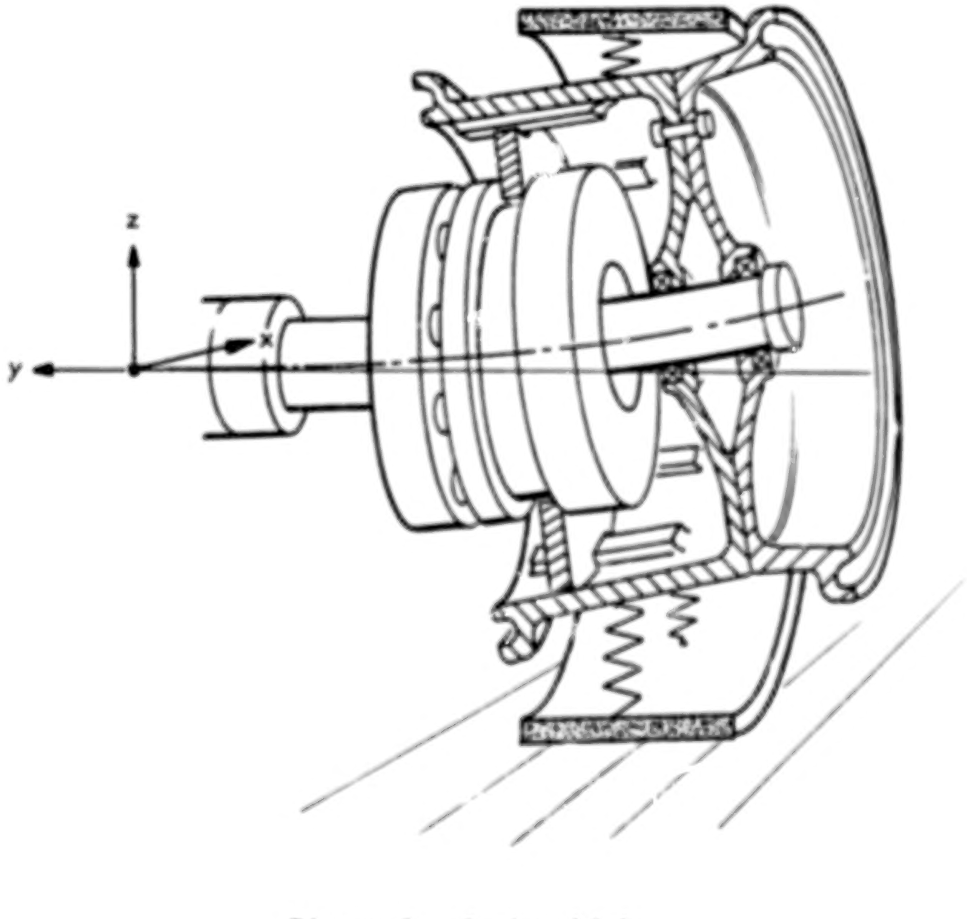

Figure 9.- Brake whirl.

BEST DOCUMENT AVAILABLE

The specific tire parameters are:

K_r = spring rate of tire associated with radial displacement of the wheel with the tread held fixed (N/m)

η_r = loss factor associated with K_r

K_α = diametral angular spring rate of the tire associated with twist of the wheel with the tread held fixed (N-m/rad)

$\eta_{\alpha r}$ = loss factor associated with K_α

M_{tw} = mass of the tire moving with the wheel (the bead area of the tire) (kg)

I_p = polar moment of inertia of m_{tw} ($kg \cdot m^2$)

I_{dt} = diametral moment of inertia of M_{tw} ($kg \cdot m^2$)

R_r = tire rolling radius (m)

Brake whirl stability is a somewhat more serious problem on carbon brake systems because of their mass distribution properties. A careful analysis as well as design changes to stabilize the motion are important in the initial stages of the brake development.

Measurement of the tire stiffness parameters is difficult. As a first approximation K_r is taken to be the average of the fore and aft tire stiffness and the vertical stiffness of the tire. The value of K_α is calculated based on lateral deformation of the tire at both the footprint and 180° from the footprint. The loss factor is estimated to be approximately 0.15 for typical aircraft tires. The mass M_{tw} is roughly 30% of the tire for typical aircraft tires. Calculation of I_p and I_{dt} can be carried out knowing M_{tw} and the location of the bead bundle. The rolling radius can be determined by conventional methods and is equal to the undeflected radius of the tire minus one-third of the tire deflection as a very close approximation.

BRAKE CHATTER AND SQUEAL

Brake chatter and squeal are self excited motions of the brake and landing gear system brought on by so called negative damping at the rotor-stator interface. The negative damping results from an increase in brake torque for a decrease in the instantaneous brake slip velocity. This characteristic yields a term in the equations of motion which looks like a damping term in that it is a force or torque proportional to velocity, but has a sign opposite to that of the dissipative damping of the motion. Thus, the lining characteristic has been termed negative damping.

The chatter motion is a low frequency motion (5 Hz to 15 Hz) and consists of fore and aft bending motion of the shock strut. Squeal consists of wind-up of the stationary parts against the torque take-out system and has a natural frequency of 150 to 500 Hz.

A relatively simple model of brake chatter and squeal uses three degrees of freedom. These are the fore and aft bending motion of the landing gear shock strut, the torsional wind-up of the nonrotating parts of the brake against the torque take-out system, and the forward velocity of the airplane. The nonrotating parts of the brake consist of the brake piston housing, the pressure plate, the backing plate, the stators of the brake, and the torque tube of the brake which carries the stators. The torque take-out system consist of an axle flange on most single and dual wheel landing gears and a brake equalizer rod on truck type landing gears commonly used on larger aircraft.

The tire parameters used in the simplified chatter and squeal analysis consist of the following:

R_r = tire rolling radius (m)

R_g = loaded radius of tire (m)

C_w = slope of drag force versus slip ratio for small slip ratios (N)

M_t = mass of tire (kg)

I_p = polar moment of inertia of tire ($kg \cdot m^2$)

C_x = ratio between the shift in the center of pressure and the aft deflection of the footprint

This three degree of freedom analysis is quite simplified but is useful for preliminary studies of stability of chatter and squeal, particularly for the selection of lining materials that will not result in self-excitation of the vibratory motions. At a later stage in the landing gear development, a more detailed analysis of brake chatter and squeal such as the one that is described in the next section can be carried out.

COMPLEX COMBINATIONS OF CHATTER AND SHIMMY

For most modern main landing gear systems the chatter motion is not simply a fore and aft bending action of the shock strut but rather consists of a complex motion of the gear involving fore and aft, lateral, roll, and yaw motions of the gear. Thus many of the same tire parameters that are used in shimmy analysis are also needed for an analysis of the brake chatter and squeal.

Figure 10 shows a typical truck type main landing gear system and some of the nomenclature and motions considered. There are ten degrees of freedom in the model:

x_B = aft deflection at the truck pivot point (m)

y_B = lateral deflection at the truck pivot point (m)

ϕ_B = roll angle of truck (rad)

θ_B = end bending angle of shock strut (rad)

ψ_B = yaw angle of truck (rad)

ω_1 = angular velocity of one of the forward wheels (rad/sec)

ω_3 = angular velocity of one of the aft wheels (rad/sec)

θ_{s1} = angular rotation of the forward brake stationary parts (rad)

θ_{s3} = angular rotation of the aft brake stationary parts (rad)

x_p = forward translational motion of airplane (m)

A fairly extensive set of tire parameters is needed for the model. The shimmy action uses the simple cornering relationship equating the tire lateral force to a sideslip angle divided by the coefficient of yaw. This is equivalent to the modified Moreland model with $C_1 = 0$.

The tire parameters used in the model are:

K_x = fore and aft tire spring rate (N/m)

K_z = vertical tire spring rate (N/m)

C = coefficient of yaw (rad/N)

μ_ψ = lateral coefficient of friction between tire and runway, a function of slip ratio

$\mu_{\psi m}$ = maximum value of μ_ψ

μ_1 = ratio between self-aligning torque and sideslip angle (N·m/rad)

μ_x = maximum fore and aft coefficient of friction between tire and runway

C_w = ratio between the drag force and the slip ratio for small slip ratios (N)

C_γ = ratio between the shift in the center of pressure and the aft deflection of the tire

M_t = mass of tire (kg)

I_{pt} = polar moment of inertia of inflated tire ($kg \cdot m^2$)

I_{dt} = diametral moment of inertia ($kg \cdot m^2$)

R_g = loaded radius of tire (m)

R_r = rolling radius of tire (m)

A sample result of the nonlinear analysis is shown in Figure 11. In this run the negative damping from the brake lining was set relatively high and the system damping, made up of several nonlinear terms, was set at about one half the expected value. A pulse was added to the torque to cause excitation at the midpoint of the 10 mph stop. It can be seen in Figure 11 that the initial motion is stable but that the pulse causes enough disturbance that the resulting motion is near neutral stability. The mode shape of the motion is far from a simple fore and aft truck motion. Note that the lateral motion of the truck is the same order of magnitude as the aft motion of the truck. Also, there is some yaw motion and considerable roll motion of the truck.

Studies of this type help to establish the amount of negative damping that can be tolerated by both the chatter motion and the high frequency squeal motion of the landing gear. Also mode shapes and frequencies of the several low frequency chatter motions can be established together with the margin of stability of each mode.

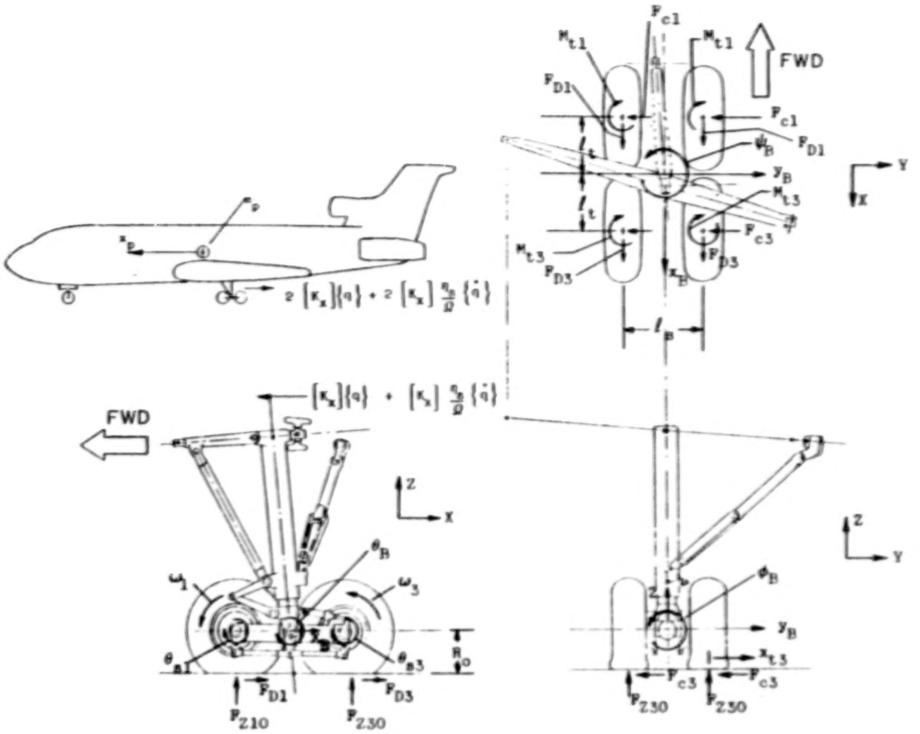
FWD
F_{c1}
M_{t1}
F_{D1}
ψ_B
y_B
M_{t3}
F_{c3}
F_{D3}
x_B
l_t
l_B
Y
X
$2[K_x]\{q\} + 2[K_x]\frac{\eta_s}{\Omega}\{\dot{q}\}$
$[K_x]\{q\} + [K_x]\frac{\eta_s}{\Omega}\{\dot{q}\}$
Z
θ_B
ω_1
ω_3
θ_{B1}
θ_{B3}
R_0
F_{Z10}
F_{Z30}
ϕ_B
x_{t3}

Figure 10.- Nomenclature and motions for complex chatter and shimmy analytical model.

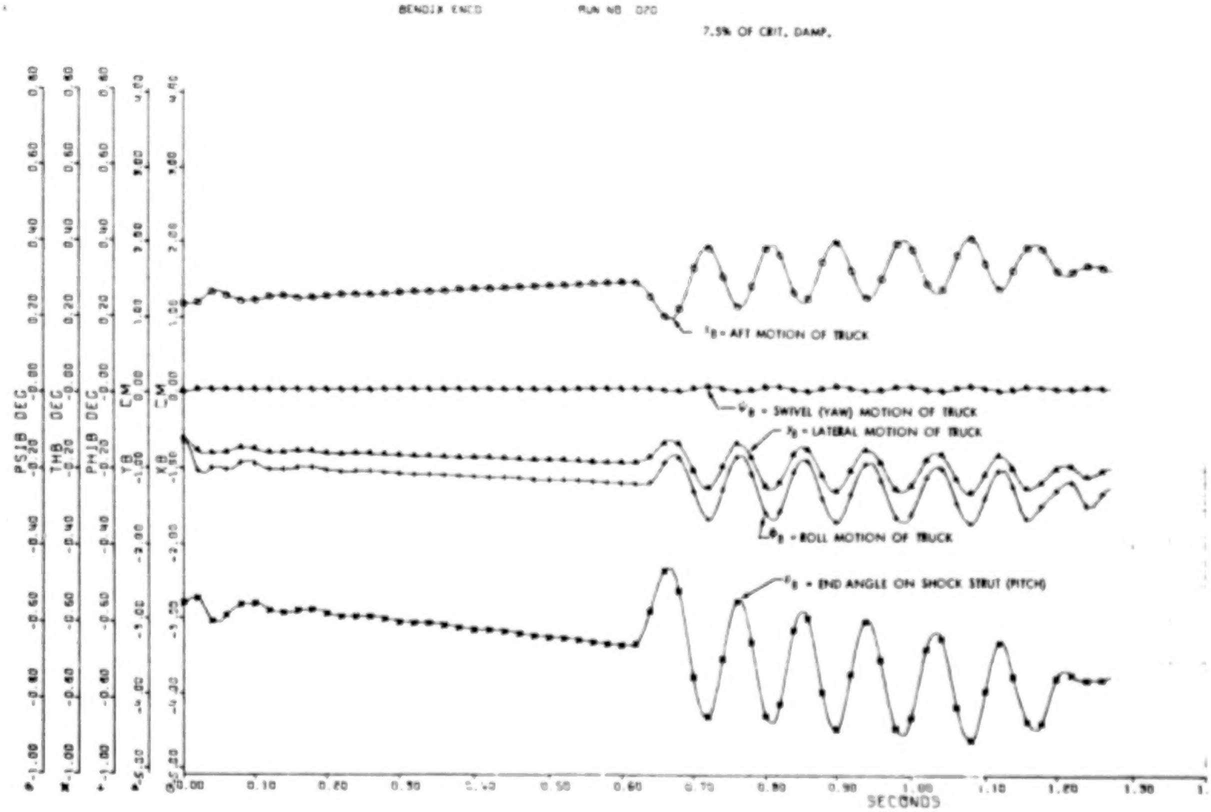

Figure 11.- Sample computer run for MLG chatter and shimmy analytical model.

BEST DOCUMENT AVAILABLE

OTHER ANALYSIS AREAS

The other analysis areas mentioned at the beginning of this paper also require detailed information on tire characteristics. Anti-skid performance requires a model of the brake pressure to brake torque transfer function along with the dynamic characteristics of the anti-skid system. The remainder of the model is similar to that used for chatter and squeal. Gear walk which is a stick-slip motion similar to chatter can come about due to stick-slip action at either the ground surface or the brake interfaces. Rough terrain operations require a tire model capable of predicting vertical and drag loads due to obstacle or hole impact at obstacle lengths which range from a small fraction of the footprint length up to several times the footprint length. The short lengths present more of a problem but methods are available for predictions of tire loads for all lengths. Rough terrain operations analysis also requires a detailed model of the shock strut stroking dynamics in addition to the tire model.

CONCLUSIONS

Tire dynamic parameters play a key part in many design analysis areas for aircraft landing gear systems. Advanced analytical methods to predict tire parameters, such as finite element methods, are needed together with experimental methods for verification of predictions for selected cases and determination of parameters that cannot be determined analytically. Accurate tire data allows more accurate design analyses and correct prediction of dynamic performance of aircraft landing gear. The net result is a more reliable and more efficient system.

REFERENCES

1. Moreland, W. J.: The Story of Shimmy. J. Aeronaut. Sci., Dec. 1974, pp. 793-808.

2. Von Schlippe, V.; and Dietrich, R.: Shimmying of a Pneumatic Wheel. Papers on Shimmy and Rolling Behavior of Landing Gear Presented at Stuttgart Conference, NACA TM-1365, Aug. 1954, pp. 125-160.

3. Edman, J. L.: Experimental Study of Moreland's Theory of Shimmy. WADC Technical Report 56-197, Wright Air Development Center, Wright-Patterson Air Force Base, July 1956.

4. Collins, R. L.; and Black, R. J.: Tire Parameters for Landing Gear Shimmy Studies. AIAA J. Aircraft, May-June 1969, pp. 252-258.

5. Papers on Shimmy and Rolling Behavior of Landing Gear Presented at Stuttgart Conference. NACA TM-1365, Aug. 1954.

6. Smiley, R. F.: Correlation, Evaluation, and Extension of Linearized Theories for Tire Motion and Wheel Shimmy. NACA TN-3632, June 1956.

7. Black, R. J.: Realistic Evaluation of Landing Gear Shimmy Stabilization by Test and Analysis. SAE Paper No. 76-0496, 1976.

A TIRE CONTACT SOLUTION TECHNIQUE

John T. Tielking
Civil Engineering Department
Texas A&M University

EXPANDED ABSTRACT

An efficient method for calculating the contact boundary and interfacial pressure distribution has been developed. This solution technique utilizes the discrete Fourier transform to establish an influence coefficient matrix for the portion of the pressurized tire surface that may be in the contact region. This matrix is used in a linear algebra algorithm to determine the contact boundary and the array of forces within the boundary that are necessary to hold the tire in equilibrium against a specified contact surface. The algorithm also determines the normal and tangential displacements of those points on the tire surface that are included in the influence coefficient matrix. Displacements within and outside the contact region are calculated.

The solution technique is implemented here with a finite-element tire model that is based on orthotropic, nonlinear shell of revolution elements which can respond to nonaxisymmetric loads (refs. 1, 2). The basic characteristics of this relatively comprehensive tire model are described in reference 3. This presentation will focus on the contact solution technique published in reference 4. A sample contact solution is presented for the 32 × 8.8 Type VII aircraft tire that was studied in reference 5.

FINITE-ELEMENT TIRE MODEL

The tire is modeled by an assemblage of axisymmetric curved shell elements. The elements are connected to form a meridian of arbitrary curvature and are located at the carcass midsurface. Figure 1 shows the assembly of 21 elements along the midsurface of a G78-14 tire, for which calculated results are shown in this paper. A cylindrical coordinate system is used, with r, θ, and z indicating the radial, circumferential, and axial directions, respectively. Each element forms a complete ring which is initially axisymmetric with respect to z. The elements are connected at nodal circles, hereafter referred to as nodes.

The finite elements are homogeneous orthotropic with a set of moduli specified for each individual element. The orthotropic moduli for each element are determined by the ply structure surrounding the element. Each ply (on each element) is specified separately, thereby allowing the model to include carcass details such as an overhead belt, sidewall reinforcement, and turnups. A turnup is included in the G78-14 tire model. It was found necessary to include the turnup in the model to obtain the correct inflated shape.

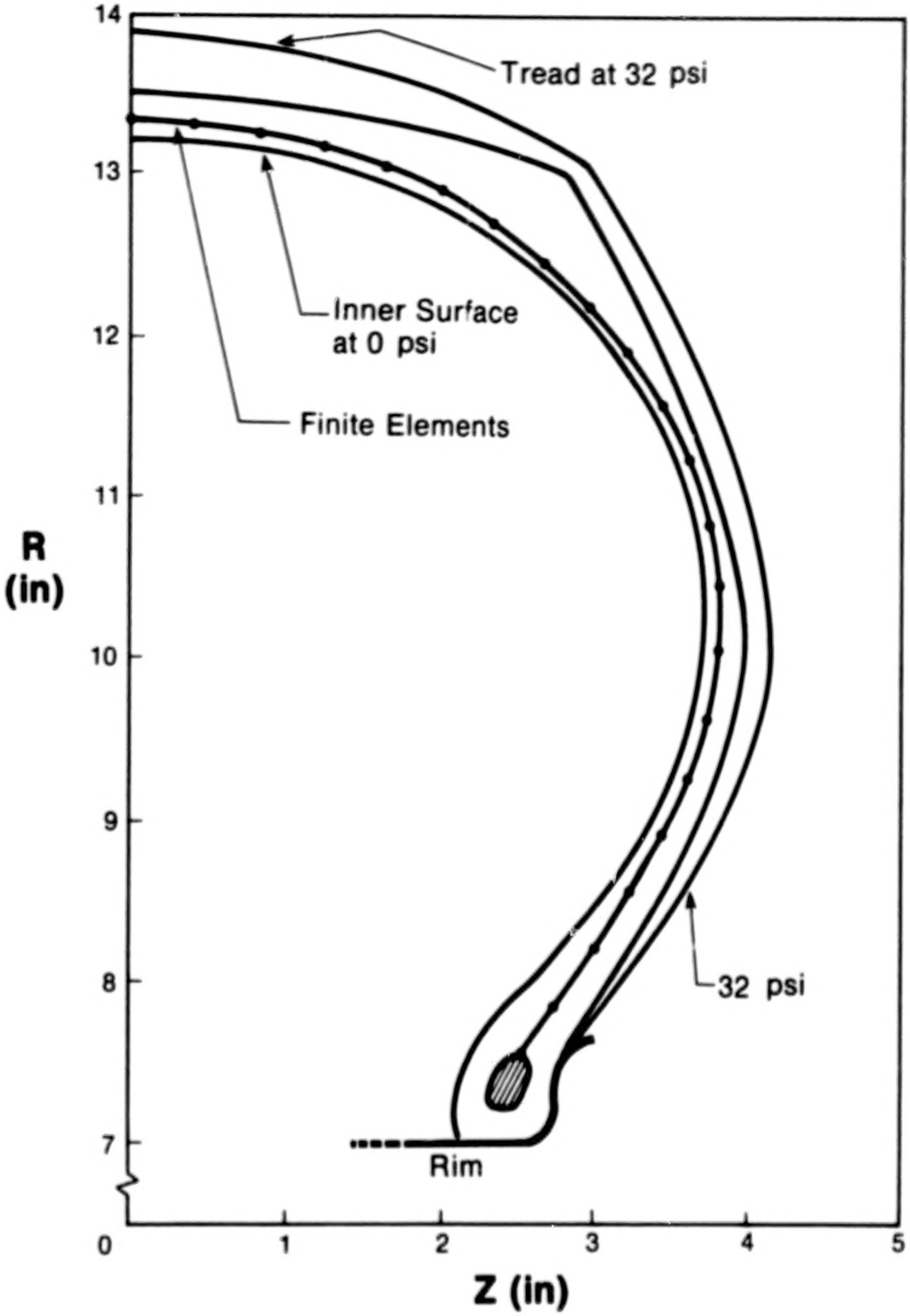
Tread at 32 psi
Inner Surface at 0 psi
Finite Elements
32 psi
Rim
R (in)
14
13
12
11
10
9
8
7
0
1
2
3
4
5
Z (in)

Figure 1

SINGLE HARMONIC RING LOADS

The finite element tire model will respond to single harmonic ring loads on the nodal circles. An approximately linear load-deflection response is obtained when an individual ring load is applied to any node of the pressurized tire model. An example ring load-deflection calculation for the G78-14 tire model is shown in figure 2. A harmonic sequence of stiffness matrices is obtained by applying a sequence of single harmonic ring loads to each of the nodes that may be in the tire-pavement contact region.

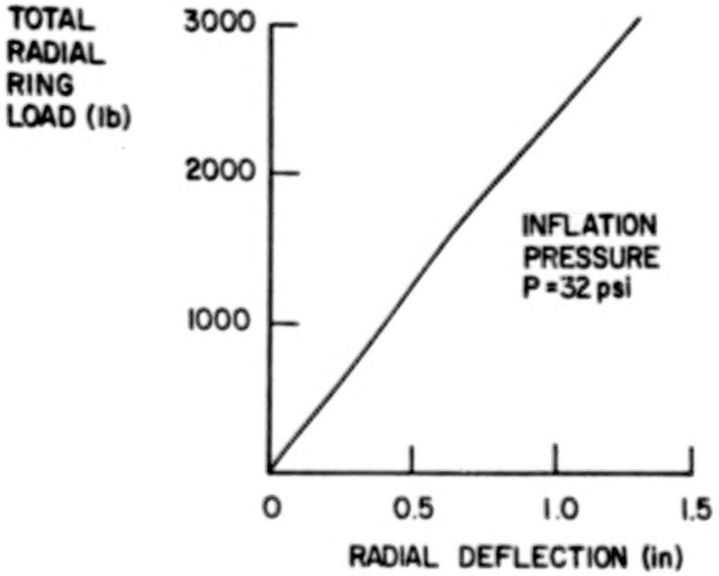

CROWN LOAD-DEFLECTION DATA CALCULATED WITH A UNIFORM RING LOAD APPLIED TO THE CROWN NODE

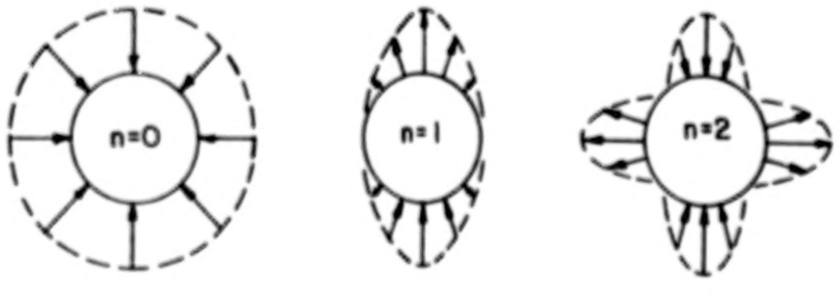

SINGLE HARMONIC RING LOADS APPLIED TO A FINITE ELEMENT NODE

Figure 2

TRANSFER-FUNCTION DEFINITION

As a consequence of the linearity of the ring load-deflection response, the application of a single harmonic ring load produces a displacement field that varies circumferentially in the same harmonic as the applied ring load. Figure 3 gives the definition of the transfer function T_n as the ratio of the output and input amplitudes. Since each node responds differently, a transfer-function matrix, $T_{ik|n}$, is needed to store the stiffness information generated by the ring loads.

INPUT: Single Harmonic Ring Load $A_n \cos n\theta$

OUTPUT: Single Harmonic Displacement $B_n \cos n\theta$

TRANSFER FUNCTION $T_n = \frac{B_n}{A_n}$

$T_{ik|n}$ = n^{th} harmonic transfer function relating displacement of node i to an n^{th} harmonic ring load on node k

Figure 3

POINT LOAD VECTOR {p} AND THE DISCRETE FOURIER TRANSFORM (DFT)

This application of the discrete Fourier transform uses an even number of points (N), equally spaced around the circumference. The example shown in figure 4 uses N = 8 points. A unit load is applied at any point, say point 0. The DFT of the load vector yields a set of N coefficients, G_j, which are approximate values of the coefficients of the conventional Fourier series defined on the continuous interval $0 \leq \theta \leq 2\pi$ and representing the unit point load. The point load is applied, sequentially, in the radial, axial, and circumferential directions.

INFLUENCE COEFFICIENT GENERATION

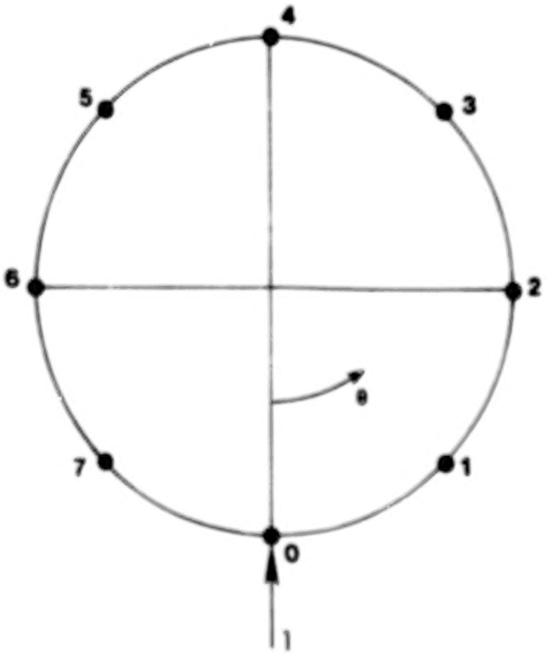

$\{p\} = \{1, 0, 0, 0, 0, 0, 0, 0\}$ load vector

DFT $G_j = \frac{1}{N}\sum_{k=0}^{N-1} g_k W_e^{jk}$ $\qquad W_e = e^{-i2\pi/N}$

$g_k = \{p\}$, $G_j = \frac{1}{N}$ $\qquad j = 0, 1, \ldots, N-1$

Figure 4

INVERSE DISCRETE FOURIER TRANSFORM (IDFT) AND THE INFLUENCE COEFFICIENTS

Having the unit point load represented by a conventional Fourier series, whose coefficients a_n are approximately given by the DFT coefficients, the transfer functions $T_{ik|n}$ are used, on each harmonic, to obtain the coefficients b_n of the Fourier series representing the response of the nodal circle to the unit point load. The inverse discrete Fourier transform is then used to evaluate the displacements, u_m, at the N points. These displacements are the elements of the influence coefficient matrix $[A_{ijk\ell}]$ as seen in figure 5.

INPUT SERIES COEFFICIENTS $a_n = G_n = \frac{1}{N}$

OUTPUT SERIES COEFFICIENTS $b_n = a_n T_{ik|n} = \frac{1}{N} T_{ik|n}$

DFT OF DISPLACEMENT VECTOR $G_n = b_n$

IDFT $u_m^{ik} = \sum_{n=0}^{N-1} G_n W_e^{-mn}$ $\quad m = 0, 1, \ldots, N-1$

INFLUENCE COEFFICIENTS $A_{ijk1} = u_{j-1}^{ik}$ $\quad j = 1, 2, \ldots, N$

SHIFT: $A_{ijk\ell} = u_{j-\ell}^{ik}$ $\quad j = \ell, \ell+1, \ldots, N$

SYMMETRY: $A_{k\ell ij} = A_{ijk\ell}$

$$\{d_{ij}\} = [A_{ijk\ell}]\{P_{k\ell}\}$$

Figure 5

INFLUENCE COEFFICIENT MATRIX

The influence coefficient matrix relates the radial, axial, and circumferential components of the displacement of points on the tire surface to the radial, axial, and circumferential components of load at these points. The radial response partition shown in figure 6 is used to obtain a solution for frictionless contact, in which the axial and circumferential force components are known to be zero. The matrix here covers 3 points on each of 5 nodes. The point separation with this matrix is 11.25 degrees.

$P_{k\ell}$ = load at point ℓ on node k

d_{ij} = deflection of point j on node i

$$\{d_{ij}\} = [A_{ijk\ell}] \{P_{k\ell}\}$$

$$\begin{Bmatrix} d_{11} \\ d_{21} \\ d_{31} \\ d_{41} \\ d_{51} \\ d_{12} \\ d_{22} \\ d_{32} \\ d_{42} \\ d_{52} \end{Bmatrix} = \begin{bmatrix} A_{1111} & & & & & & & & & \\ A_{2111} & A_{2121} & & & & & & & & \\ A_{3111} & A_{3121} & A_{3131} & & & & & & & \\ A_{4111} & A_{4121} & A_{4131} & A_{4141} & & & & & & \\ A_{5111} & A_{5121} & A_{5131} & A_{5141} & A_{5151} & & & & & \\ A_{1211} & A_{1221} & A_{1231} & A_{1241} & A_{1251} & A_{1212} & & & & \\ A_{2211} & A_{2221} & A_{2231} & A_{2241} & A_{2251} & A_{2212} & A_{2222} & & & \\ A_{3211} & A_{3221} & A_{3231} & A_{3241} & A_{3251} & A_{3212} & A_{3222} & A_{3232} & & \\ A_{4211} & A_{4221} & A_{4231} & A_{4241} & A_{4251} & A_{4212} & A_{4222} & A_{4232} & A_{4242} & \\ A_{5211} & A_{5221} & A_{5231} & A_{5241} & A_{5251} & A_{5252} & A_{5222} & A_{5232} & A_{5242} & A_{5252} \end{bmatrix} \begin{Bmatrix} P_{11} \\ P_{21} \\ P_{31} \\ P_{41} \\ P_{51} \\ P_{12} \\ P_{22} \\ P_{32} \\ P_{42} \\ P_{52} \end{Bmatrix}$$

Figure 6

TOROIDAL SHELL CONTACT SCHEMATIC

After the inflation solution has been obtained, the tire model is deflected against a frictionless, flat surface. The contact surface is perpendicular to the wheel plane of symmetry and located at the specified loaded radius R_ℓ, as shown in figure 7. The vertical load and the contact boundary are unknown a priori.

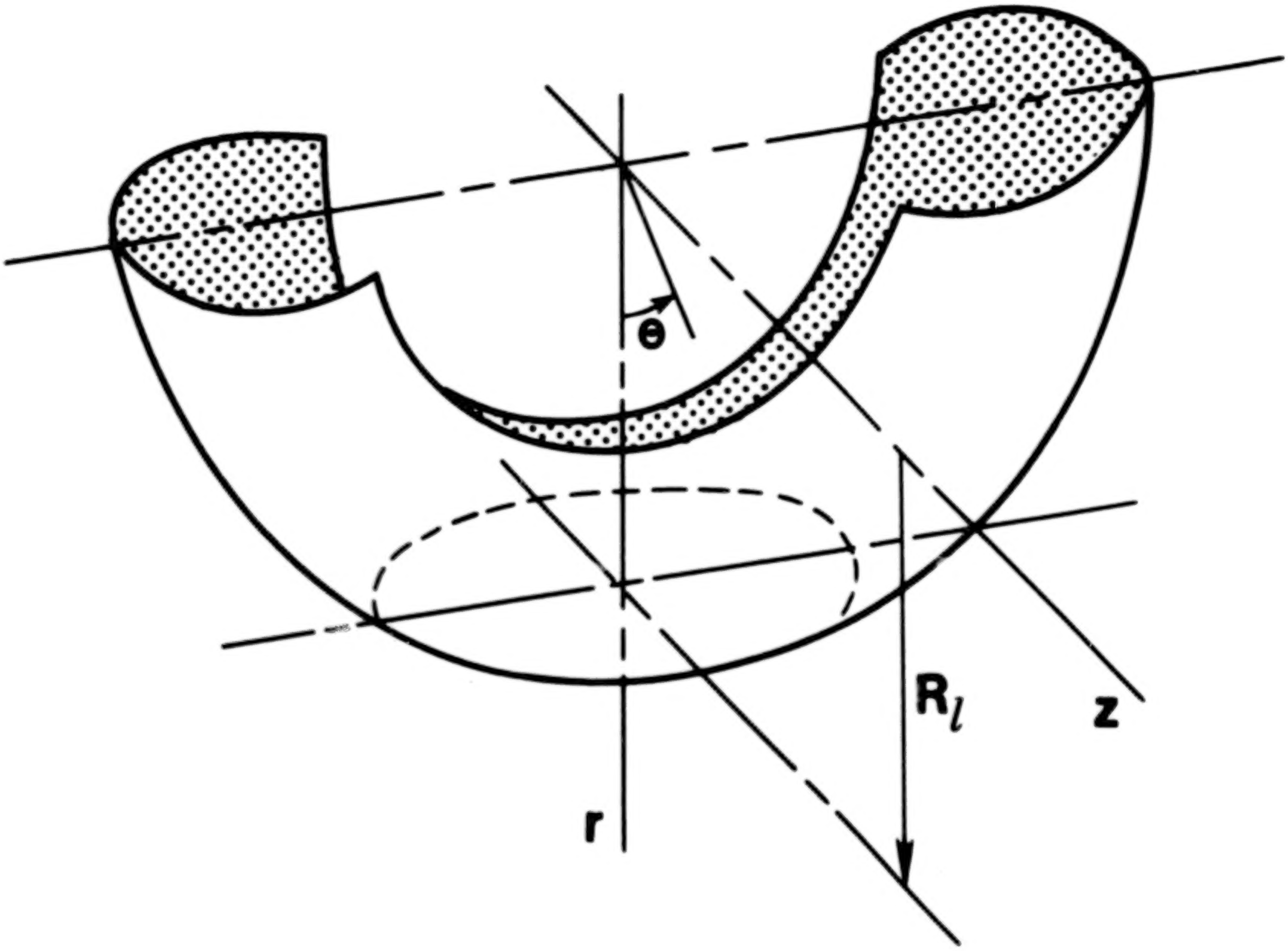

Figure 7

RADIAL DEFLECTIONS IN THE CONTACT REGION

When the radius R_ℓ is specified, the radial deflections are given approximately by $r_{ij} = R_i \cos [(j-1)\Delta\theta] - R_\ell$, where R_i is the inflation radius of node i and $\Delta\theta = 2\pi/N$ is the point spacing. Since the contact half-angle is usually less than 20°, the error in approximating the radial deflections by the above equation is not large. An initial estimate of the contact boundary is taken as the geometric intersection of the tire model and the contact surface. (See fig. 8.)

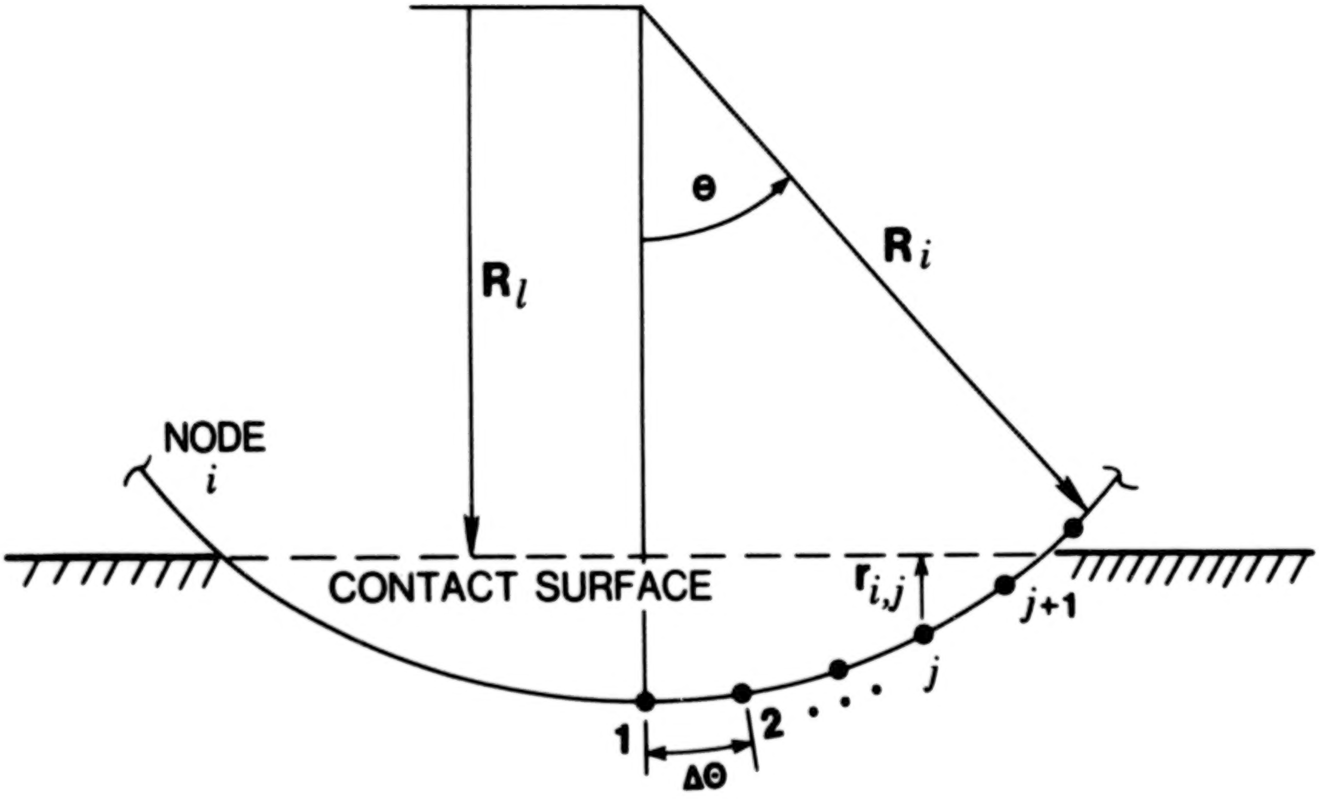

Figure 8

LINE LOAD VECTORS

The radial deflections within the contact boundary are known but the forces that produce these deflections are unknown. The tangential (axial and circumferential) deflections within the contact boundary are unknown but the tangential forces are zero because the contact is frictionless. All surface forces are zero outside of the contact boundary. Since the number of unknowns (deflections and loads) is less than or equal to the number of equations established by the influence coefficient matrix, an initial contact solution can be found. The contact boundary is then adjusted to exclude negative radial forces. Three to five boundary adjustments are normally needed to converge on the contact solution. Figure 9 shows the load vectors obtained in a solution for the G78-14 tire with 221 kPa (32 psi) inflation pressure. The elements of $\{p\}$ are values of the line load at 32 points on the tire model equator. The other vectors give line load values in the right (and left) half of the contact region. Seven nodal circles are in the contact region in this example.

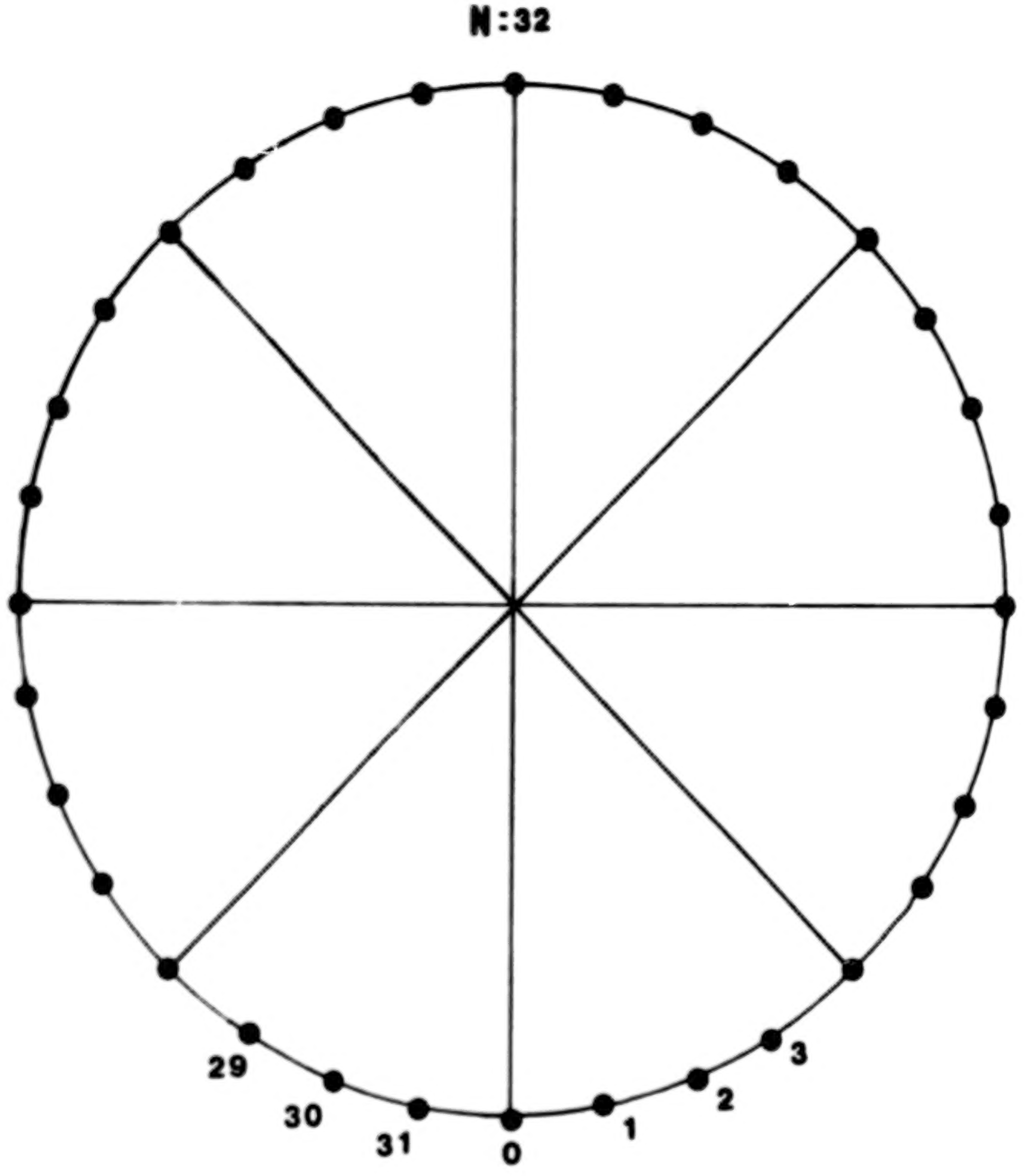
N:32
29
30
31
0
1
2
3

$$\{p^1\} = \{\overset{0}{11.48},\ \overset{1}{5.67},\ \overset{2}{0},\ .\ .\ .\ .,\ \overset{30}{0},\ \overset{31}{5.67}\} \quad \text{lb/in}$$

$$\{p^2\} = \{16.27,\ 4.61,\ 0,\ .\ .\ .\ .,\ 0,\ 4.61\}$$

$$\{p^3\} = \{22.28,\ 0,\ .\ .\ .\ .,\ 0\}$$

$$\{p^4\} = \{13.78,\ 0,\ .\ .\ .\ .,\ 0\}$$

Figure 9

CONTACTING MERIDIAN AND EQUATOR

The line load values shown in figure 9 are divided by the point spacing to obtain the contact pressure at each point in the contact region. Figure 10 gives the contact pressure values at points on the meridian passing through the center of the contact region and at the three contacting points on the equator of the G78-14 tire. The tire surface points before contact are indicated by • and the same points after contact are indicated by ⊙ .

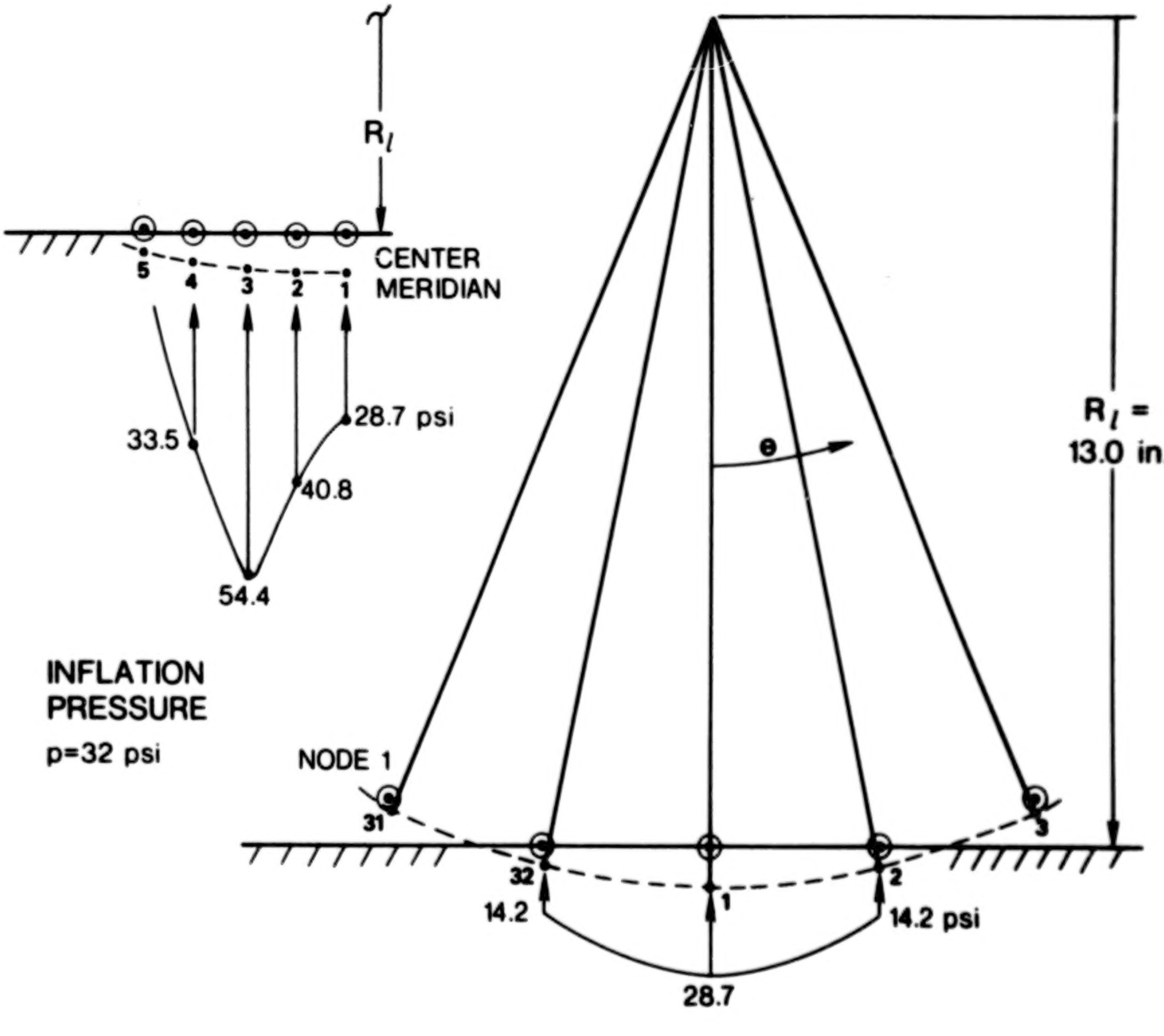

R_l
CENTER
MERIDIAN
5
4
3
2
1
28.7 psi
33.5
40.8
54.4
INFLATION
PRESSURE
p=32 psi
θ
R_l =
13.0 in.
NODE 1
31
32
1
2
3
14.2
14.2 psi
28.7

Figure 10

CONTACT PRESSURE DISTRIBUTION

All of the contact pressure values (psi) calculated for the G78-14 tire with 221 kPa (32psi) inflation pressure are shown in figure 11. The estimated location of the contact boundary is shown as a dashed oval. The contact boundary will be more accurately located when the density of points covered by the influence coefficient matrix is increased. The point density is limited only by the size and speed of the computer used to execute the tire model program.

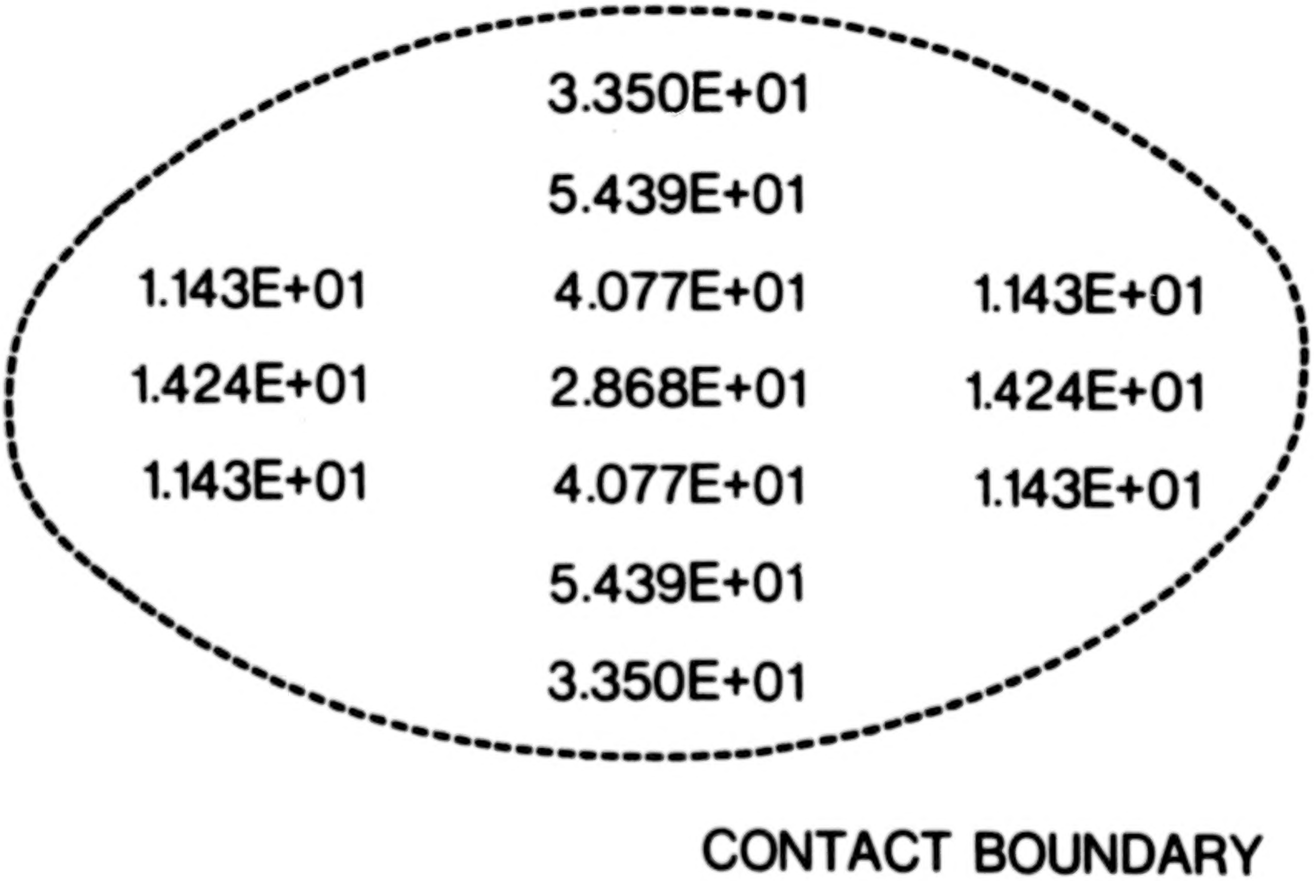
3.350E+01
5.439E+01
1.143E+01
4.077E+01
1.143E+01
1.424E+01
2.868E+01
1.424E+01
1.143E+01
4.077E+01
1.143E+01
5.439E+01
3.350E+01
CONTACT BOUNDARY

Figure 11

BEST DOCUMENT AVAILABLE

AIRCRAFT TIRE SECTION

The remainder of this presentation shows the contact solution calculated for a 32 × 8.8 Type VII aircraft tire. A theoretical and experimental study of this tire under inflation pressure loading was made by Brewer (ref. 5). The photograph in figure 12 and the tire data shown in figure 13 are taken from reference 5. The white curve drawn on the tire section below marks the location of the carcass midsurface.

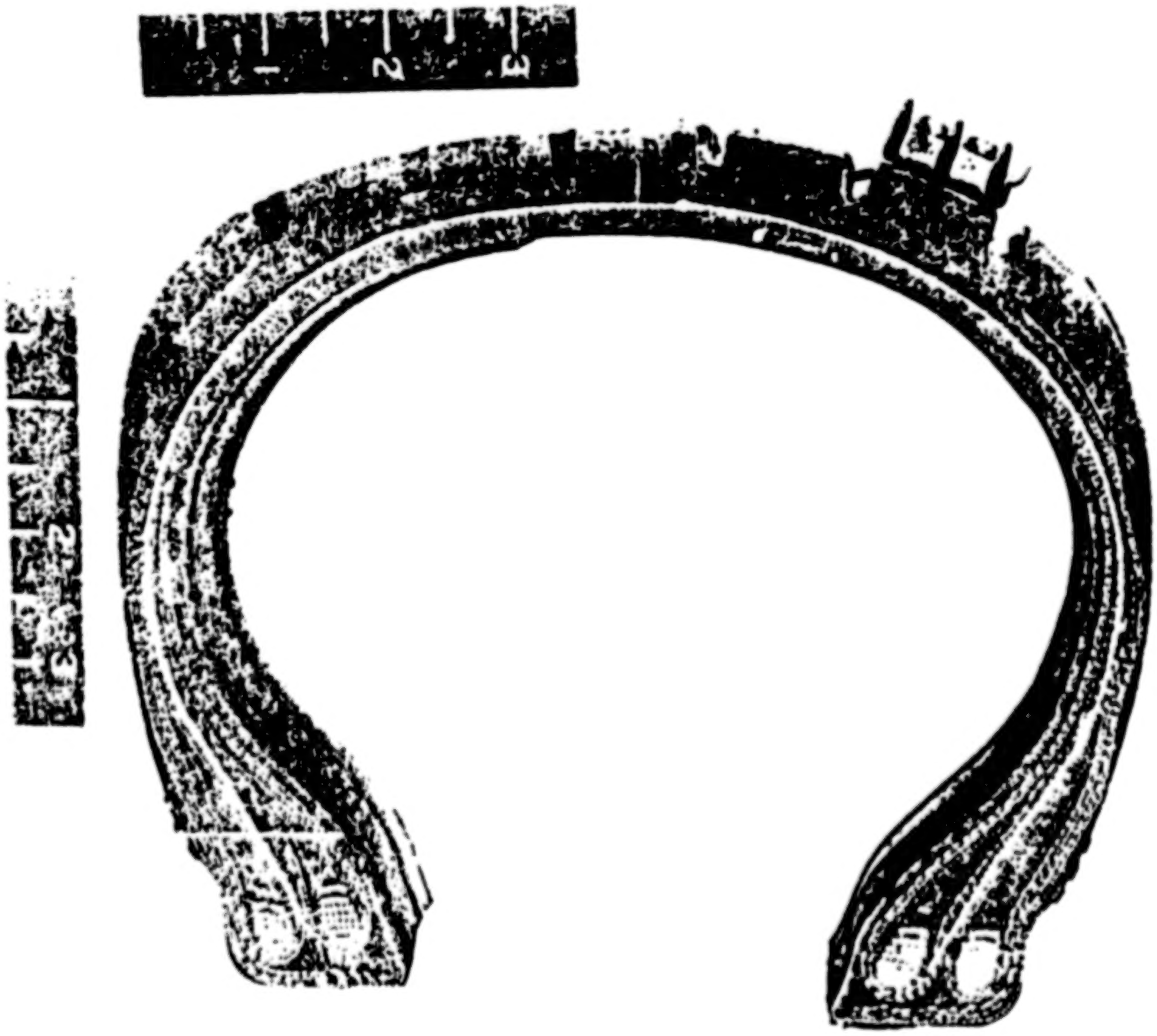

MERIDIAN SECTION OF 32 X 8.8 AIRCRAFT TIRE

Figure 12

MATERIAL PROPERTIES AND CARCASS GEOMETRY

The parameters shown in figure 13 are used in a preprocessing subroutine to calculate homogeneous orthotropic properties for the finite element tire model.

32 x 8.8 TYPE VII
AIRCRAFT TIRE

Material Properties and Carcass Geometry

Rubber: $E_R = 450$ psi, $\nu_R = 0.49$, $G_R = 151$ psi

Nylon Cord: $E_C = 156{,}000$ psi, $\nu_C = 0.70$, $G_C = 700$ psi

Cord Diameter: $d_C = 0.031$ in.

Ply Thickness: $h = 0.043$ in. (all plies)

Cord Angle β (measured from meridian) and Cord Density N, by Lift Formula

Element	β(deg)	N(epi)	Element	β(deg)	N(epi)
1	55.44	25.42	12	46.97	23.81
2	55.35	25.39	13	45.34	23.75
3	55.20	25.34	14	43.71	23.78
4	54.96	25.26	15	41.99	23.88
5	54.60	25.15	16	40.25	24.08
6	54.08	25.00	17	38.64	24.35
7	53.33	24.79	18	37.13	24.68
8	52.34	24.55	19	35.73	25.05
9	51.18	24.32	20	34.39	25.48
10	49.90	24.10	21	33.37	25.85
11	48.49	23.93			

Construction: 6-ply, double bead

Figure 13

FINITE ELEMENTS ON THE CARCASS MIDSURFACE

The aircraft tire is modeled with 21 finite elements positioned along the carcass midsurface. The ply structure in each element is specified separately in determining the homogeneous moduli for each element. Node 22 is a fixed node, positioned to represent the tire bead which does not displace or rotate. (See fig. 14.)

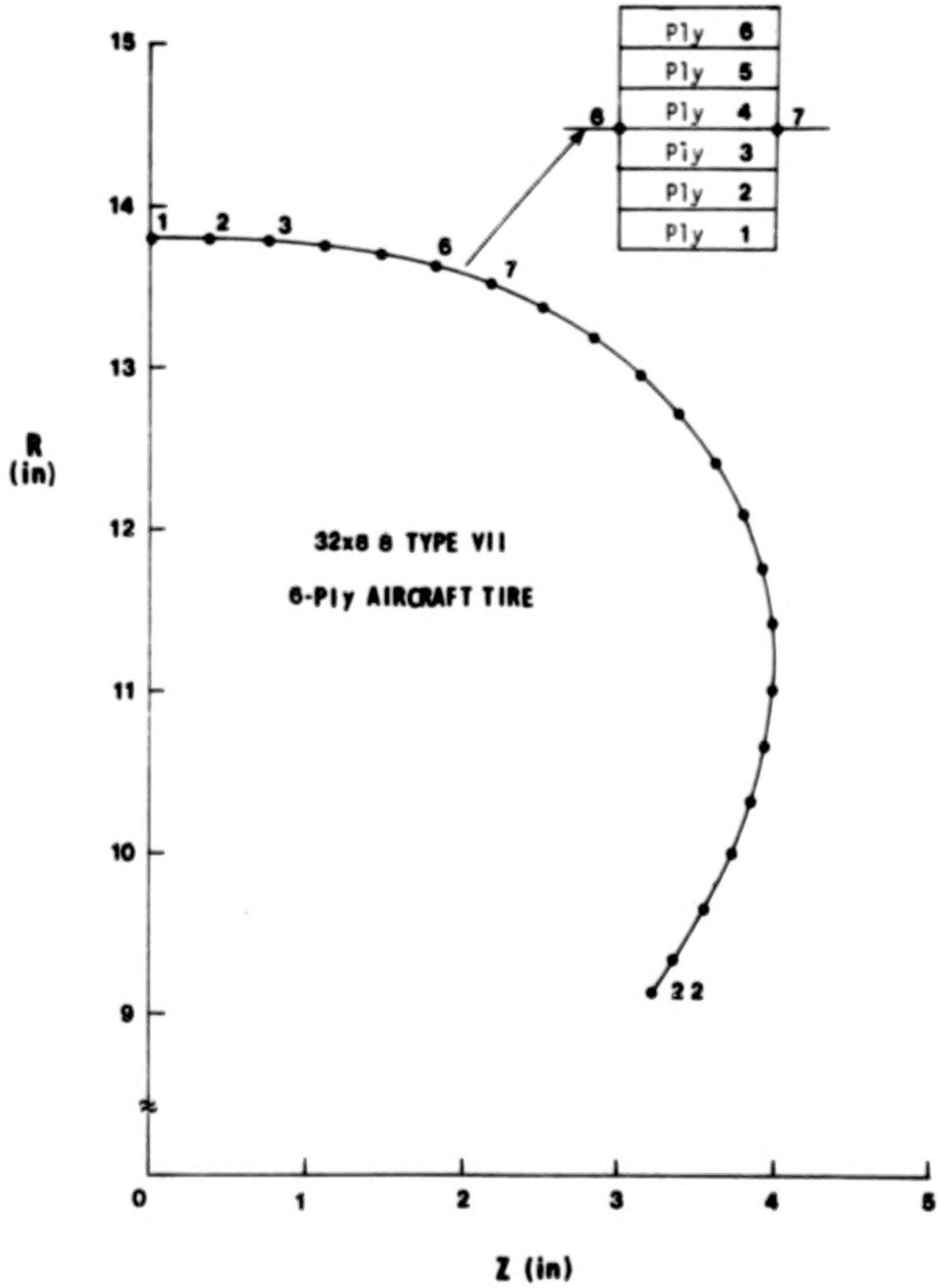

Figure 14

LOAD VECTOR CORRECTION DATA

The problem of calculating tire shape due to inflation pressure is highly nonlinear. As recognized by Stafford and Tabaddor (ref 6.), a successful solution can only be obtained by a nonlinear finite element analysis which includes updating the pressure load vector direction during the inflation solution procedure. Table 1-1, in figure 15, gives the input load vector components, p_n and p_s, that are needed in order to have the resultant pressure load normal to the inflated tire model.

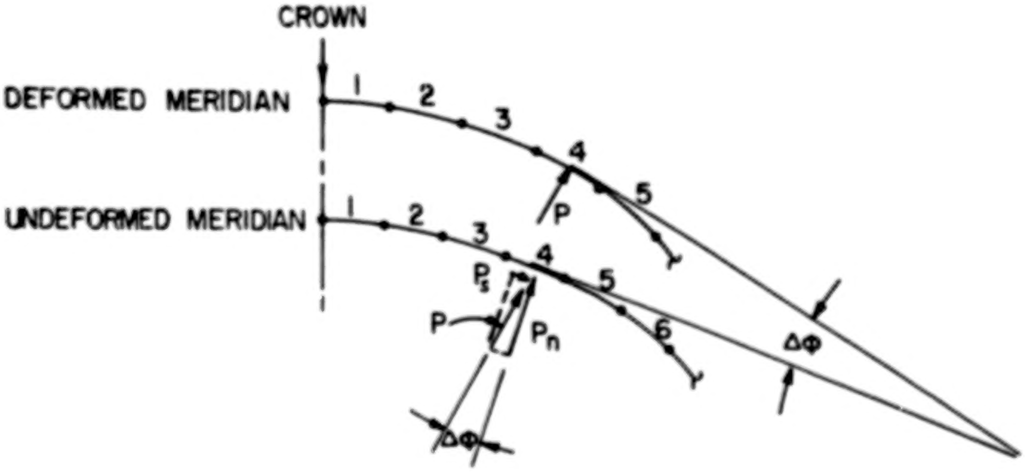

TABLE 1-1. INPUT LOAD DATA FOR FINITE ELEMENT MODEL OF AIRCRAFT TIRE ANALYZED BY BREWER

Element Number	Rotation $\Delta\phi$ (deg)	TIRELOAD Input Pressure(psi)	
		P_n	P_s
1	1.46	94.97	2.41
2	4.61	94.69	7.63
3	7.68	94.15	12.70
4	10.10	93.53	16.64
5	11.23	93.17	18.55
6	10.71	93.35	17.65
7	9.19	93.78	15.17
8	7.90	94.09	13.11
9	7.18	94.26	11.87
10	6.48	94.39	10.71
11	5.39	94.58	8.92
12	3.00	94.87	4.97
13	2.24	94.93	3.70
14	0	95.00	0
.	.	.	.
.	.	.	.
.	.	.	.
21	0	95.00	0

Figure 15

CROWN DISPLACEMENT VERSUS INFLATION PRESSURE

The effect of correcting the load vector is clearly seen in figure 16. The finite element solution obtained when the pressure direction remains normal to the undeformed elements is indicated by Δ's. The solution found when the pressure is normal to the deformed elements is indicated by ×'s. This solution compares well with the calculation and measurements made by Brewer (ref. 5).

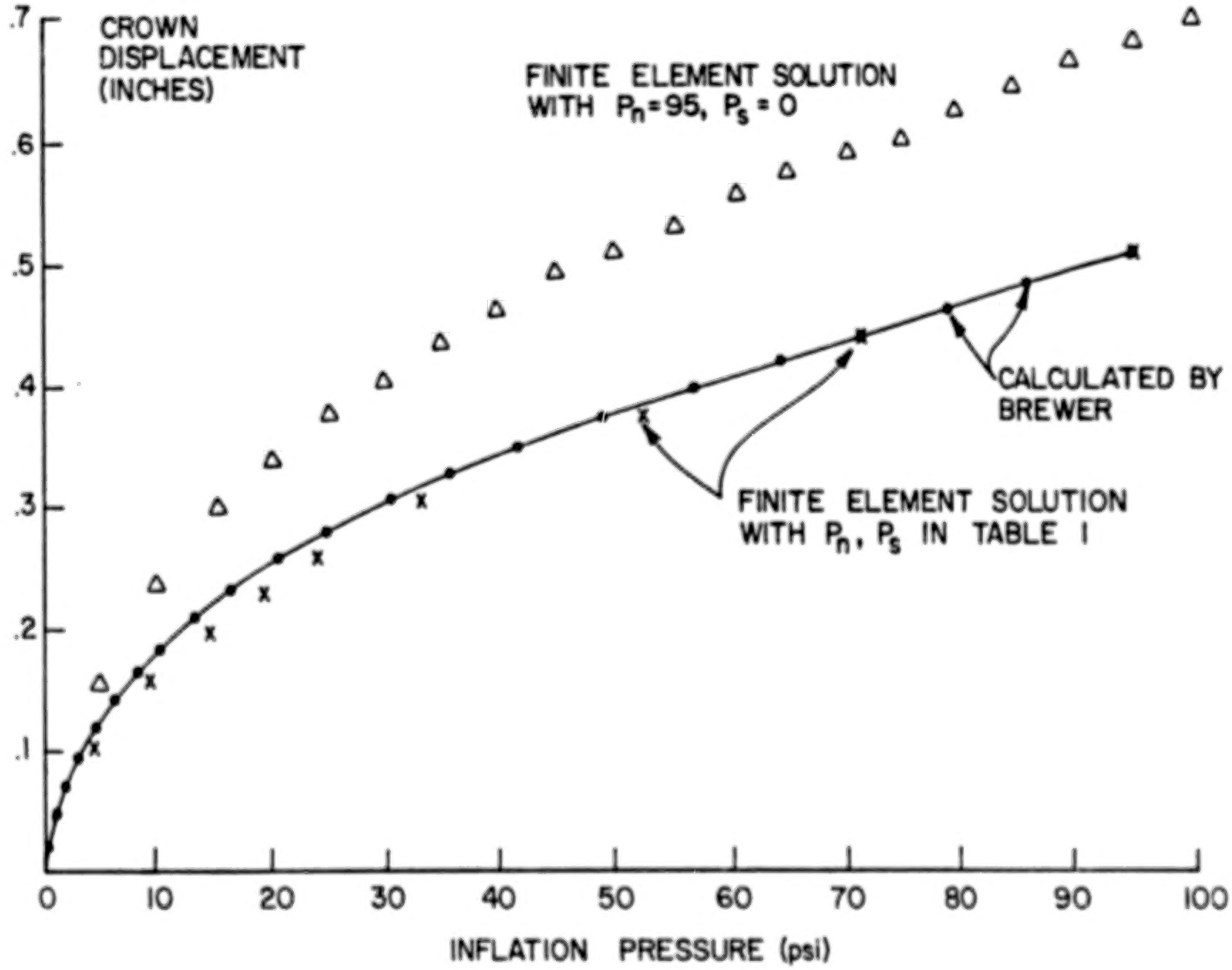

Figure 16

DEFLECTED MERIDIAN

The deflected shape of the meridian passing through the center of contact is shown in figure 17 for the deflection δ = 19 mm (0.75 in.). The tire load calculated for this deflection is F_y = 9.76 kN (2194 lb). The distribution of contact pressure along the meridian is also shown.

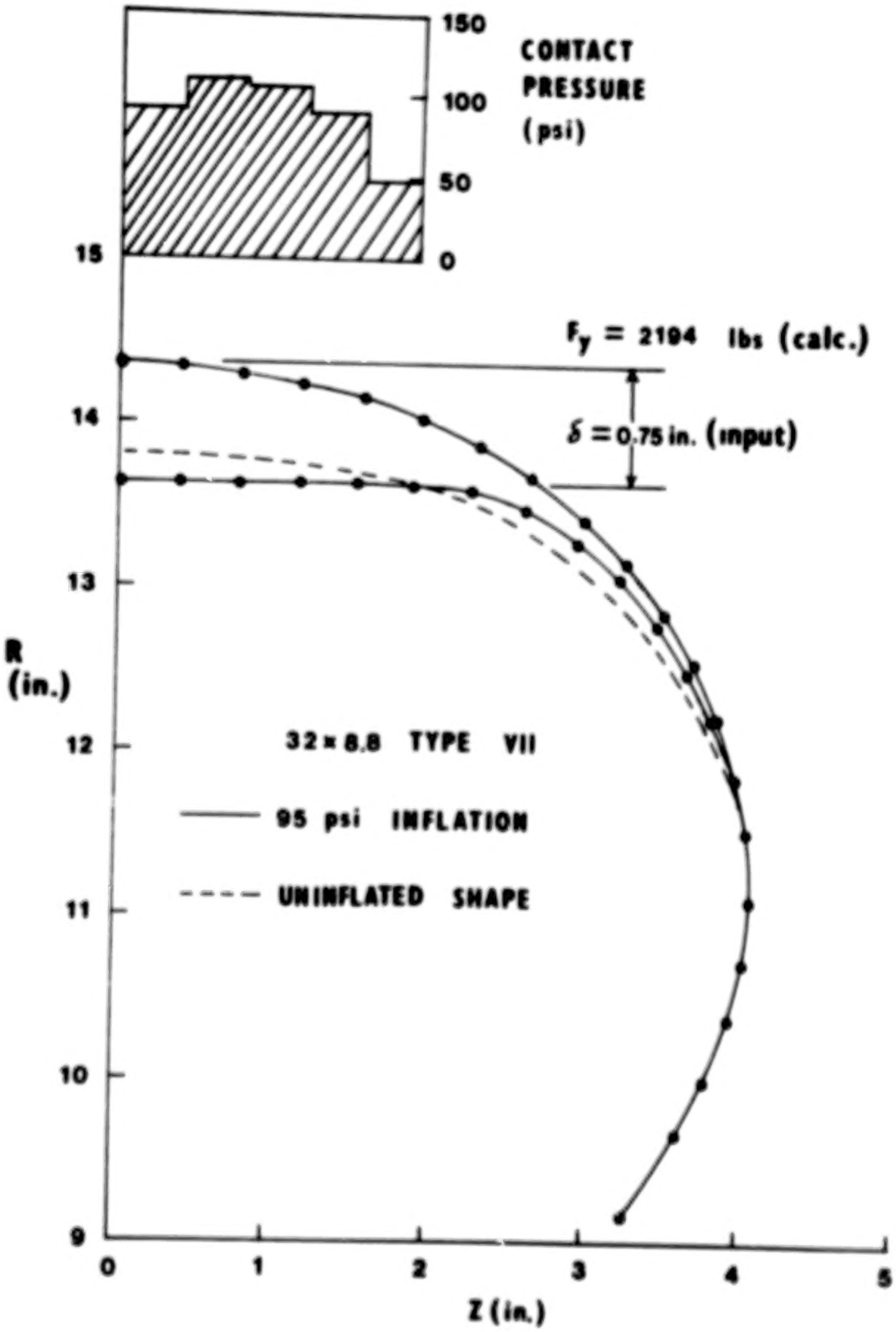

Figure 17

DEFLECTED EQUATOR

The deflected shape of the equator and the distribution of contact pressure along it are shown in figure 18. Since only three points on the equator lie in the contact region, only a rough estimate of the circumferential location of the contact boundary can be made.

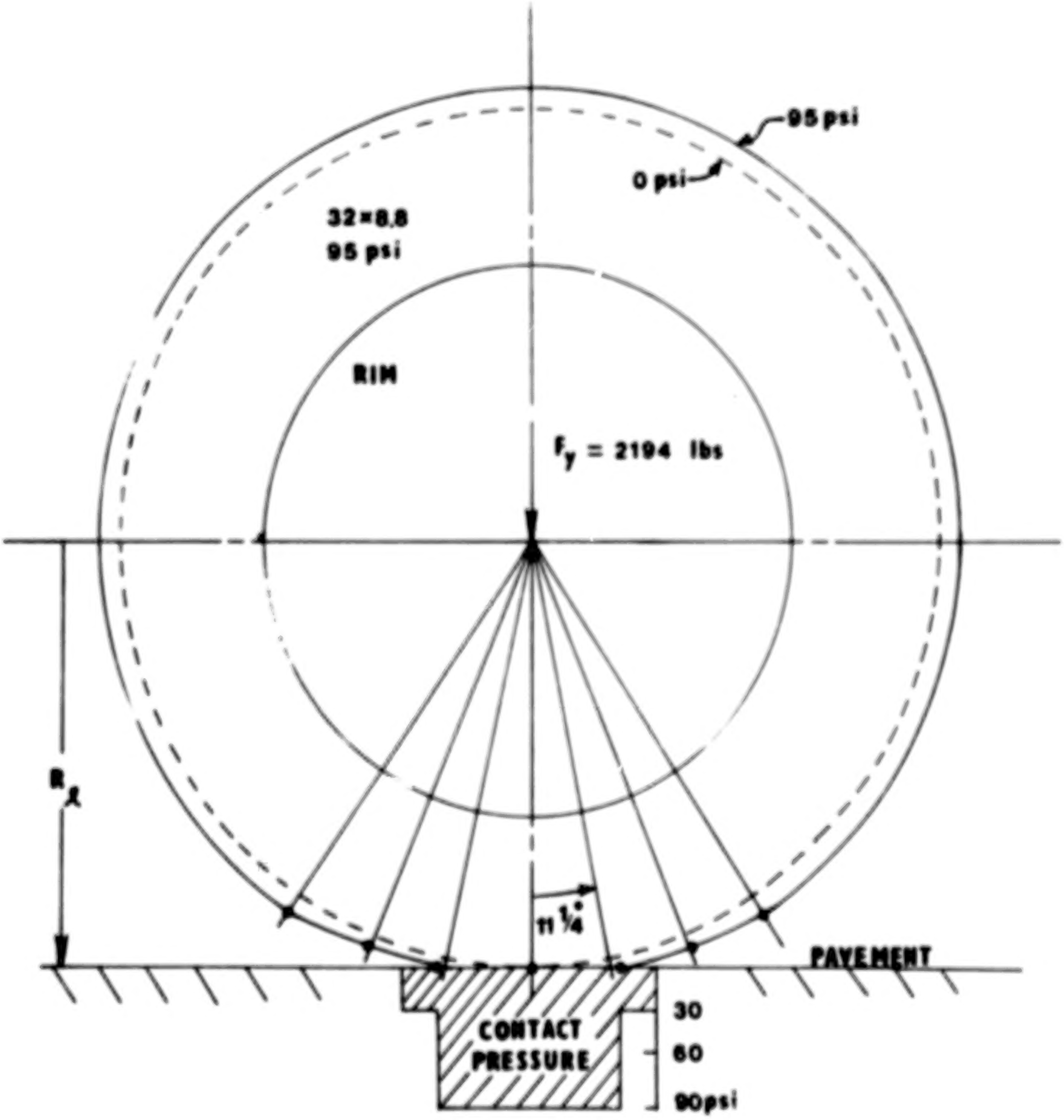
95 psi
0 psi
32×8.8
95 psi
RIM
F_y = 2194 lbs
R_ℓ
11 1/4°
PAVEMENT
CONTACT PRESSURE
30
60
90psi

Figure 18

TIRE LOAD VERSUS TIRE DEFLECTION

Calculated values of tire load for specified tire deflections are shown in figure 19.

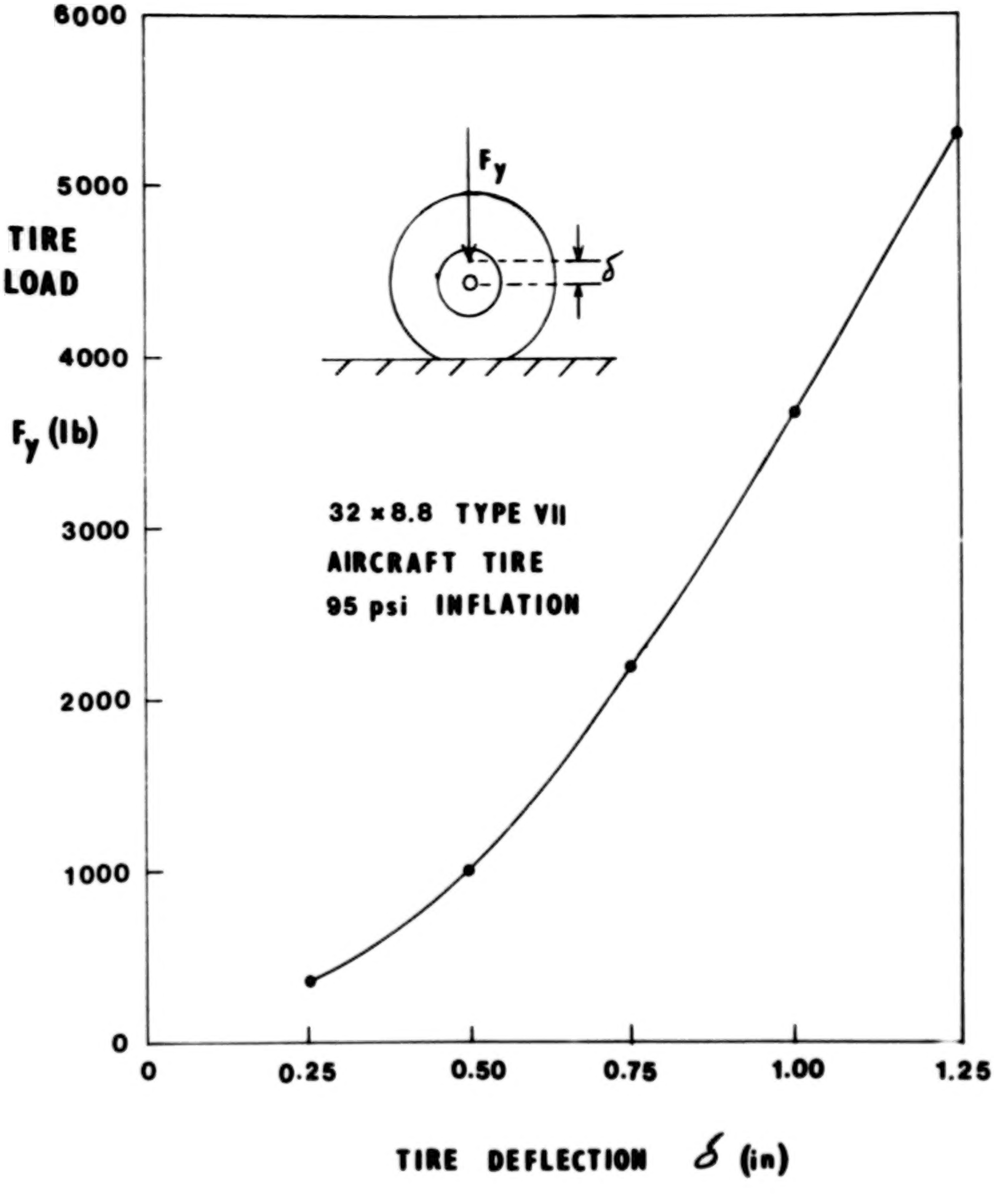

Figure 19

CONTACT AREA VERSUS TIRE DEFLECTION

Calculated values of contact area for specified tire deflections are shown in figure 20. The calculated contact area increases in finite increments as additional points enter the contact region (as the load is increased).

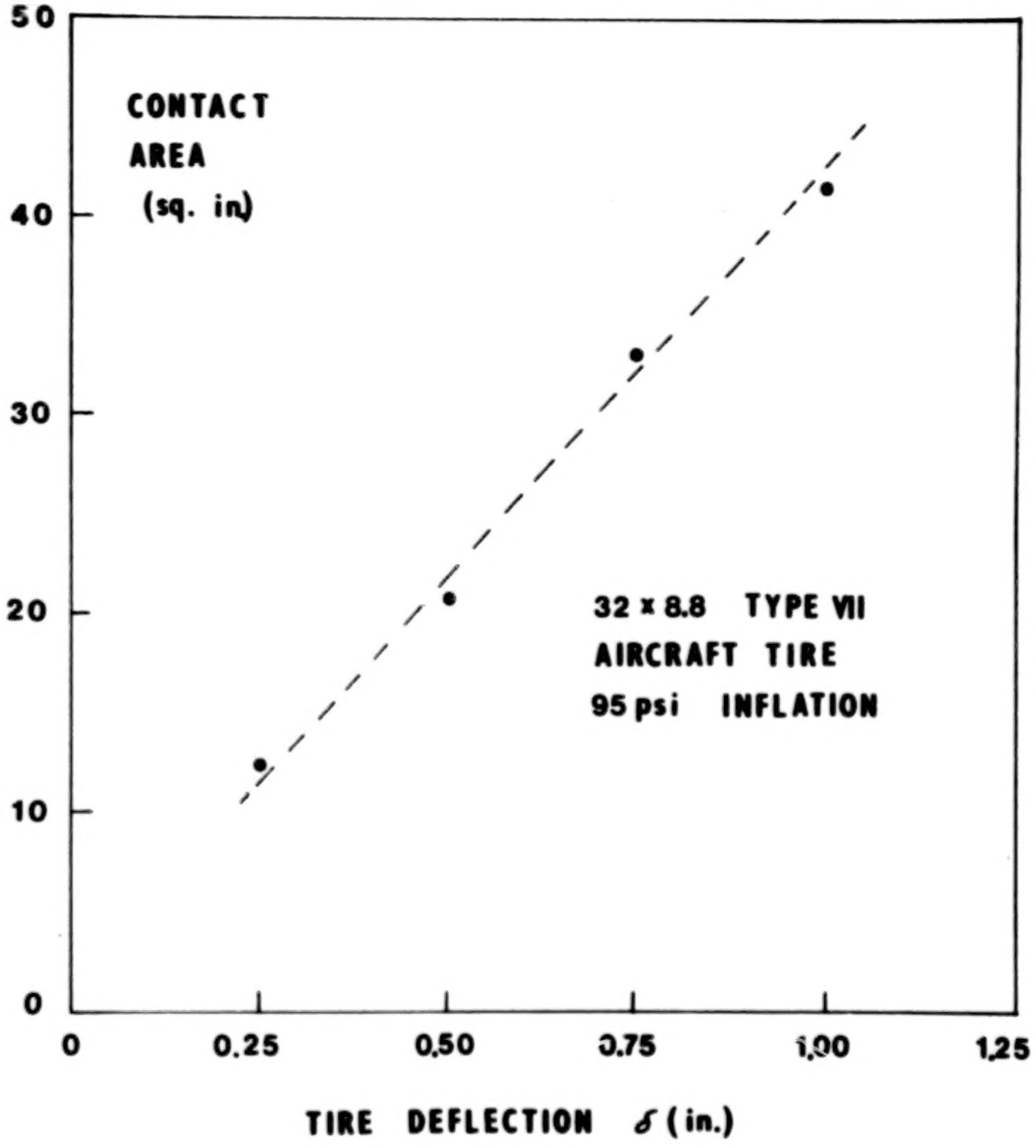

Figure 20

CALCULATED CONTACT PRESSURE DISTRIBUTIONS

All of the contact pressure values (psi) calculated for two different tire loads are shown in figure 21. The tire inflation pressure is 655 kPa (95 psi).

AIRCRAFT TIRE CONTACT PRESSURE DISTRIBUTIONS

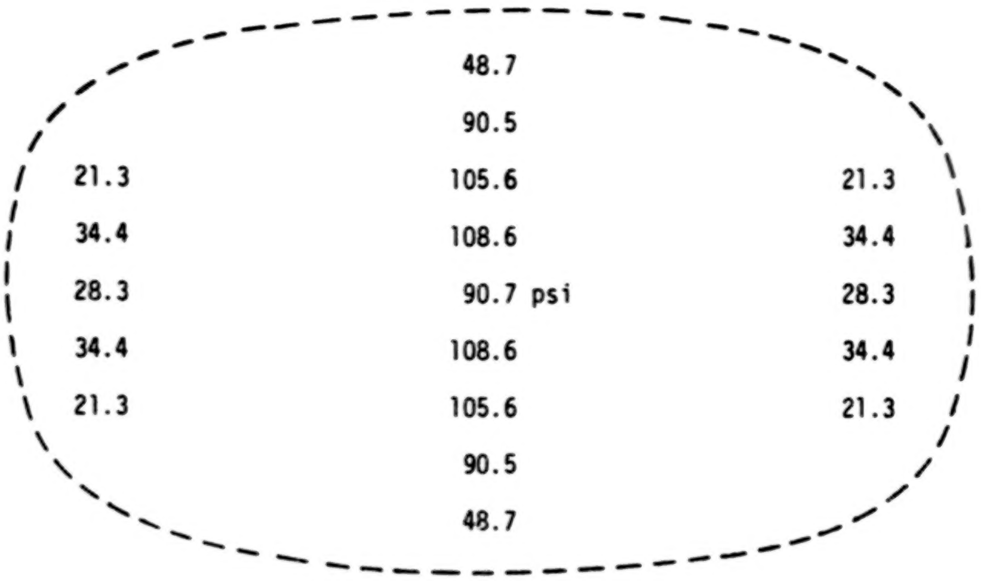

	48.7	
	90.5	
21.3	105.6	21.3
34.4	108.6	34.4
28.3	90.7 psi	28.3
34.4	108.6	34.4
21.3	105.6	21.3
	90.5	
	48.7	

(a) δ = 0.75 in., Fz = 2200 lb

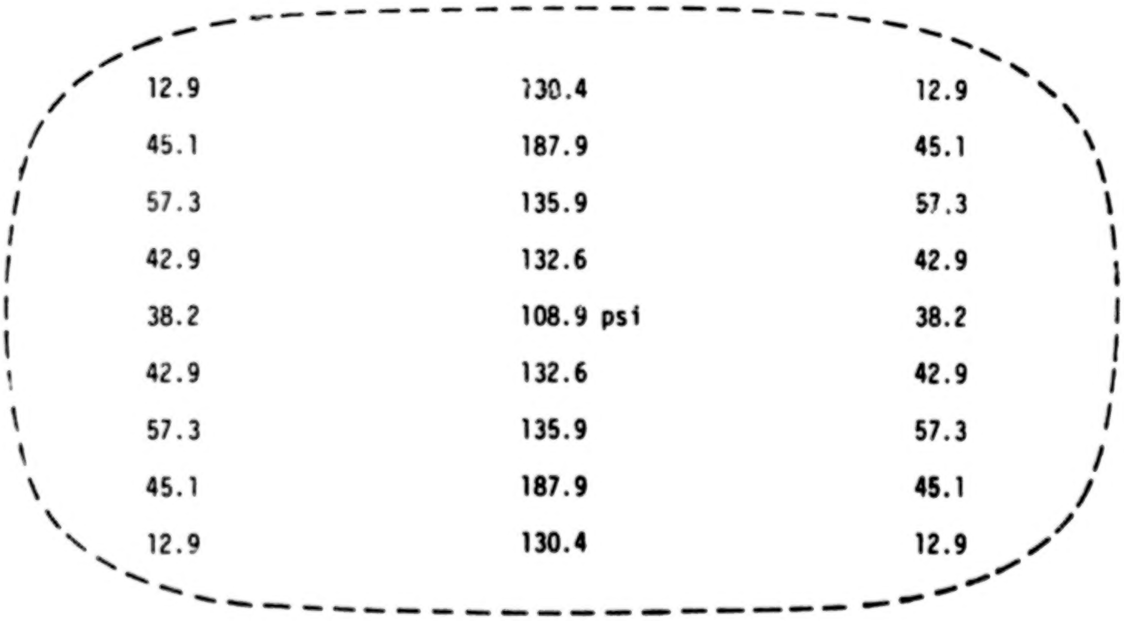

12.9	130.4	12.9
45.1	187.9	45.1
57.3	135.9	57.3
42.9	132.6	42.9
38.2	108.9 psi	38.2
42.9	132.6	42.9
57.3	135.9	57.3
45.1	187.9	45.1
12.9	130.4	12.9

(b) δ = 1.00 in., Fz = 3700 lb

Figure 21

EXTENSIONAL STRAINS DUE TO INFLATION PRESSURE

The extensional (membrane) strains produced by inflation pressure only are shown in figure 22. In this plot, e_s is the strain in the direction of the meridian and e_θ is the strain in the circumferential direction. These strain distributions are axisymmetric and agree with the strains calculated by Brewer (ref. 5).

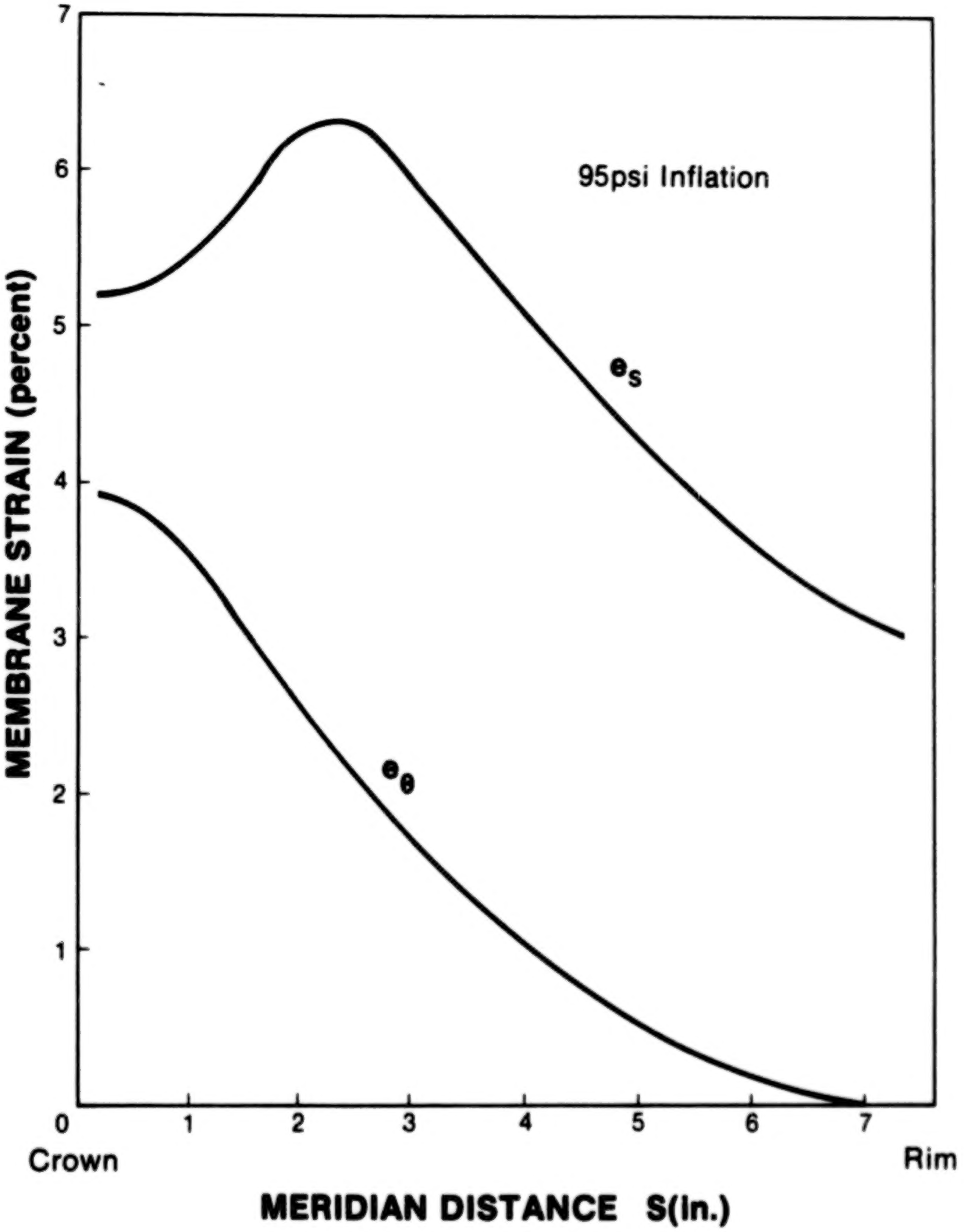

Figure 22

FORCE RESULTANTS DUE TO INFLATION PRESSURE

The membrane forces (per unit length) produced by inflation pressure only are shown in figure 23. The forces N_s and N_θ are in the meridional and circumferential directions, respectively. These force distributions are axisymmetric.

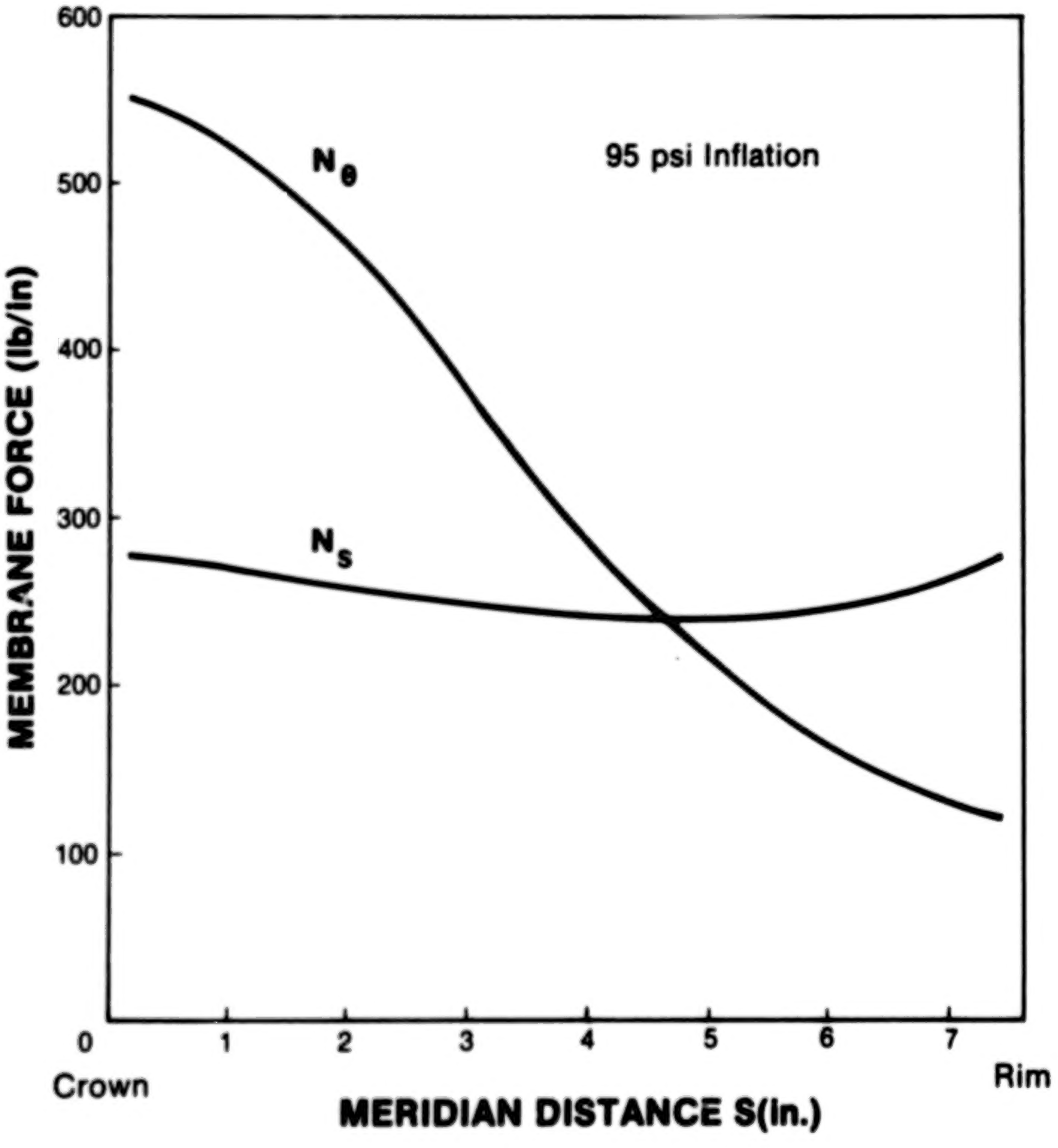

Figure 23

REFERENCES

1. Tillerson, J. R.; and Haisler, W. E.: SAMMSOR II - A Finite Element Program to Determine Stiffness and Mass Matrices of Shells of Revolution. TEES-RPT-70-18, Texas A&M University, Oct. 1970.

2. Haisler, W. E.; and Stricklin, J. A.: SNASOR II - A Finite Element Program for the Static Nonlinear Analysis of Shells of Revolution. TEES-RPT-70-20, Texas A&M University, Oct. 1970.

3. Schapery, R. A.; and Tielking, J. T.: Investigation of Tire-Pavement Interaction During Maneuvering: Theory and Results. Report No. FHWA-RD-78-72, Federal Highway Administration, June 1977.

4. Tielking, J. T.; and Schapery, R. A.: A Method for Shell Contact Analysis. Computer Methods in Applied Mechanics and Engineering, Vol. 26, No. 2, pp. 181-195, May 1981.

5. Brewer, H. K.: Stresses and Deformations in Multi-Ply Aircraft Tires Subject to Inflation Pressure Loading. Report No. AFFDL-TR-70-62, Air Force Flight Dynamics Laboratory, June 1970.

6. Stafford, J. R.; and Tabaddor, F.: ADINA Load Updating for Pressurized Structures. Symposium on Finite Element Analysis of Tires, ASTM F-9, May 1980.

ANALYTICAL AND EXPERIMENTAL STUDY OF A STANDING TORUS WITH NORMAL LOADS

Michael J. Mack, Jr.
Hewlett-Packard Co.

Daniel E. Hill
Deere & Company, Technical Center

Joseph R. Baumgarten
Department of Mechanical Engineering
Iowa State University

ABSTRACT

Finite element analysis is applied to study the large deflection and stress of a thin-walled pressurized torus loaded by normal contact with a plane. The torus is found to have an elliptical footprint area, and considerable bulge occurs in the sidewall in the vicinity of the load plane. In large load ranges, the finite element calculations show compressive circumferential stress and negative curvature in the footprint region. An experimental study of the standing torus, using liquid metal strain gages, is outlined. Experimentally determined stresses are compared to those resulting from finite element analysis at various meridional and circumferential coordinates of the torus, including the footprint area. Circumferential strains compare favorably while meridional strains are higher in the finite element analysis, probably due to slippage of the boundary at the rim.

This study utilized the STAGS finite element computer program. The purpose of the study was to evaluate the various program options for structural loading, for material modeling, for stress analysis, and for grid refinement. The experimental model, a thin-walled rubber tube mounted on a steel cylindrical rim, provided measured results to compare with various analytical trade-offs. It was found that there was almost no difference in predicted deflections or stress distributions between linear and nonlinear material description. However, the difference between linear analysis and that of geometric nonlinearities utilizing incremental loading was marked.

TORUS DIMENSIONS AND GLOBAL COORDINATE SET

STAGS (ref. 1) uses a first order shell theory to reduce a 3-dimensional structural problem to a dependency on 2 spatial coordinates, here the meridional coordinate α and circumferential coordinate θ . The deflection of the plane into the torus is δ . An example of an 11 x 15 torus grid is shown and dimensions of the cylindrical rim and inflated rubber tube are given.

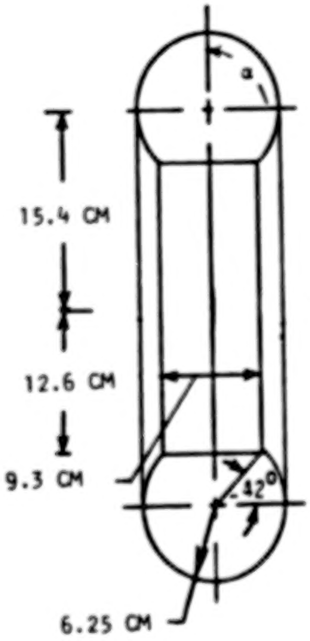
α
15.4 CM
12.6 CM
9.3 CM
-42°
6.25 CM

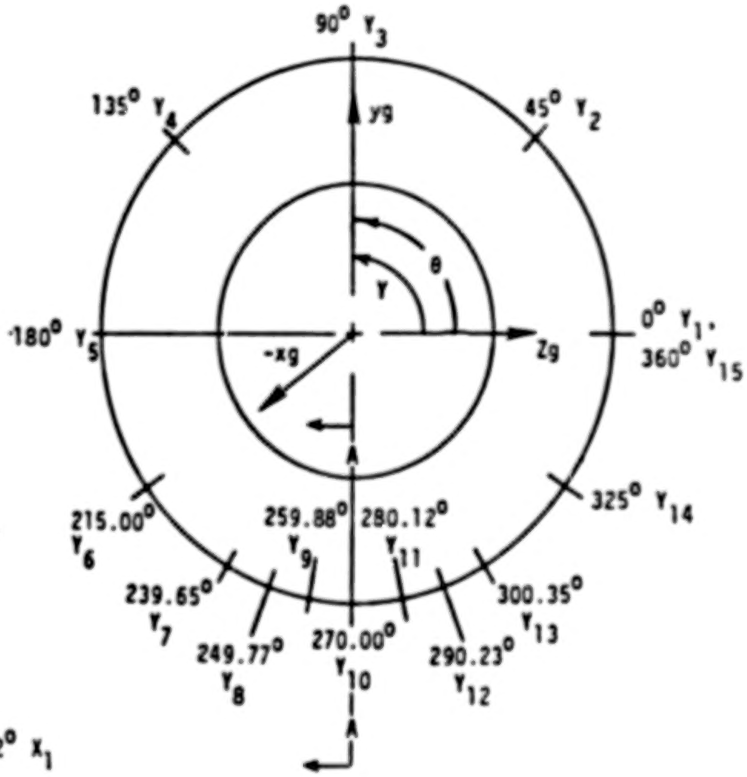
90° Y3
135° Y4
45° Y2
yg
θ
γ
-180° Y5
-xg
Zg
0° Y1,
360° Y15
A
215.00° Y6
259.88° Y9
280.12° Y11
325° Y14
239.65° Y7
300.35° Y13
249.77° Y8
270.00° Y10
290.23° Y12
A

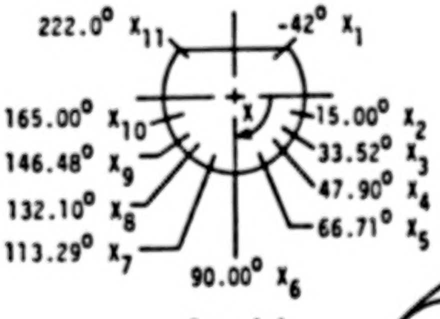
222.0° X11
-42° X1
165.00° X10
χ
15.00° X2
146.48° X9
33.52° X3
132.10° X8
47.90° X4
113.29° X7
66.71° X5
90.00° X6

Sec. A-A

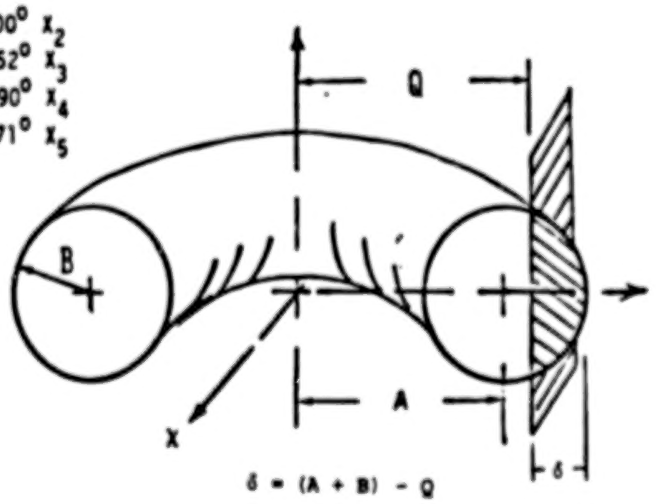

BEST DOCUMENT AVAILABLE

EXPERIMENTAL SET-UP SHOWING ELLIPTICAL FOOTPRINT

The tube was inflated to 0.034 atm. (0.5 psi) and test loads of 34.3 N (7.7 lbs), 69.9 N (15.7 lbs), and 114.4 N (25.7 lbs) were applied. Deflection, footprint area, circumferential and meridional strain, and final pressure were observed.

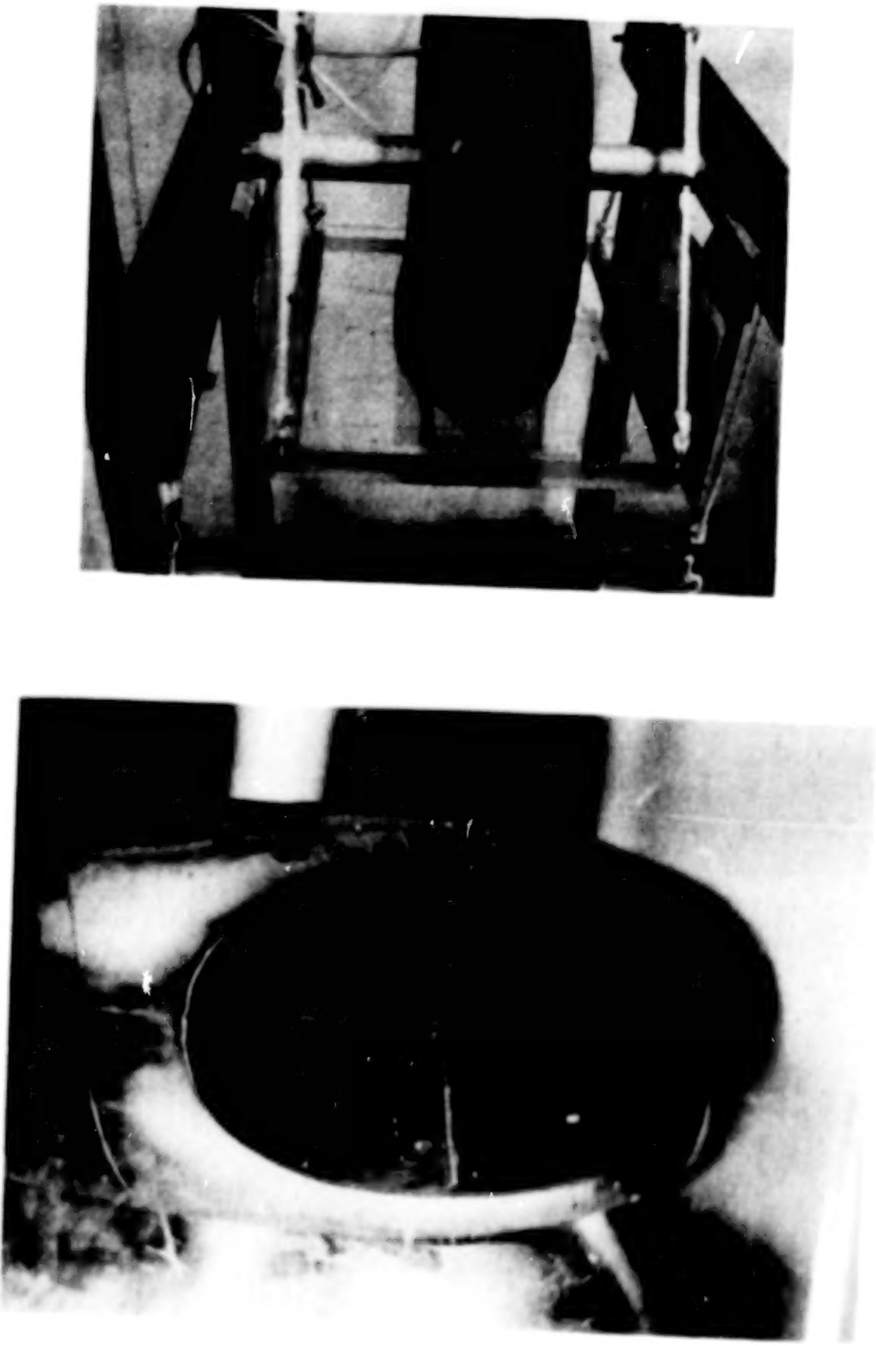

LIQUID METAL STRAIN GAGE AND CALIBRATION DEVICE

In order to measure the large strain encountered, strain gages with a rubber housing and capillary column of mercury were used. The gages are inherently nonlinear by nature, and individual calibration is required (ref. 2). Derivation of gage factor versus strain is given in the appendix.

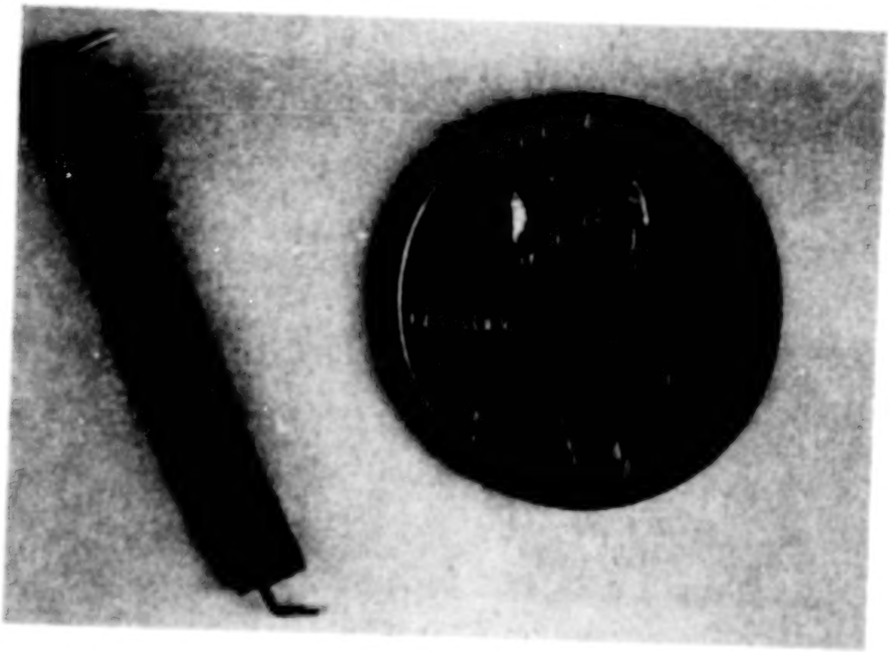

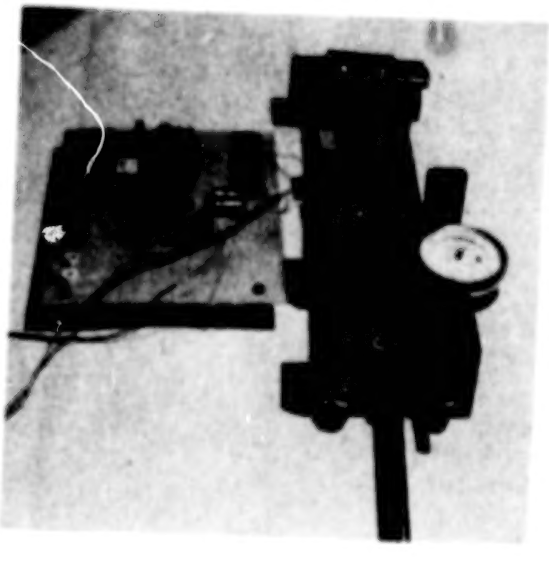

BEST DOCUMENT AVAILABLE

GAGE PLACEMENT AT 0° MERIDIONAL ANGLE - COMPLETE SYSTEM WITH DATA AQUISITION

Calibrated gages were mounted on the torus with silicone rubber cement. The torus was inflated to test pressure and rotated to the desired circumferential angle, load was applied, and readings were recorded. The microprocessor shown below tabulated and recorded, on magnetic tape, data for strain versus circumferential angle at given values of load and meridional angle.

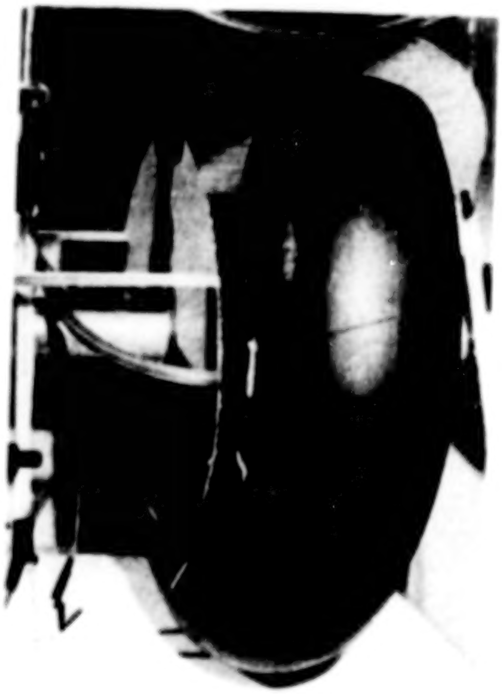

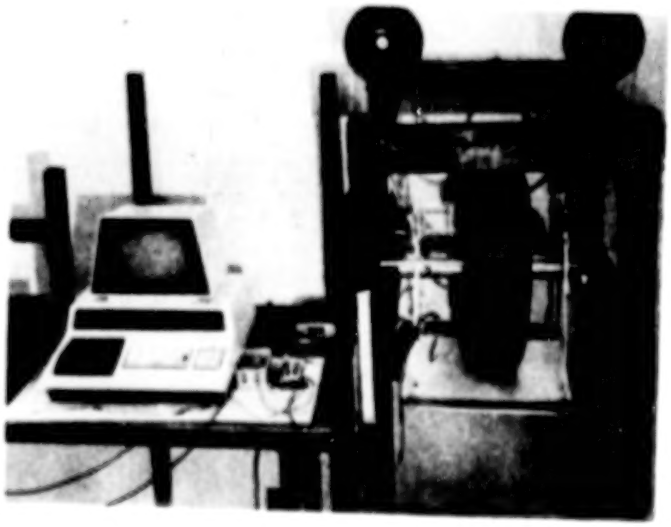

BEST DOCUMENT AVAILABLE

DATA ACQUISITION FLOW CHART

The logic flow chart for the data acquisition scheme is shown below. The buffer for the strain signals and the program controller with the stored logic of the acquisition system are encompassed in the microprocessor. The microprocessor is programmed in the BASIC language, and the digitizing of analog gage voltage is accomplished by a digital voltmeter. The three channels referred to are the meridional strain, the circumferential strain, and a dummy gage voltage.

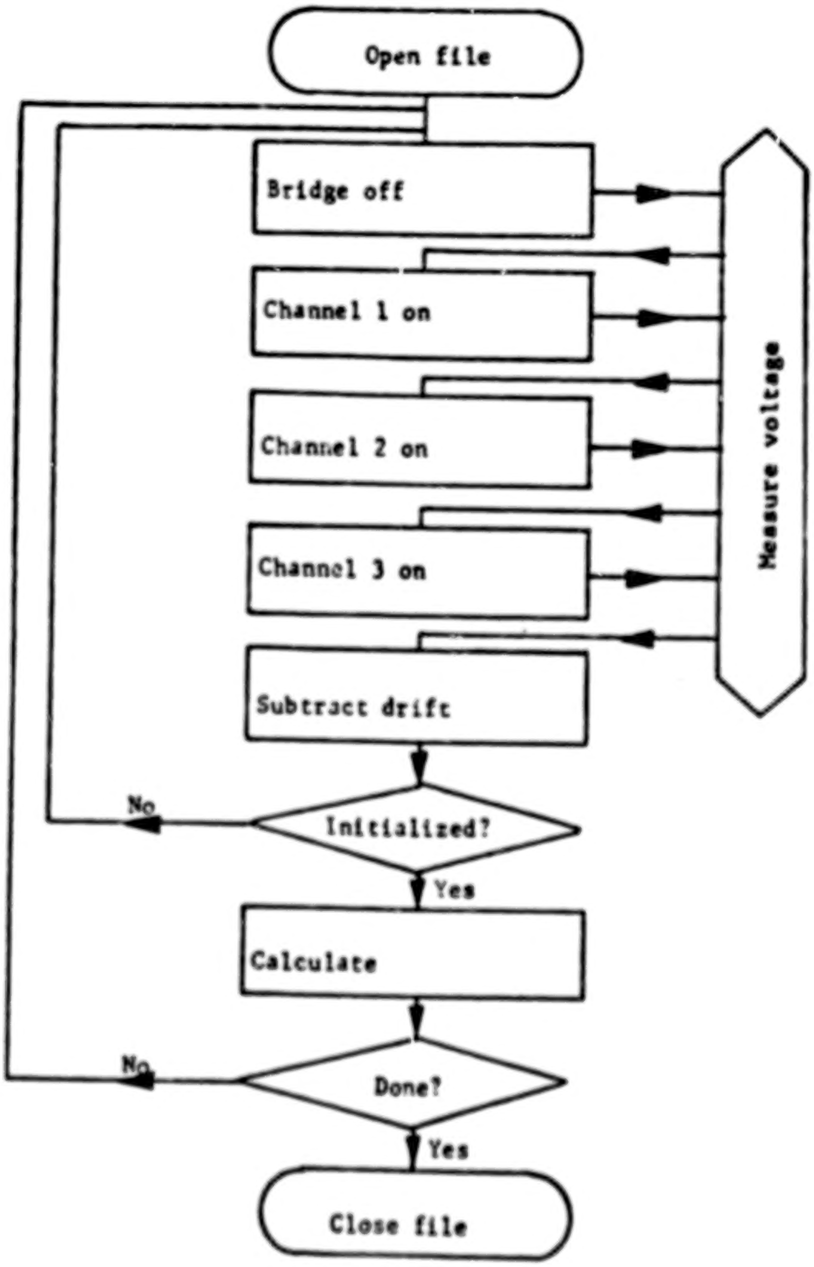
Open file
Bridge off
Channel 1 on
Channel 2 on
Channel 3 on
Subtract drift
Measure voltage
No
Initialized?
Yes
Calculate
No
Done?
Yes
Close file

LOAD-DEFLECTION CURVES FOR ANALYTICAL FINITE ELEMENT AND EXPERIMENTAL DATA FOR TORUS AT P_i = 0.034 ATM

This figure shows points on the load-deflection curve obtained from a STAGS analysis using a 13 x 15 quarter torus at loads of 34.3 N (7.7 lbs), 69.9 N (15.7 lbs), and 114.4 N (25.7 lbs). The deflections predicted from STAGS are lower since minimum potential theory is employed and structural stiffness is overestimated with a coarse grid. As grid size is refined, predicted deflections approach the experimental values, but computer run time also increases (ref. 3). At a load of 34.3 N, three different grid sizes were modeled.

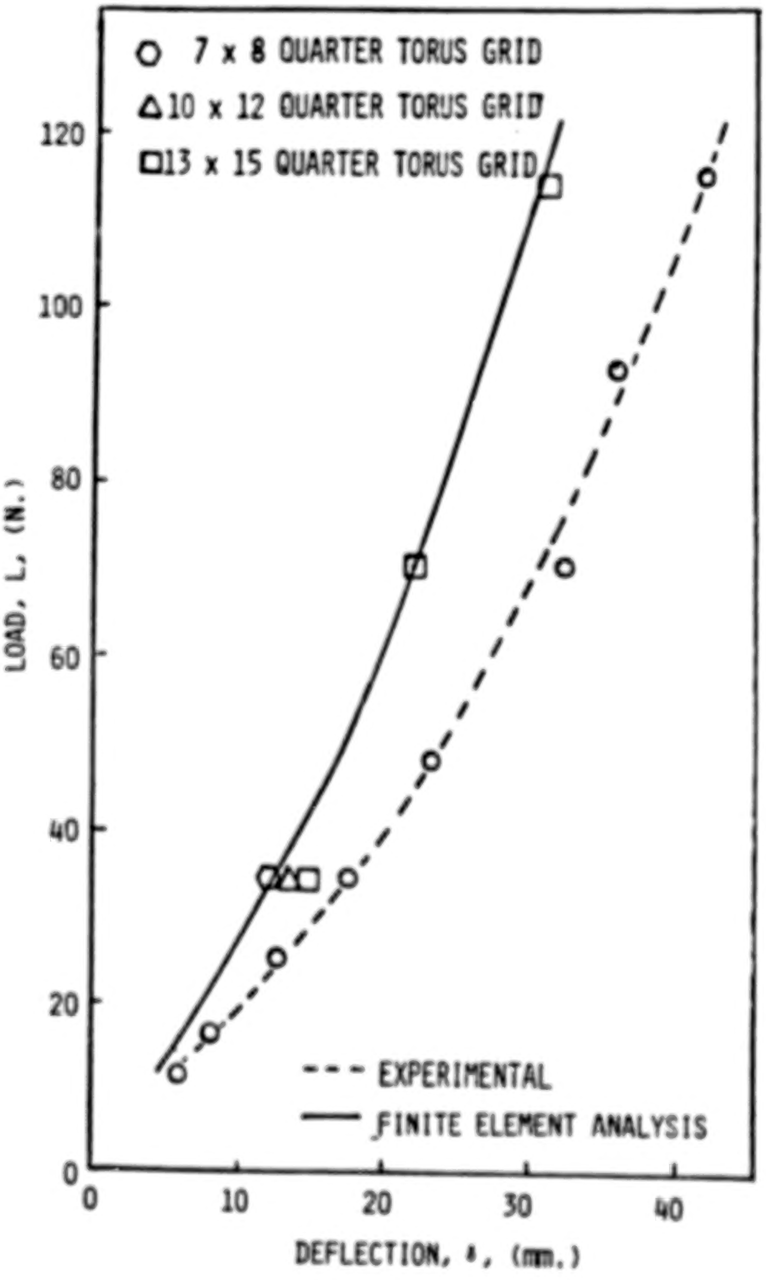

13 x 15 QUARTER TORUS GRIDS WITH
34.3 N (7.7 lbs) LOAD - NONLINEAR ANALYSIS

This figure gives the computer-generated plot of the quarter torus with a 13 x 15 grid. Exploitation of the torus symmetry allows analysis of one-fourth of the structure, giving a grid density four times greater than that of a 13 x 15 grid applied to the full torus. The unloaded grid geometry is overplotted on the the deformed geometry. Note the plane surface at the load point (footprint) and the side wall bulge. The nonlinear geometric analysis option of STAGS gave convergence to a final deflection of 84% of the experimental value while the linear analysis yielded only 21% of the experimental value. This result is significant when compared to toroidal analysis using other finite element procedures (refs. 4 and 5).

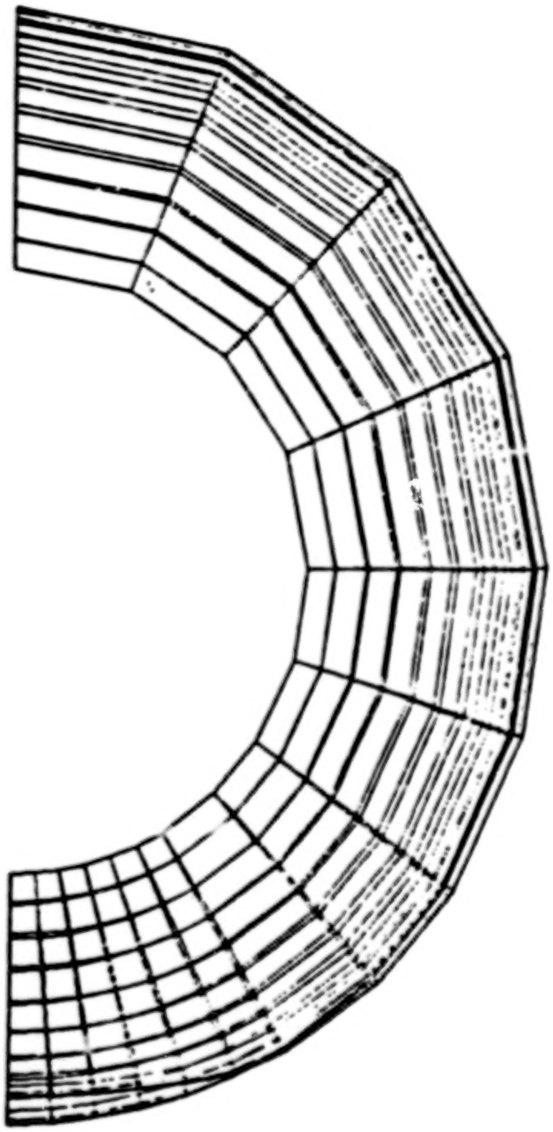

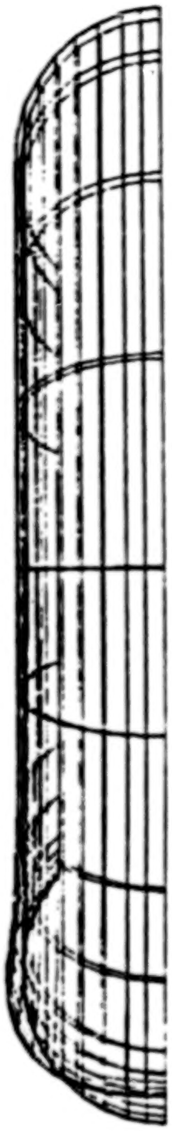

BEST DOCUMENT AVAILABLE

CALCULATED STRESS DISTRIBUTION AT 90° MERIDIONAL ANGLE FOR 13 x 15 QUARTER TORUS GRID - L = 34.3 N (7.7 lbs.)

Calculated values of meridional stress and circumferential stress versus circumferential angle θ are shown below. The variation of stress in the footprint and bulge regions is significant. The values remain constant away from the contact area and are mainly due to internal pressure. These values, with this grid refinement, agree favorably with other investigators (ref. 6).

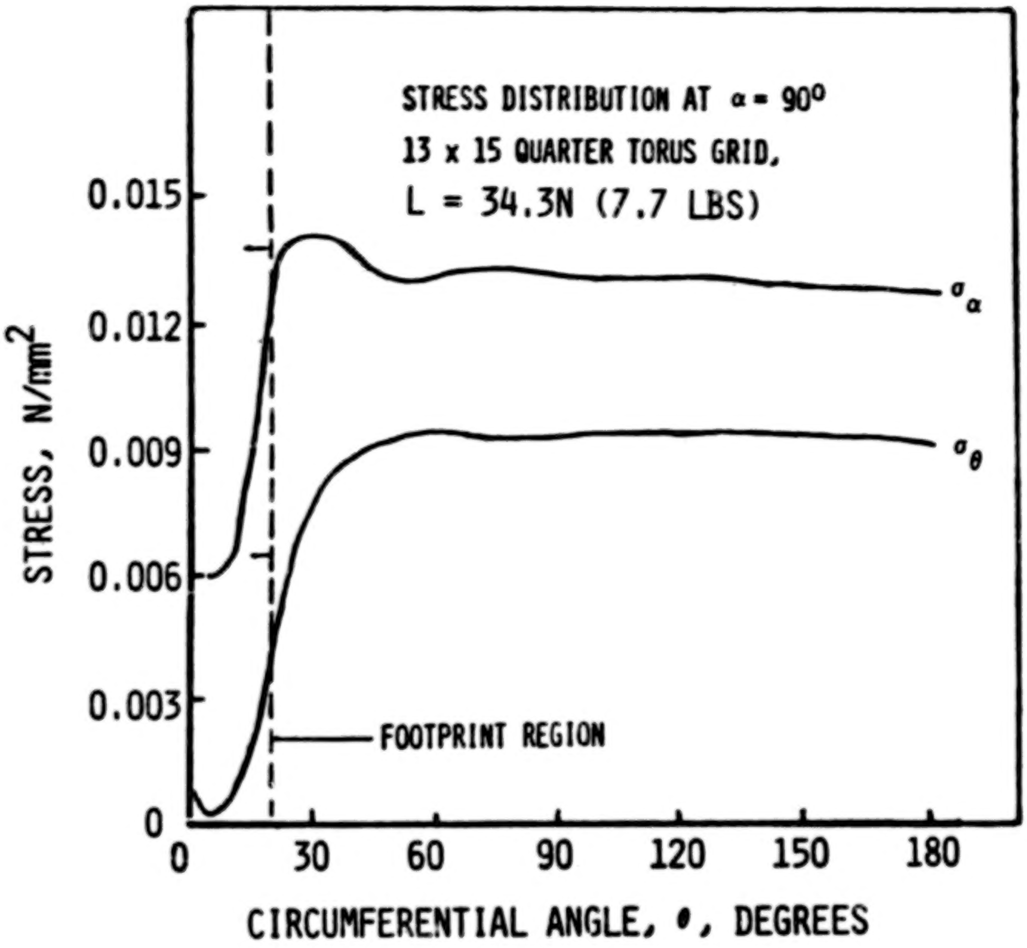

CALCULATED MERIDIONAL STRESS DISTRIBUTION, σ_α, 13 x 15 QUARTER TORUS GRID - NONLINEAR ANALYSIS, LOAD = 34.3 N (7.7 lbs)

The three dimensional plot below shows meridional stress distribution over the surface of the torus at a 34.3 N load. Even tensile stress appears in both the meridional and circumferential directions in the upper half of the torus, as a result of internal gas pressure. However, the compressive effect of contact with the flat plate reduces these tensile stresses in the footprint region.

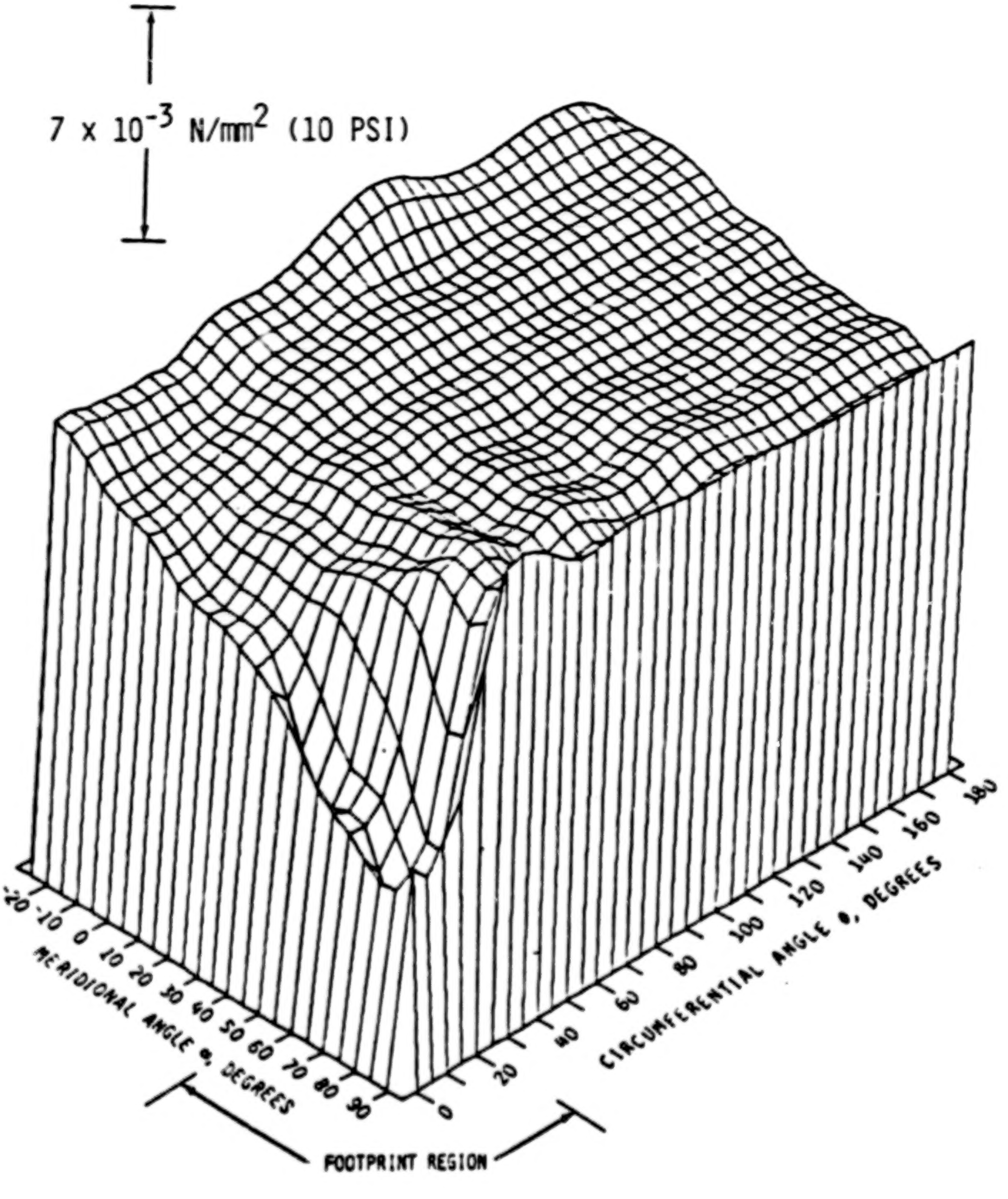

BEST DOCUMENT AVAILABLE

CALCULATED CIRCUMFERENTIAL STRESS DISTRIBUTION, σ_θ, 13x15, QUARTER TORUS GRID - NONLINEAR ANALYSIS, LOAD = 34.3 N (7.7 lbs)

A three dimensional plot of circumferential stress distribution over the upper half of the torus is shown below. As with the previous figure, uniform tensile stress due to gas pressure is significantly reduced in the footprint region, to almost 0 N/mm^2 in the center. Results of an intermediate load step of 69.9 N (15.7 lbs) are contained in the literature (ref. 7).

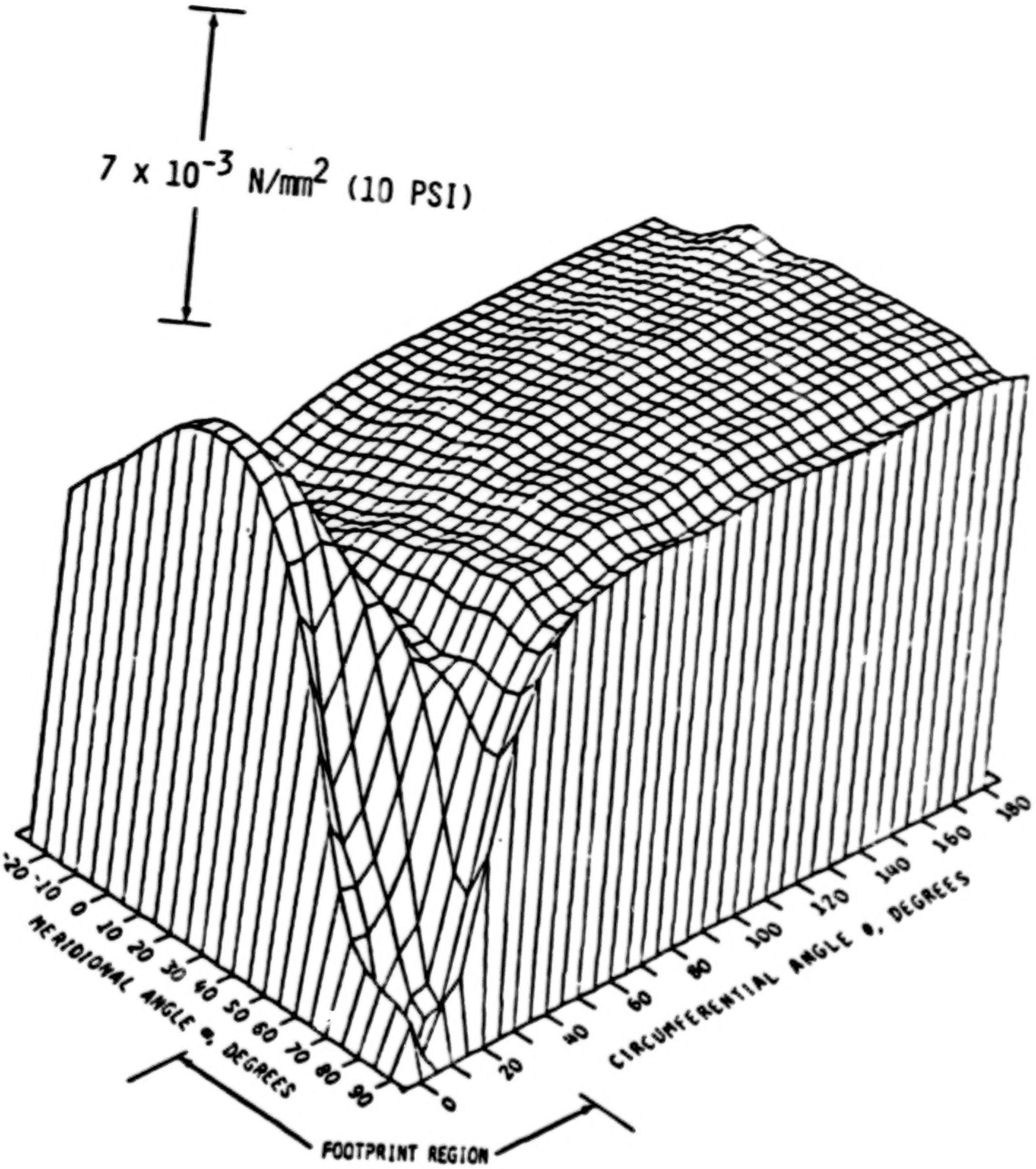

BEST DOCUMENT AVAILABLE

13 x 15 QUARTER TORUS GRID WITH
114.4 N (25.7 lbs) LOAD - NONLINEAR ANALYSIS

The figure below shows the STAGS generated plot of a quarter torus in the unloaded and deformed configurations under a test load of 114.4 N. The deflection has increased significantly and the degree of bulge in the sidewall is more pronounced. The center of the footprint region shows negative curvature.

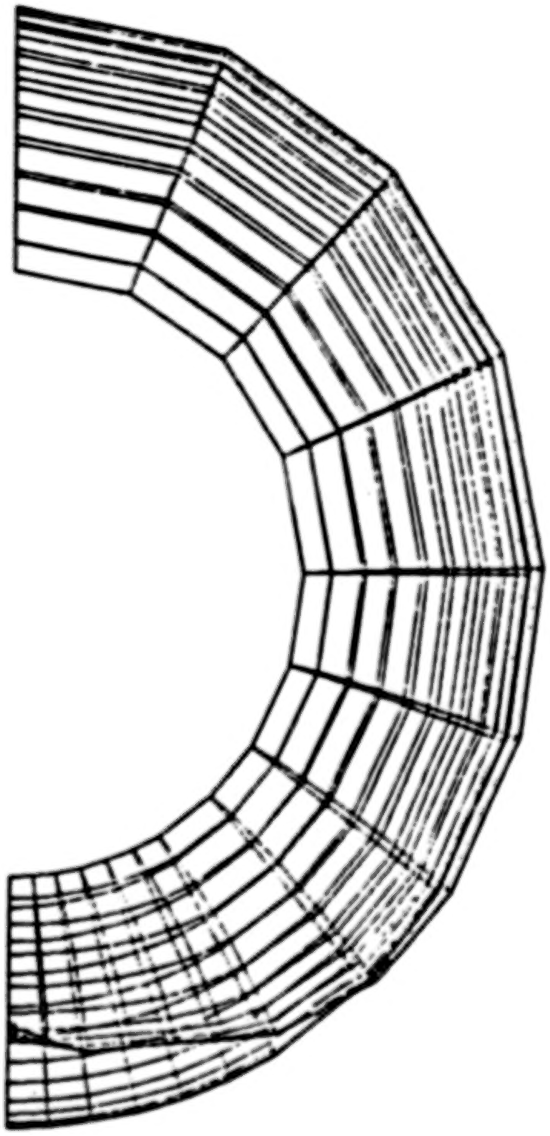

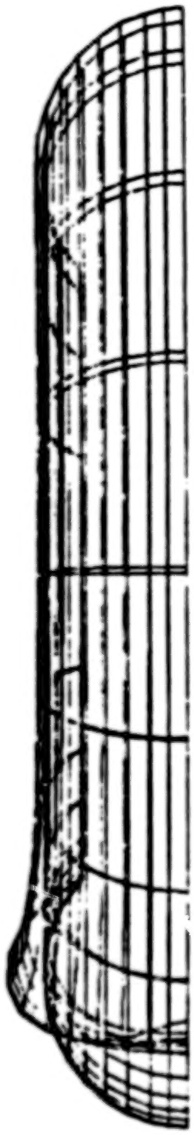

BEST DOCUMENT AVAILABLE

CALCULATED CIRCUMFERENTIAL STRESS DISTRIBUTION, σ_θ , AT LOAD = 114.4 N (25.7 lbs.)

A three dimensional plot of circumferential distribution over the quarter torus is given below for the 114.4 N load. Note the scale change from that of the previous two three dimensional plots. Increased compressive stress in the footprint region is seen to cause a stress reversal in the center of the footprint region. The stress becomes compressive near the center, then suddenly reverses and becomes tensile, suggesting that a local limit point on the structure load deflection path has been reached and snap-through has occurred.

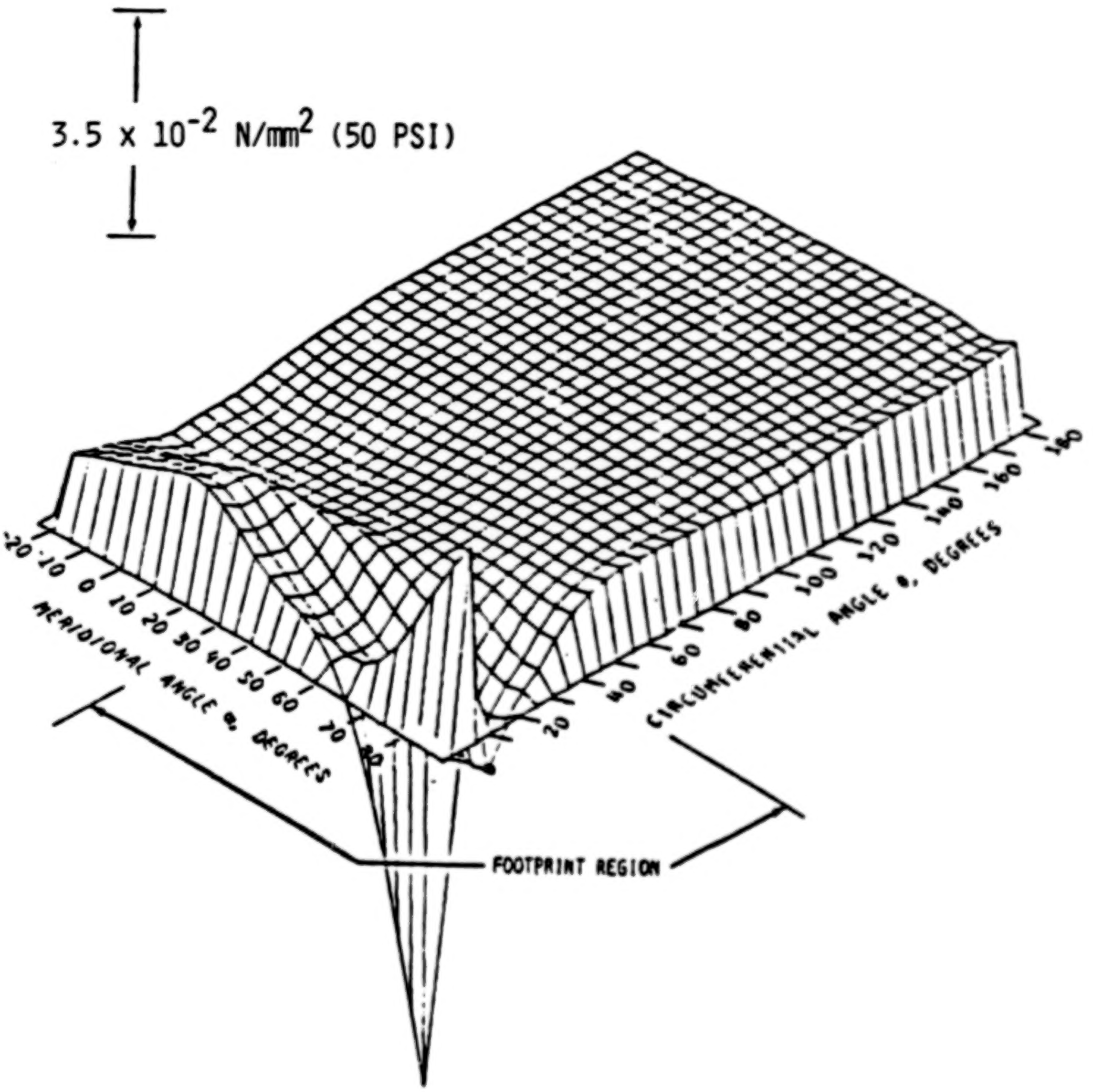

BEST DOCUMENT AVAILABLE

FOOTPRINT OF AN INNER TUBE SHOWING NEGATIVE CURVATURE

The figure below is a photograph of an inner tube under relatively heavy load. An initial eccentricity has been introduced. The negative curvature near the center of the footprint is considerably reduced in the presence of friction at the contacting surfaces (not modeled here).

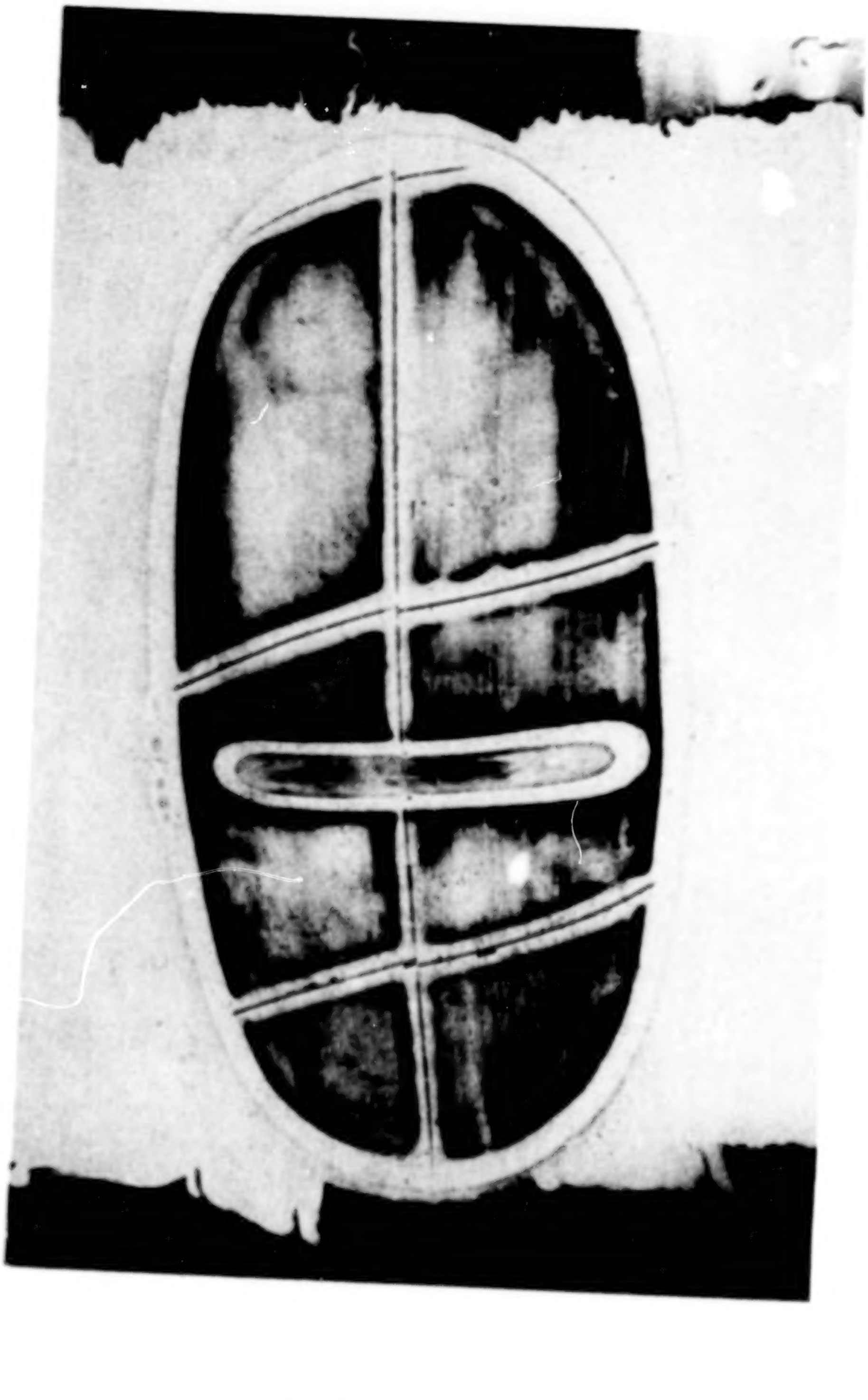

BEST DOCUMENT AVAILABLE

EXPERIMENTAL AND CALCULATED STRAINS AT -10° MERIDIONAL ANGLE - LOAD = 34.3 N (7.7 lbs.)

The figure below compares measured and calculated meridional and circumferential strains for varying θ at $\alpha = -10^\circ$. This -10° meridional angle places the strain gages in the region near the rim. Good agreement is achieved in observed and calculated values of circumferential strain. The disagreement between observed and calculated meridional strain is attributed to slipping of the membrane under the rim on the test fixture. The computer model had a fixed boundary at the rim.

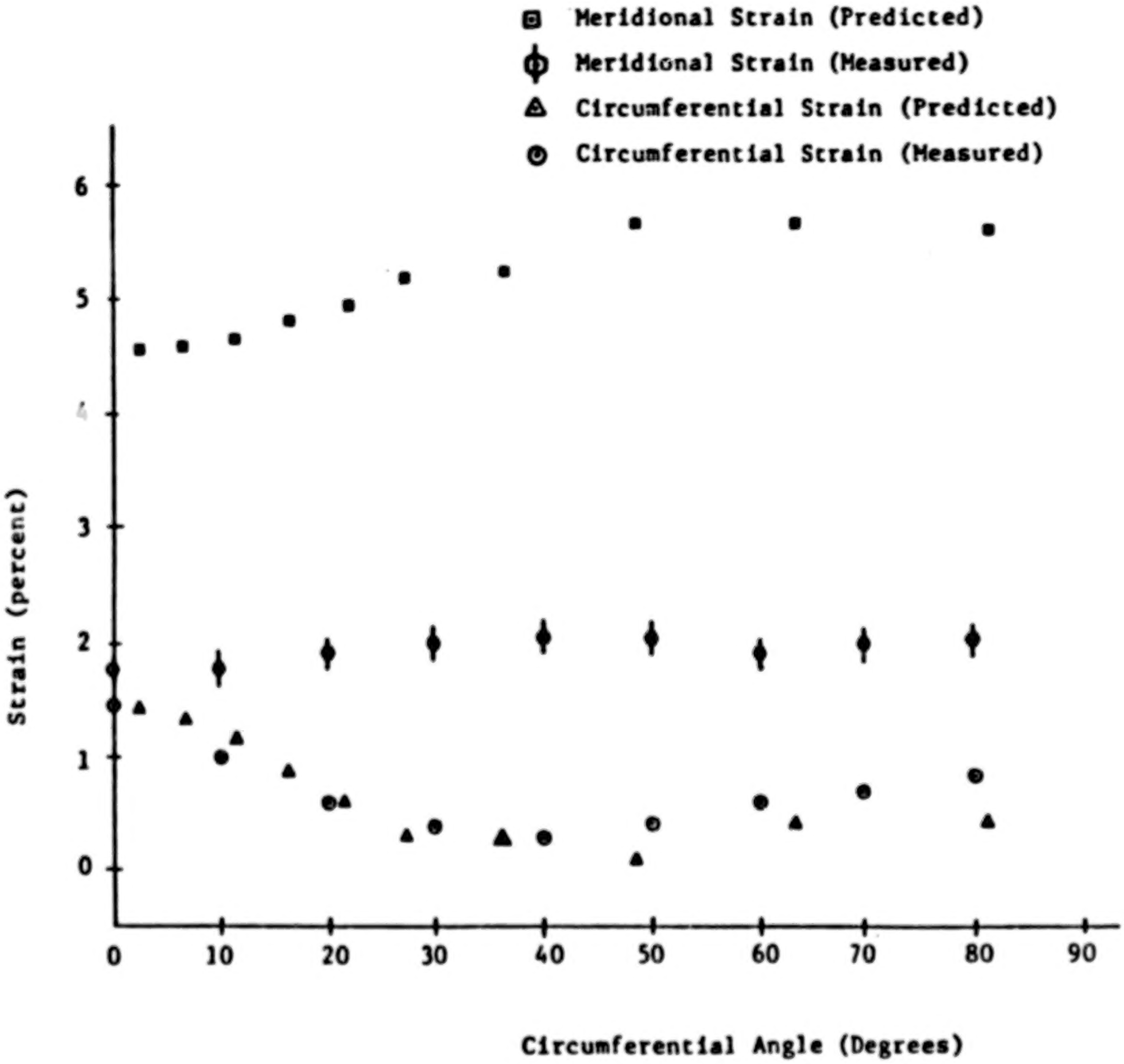

EXPERIMENTAL AND CALCULATED STRAINS AT 90° MERIDIONAL ANGLE - LOAD = 69.9 N (15.7 lbs.)

This figure compares measured and calculated strains for varying circumferential angle θ at $\alpha = 90^\circ$. At this farthest point from the rim, meridional strains are in good agreement. Note here that for all measurements below $\alpha = 30^\circ$, the strain gage is in the footprint region. Measured strain did not become compressive here, probably due to friction between the contacting surfaces. Reports of strain comparison at other loads are contained in the literature (ref. 8).

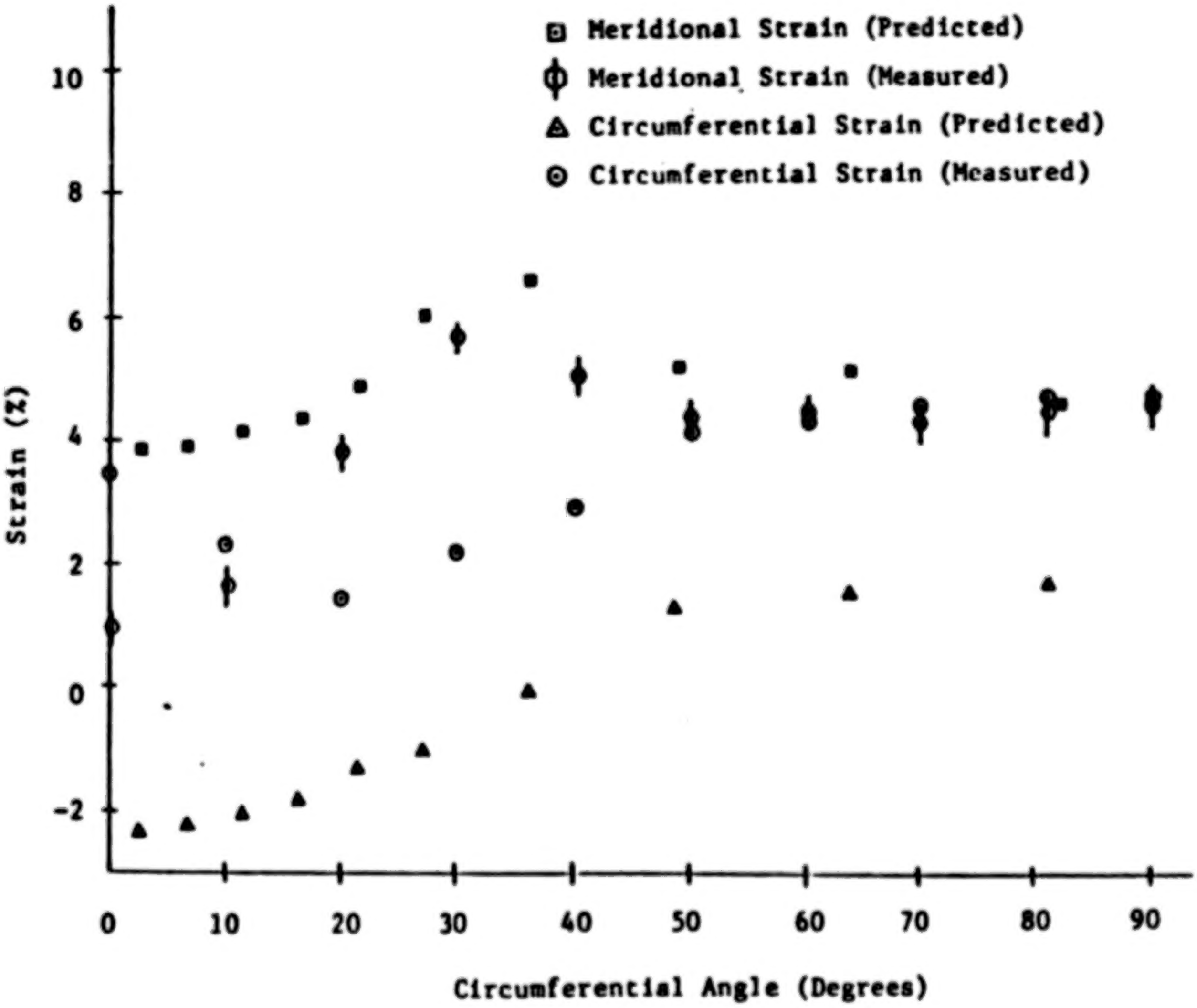

REFERENCES

1. Almroth, B. O.; Brogan, F. A.; and Stanley, G. M.: Structural Analysis of General Shells. Vol. 2, Users Instructions for STAGS C-1. LMSC-D 633873, Lockheed-California, April 1979.

2. Hill, D. E.; and Baumgarten, J. R.: The Experimental Stress Analysis of a Thin-Walled Pressurized Torus Loaded by Contact With a Plane. Volume A - Structures and Materials, AIAA/ASME 23rd Structures, Structural Dynamics and Materials Conference May 1982, pp 93 -97.

3. Mack, M. J.; Gassman, P. M.; and Baumgarten, J. R.: The Analysis of a Thin-Walled Pressurized Torus Loaded by Contact with a Plane. Volume A - Structures and Materials, AIAA/ASME 23rd Structures, Structural Dynamics and Materials Conference, May 1982, pp 181 -187.

4. Durand, M.; and Jankovich, E.: Nonapplicability of Linear Finite Element Programs to the Stress Analysis of Tires. NASA TM X-2637, September 1972, pp 263 - 276.

5. Deak, A. L.; and Atluri, S.: The Stress Analysis of Loaded Rolling Aircraft Tires. Vol. 1, Analytical Formulation. AFFDL-TR-73-130, Air Force Flight Dynamics Laboratory, October 1973.

6. DeEskinazi, J.; Soedal, W.; and Yang, T. Y.: Contact of an Inflated Torodial Membrane with a Flat Surface as an Approach to the Tire Deflection Problem. Tire Science and Technology, TSTCA, Vol. 3, February 1975, pp 43 - 61.

7. Mack, M. J.: The Finite Element Analysis of an Inflated Torodial Structure. M. S. Thesis, Iowa State University, 1981.

8. Hill, D. E.: Experimental Stress Analysis of an Inflated Torodial Structure. M. S. Thesis, Iowa State University, 1981.

BEST DOCUMENT AVAILABLE

APPENDIX

In describing the operation of a liquid metal strain gage, one assumes that the liquid metal column obeys the fundamental resistance relation (there are no voids in the column). Further, the resistivity of the conducting medium is assumed constant, and the volume of the capillary cylindrical cavity is assumed constant. Rubber is essentially incompressible; the assumption of constant volume under elongation is a valid one. The fundamental resistance is

$$R = \frac{\rho L}{A} = \frac{\rho L^2}{V} \qquad (1)$$

when $\rho \equiv$ resistivity, ohm-in.

$L \equiv$ length, in.

$A \equiv$ cross-sectional area, in.^{2}

$V \equiv$ volume, in.$^3 = AL$

Using a Taylor series expansion about the initial length,

$$\Delta R = \frac{\partial R}{\partial L}(L - L_o) + \frac{\partial^2 R}{\partial L^2}\frac{(L - L_o)^2}{2!}$$

$$\Delta R = \frac{\rho}{v}\left[2L_o(L - L_o) + \frac{2(L - L_o)^2}{2}\right] = \frac{\rho}{v}\left[2L\Delta L + \Delta L^2\right]$$

$$\frac{\Delta R}{R} = 2\,\frac{\Delta L}{L_o} + \frac{\Delta L^2}{L_o^2} = 2\varepsilon + \varepsilon^2 \qquad (2)$$

where ε = strain, in./in.

Equation 2 establishes a quadratic relationship between resistance change and strain. It is seen from (2) that for small strains, the gage factor is two.

EXPERIMENTAL AND FINITE ELEMENT STUDY OF A STANDING TORUS UNDER NORMAL AND TANGENTIAL LOADS

Donald R. Flugrad and Bruce A. Miller
Iowa State University

EXPANDED ABSTRACT

There continues to exist a strong interest in the load deflection attributes of both automotive and aircraft tires. Considerations of safety, handling and performance during such maneuvers as landing, braking and cornering are intimately tied to the adequacy of a vehicle's tire design. In the past, the qualitative and quantitative information needed for a basic understanding of tire characteristics has been derived by strictly empirical methods. Of late, however, numerical techniques such as finite element analysis have been brought to bear on certain aspects of the problem.

This paper describes work that is presently in progress at Iowa State University to determine the effect of a combined external load consisting of a normal component and a tangential braking force applied to an inflated torus. Experimental results obtained by photographic study of the contact area between the torus and load plate are presented as well as measurements of the vertical and horizontal displacement of the torus under load. A numerical procedure for displacement analysis is developed in which the finite element program STAGS (Structural Analysis of General Shells) is used in an iterative manner to produce a flat, horizontal footprint surface under force loading. The redistributed force distribution obtained by the iterative process is displayed along with computed meridional and circumferential stresses. Finally, an extension of the iterative method is introduced which eliminates the need to experimentally determine the footprint area.

LINE DRAWING OF TEST FIXTURE

Figure 1 shows the torus mounted on a rim and axle. The axle is clamped to the frame to prevent rotation of the unit. Two load tables work independently to produce an externally applied load on the torus. The table directly below the torus acts through the pulleys at the top of the fixture to pull the plate in contact with the torus upward, providing a normal load. The table shown to the left of the fixture is then loaded to exert a tangential force in the fore-aft or braking direction.

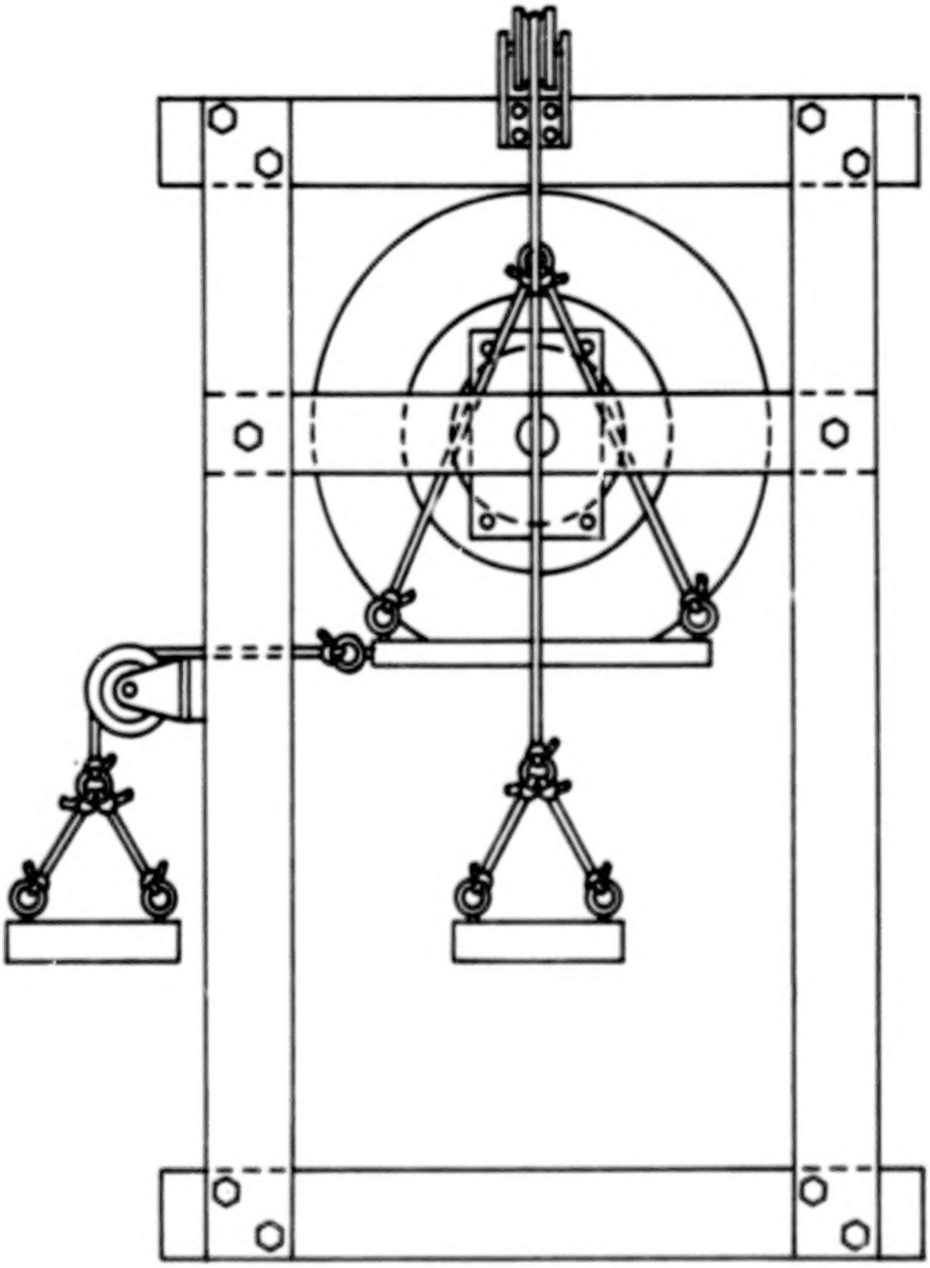

Figure 1

PHOTOGRAPH OF TEST FIXTURE

The actual test fixture is depicted in Figure 2 with weights mounted on the normal load table directly below the 8.00 × 20 inner tube used as the torus. A plastic milk container is shown in place of the tangential load table of Figure 1. By introducing water into the milk container, it is possible to vary the tangential load continuously instead of incrementally as would be the case if weights were placed on a load table. The plate in contact with the torus is made of transparent lucite allowing photographs of the footprint area to be taken from below the plate. Graph paper "targets" are affixed to the lucite plate for the purpose of tracking the vertical and horizontal displacement of the plate under prescribed load conditions. The manometer at the right is used to monitor the internal pressure of the torus.

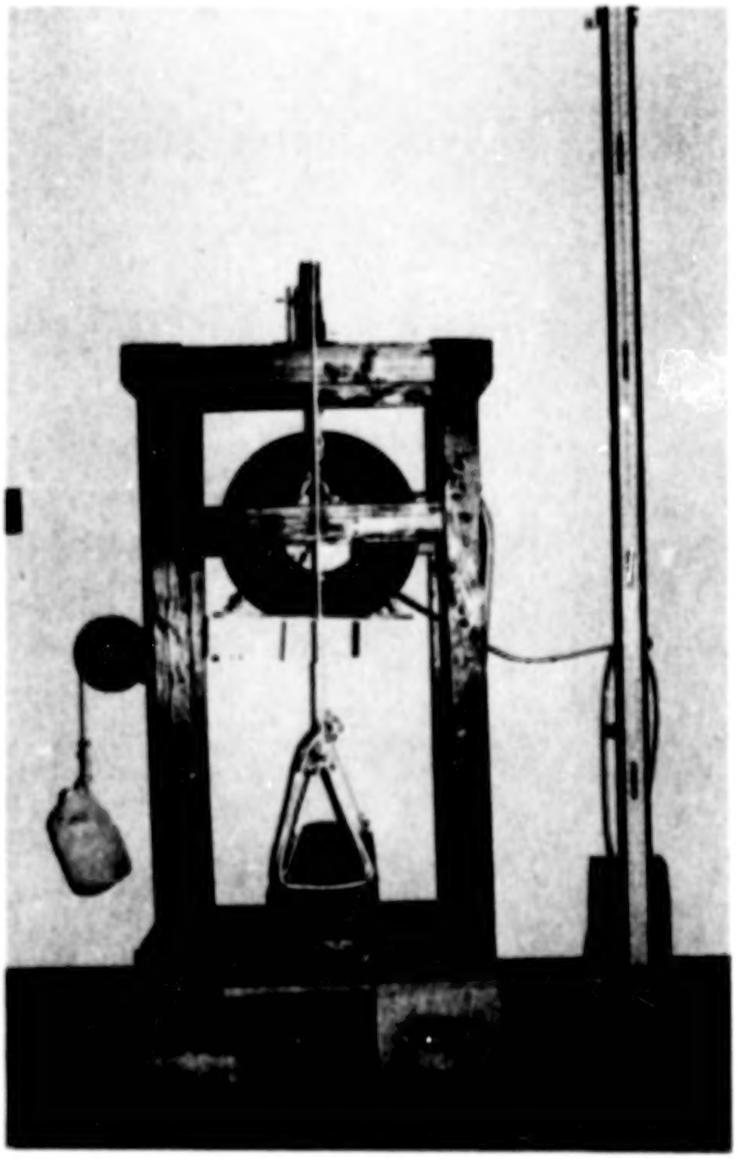

Figure 2

BEST DOCUMENT AVAILABLE

PHOTOGRAPHS OF FOOTPRINT AREAS

The two photographs of Figure 3 show footprint areas viewed through the transparent lucite plate. In both cases the torus is subjected to a normal load of 70 N and an internal pressure of 3450 Pa. Figure 3(a) was taken with no tangential load applied, and figure 3(b) shows the footprint area produced when a tangential load equal to 80% of the normal load is added. The photographs show that the contact area for each case is generally elliptical in shape. Closer inspection of the two photos verifies that there is little if any distortion introduced by the inclusion of a tangential component of force acting on the torus.

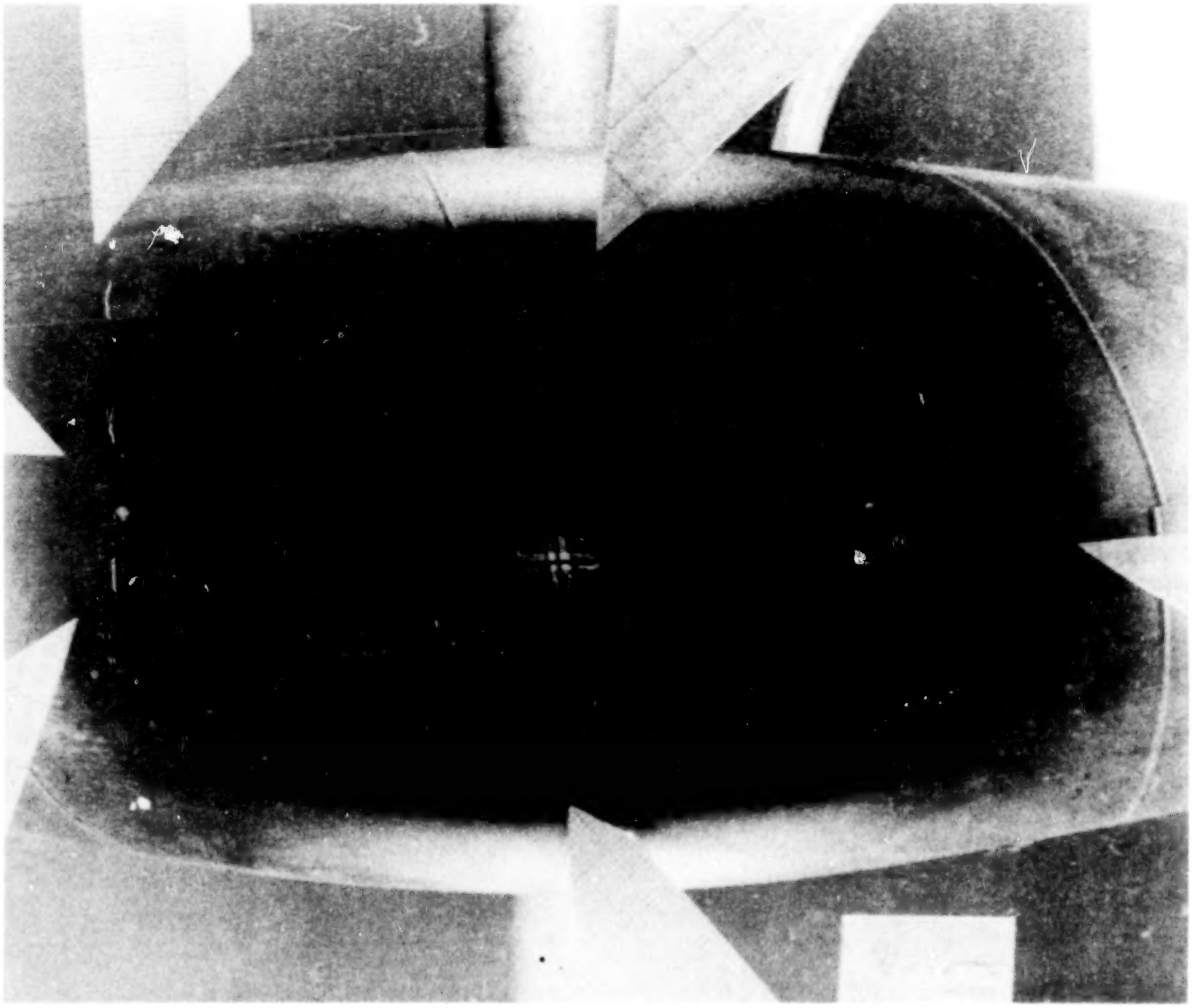

(a) Load = 70 N; braking = 0%; inflation = 3450 Pa.

Figure 3

BEST DOCUMENT AVAILABLE

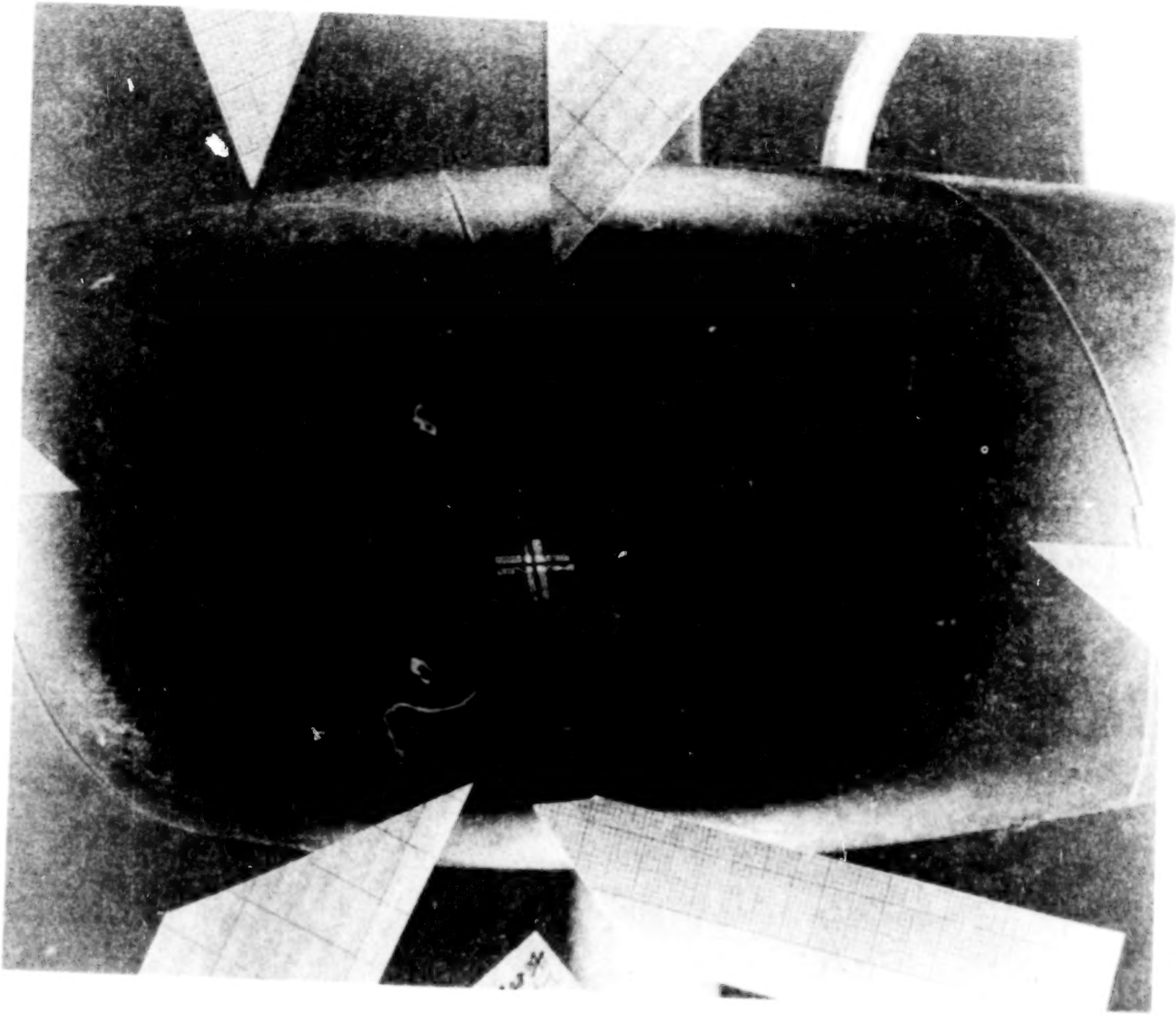

(b) Load = 70 N; braking = 80%; inflation = 3450 Pa.

Figure 3

BEST DOCUMENT AVAILABLE

EXPERIMENTAL MEASUREMENT OF DISPLACEMENT

The experimental set-up for the measurement of vertical and horizontal displacements of the torus under prescribed load conditions is depicted in Figure 4. In actuality the center of the inner tube on its rim and axle is held stationary and the displacement of the lucite plate in contact with the torus is measured. Three graph paper "targets" are attached to the load plate, two of which are visible hanging from the front edge of the plate in the photograph. The third is attached to the back edge of the plate. Three separate optical devices are trained on the grid patterns of the "targets" to record vertical and horizontal displacements of three distinct points on the plate as normal and tangential braking forces are applied to the torus. Only two of the three optical devices appear in the photo. The third, a surveying transit with a much longer focal length, is stationed some distance from the test fixture. The three separate measurements of displacement are then used to estimate the vertical and horizontal movement of a point located at the center of the footprint area.

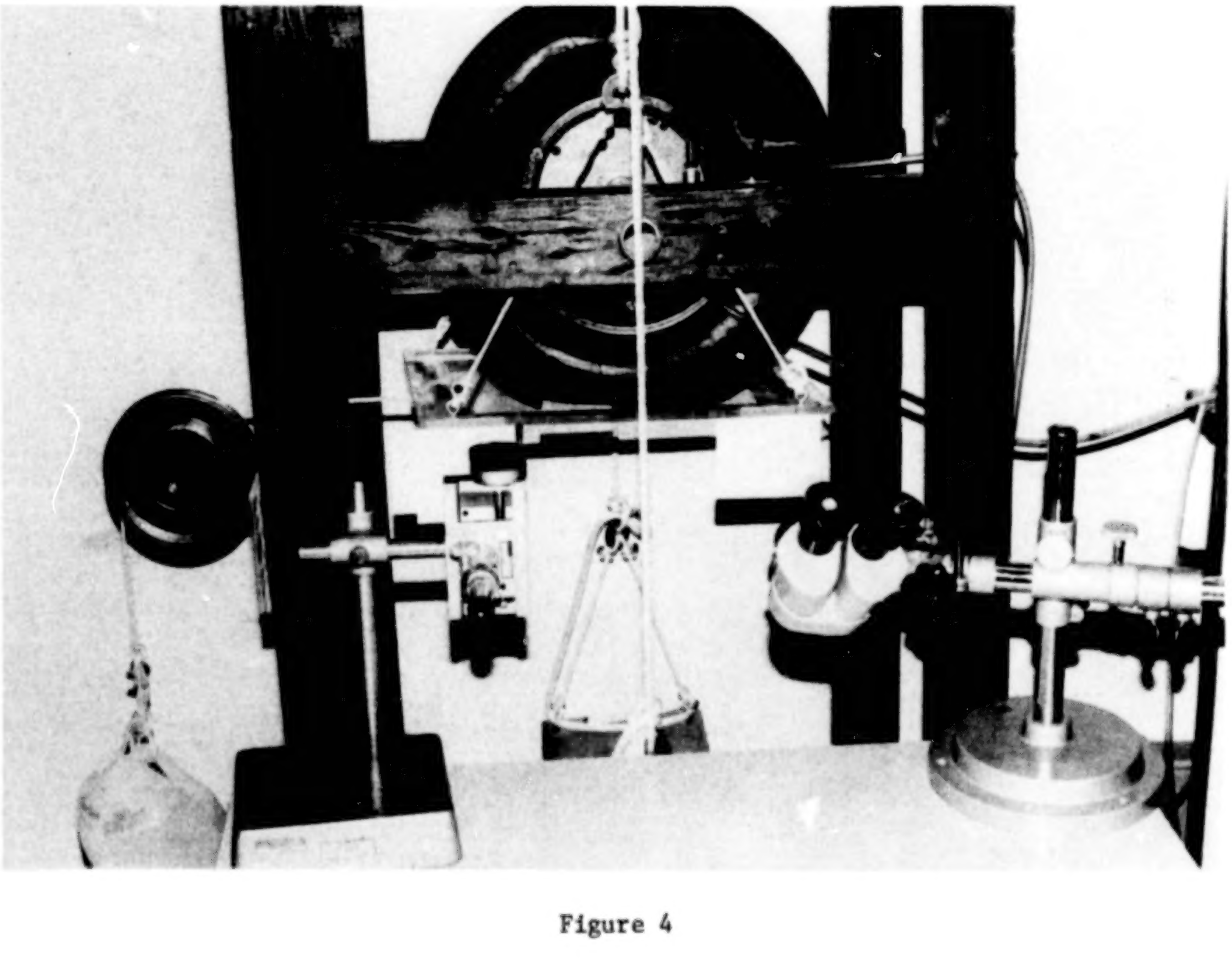

Figure 4

BEST DOCUMENT AVAILABLE

VERTICAL DISPLACEMENT OF TORUS

The graph of Figure 5 illustrates the relationship between the vertical displacement of the torus and the magnitude of the applied tangential braking force for a constant normal load of 70 N. Experimental results plotted on the graph are those obtained by the set-up of Figure 4. The solid line represents a least squares linear fit of the experimental data. Also shown are results obtained from STAGS, a finite element program particularly suited for analysis of plates and shells, for three different tangential load cases. The tangential force associated with the horizontal axis is a non-dimensional quantity which represents the braking force as a decimal fraction of the applied normal load. It is evident that the vertical displacement of the torus is relatively insensitive to the tangential force applied. It is also clear that the finite element analysis predicts a vertical displacement which is consistently less than that obtained by measurement.

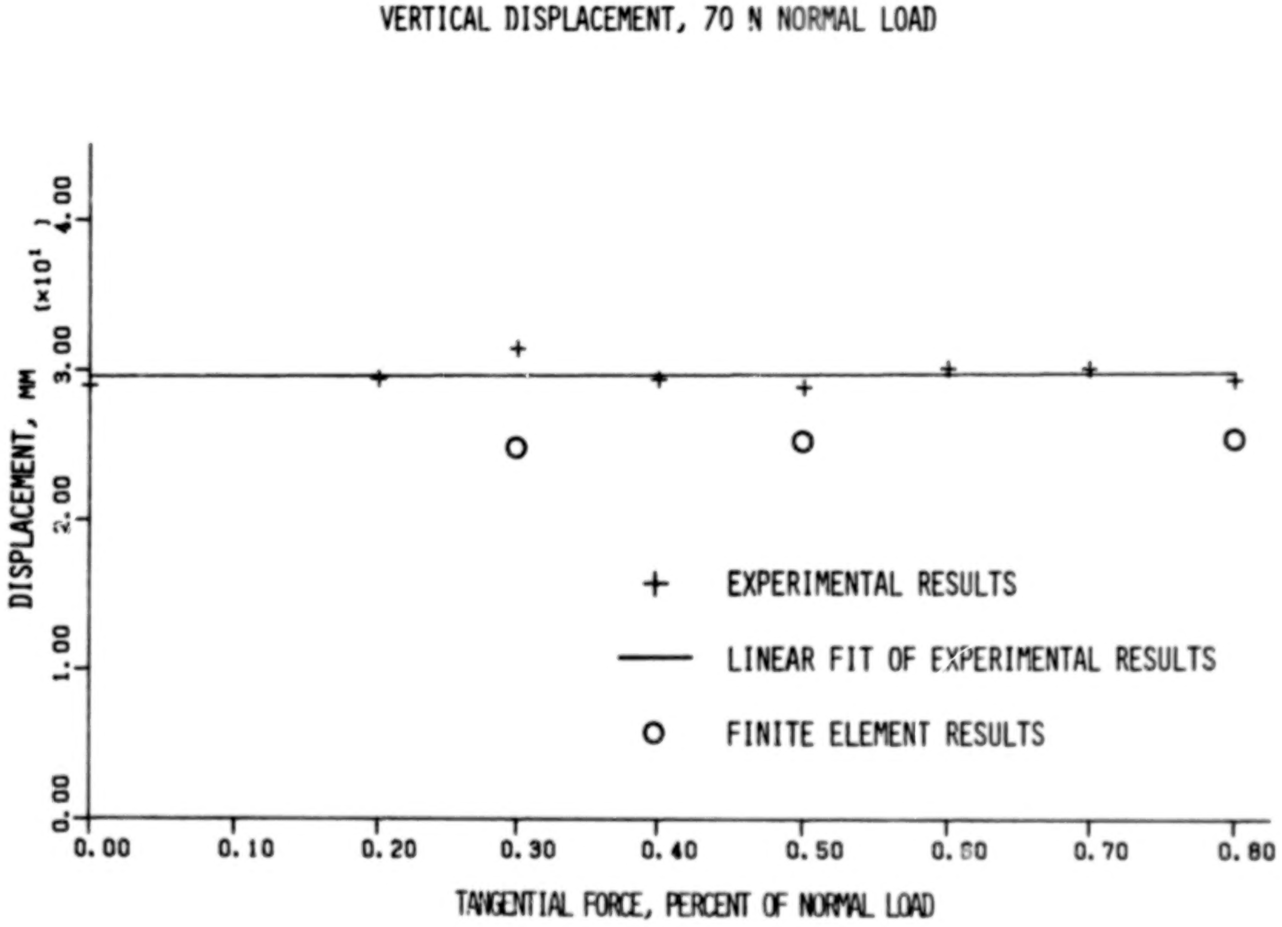

Figure 5

HORIZONTAL DISPLACEMENT OF TORUS

The graph of Figure 6 is similar to that of Figure 5 except that horizontal displacements of the torus are recorded rather than vertical displacements. A least squares cubic fit curve was chosen to best represent the experimental data after first considering both linear and quadratic forms. Of the three cases analyzed by finite element techniques, the first two are seen to agree remarkably well with the experimental results. For the greatest tangential force, however, STAGS predicts a horizontal displacement which is approximately only 50% of the measured value. Such a large discrepancy suggests that some undetected slip may have occurred between the lucite plate and inner tube for this case involving a high tangential braking force. Separate consideration of the three results arrived at by finite element analysis indicates the possibility of a more nearly linear relationship between horizontal displacement and tangential force. However, more data would have to be gathered before such a conclusion could be drawn.

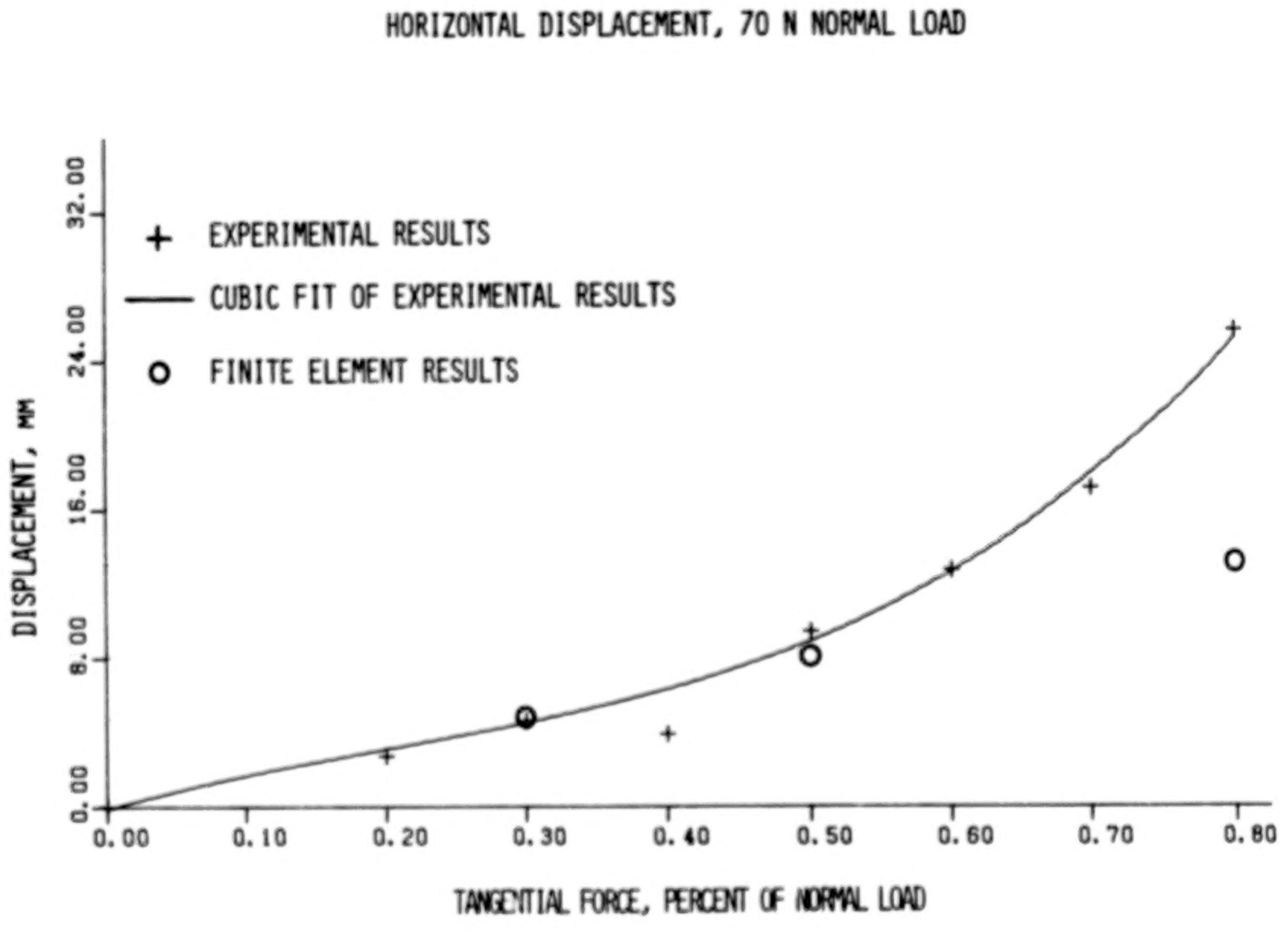
HORIZONTAL DISPLACEMENT, 70 N NORMAL LOAD

Figure 6

FINITE ELEMENT COORDINATES

Nominal dimensions of the inner tube used in this study are shown in Figure 7 along with the two coordinate angles required by STAGS to describe a toroidal shaped element. The angle θ is the circumferential angle. It varies from -180° to +180° for the torus. The meridional angle, α, varies from -42° to 90°. At α = -42° the torus is assumed to be clamped at the rim. Because there exists a plane of symmetry through the equator of the torus with respect to geometry as well as to the externally applied loads, it is possible to perform a complete finite element analysis by considering just half the inner tube. Hence, the maximum value for α is just 90° rather than 222°.

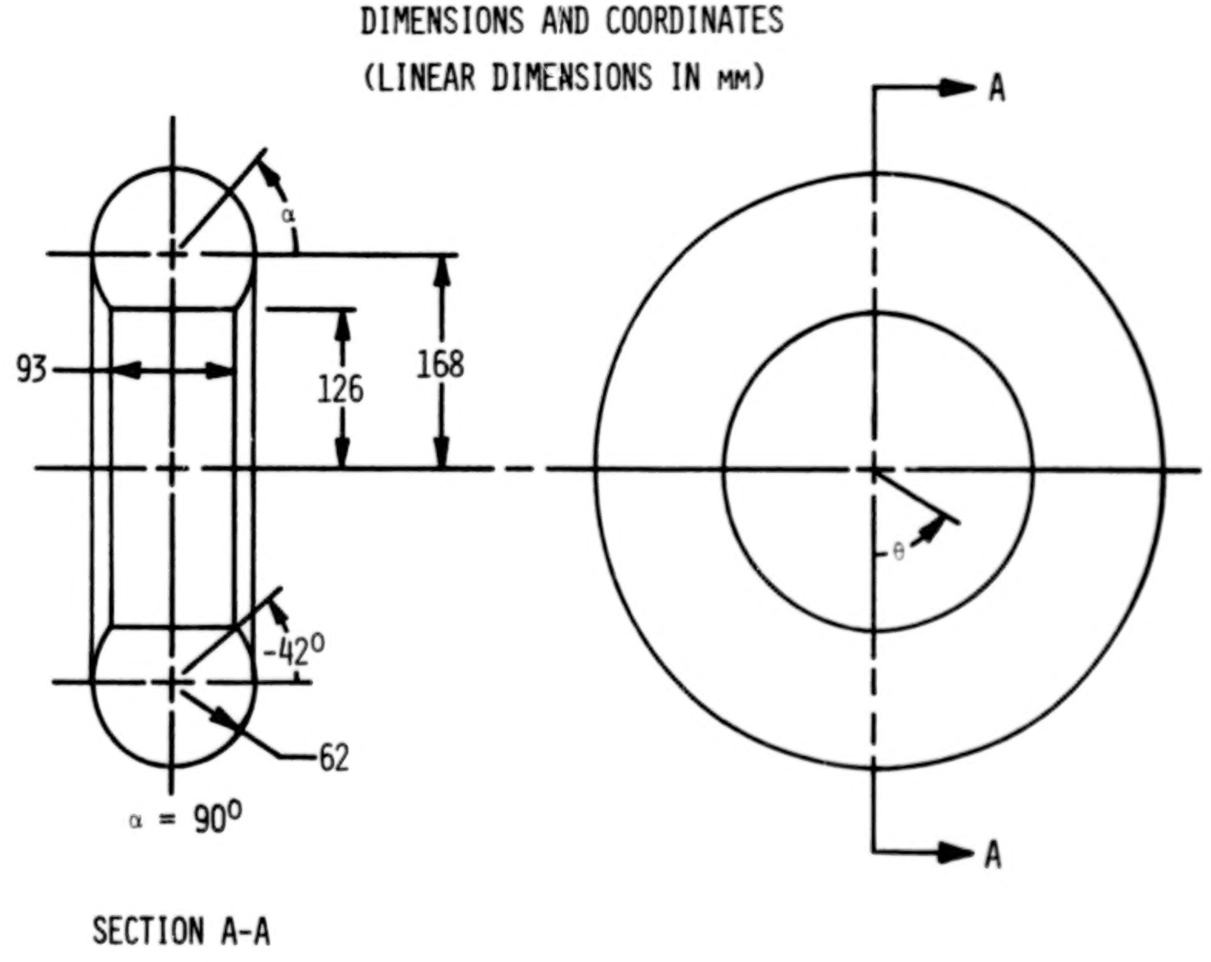
DIMENSIONS AND COORDINATES
(LINEAR DIMENSIONS IN MM)
A
α
93
126
168
-θ
-42°
62
α = 90°
A
SECTION A-A

Figure 7

FINITE ELEMENT DISPLACEMENT RESULTS FOR QUARTER TORUS WITH NORMAL LOAD

Shown in Figure 8 is the deformed as well as the undeformed geometry of the quarter torus analyzed by Mack (ref. 1) in a previous study. The finite element analysis was conducted with STAGS using a 13 x 15 grid pattern to define the location of the element nodes. A quarter torus was adequate in this case because there are two planes of symmetry in the absence of tangential loading. The 70 N normal load was evenly distributed over the nodes located within the experimentally determined footprint area. As can be seen, the evenly loaded nodes situated along the bottom of the torus in both views appear to lie on a relatively flat horizontal plane. Since the load plate is assumed to be horizontal and rigid, this result justified the use of an even load distribution in the footprint area for this particular case.

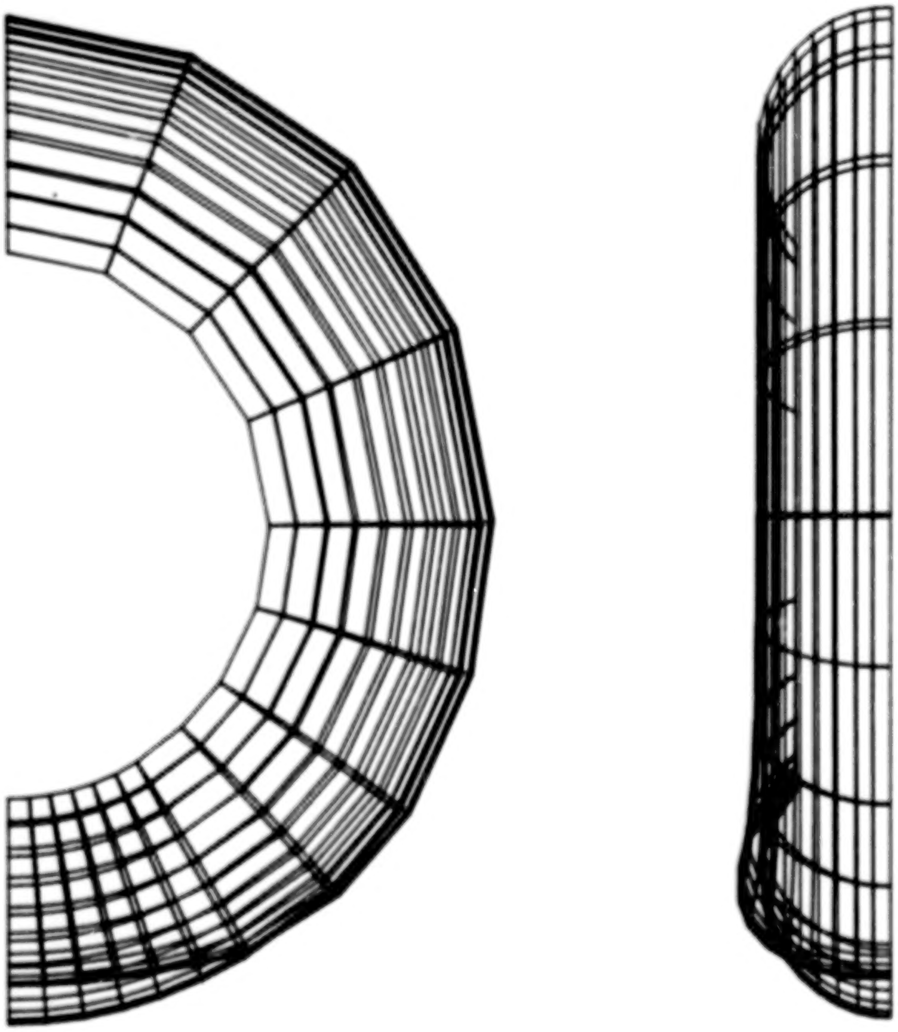

Figure 8

BEST DOCUMENT AVAILABLE

INITIAL RESULTS FROM FINITE ELEMENT DISPLACEMENT ANALYSIS WITH TANGENTIAL LOADING

The deformation of the half torus used to analyze the effect of combined normal and braking forces is illustrated in Figure 9. A 10 x 21 grid pattern was chosen in an attempt to provide a fine enough mesh for reasonably accurate results at a reasonable cost. The 70 N normal load is identical to that used for the quarter torus of Figure 8. In this initial run both the normal and tangential forces were evenly distributed over the nodes experimentally determined to lie within the footprint area. Unlike the normal load case of Figure 8, however, the loaded nodes along the bottom of the torus do not appear to lie on a horizontal plane. The tangential force, which acts to the left in the left-hand view, has the effect of tilting that portion of the toroidal surface meant to be in contact with the horizontal load plate. In an effort to correct this problem, an iterative method was devised to achieve a comparatively flat and horizontal surface across the bottom of the torus by systematically redistributing the forces on the nodes within the footprint area.

HALF TORUS, 70 N NORMAL, 80% TANGENTIAL, INITIAL RUN

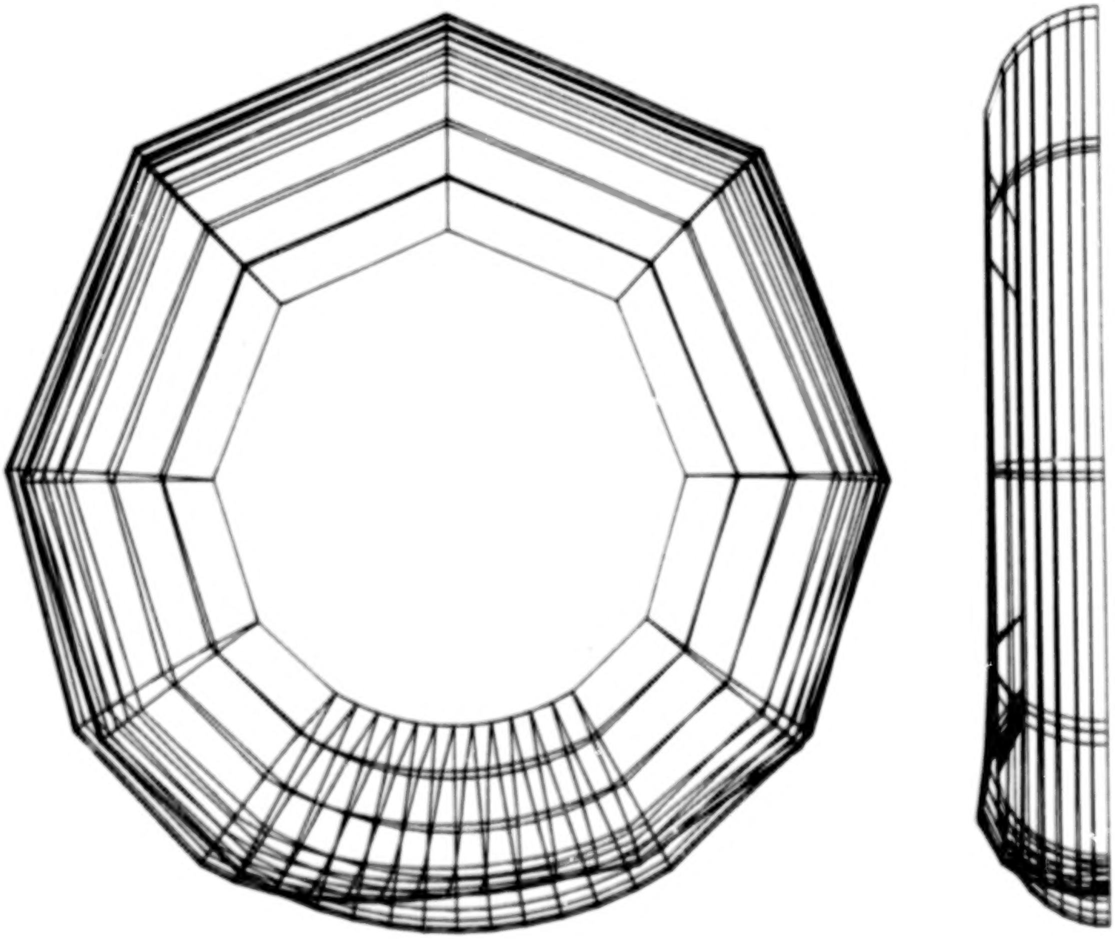

Figure 9

BEST DOCUMENT AVAILABLE

REDISTRIBUTION OF FORCES

The simplified model of Figure 10 illustrates the method developed to redistribute the forces in the footprint region. Suppose several springs of different lengths with different spring rates are suspended from a horizontal beam as shown. The total force to be exerted upward on the group of springs is known, and the individual forces to be applied to each of the springs is to be determined so that they all deflect to a common vertical equilibrium position denoted by Z_E. An arbitrary distribution of forces is chosen to begin the procedure. For example, the total force might initially be uniformly distributed over all the springs. The resulting deflection of each of the springs is observed, and a corresponding set of spring rates is calculated. From a consideration of the total force, the common equilibrium position, Z_E, is determined from the equation given in the lower right hand corner of the figure. Once Z_E is known the forces to be exerted on each of the individual springs are calculated from the equation provided for F_I. For a linear set of springs which act independently, these forces will, in fact, produce a common equilibrium position for all the springs. The situation with the inflated torus, however, is more complicated and requires an iterative scheme. The nodes within the footprint region are first loaded evenly. The STAGS analysis then gives the resulting deflections from which individual nodal spring rates are determined. A trial value is next computed for the equilibrium position just as in the case of the simplified model, and forces to be applied to the individual nodes are evaluated. These forces are then used to perform another STAGS analysis. Since the spring rates of the nodes are expected to be nonlinear, and since the nodes do not act independently, this second application of STAGS will not, in general, produce a flat, horizontal surface on the torus. Therefore, the entire procedure must be repeated until the deflected nodes are found to lie on a surface which is sufficiently flat and sufficiently horizontal.

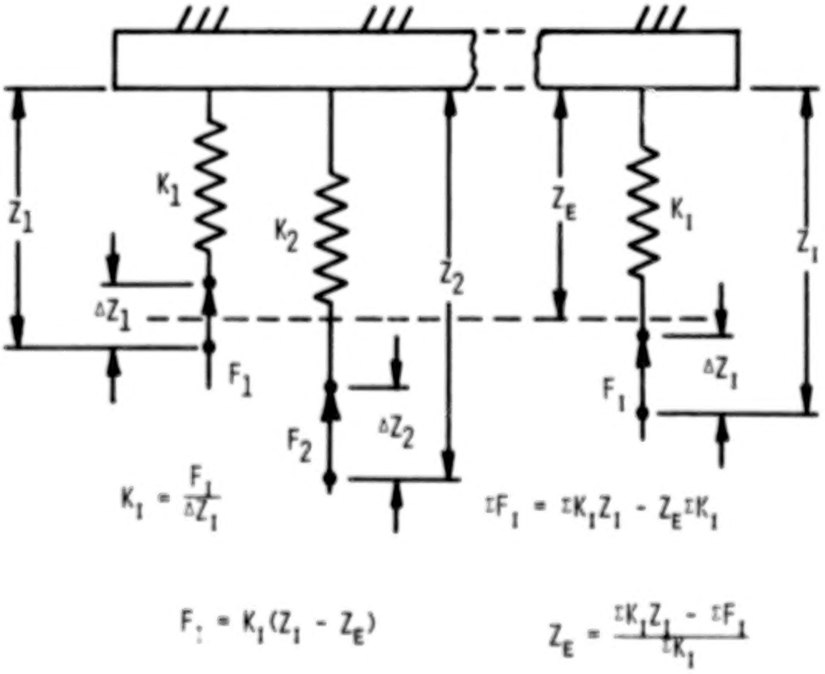

Figure 10

FINITE ELEMENT DISPLACEMENT ANALYSIS FOR FIRST ITERATION

After redistributing the forces on the torus of Figure 9 by the method described in Figure 10, the STAGS analysis was performed again. The results of that analysis are shown in Figure 11. As can be seen, the footprint area is still not flat, but the severe tilt evident in Figure 9 has been greatly reduced.

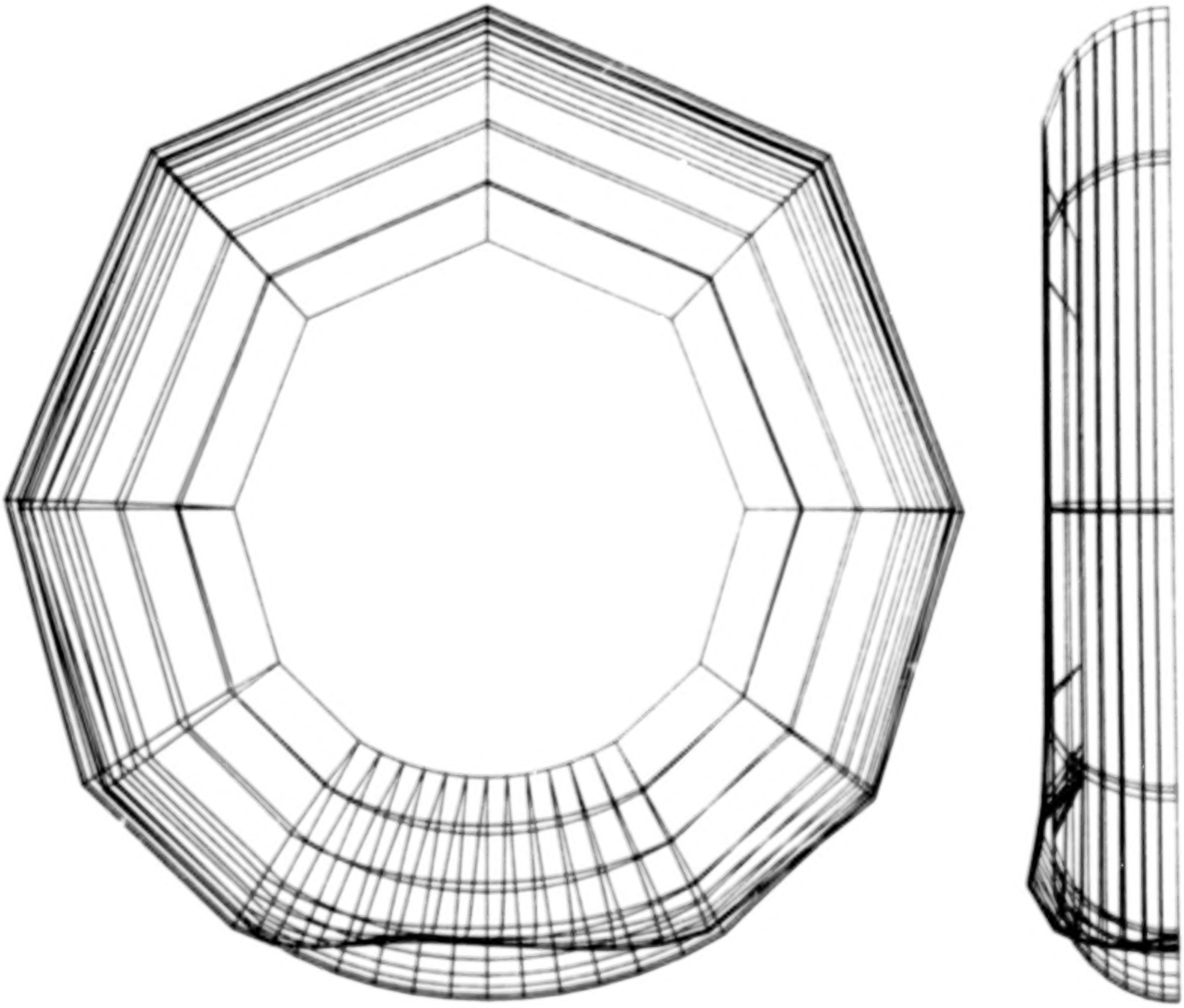

HALF TORUS, 70 N NORMAL, 80% TANGENTIAL, FIRST ITERATION

Figure 11

BEST DOCUMENT AVAILABLE

FINITE ELEMENT DISPLACEMENT ANALYSIS FOR FINAL ITERATION

Figure 12 depicts the displacement results for the third iteration on the torus of Figures 9 and 11. Although some waviness is still apparent in the footprint region, the surface is relatively flat and horizontal. In fact, further iterations failed to produce any significant improvement. The common equilibrium position calculated for this case was used to establish the vertical deflection plotted in Figure 5 for a non-dimensional tangential force of 0.8. Only the normal components of force were considered in the redistribution process. Once the normal forces were established for each of the nodes, a tangential component of force equal to 0.8 of the corresponding normal force was added. Consequently, the resulting horizontal displacements of the nodes in the footprint region showed some variation. In order to arrive at a single value to characterize the horizontal deflection of the torus, the average of the horizontal displacements of the nodes across the center of the footprint area at a circumferential angle of 0° was computed. This value was then plotted in Figure 6 as one of the three data points found by the finite element method.

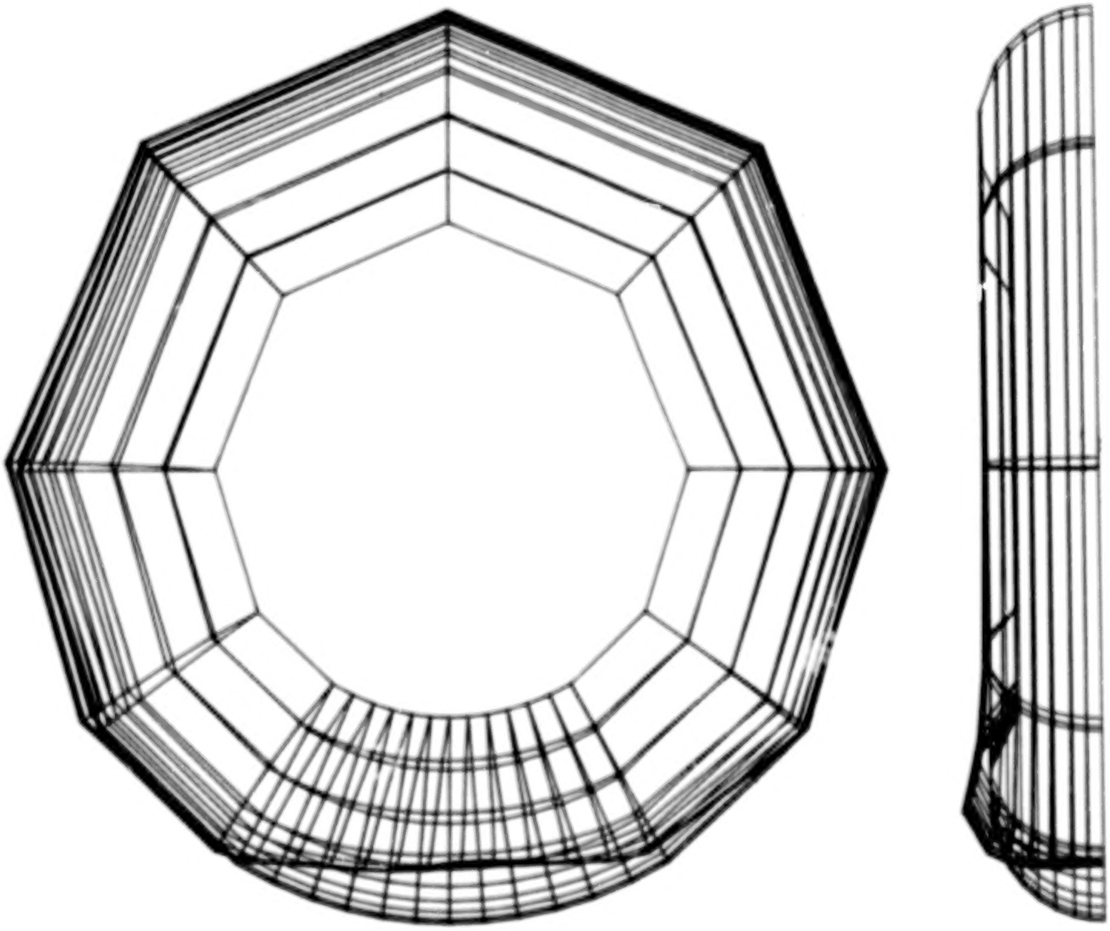

HALF TORUS, 70 N NORMAL, 80% TANGENTIAL, FINAL ITERATION

Figure 12

The footprint force distribution determined for the final iteration of Figure 12 is displayed in Figure 13. The sense of the tangential force applied to the torus is down and to the left with respect to the three dimensional plot. As shown, the force is greater along the sides of the footprint and at the left hand leading edge than in the middle. While the distribution appears to vary significantly, the minimum force at the middle of the footprint is actually 83% of the maximum force at the leading edge.

FOOTPRINT FORCES, 70 N NORMAL, 80% TANGENTIAL, FINAL ITERATION

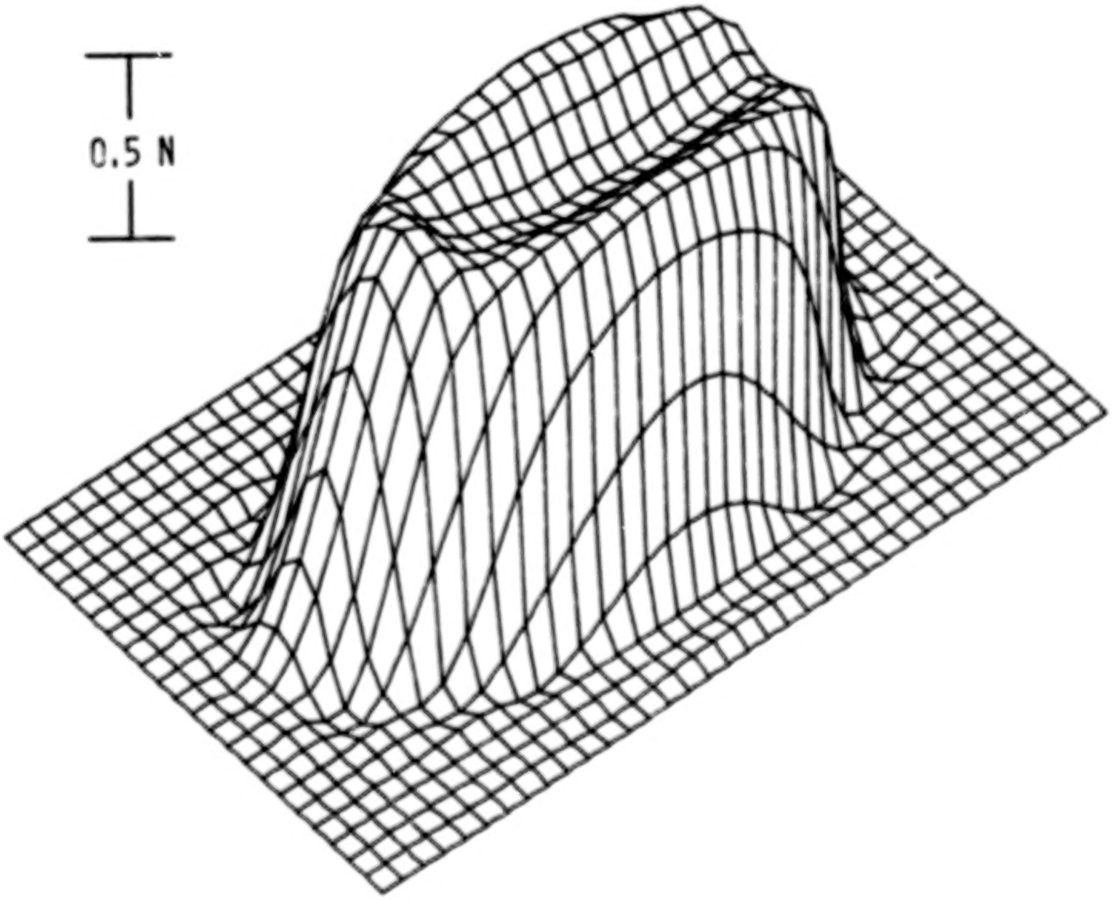

Figure 13

MERIDIONAL STRESSES FOR INITIAL RUN

The meridional stresses computed by STAGS for the initial run of Figure 9 are shown in Figure 14. The footprint area extends from approximately -25° to +25° in the circumferential direction and from approximately 90° to 45° in the meridional direction. The three dimensional display suggests the existence of a great deal of variation in the stresses throughout the torus with the stress even becoming compressive for a small area in the neighborhood of $\theta = 0°$. However, caution must be exercised in using this plot and those of the next three figures. There have been no experimental stress measurements made to verify these results, and no other grid patterns have as yet been tried to determine the effect of changing the finite element mesh on the computation of stresses. Another point that should be made with respect to Figures 14 through 17 is the fact that in executing the STAGS analysis the nodes located at circumferential angles of -180° and +180° were constrained to remain in a vertical plane. Hence, the stresses calculated at these extreme values of θ turned out to be quite different even though they represent the same points on the torus. Elimination of this constraint could have a significant effect on the predicted stress distribution.

MERIDIONAL STRESS, 70 N NORMAL, 80% TANGENTIAL, INITIAL RUN

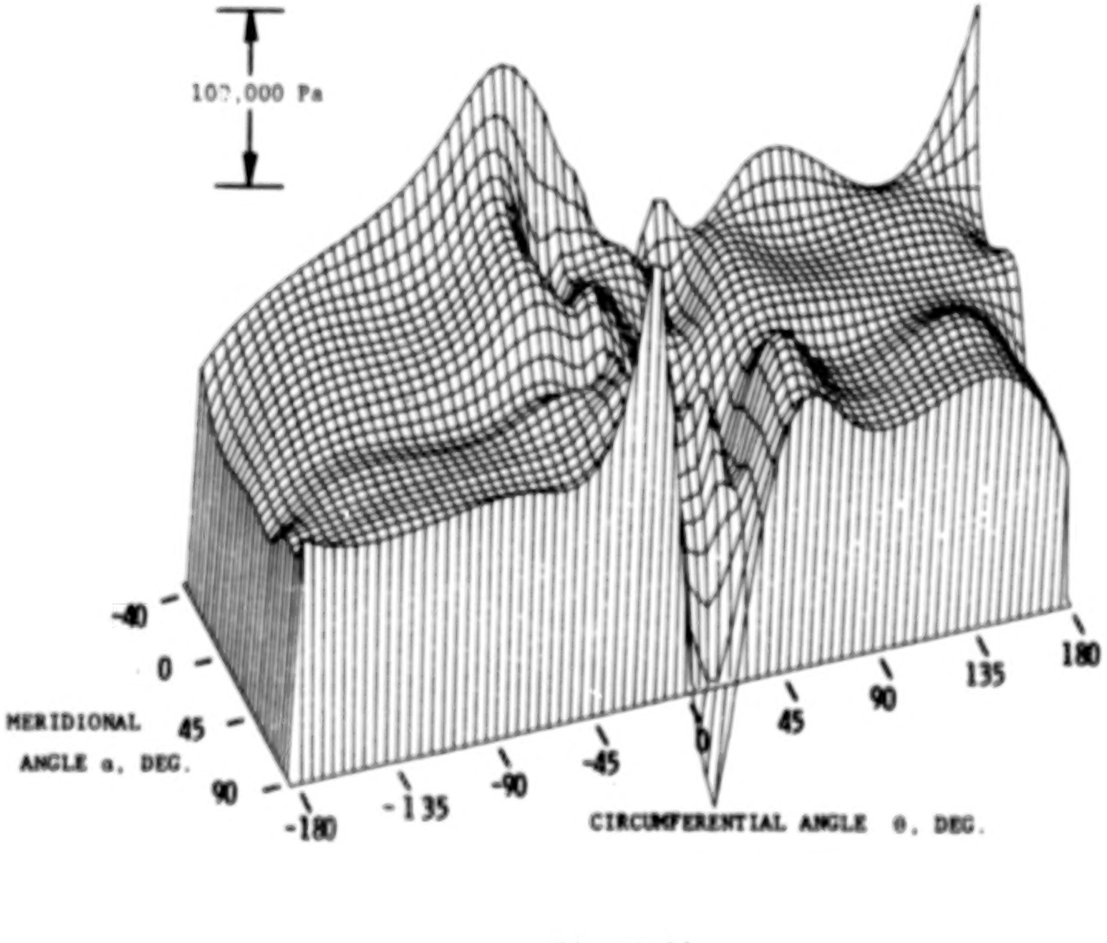

Figure 14

BEST DOCUMENT AVAILABLE

MERIDIONAL STRESSES FOR FINAL ITERATION

The meridional stresses for the final iteration of Figure 12 are depicted in Figure 15. Comparison with Figure 14 indicates that redistribution of the forces in the footprint area produces a dramatic effect on the stress distribution.

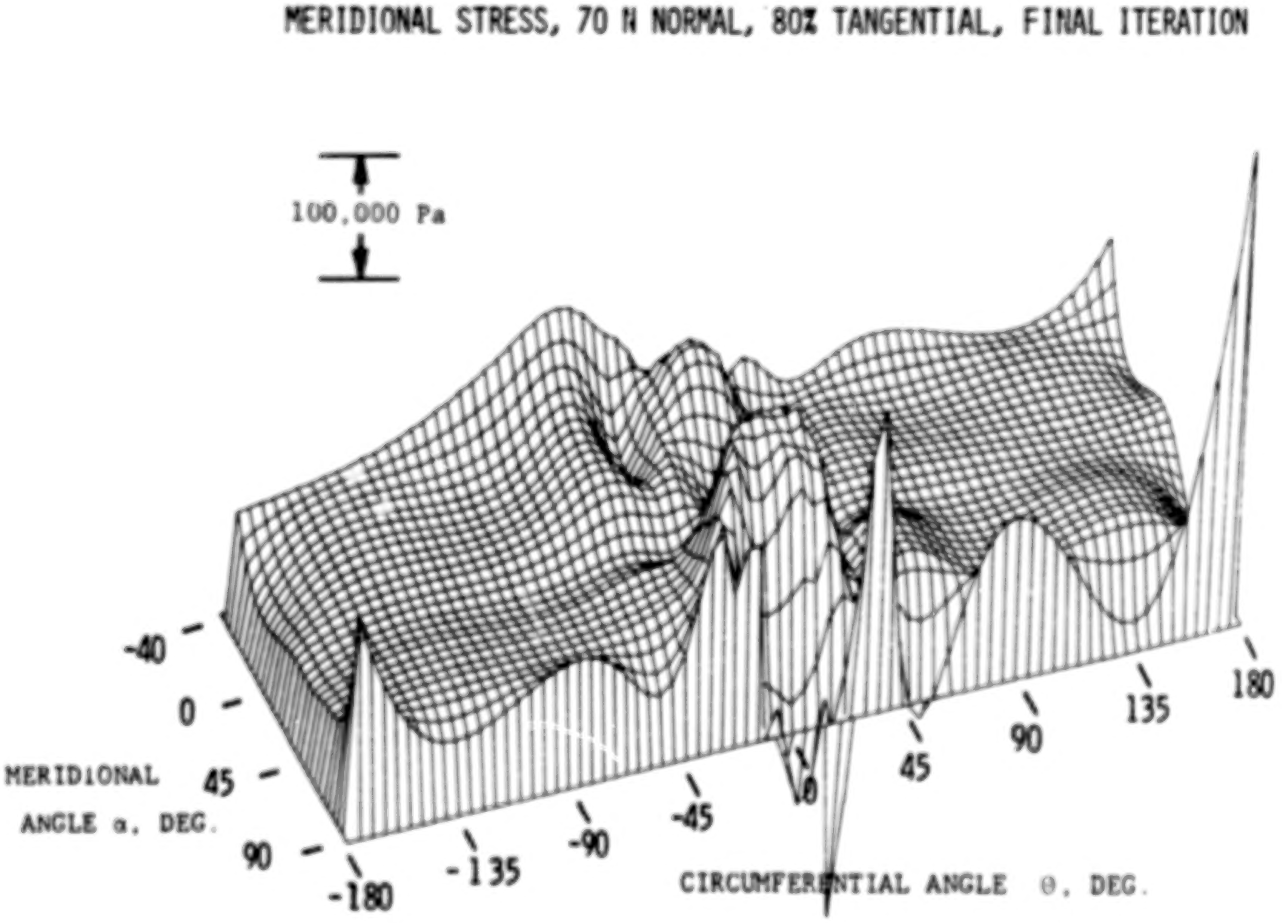

Figure 15

BEST DOCUMENT AVAILABLE

CIRCUMFERENTIAL STRESSES FOR INITIAL RUN

Figure 16 shows the circumferential stresses obtained from the STAGS analysis for the initial run of Figure 9. It is interesting to note the sharp decrease in stress at the leading edge of the footprint at a circumferential angle of approximately -40°. This seems reasonable in light of the fact that the tangential force is directed to the left with respect to the three dimensional plot.

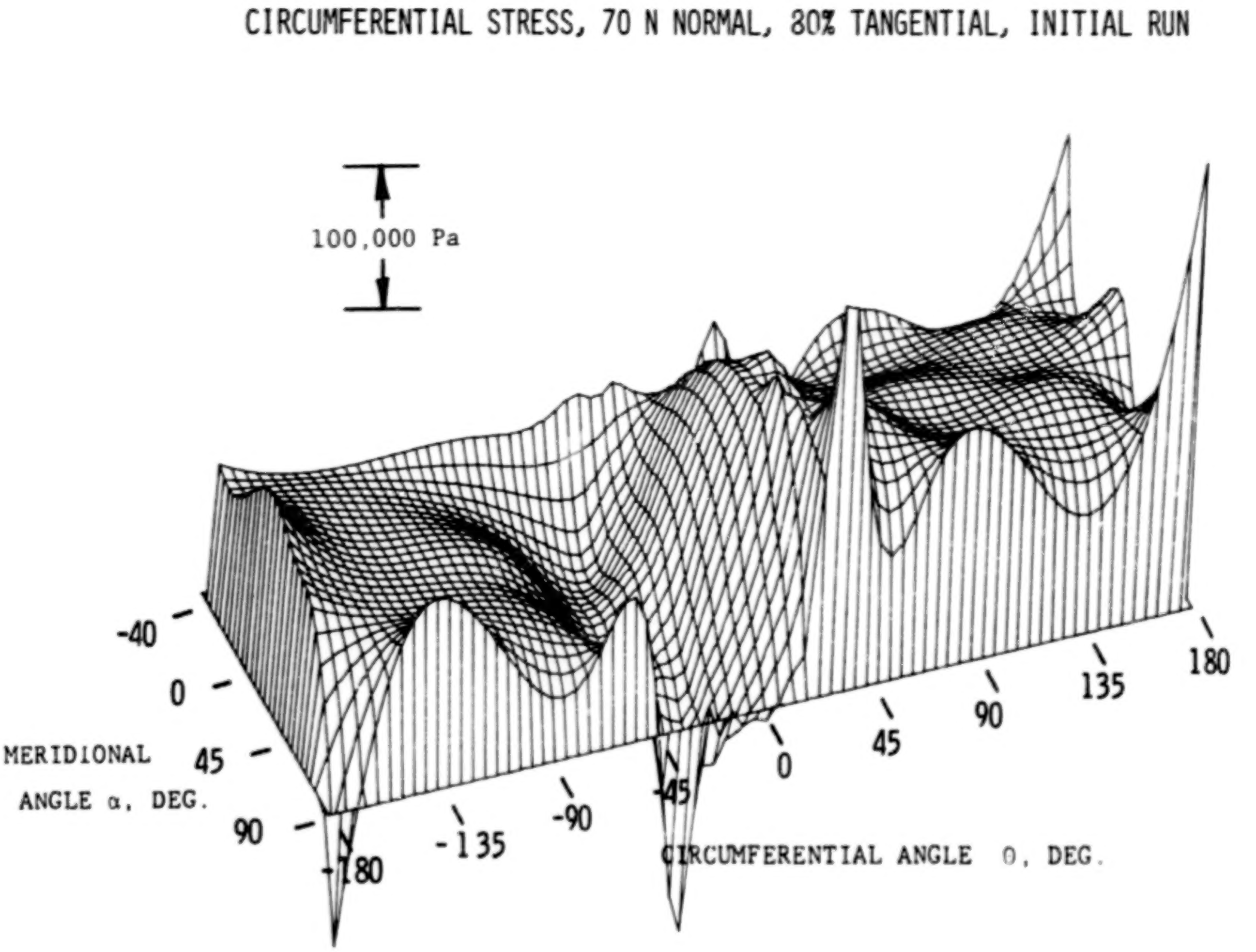

Figure 16

BEST DOCUMENT AVAILABLE

CIRCUMFERENTIAL STRESSES FOR FINAL ITERATION

Figure 17 depicts the circumferential stress results for the final iteration of Figure 12. The high stresses in the footprint region and the sharp decrease just to the left of the contact area are even more pronounced for this case with redistributed forces than for the initial run of Figure 16.

CIRCUMFERENTIAL STRESS, 70 N NORMAL, 80% TANGENTIAL, FINAL ITERATION

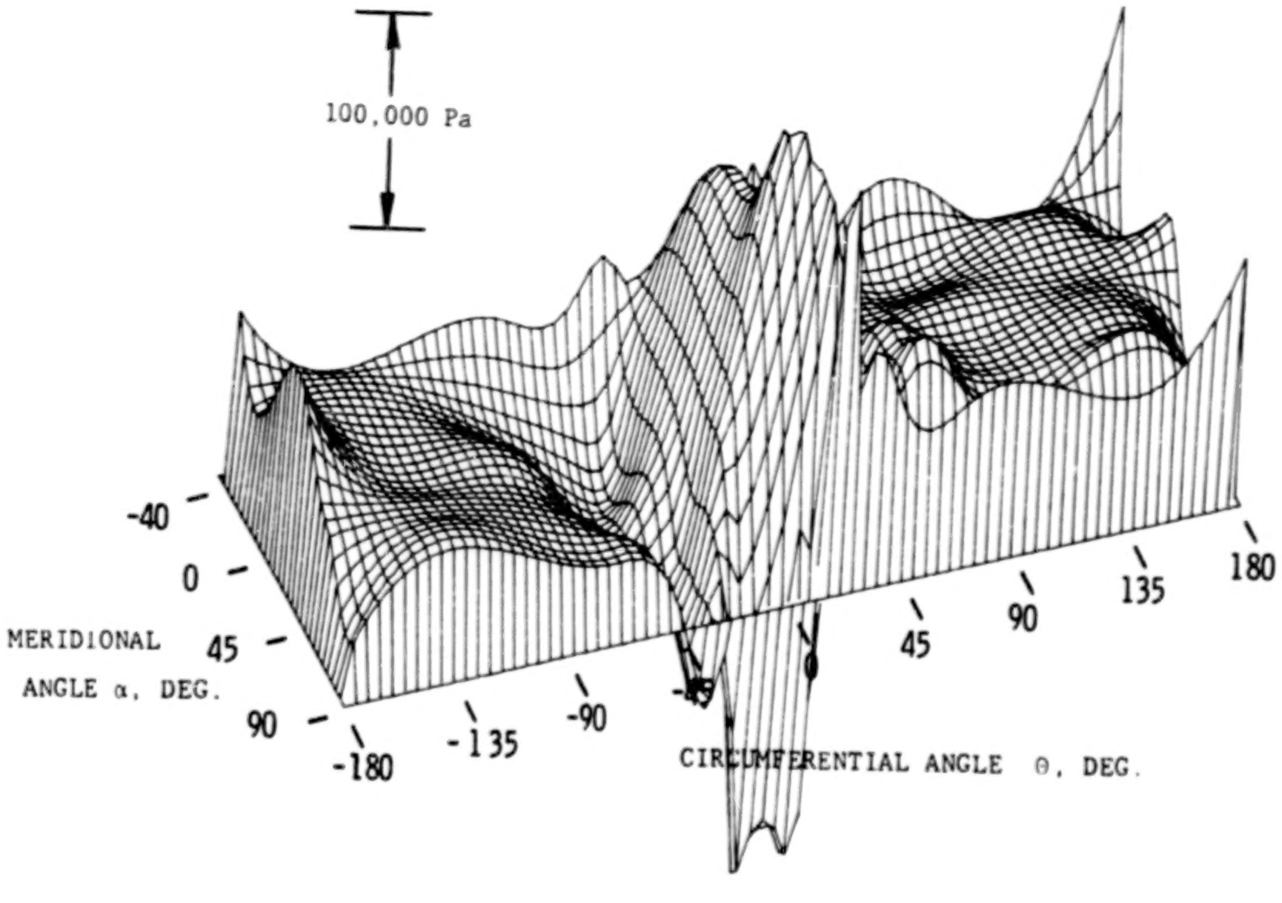

Figure 17

BEST DOCUMENT AVAILABLE

FINITE ELEMENT DISPLACEMENT RESULTS FOR INITIAL RUN OF SIX NODE CASE

In all the finite element work described thus far, the area of the footprint region was known beforehand from photographs taken on the test fixture of Figure 2. Nodes that were found to fall within the footprint area were then subjected to normal and tangential forces. In an attempt to eliminate the need to experimentally determine the contact area, a procedure was developed to start the iteration process described in Figure 10 by initially loading just six nodes centered about $\theta = 0°$ and $\alpha = 90°$. Theoretically, it should be possible to start with a single node, but it was decided that such a choice would only delay convergence to a final solution. The displacement results obtained when the full normal load of 70 N and the 80% tangential braking force were uniformly distributed over just six nodes are displayed in Figure 18. After spring rates were calculated for the six nodes and the first estimate of the common equilibrium position was determined, it was discovered that 102 nodes lay below Z_E. In the next run the total normal and tangential forces were evenly distributed over all 102 nodes. The next estimate of Z_E turned out to be considerably lower with only 83 nodes located below it. A second iteration reduced to 60 the number of nodes to be loaded. This corresponds to the number of nodes found experimentally to be within the footprint area for this particular load case. Three additional iterations were conducted to redistribute the forces by the method of Figure 10 in order to refine the flatness of the contact area.

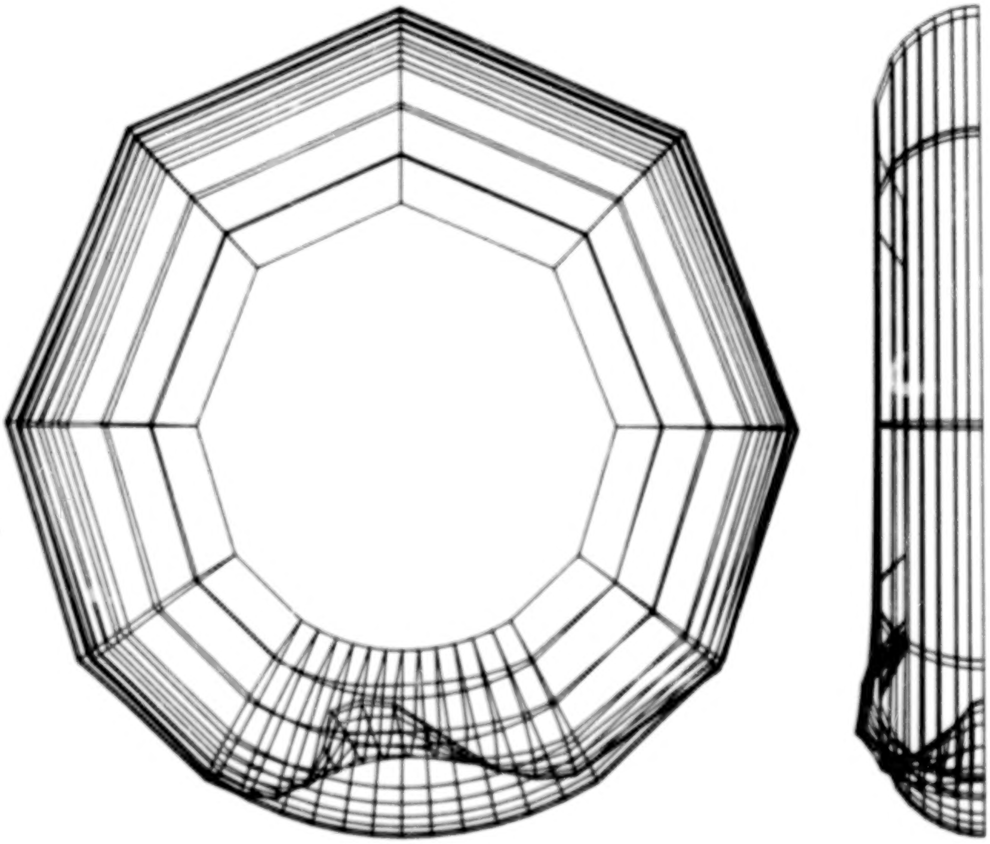

SIX NODE CASE, HALF TORUS, 70 N NORMAL, 80% TANGENTIAL, INITIAL RUN

Figure 18

FINITE ELEMENT DISPLACEMENT RESULTS FOR FINAL RUN OF SIX NODE CASE

The deformed geometry for the fifth iteration of the six node case is shown in Figure 19. Although not perfectly flat, the results are comparable to those of the final iteration depicted in Figure 12. While not included in this report, the final force distribution was also found to be very similar to that shown in Figure 13.

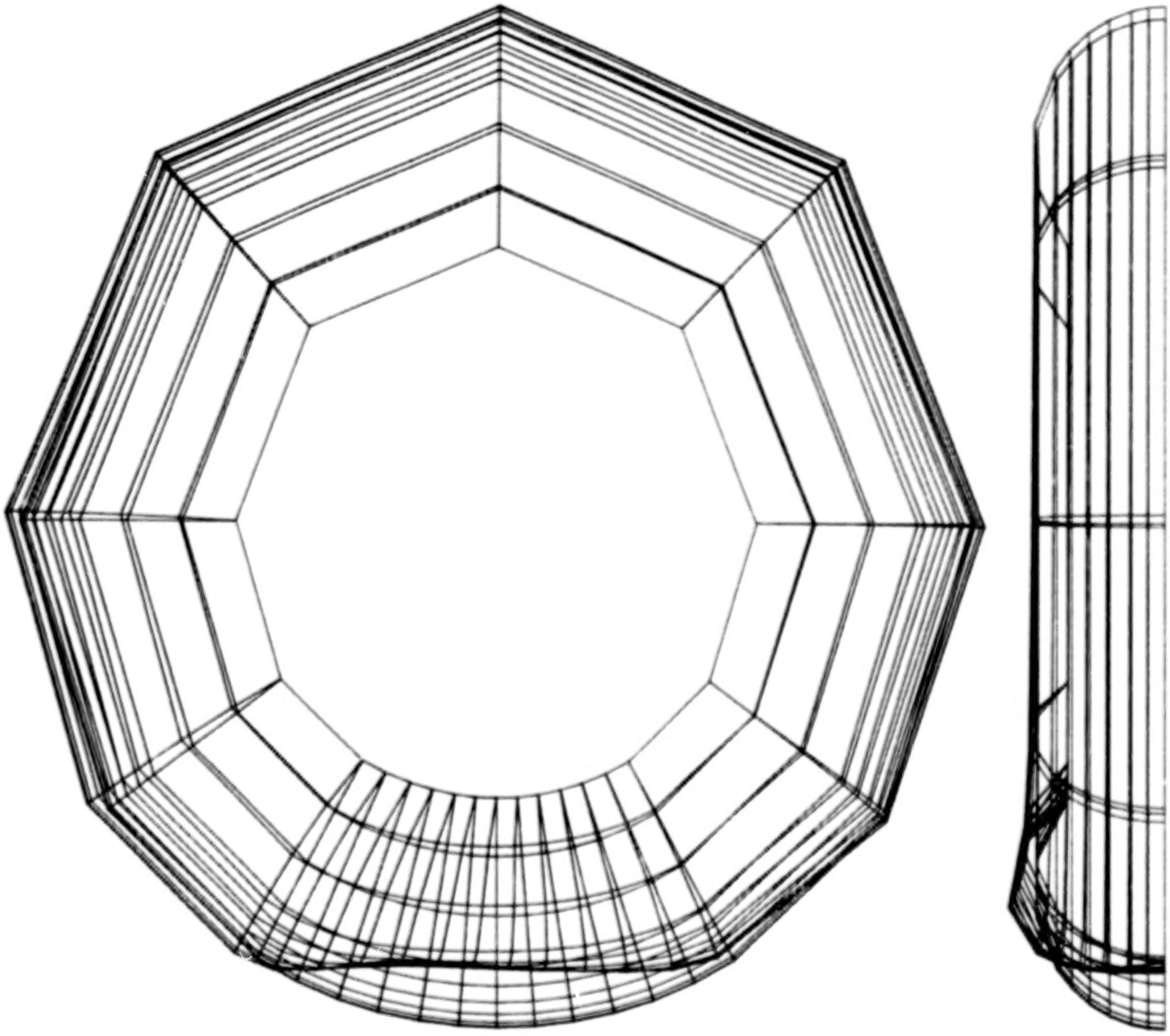

SIX NODE CASE, HALF TORUS, 70 N NORMAL, 80% TANGENTIAL, FINAL RUN

Figure 19

REFERENCES

1. Mack, M. J., Jr., "The Finite Element Analysis of an Inflated Toroidal Structure", M.S. Thesis, Dept. of Mechanical Engineering, Iowa State University, 1981.

OVERVIEW OF NASA TIRE EXPERIMENTAL PROGRAMS

John A. Tanner
NASA Langley Research Center

ABSTRACT

The experimental measurement of various tire properties is an important step in the tire modeling process. Some properties are needed to define the complex loading distributions that must be imposed on a tire model to simulate typical operational environments. Others, such as tire stresses and displacements resulting from various loading conditions, can be used to assess the accuracy of candidate finite element codes. In many cases these properties are used to establish the tire response characteristics which are useful in the simulation of operational problems and support the design of vehicle suspension systems and aircraft landing gear systems.

This paper reports on the interim results from a number of ongoing aircraft tire experimental programs. These programs are designed to measure profile growth due to inflation pressure and vertical loading, contact pressures in the tire footprint, and a number of tire mechanical properties including spring, damping, and relaxation characteristics.

APPARATUS FOR TIRE PROFILE MEASUREMENTS

Profile growth measurements of a 40 x 14 aircraft tire for various inflation pressure and vertical loading combinations are under way using the equipment shown in figure 1. The tire is mounted in the tire vibration stand described in reference 1 and a pair of linear variable displacement transducers is connected to an x-y plotter to produce full scale profiles. Figure 2 is a close-up view of the tire showing the markings that were used to insure repeatable test results.

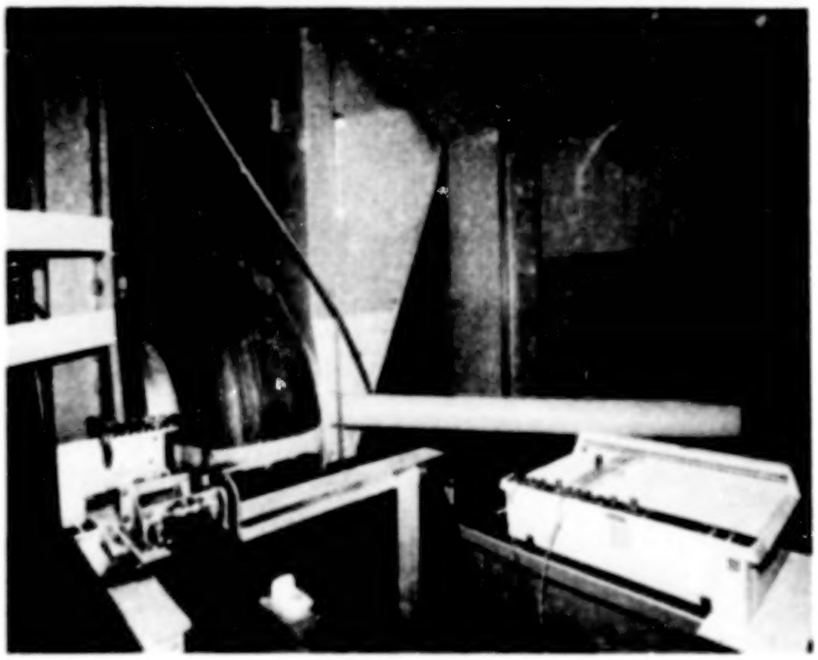

Figure 1

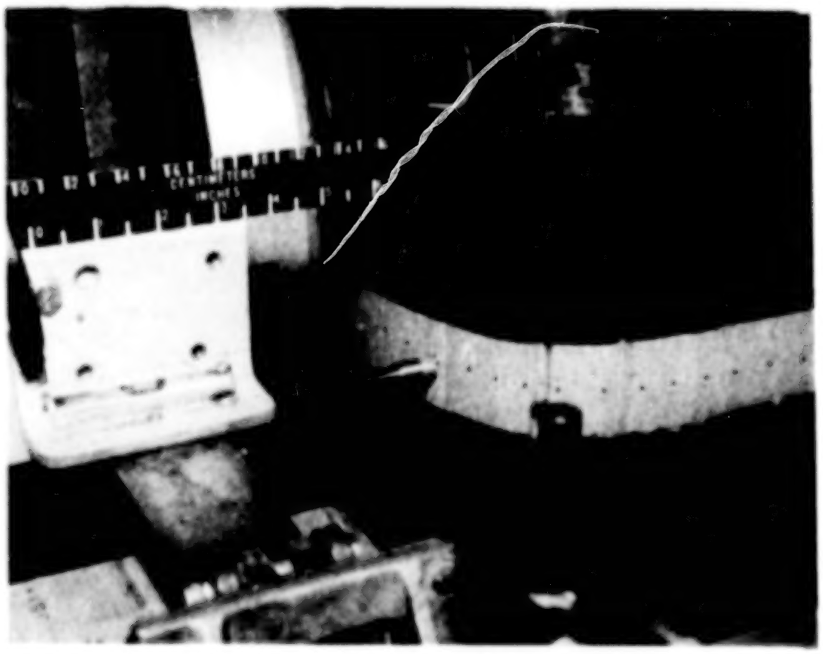

Figure 2

BEST DOCUMENT AVAILABLE

PROFILE GROWTH DUE TO INFLATION PRESSURE

Typical profile growth data for the 40 x 14 aircraft tire during inflation are presented in figure 3. For this particular test the tire was inflated to 1.17 MPa (170 psi) from an uninflated state and the arrows in the figure denote the direction of growth for selected points on the tire periphery. The profile growth involved both radial and tangential tire displacements. The tire inflation problem is axisymmetric and the tire displacements are symmetric about the tire equator.

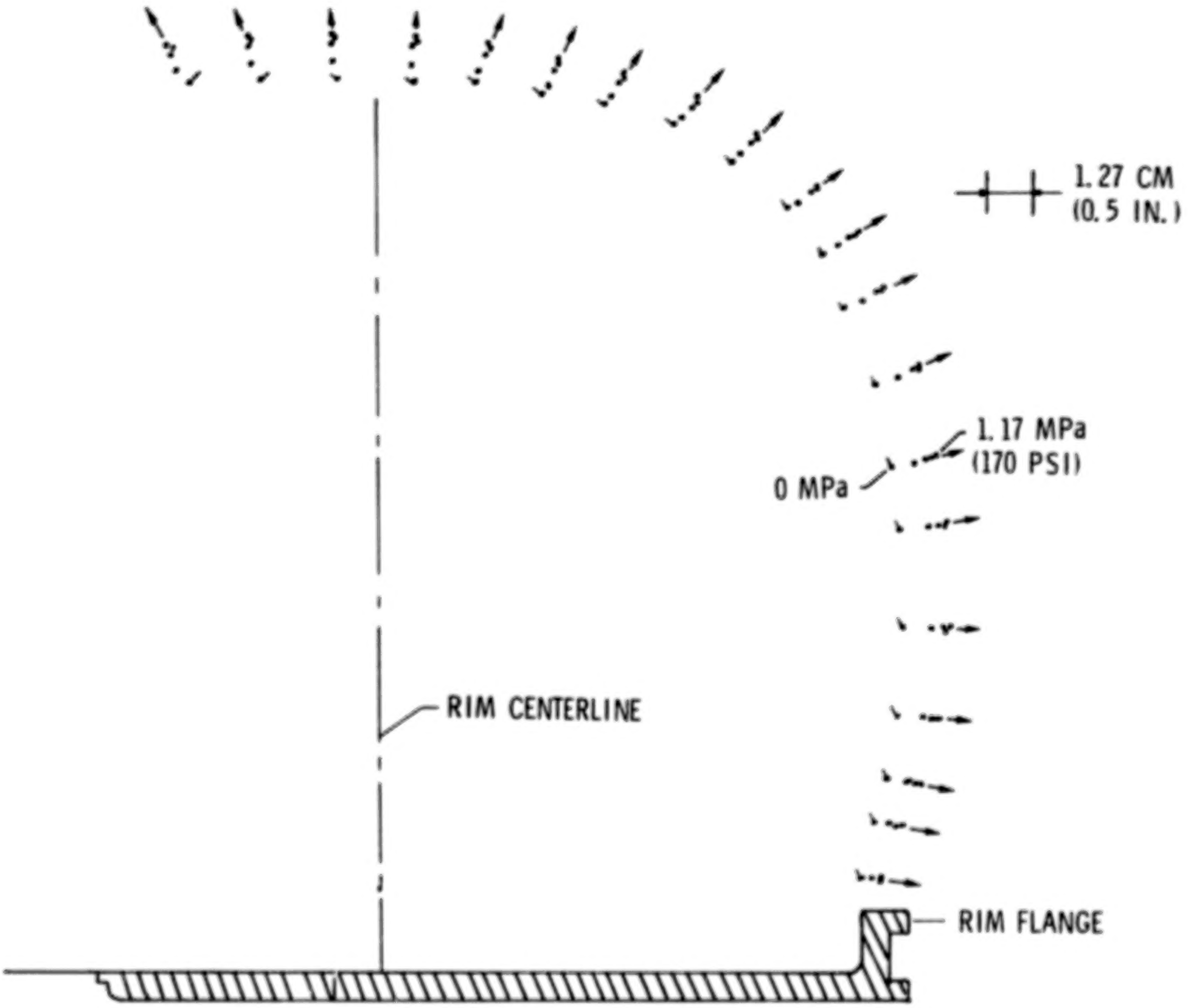

Figure 3

BEST DOCUMENT AVAILABLE

PROFILE GROWTH DUE TO COMBINED INFLATION PRESSURE AND VERTICAL LOADING

Typical growth measurements of a 40 x 14 aircraft tire for vertical loads ranging up to 89 kN (20 000 lbf) are presented in figure 4. For this test the inflation pressure was 1.07 MPa (155 psi) and the profile measurements were along a line which was displaced 5° from the contact centerline as shown in the sketch. The ground lines for each of the vertical loading conditions are also shown in the figure. The arrows again denote the direction of growth and in this case depict the growth of the sidewall bulge for increasing vertical load. The displacement data from these loading conditions should exhibit symmetry about the tire equator but the axial symmetry associated with the inflation process is now lost.

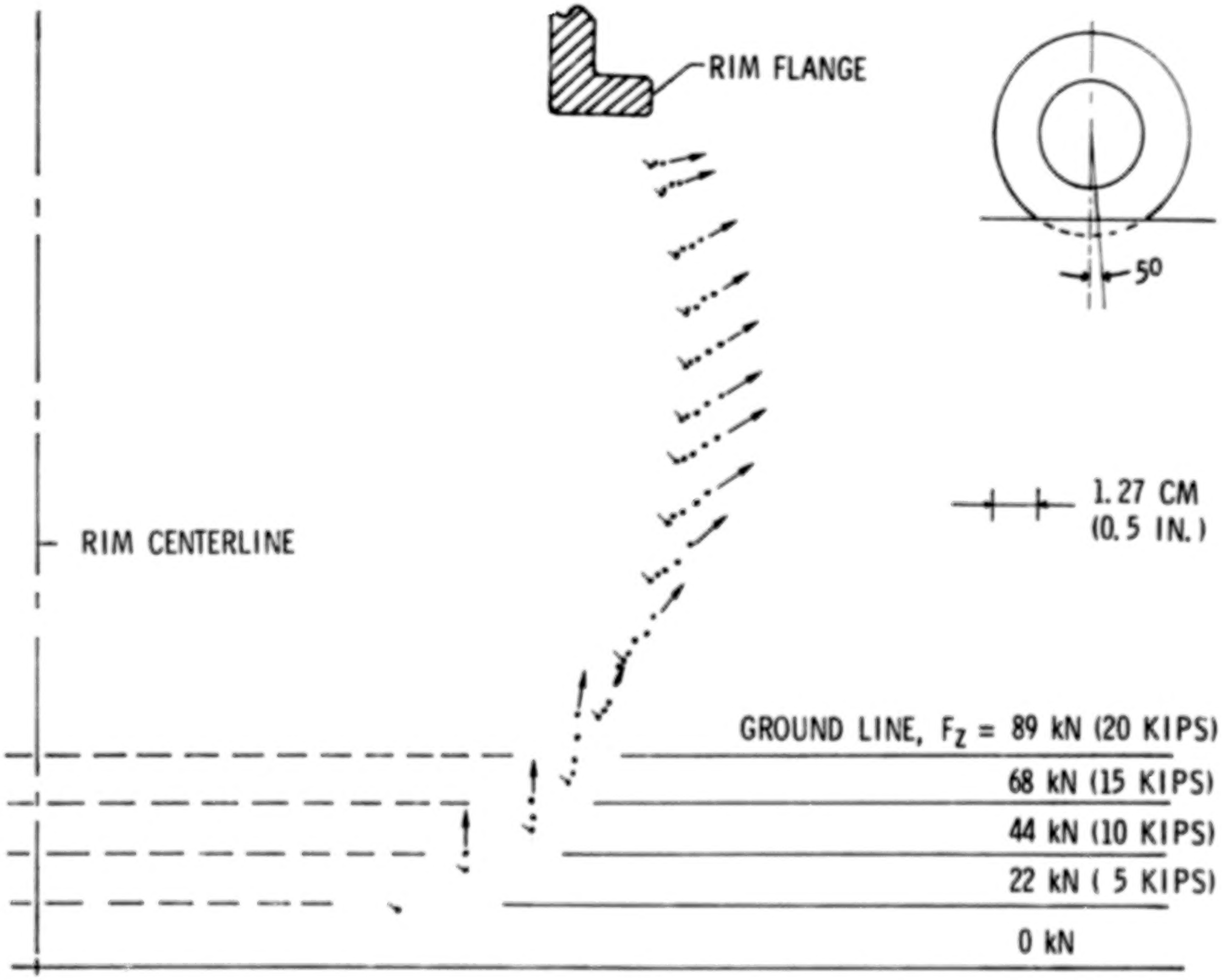

TIRE SIDEWALL DISPLACEMENT DUE TO VERTICAL LOAD, INFLATION PRESS., 1.07 MPa (155 PSI)

RIM FLANGE
5°
1.27 CM
(0.5 IN.)
RIM CENTERLINE
GROUND LINE, F_Z = 89 kN (20 KIPS)
68 kN (15 KIPS)
44 kN (10 KIPS)
22 kN (5 KIPS)
0 kN

Figure 4

TIRE FOOTPRINT

The forces and moments developed in the tire footprint must be modeled accurately to simulate the tire operational environment. Figure 5 is a typical footprint from a 40 x 14 aircraft tire inflated to 1.07 MPa (155 psi) and subjected to a vertical load of 89 kN (20 000 lbf). Instrumentation is currently under development to measure the pressure distribution and tangential friction force variation throughout the tire/surface contact region.

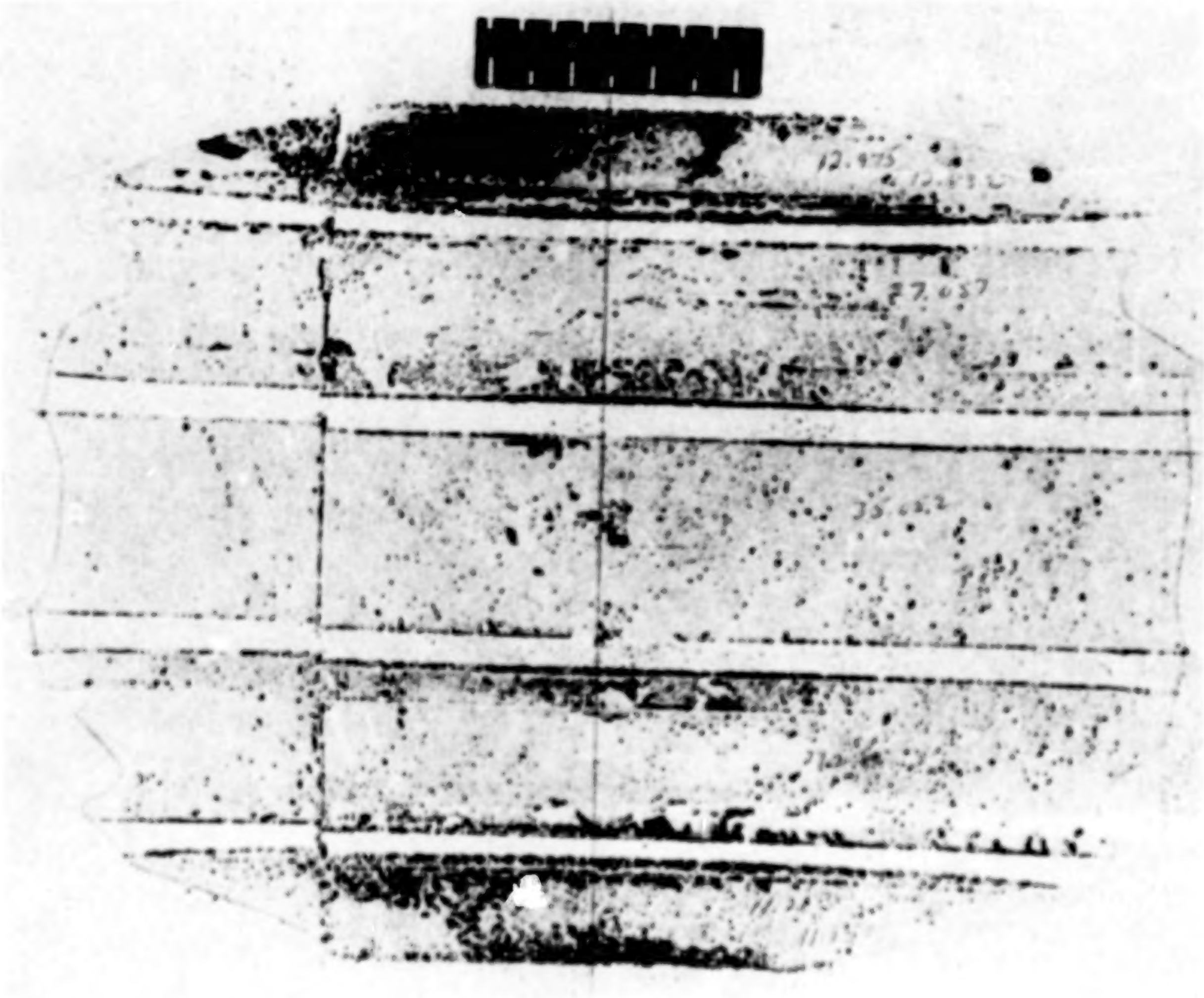

Figure 5

BEST DOCUMENT AVAILABLE

FOOTPRINT LENGTH

The length of the tire footprint L_f for two tire sizes is presented as a function of tire vertical deflection δ in figure 6 where both parameters have been nondimensionalized by the tire outside diameter d. The data for the two tire sizes can be faired in a least squares manner by a single-valued, nonlinear curve defined by the following expression (ref. 1),

$$L_f/d = 1.66\sqrt{(\delta/d) - (\delta/d)^2} \qquad (1)$$

This expression is similar to an expression in reference 2 for various type VII aircraft tires. Also included in the figure is the curve for the expression which defines the relationship between footprint length and vertical deflection if the tire is not distorted by the vertical load:

$$L_f/d = 2\sqrt{(\delta/d) - (\delta/d)^2} \qquad (2)$$

Without distortion the footprint length equals the length of the geometric chord formed by the intersection with the ground plane of a circle having a diameter equal to that of the tire. The data for both tires indicate that the footprint is about 83 percent of the geometric-chord length.

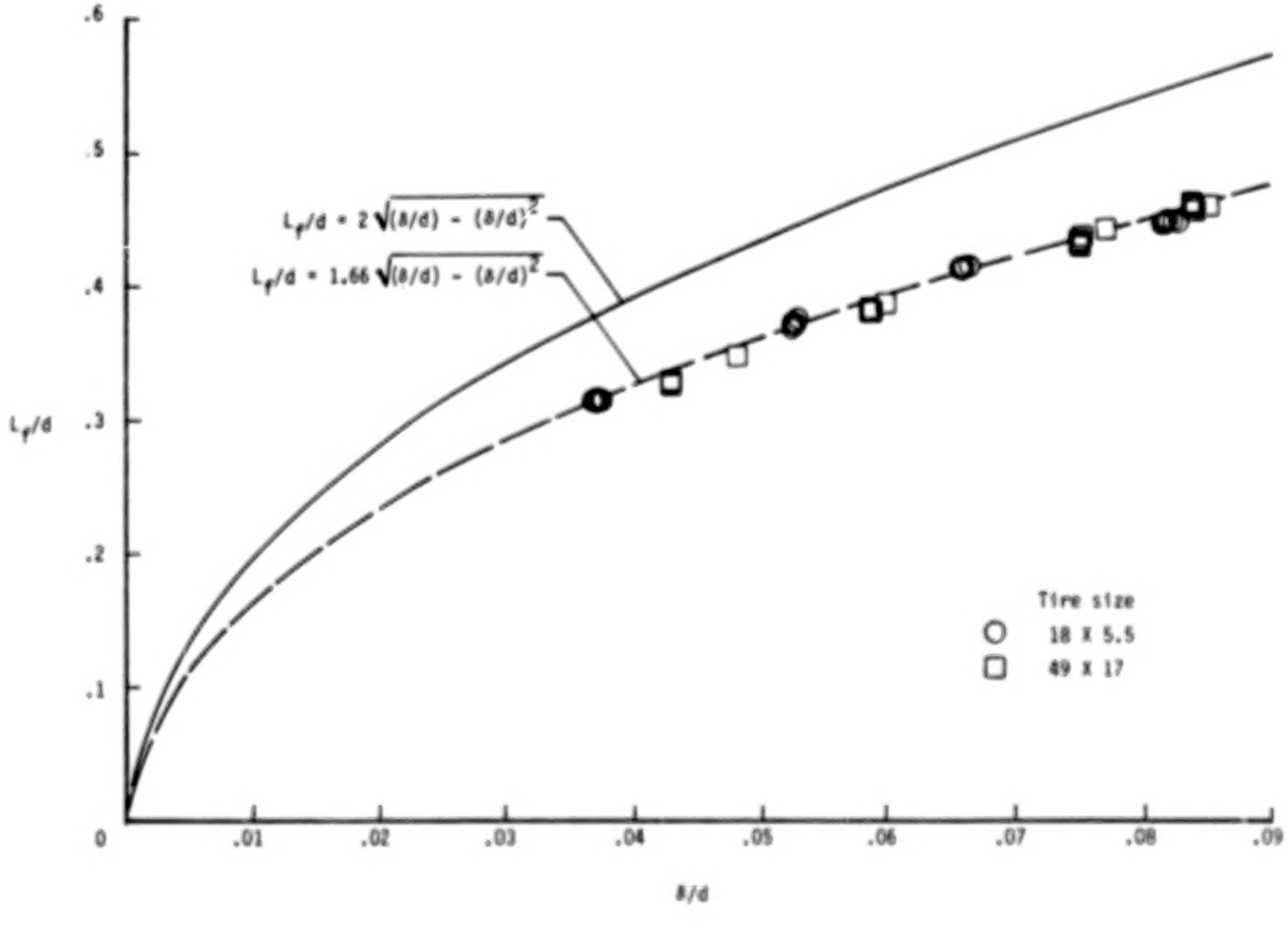

Figure 6

STATIC LOAD-DEFLECTION CHARACTERISTICS

Typical lateral load deflection curves for an aircraft tire are presented in figure 7. This family of curves was generated by varying the lateral load while holding the vertical load constant. For this test the lateral loading was decreased with each successive cycle as identified by the numbers in the figure which denote the loading sequence. The tire response to this loading condition is characterized by a number of large hysteresis loops. The area enclosed within each loop is a measure of dissipated energy or hysteresis loss and the slope of the load deflection curve is a measure of the tire spring characteristics. Similar load deflection curves can be generated in the vertical and fore and aft or braking directions to establish additional tire response characteristics.

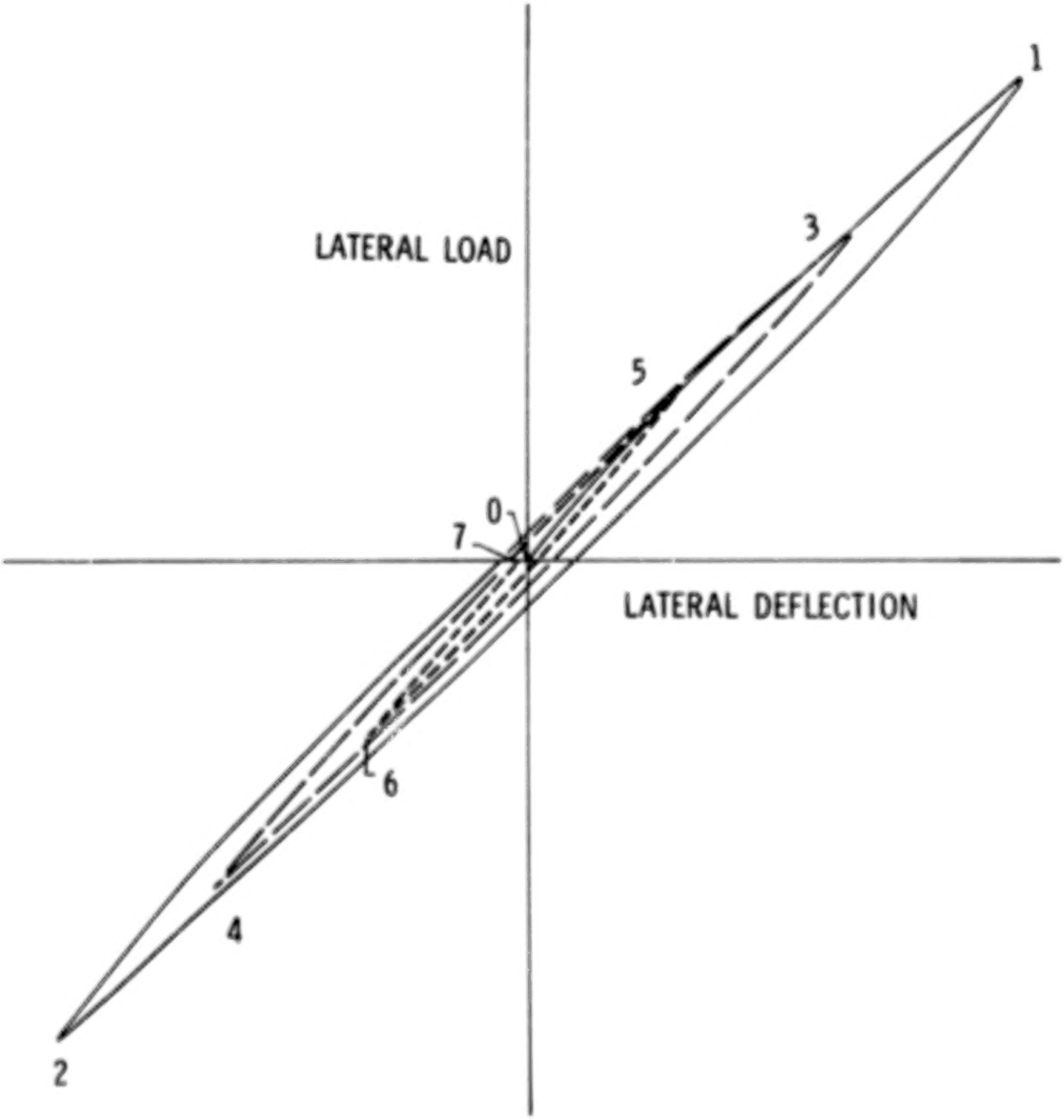

Figure 7

HYSTERESIS LOSS

The static lateral hysteresis loss of a tire can be obtained from load deflection curves such as that shown in figure 7 by measuring the area enclosed within the lateral loading and unloading cycle. Typical values of the lateral hysteresis loss ratio are plotted as a function of lateral load in figure 8. The lateral hysteresis loss ratio, the ratio of hysteresis loss to total energy input to the tire, is obtained by dividing the area within the hysteresis loop by the area under the load deflection curve including the hysteresis loop. The data in the figure indicate that increasing the lateral load increases the energy input lost to hysteresis, and the influence of vertical load is inconsequential.

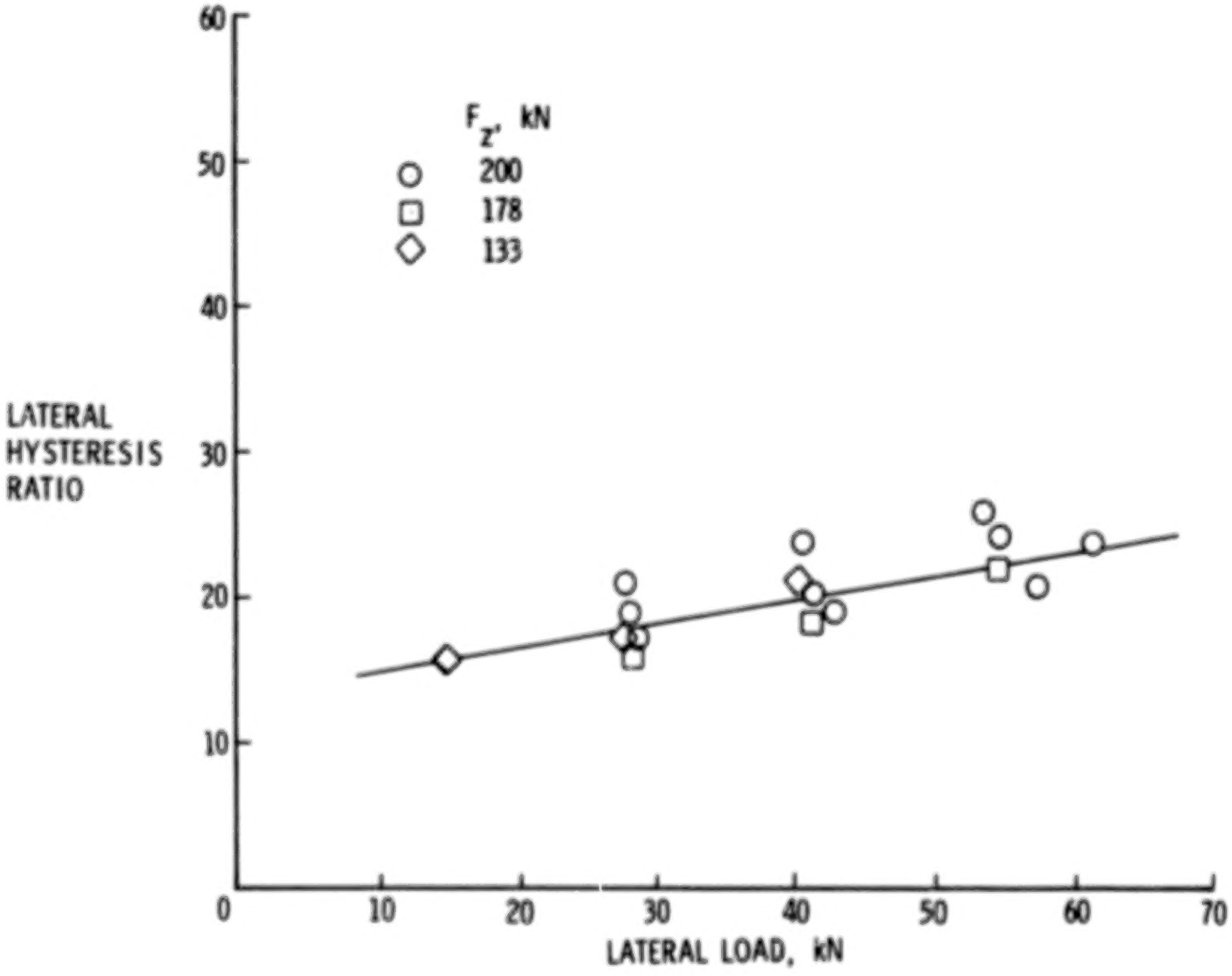

Figure 8

STATIC AND DYNAMIC LATERAL SPRING RATES

Typical tire lateral spring rates obtained from static and dynamic tests are plotted in figure 9 as a function of vertical load. As shown in the sketch, two spring rate values were obtained from the static tests. One spring rate corresponds to the linear portion of the load-deflection curve during load application and is denoted by the short dashed line in the figure. The other static spring rate approximates the slope of the load-deflection curve at initial load relief and is denoted by the long dashed line. These two static spring rates represent the lower and upper bounds for each vertical loading condition. The dynamic spring rates were determined from free vibration tests described in reference 3 and are denoted by the solid line. The data presented in the figure indicate that dynamic spring rates lie between the two bounds established by the static tests.

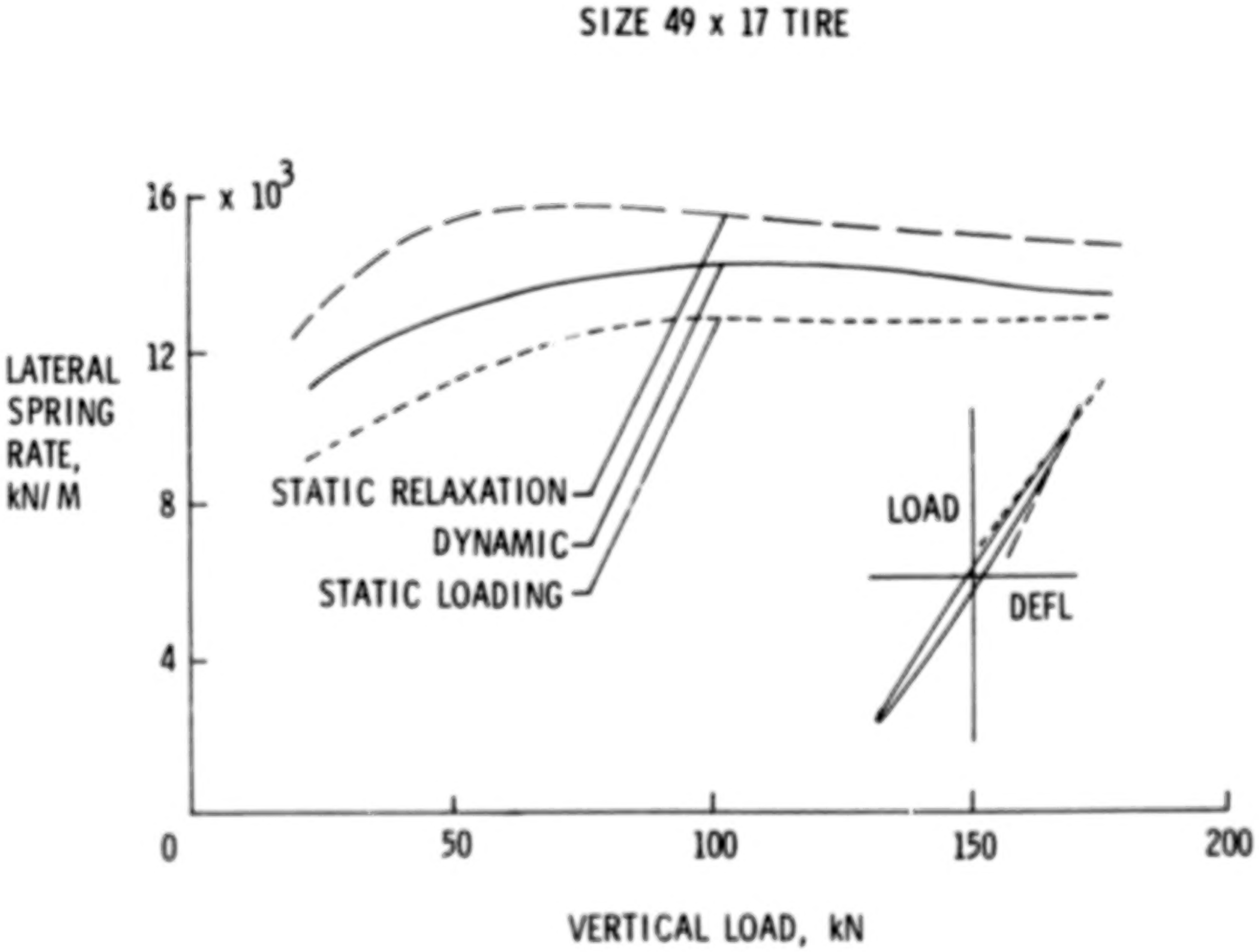

Figure 9

Another parameter available from static tests is the static relaxation length which is obtained from displacements of the tire equator at various angular positions around the circumference. Such measurements taken on a 49 x 17 aircraft tire under four combinations of vertical loading F_z and lateral loading F_y are presented in figure 10. Lateral deformation of the tire equator λ is plotted as a function of the tire peripheral angle θ measured from the footprint centerline. The lateral displacement of the free-tread periphery of the tire near the edge of the footprint varies exponentially with circumferential angular position and can be expressed in the following form:

$$\lambda = Ae^{-s/L_s} \tag{3}$$

where A is a constant, s is the circumferential distance from the footprint edge, and L_s is called the tire static relaxation length.

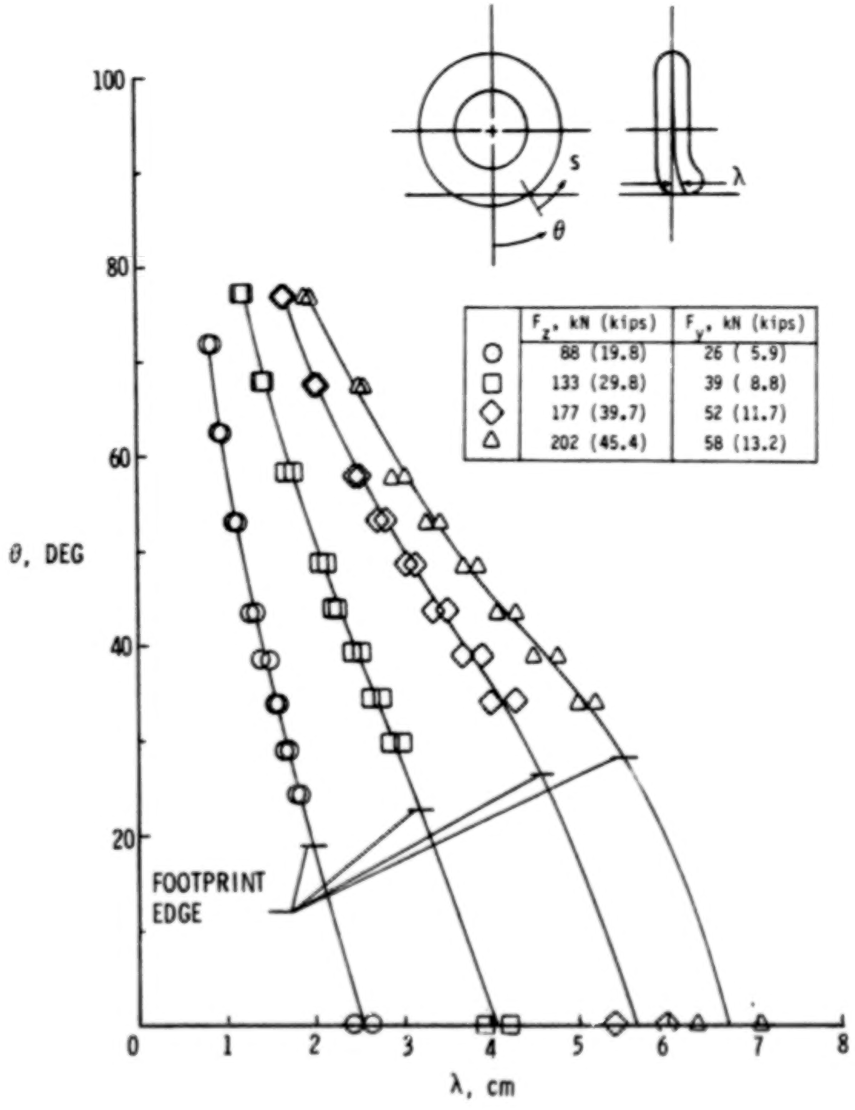

Figure 10

VARIATION OF STATIC RELAXATION LENGTH WITH VERTICAL DEFLECTION

Relaxation lengths computed from data such as that presented in figure 10 are plotted in figure 11 as a function of tire vertical deflection. Both parameters are nondimensionalized by the tire width w. Data from two tire sizes are presented and faired by separate linear curves. Relaxation lengths from both tires tend to decrease with increasing tire deflection.

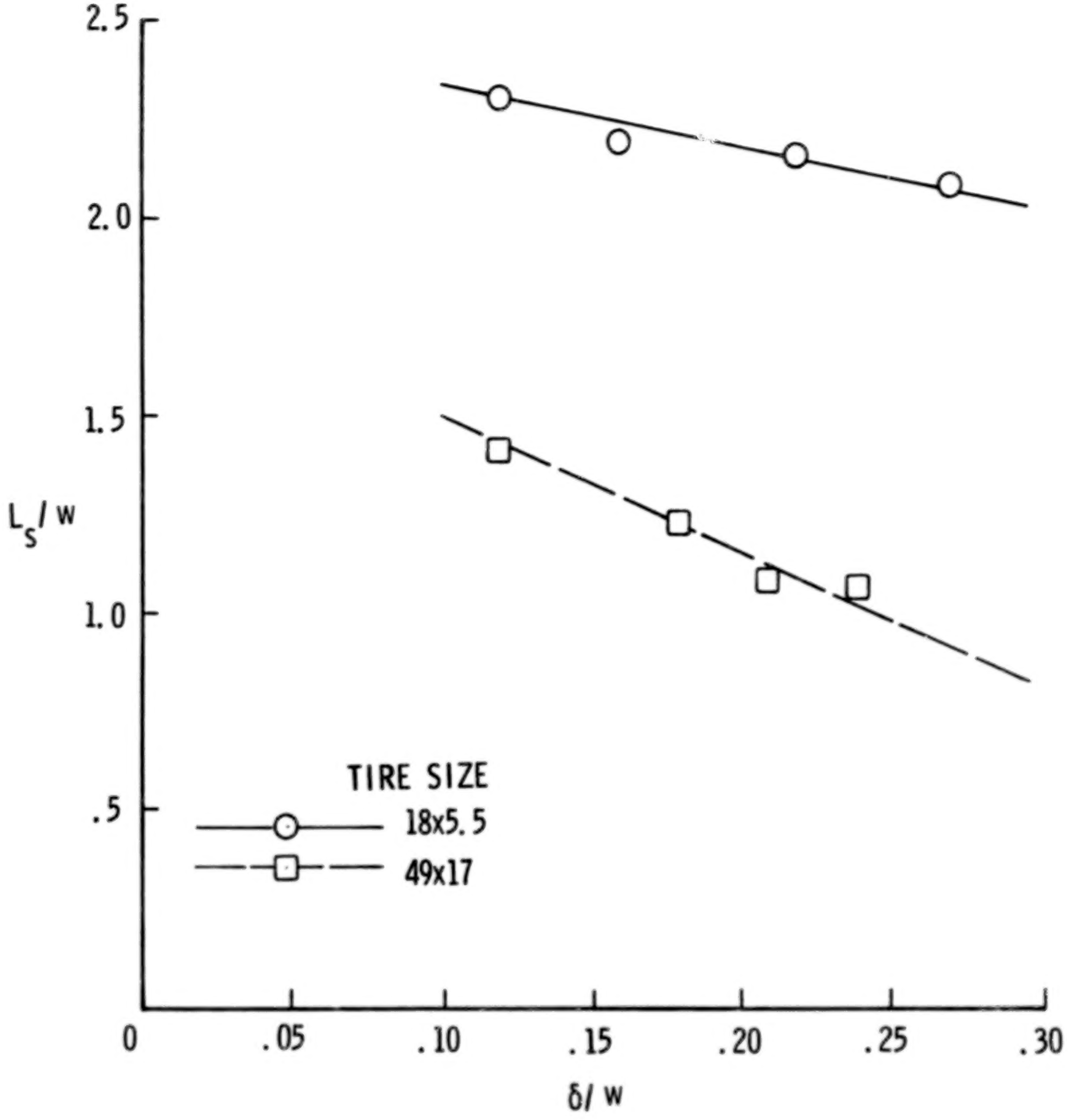

Figure 11

CONCLUDING REMARKS

Some of the data reviewed in this paper are typical of the experimental measurements necessary to verify the performance of tire analytical models and to establish footprint loading conditions for tire contact problems. Other data presented are used in defining tire spring and damping properties and the transient response characteristics necessary to model the tire's role as a component of a vehicular suspension system or an aircraft landing gear system. Experimental measurements of tire properties will continue to be an important step in the tire modeling process, regardless of the level of sophistication of the modeling technique.

REFERENCES

1. Tanner, John A.; Stubbs, Sandy M.; and McCarty, John L.: Static and Yawed-Rolling Mechanical Properties of Two Type VII Aircraft Tires. NASA TP-1863, 1981.

2. Smiley, Robert F.; and Horne, Walter B.: Mechanical Properties of Pneumatic Tires with Special Reference to Modern Aircraft Tires. NASA TR R-64, 1960.

3. Sleeper, Robert K.; and Dreher, Robert C.: Tire Stiffness and Damping Determined from Static and Free-Vibration Tests. NASA TP-1671, 1980.

ADHESION TESTING OF AIRCRAFT TIRES

Stephen N. Bobo
U.S. Department of Transportation
Transportation System Center

In December 1979 the FAA issued a new Technical Standard Order TSO-C62c to all users and manufacturers of aircraft tires. It was designed to upgrade the testing required to meet minimum airworthiness standards.

These changes to the testing requirements for new tires necessitated similar improved standards for retreads used in the national air carrier fleet.

Accordingly, an advisory circular (ref. 1) was prepared for comment which upgraded the testing standards for retreads to reflect the changes made in testing new tires under TSO-C62c. The advisory circular recommending the new dynamometer testing requirements called for testing every retread level of every tire size in an effort to accumulate sufficient tests and data to provide confidence that the retreading process including casing selection contained procedures which would provide for the continued airworthiness of the tires in service.

However, the number of tires to be tested to accumulate confidence would have presented an unacceptable and unrealistic cost to retreaders and their customers and an alternative approach was necessary.

For many years tire manufacturers and retreaders have been using laboratory adhesion tests as means for determining the effectiveness of the vulcanizing process in adhering the various tire components to one another. Adhesion testing appeared to offer a less burdensome alternative to replace some of the dynamometer tests recommended in the AC. Accordingly, test results and data were requested from retreaders who had used adhesion testing.

All of the American retreaders of aircraft tires submitted data, as did Goodyear, which obtained additional data from European adhesion tests. For some tires the Navy has required adhesion tests as a part of their purchasing procedure and this data was also made available. Such data was collected from various sources for over 700 tires, both commercial and military.

In meetings with industry, the FAA was presented with the industry consensus regarding the use of ply and tread adhesion tests to qualify tire retreading process specifications. The FAA has accepted this means of testing as one which can be used in the qualification of a tire retreading process specification.

The adhesion testing procedure used by most retreaders was a modification of the Hascar-Reiger method (ref. 2) in which a 1" strip of rubber is slit and introduced into a tensilometer. Variations of this method are described in references 1 and 3 to 6.

Figure 1 gives an example of the output from an adhesion test. The data is subject to wide variations in interpretation because of the stress-tear-relaxation characteristic of the rubber sample. Several methods of reporting the data have been adopted, including averaging all maximum values, averaging all minimum values and taking the mean of the maximum and minimum average values. The reporting sources usually list the method of recording and this is so noted in the data. Several other variations in method account for variations in test results, the three most important of which relate to sample preparation. Some laboratories attempt to cut the sample to the exact dimension, others correct for errors in size by normalizing the cut dimension to 25.4 mm (1 in.) width. Some laboratories cut the sample approximately 3.2 mm (1/8 in.) oversize and using a razor blade slit the intended path of travel of the tear line around the edge of the sample.

Several individuals have reported high values of adhesion when excess sample rubber thickness is not cut away, however laboratories as a rule do nothing to alter the thickness of the sample.

The location of the tear region varies depending upon the agency requesting the testing, and when it is known this information has been included in the data. Most organizations have reported buffline adhesion data, although some have reported maximum rather than average results.

Some organizations have reported adhesion data from the outside of the outer ply while some have reported between the second and third ply. Since there was no statistically detectable difference between these reported values they were lumped in the data.

The data was tabulated and placed in a data base called BANK (ref. 7). The fields are described in a listing. Most of the data on buffline adhesion is taken from TAV although TMX contains some buffline data. These two fields were separated because of uncertainty about the method of reading the primary recorder traces.

PAV gives values of outer ply adhesion. Some readings of maximum and minimum adhesion averages were available and these were recorded as PMX and PMN. Tire size is structured so that mathematical transformations such as linear regression or rank order correlation can be performed on the size variable.

Other information, such as R level, durometer tensile, and elongation measurements, is included where a sufficient amount of data was obtained.

The BANK program provides an interesting first level statistic printout of the data in each field (Figures 2 through 13). These include mean, standard deviation, and maximum and minimum values, as well as a data histogram.

In order to use simplified procedures for establishing minimum adhesion thresholds and realistic test sample sizes it is important to confirm the character of the distribution of the data. This may be accomplished by analysis of the data in terms of the probability that it fits on a normal distribution curve (Figure 14).

Figure 15 is a scatter plot of the probability that any given sample will lie below a given value, against ordinal value. To the extent that this plot is a straight line the distribution is normal. If the plot deviates greatly from a straight line the data does not have normal distribution. It may be seen that the plot in Figure 15 is a relatively straight line. A surer test is to use the log of probability and the log of the order value (Figure 16). This is useful to test the values lying in the skirts of the distribution curve. Since there is always a small number of data points in the region of the lower adhesion values, the use of the log plot highlights any abnormality of these values.

Our analysis of these data have allowed us to conclude that the data is fairly normally distributed and can therefore be used to establish criteria for minimum threshold levels based on normal distribution. These criteria have been determined using an algorithm giving the probability that any number R of adhesion values will fall below the n lowest values.

For the FAA we selected a test sample size of 20 tires and used the three lowest readings as the threshold criteria. Using the algorithm, we determined that, using values of 30, 33, and 36 for buffline adhesion and 20, 23, and 26 for ply adhesion, the probability that a retreader having good tires would fail the test was about fifteen percent. The probability of failing a retest was about 2%. One the other hand the probability of detection of a sample of tires having a mean less than the threshold values increases very rapidly to 98% at a value of 1 standard deviation away from the threshold mean (Figure 17).

Tread and ply adhesion values are a very good measure of tire production uniformity and can therefore be used as a monitor of quality during production in statistical QC devices such as control charts. The threshold values given represent tires taken from a fleet in which a very small number of tire related incidents have occurred. They can therefore be considered as representing a safe population of tires.

REFERENCES

1. Inspection, Retread, Repair, and Alterations of Aircraft Tires. Federal Aviation Advisory Circular AC 145-4, FAA, Sept. 1982.

2. Harscar, F. G.: Determination of Tire Components Adhesion. Test Engineering, November 1970, pp. 10-11.

3. Clark, S. K. (ed.): Mechanics of Pneumatic Tires. National Highway Traffic Safety Administration, U.S. Dept. of Transportation, 1981.

4. Adhesion to Flexible Substrate. ASTM D-413-76, 1981 Annual Book of ASTM Standards, p. 357.

5. Rebuilt Tire Aircraft Laboratory Quality Assurance Requirements, Military Standard MS3377. Paragraph 4.6.8, MIL-R-7726, Dept. of Defense, June 1975.

6. Standards for Retreading Aircraft Tires. Appendix 6, Association of European Airlines, Jan. 5, 1977.

7. Houchard, Richard: BANK DATA Management Package. Computer Center Library Program 3.9.1, Westerm Michigan Univ., Kalamazoo, Mich., Oct. 1974.

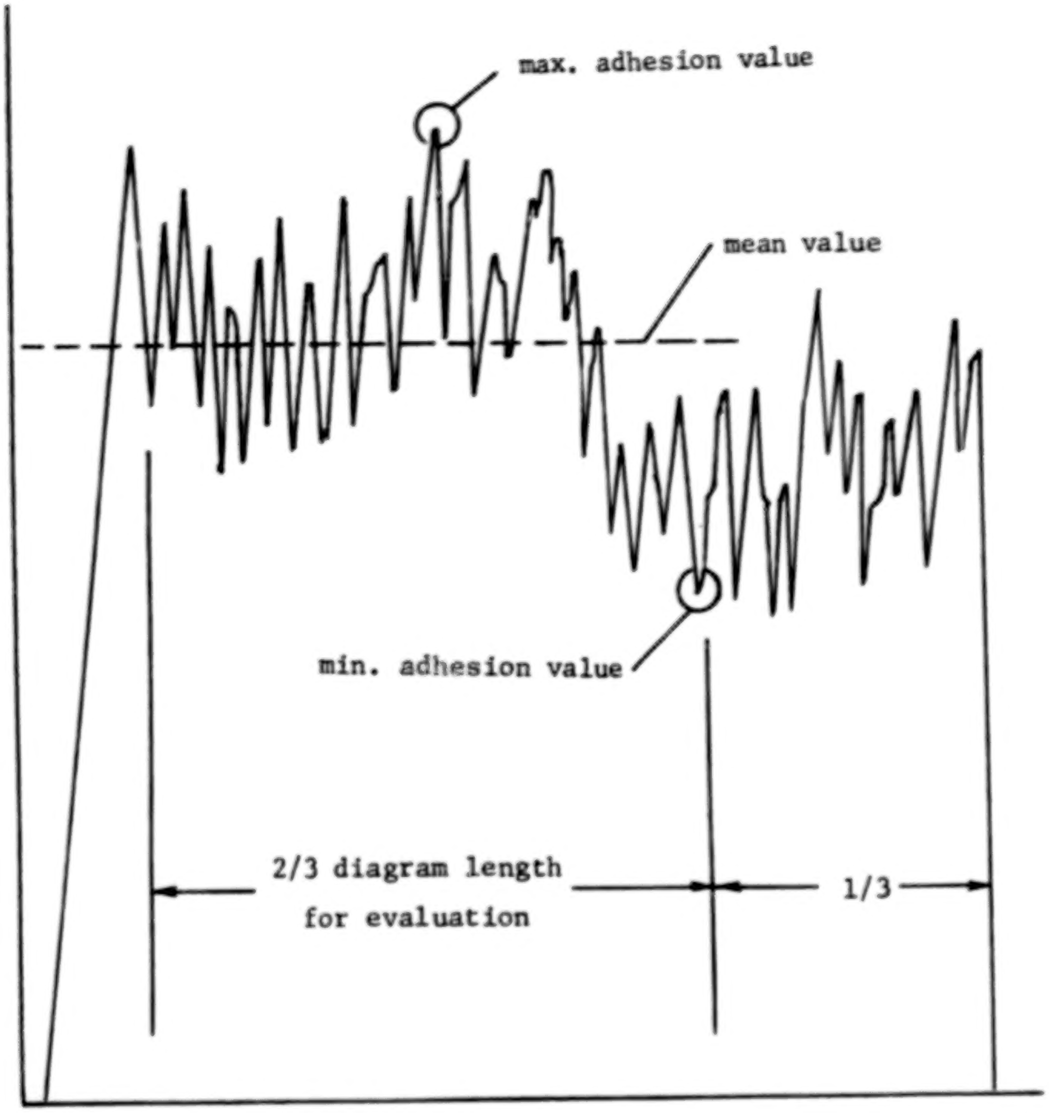
max. adhesion value
mean value
min. adhesion value
2/3 diagram length
for evaluation
1/3

Figure 1

```
VARIABLE: SIZE      NUMBER:     2      DESCRIPTION:                              VARIABLE TYPE: FLOAT
THERE WERE   706 OBSERVATIONS, WHICH INCLUDED  0 CASES OF MISSING DATA SELECTED FROM A TOTAL OF  706 OBSERVATIONS

SUM OF OBSERVATIONS =  23559.43               SUM OF OBSERVATIONS SQUARED =  838052.0    NUMBER OF OBSERVATIONS =
MEAN =  33.37030                              MEDIAN =  29.50750                         MODE =  24.55000
MAXIMUM =  56.16000                           MINIMUM =  20.20000                        RANGE =  35.96000
STANDARD ERROR OF MEAN =  0.3228110           STANDARD DEVIATION =  8.577303             VARIANCE =  73.57012
COEFFICIENT OF SKEWNESS =  0.5019920          COEFFICIENT OF VARIATION =  25.70341       KURTOSIS =  2.321392


                                                                 CUMULATIVE
VALUE                          FREQUENCY      PERCENTAGE         PERCENTAGE

20.20000                              1          0.142             0.142
20.55000                              9          1.275             1.416
22.55000                             50          7.082             8.499
24.55000                            139         19.688            28.187
26.66000                             17          2.408            30.595
28.77000                             72         10.198            40.793
28.90000                             65          9.207            50.000
30.11500                             14          1.983            51.983
36.11000                             94         13.314            65.297
37.11500                              8          1.133            66.431
40.14000                            129         18.272            84.703
41.15000                             10          1.416            86.119
44.13000                             18          2.550            88.669
44.16000                              8          1.133            89.802
46.14000                              2          0.283            90.085
46.16000                             23          3.258            93.343
47.18000                              1          0.142            93.484
49.17000                             26          3.683            97.167
50.20000                              3          0.425            97.592
52.20000                              6          0.850            98.442
56.16000                             11          1.558           100.000
                               --------
                                    706


          5.0       10.0      15.0      20.0      25.0
+---------+---------+---------+---------+---------+
I
IXXX
IXXXXXXXXXXXXXX
IXXXXXXXXXXXXXXXXXXXXXXXXXXXXXXXXXXXXXXX
IXXXXX
IXXXXXXXXXXXXXXXXXXXX
IXXXXXXXXXXXXXXXXXX
IXXXX
IXXXXXXXXXXXXXXXXXXXXXXXXXXX
IXX
IXXXXXXXXXXXXXXXXXXXXXXXXXXXXXXXXXXXXX
IXXX
IXXXXX
IXX
IX
IXXXXXXX
I
IXXXXXXX
IX
IXX
IXXX
+---------+---------+---------+---------+---------+
          5.0       10.0      15.0      20.0      25.0
```

Figure 2

```
VARIABLE:  RL      NUMBER:    3      DESCRIPTION:  R LEVEL                      VARIABLE TYPE: FIXED
THERE WERE  706 OBSERVATIONS, WHICH INCLUDED      623 CASES OF MISSING DATA SELECTED FROM A TOTAL  706 OBSERVATIONS

SUM OF OBSERVATIONS =  269.00                   SUM OF OBSERVATIONS SQUARED =  1201.000   NUMBER OF OBSERVATIONS =
MEAN =  3.240964                                MEDIAN =  3.000000                        MODE =  24.55000
MAXIMUM =  12                                   MINIMUM =  1                              RANGE =  35.96000
STANDARD ERROR OF MEAN = 0.2199233              STANDARD DEVIATION =  2.003597            VARIANCE =  73.57012
COEFFICIENT OF SKEWNESS =  1.395565             COEFFICIENT OF VARIATION =  61.82101      KURTOSIS =  2.321392


                                                                    CUMULATIVE
       VALUE                        FREQUENCY      PERCENTAGE       PERCENTAGE


         1                              19           22.892           22.892
         2                              13           15.663           38.554
         3                              17           20.482           59.036
         4                              16           19.277           78.313
         5                              11           13.253           91.566
         6                               3            3.614           95.181
         7                               1            1.205           96.386
         8                               1            1.205           97.590
         9                               1            1.205           98.795
        12                               1            1.205          100.000
                                    ------
                                        83




                     5.0       10.0      15.0      20.0      25.0
           +---------+---------+---------+---------+---------+
           IXXXXXXXXXXXXXXXXXXXXXXXXXXXXXXXXXXXXXXXXXXXXXX
           IXXXXXXXXXXXXXXXXXXXXXXXXXXXXXXX
           IXXXXXXXXXXXXXXXXXXXXXXXXXXXXXXXXXXXXXXXXX
           IXXXXXXXXXXXXXXXXXXXXXXXXXXXXXXXXXXXXXXX
           IXXXXXXXXXXXXXXXXXXXXXXXXXXX
           IXXXXXXX
           IXX
           IXX
           IXX
           IXX
           +---------+---------+---------+---------+---------+
                     5.0       10.0      15.0      20.0      25.0
```

Figure 3

```
VARIABLE:  MFG      NUMBER:    4       DESCRIPTION:  MANUFACTURER          VARIABLE TYPE:  ALPHA
THERE WERE   706 OBSERVATIONS, WHICH INCLUDED  430 CASES OF MISSING DATA SELECTED FROM A TOTAL OF  706 OBSERVATIONS

MAXIMUM =  TMS                            MINIMUM = AIR




                                                                      CUMULATIVE
        VALUE                        FREQUENCY    PERCENTAGE          PERCENTAGE

        AIR                              143          51.812           51.812
        BFG                               34          12.319           64.130
        BRS                                4           1.449           65.580
        DLP                                7           2.536           68.116
        F                                  5           1.812           69.928
        GYR                               36          13.043           82.971
        KC                                 6           2.174           85.145
        TMS                               41          14.855          100.000
                                    --------
                                         276




                                   15.0      30.0      45.0      60.0      75.0
                           +---------+---------+---------+---------+---------+
                           IXXXXXXXXXXXXXXXXXXXXXXXXXXXXXXXXXXX
                           IXXXXXXXX
                           IX
                           IXX
                           IX
                           IXXXXXXXXX
                           IX
                           IXXXXXXXXXX
                           +---------+---------+---------+---------+---------+
                                   15.0      30.0      45.0      60.0      75.0
```

Figure 4

```
VARIABLE:  TMX     NUMBER:    5     DESCRIPTION:  MAX TREAD ADHSN       VARIABLE TYPE:  FIXED
THERE WERE   706 OBSERVATIONS, WHICH INCLUDED   563 CASES OF MISSING DATA SELECTED FROM A TOTAL OF 706 OBSERVATIONS

SUM OF OBSERVATIONS =  12289.00           SUM OF OBSERVATIONS SQUARED =  1114039.     NUMBER OF OBSERVATIONS =
MEAN =  85.93706                          MEDIAN =  82.00000                          MODE =  80
MAXIMUM =  143                            MINIMUM =  50                               RANGE =  93
STANDARD ERROR OF MEAN =  1.689453        STANDARD DEVIATION =  20.20292              VARIANCE =  408.1580
COEFFICIENT OF SKEWNESS =  0.5453779      COEFFICIENT OF VARIATION =  23.50897        KURTOSIS =  2.987374


                                                                     CUMULATIVE
     VALUE                          FREQUENCY       PERCENTAGE       PERCENTAGE

      50 -         53                    5            3.497              3.497
      54 -         57                    3        [illegible]            5.594
      58 -         61                    6            4.196              9.790
      62 -         65                    7            4.895             14.685
      66 -         69                   12            8.392             23.077
      70 -         73                    7            4.895             27.972
      74 -         77                   11            7.692             35.664
      78 -         81                   18           12.587             48.252
      82 -         85                   10            6.993             55.245
      86 -         89                   11            7.692             62.937
      90 -         93                    7            4.895             67.832
      94 -         97                    5            3.497             71.329
      98 -        101                   10            6.993             78.322
     102 -        105                    9            6.294             84.615
     106 -        109                    5            3.497             88.112
     110 -        113                    4            2.797             90.909
     114 -        117                    2            1.399             92.308
     118 -        121                    2            1.399             93.706
     122 -        125                    1            0.699             94.406
     126 -        129                    3            2.098             96.503
     130 -        133                    1            0.699             97.203
     134 -        137                    3            2.098             99.301
     138 -        141                    0            0.000             99.301
     142 -        145                    1            0.699            100.000
                                  -------
                                       143


        5.0       10.0      15.0      20.0      25.0
+---------+---------+---------+---------+---------+
IXXXXXXX
IXXXX
IXXXXXXXX
IXXXXXXXXXX
IXXXXXXXXXXXXXXXXX
IXXXXXXXXXX
IXXXXXXXXXXXXXXX
IXXXXXXXXXXXXXXXXXXXXXXXXX
IXXXXXXXXXXXXXX
IXXXXXXXXXXXXXXX
IXXXXXXXXXX
IXXXXXXX
IXXXXXXXXXXXXXX
IXXXXXXXXXXXXX
IXXXXXXX
IXXXXXX
IXXX
IXX
IX
IXXXX
IX
IXXXX
I
IX
+---------+---------+---------+---------+---------+
        5.0       10.0      15.0      20.0      25.0
```

Figure 5

```
VARIABLE:  TAV     NUMBER:     7      DESCRIPTION:  AVERAGE TREAD ADHSN   VARIABLE TYPE: FIXED
THERE WERE   706 OBSERVATIONS,  WHICH INCLUDED   213 CASES OF MISSING DATA SELECTED FROM A TOTAL OF
SUM OF OBSERVATIONS =  41810.00               SUM OF OBSERVATIONS SQUARED =  3771346.   706 OBSERVATIONS
MEAN =  84.80730                              MEDIAN =  85.00000
MAXIMUM =  149                                MINIMUM =  20                            NUMBER OF OBSERVATIONS =
STANDARD ERROR OF MEAN =  0.9643130           STANDARD DEVIATION =  21.41122           MODE =  90
COEFFICIENT OF SKEWNESS =  0.6466109E-01      COEFFICIENT OF VARIATION =  25.24691     RANGE =  129
                                                                                       VARIANCE =  458.4405
                                                                                       KURTOSIS =  2.747826


                                                                 CUMULATIVE
      VALUE                        FREQUENCY     PERCENTAGE      PERCENTAGE

       20 -      25                    2           0.406           0.406
       26 -      31                    0           0.000           0.406
       32 -      37                    0           0.000           0.406
       38 -      43                    7           1.420           1.826
       44 -      49                    8           1.623           3.448
       50 -      55                   26           5.274           8.722
       56 -      61                   34           6.897          15.619
       62 -      67                   34           6.897          22.515
       68 -      73                   44           8.925          31.440
       74 -      79                   38           7.708          39.148
       80 -      85                   60          12.170          51.318
       86 -      91                   52          10.548          61.866
       92 -      97                   50          10.142          72.008
       98 -     103                   38           7.708          79.716
      104 -     109                   35           7.099          86.815
      110 -     115                   29           5.882          92.698
      116 -     121                   19           3.854          96.552
      122 -     127                    3           0.609          97.160
      128 -     133                    7           1.420          98.580
      134       139                    4           0.811          99.391
      140 -     145                    2           0.406          99.797
      146 -     151                    1           0.203         100.000
                                  ------
                                     493
```

```
          5.0       10.0      15.0      20.0      25.0
+---------+---------+---------+--------->---------+
IX
I
I
IXXX
IXXX
IXXXXXXXXXXX
IXXXXXXXXXXXXXX
IXXXXXXXXXXXXXX
IXXXXXXXXXXXXXXXXXX
IXXXXXXXXXXXXXXX
IXXXXXXXXXXXXXXXXXXXXXXXX
IXXXXXXXXXXXXXXXXXXXXX
IXXXXXXXXXXXXXXXXXXXX
IXXXXXXXXXXXXXXX
IXXXXXXXXXXXXXX
IXXXXXXXXXXXX
IXXXXXXXX
IX
IXXX
IXX
IX
I
+---------+---------+---------+---------+-- ------+
          5.0       10.0      15.0      20.0      25.0
```

Figure 6

```
VARIABLE:   PMX     NUMBER:   8      DESCRIPTION:  MAX PLY ADHSN          VARIABLE TYPE: FIXED
THERE WERE    706 OBSERVATIONS, WHICH INCLUDED   538 CASES OF MISSING DATA SELECTED FROM A TOTAL  OF
                                                                                         706 OBSERVATIONS
SUM OF OBSERVATIONS =  6691.000                  SUM OF OBSERVATIONS SQUARED =  280465.0
MEAN =  39.82738                                 MEDIAN =  38.00000                   NUMBER OF OBSERVATIONS =
MAXIMUM =  73                                    MINIMUM =  26                        MODE =  39
STANDARD ERROR OF MEAN =  0.7058958              STANDARD DEVIATION =  9.149456       RANGE =  47
COEFFICIENT OF SKEWNESS =  1.399312              COEFFICIENT OF VARIATION =  22.97278 VARIANCE =  83.71254
                                                                                      KURTOSIS =  5.195022


                                                                   CUMULATIVE
        VALUE                          FREQUENCY     PERCENTAGE    PERCENTAGE

         26 -       27                        5         2.976          2.976
         28 -       29                        6         3.571          6.548
         30 -       31                       12         7.143         13.690
         32 -       33                       15         8.929         22.619
         34 -       35                       20        11.905         34.524
         36 -       37                       20        11.905         46.429
         38 -       39                       23        13.690         60.119
         40 -       41                       13         7.738         67.857
         42 -       43                       14         8.333         76.190
         44 -       45                        9         5.357         81.548
         46 -       47                        8         4.762         86.310
         48 -       49                        3         1.786         88.095
         50 -       51                        2         1.190         89.286
         52 -       53                        4         2.381         91.667
         54 -       55                        0         0.000         91.667
         56 -       57                        3         1.786         93.452
         58 -       59                        3         1.786         95.238
         60 -       61                        1         0.595         95.833
         62 -       6,                        1         0.595         96.429
         64 -       65                        1         0.595         97.024
         66 -       67                        1         0.595         97.619
         68 -       69                        1         0.595         98.214
         70 -       71                        2         1.190         99.405
         72 -       73                  -------1         0.595        100.000
                                            168


                                  5.0       10.0      15.0      20.0      25.0
                          +---------+---------+---------+---------+---------+
                          IXXXXXX
                          IXXXXXXX
                          IXXXXXXXXXXXXXX
                          IXXXXXXXXXXXXXXXXXX
                          IXXXXXXXXXXXXXXXXXXXXXXXX
                          IXXXXXXXXXXXXXXXXXXXXXXXX
                          IXXXXXXXXXXXXXXXXXXXXXXXXXXX
                          IXXXXXXXXXXXXXXX
                          IXXXXXXXXXXXXXXXXX
                          IXXXXXXXXXXX
                          IXXXXXXXXXX
                          IXXXX
                          IXX
                          IXXXXX
                          I
                          IXXXX
                          IXXXX
                          IX
                          IX
                          IX
                          IX
                          IX
                          IXX
                          IX
                          +---------+---------+---------+---------+---------+
                                  5.0       10.0      15.0      20.0      25.0
```

Figure 7

```
VARIABLE:  PMN      NUMBER:  9      DESCRIPTION:  MIN PLY ADHSN          VARIABLE TYPE:  FIXED
THERE WERE   706 OBSERVATIONS, WHICH INCLUDED   681 CASES OF MISSING DATA SELECTED FROM A TOTAL OF
SUM OF OBSERVATIONS =  711.0000             SUM OF OBSERVATIONS SQUARED =  21767.00    706 OBSERVATIONS
MEAN =  28.44000                            MEDIAN =  27.00000
MAXIMUM =  44                               MINIMUM =  14                            NUMBER OF OBSERVATIONS =
STANDARD ERROR OF MEAN =  1.605283          STANDARD DEVIATION =  8.026415           MODE =  20
COEFFICIENT OF SKEWNESS = 0.3450782         COEFFICIENT OF VARIATION =  28.22227     RANGE =  30
                                                                                     VARIANCE =  64.42333
                                                                                     KURTOSIS =  2.162221


                                                                CUMULATIVE
     VALUE                       FREQUENCY     PERCENTAGE       PERCENTAGE

      14                             1            4.000            4.000
      19                             1            4.000            8.000
      20                             3           12.000           20.000
      22                             2            8.000           28.000
      24                             2            8.000           36.000
      25                             1            4.000           40.000
      26                             2            8.000           48.000
      27                             2            8.000           56.000
      29                             1            4.000           60.000
      30                             2            8.000           68.000
      31                             1            4.000           72.000
      36                             1            4.000           76.000
      37                             1            4.000           80.000
      38                             2            8.000           88.000
      40                             1            4.000           92.000
      42                             1            4.000           96.000
      44                             1            4.000          100.000
                               -------
                                    25



          5.0       10.0      15.0      20.0      25.0
+---------+---------+---------+---------+---------+
IXXXXXXXX
IXXXXXXXX
IXXXXXXXXXXXXXXXXXXXXXXXX
IXXXXXXXXXXXXXXXX
IXXXXXXXXXXXXXXXX
IXXXXXXXX
IXXXXXXXXXXXXXXXX
IXXXXXXXXXXXXXXXX
IXXXXXXXX
IXXXXXXXXXXXXXXXX
IXXXXXXXX
IXXXXXXXX
IXXXXXXXX
IXXXXXXXXXXXXXXXX
IXXXXXXXX
IXXXXXXXX
IXXXXXXXX
+---------+---------+---------+---------+---------+
          5.0       10.0      15.0      20.0      25.0
```

Figure 8

```
VARIABLE:  PAV      NUMBER:   10      DESCRIPTION:  AVERAGE PLY ADHSN      VARIABLE TYPE:  FIXED
THERE WERE   706 OBSERVATIONS, WHICH INCLUDED   188 CASES OF MISSING DATA SELECTED FROM A TOTAL  OF
                                                                              706 OBSERVATIONS
SUM OF OBSERVATIONS =  28109.00            SUM OF OBSERVATIONS SQUARED =  1601885.
MEAN =  54.26448                           MEDIAN =  54.00000                    NUMBER OF OBSERVATIONS =
MAXIMUM =  114                             MINIMUM =  17                         MODE =  53
STANDARD ERROR OF MEAN =  0.5346928        STANDARD DEVIATION =  12.16940        RANGE =  97
COEFFICIENT OF SKEWNESS =  0.6843333       COEFFICIENT OF VARIATION =  22.42609  VARIANCE =  148.0943
                                                                                 KURTOSIS =  5.372330


                                                                    CUMULATIVE
        VALUE                     FREQUENCY       PERCENTAGE        PERCENTAGE
         17 -        20                   1            0.193             0.193
         21 -        24                   0            0.000             0.193
         25 -        28                   3            0.579             0.772
         29 -        32                   9            1.737             2.510
         33 -        36                  19            3.668             6.178
         37 -        40                  37            7.143            13.320
         41 -        44                  36            6.950            20.270
         45 -        48                  41            7.915            28.185
         49 -        52                  77           14.865            43.050
         53 -        56                  92           17.761            60.811
         57 -        60                  62           11.969            72.780
         61 -        64                  52           10.039            82.819
         65 -        68                  42            8.108            90.927
         69 -        72                  23            4.440            95.367
         73 -        76                   5            0.965            96.332
         77 -        80                   5            0.965            97.297
         81 -        84                   4            0.772            98.069
         85 -        88                   3            0.579            98.649
         89 -        92                   1            0.193            98.842
         93 -        96                   2            0.386            99.228
         97 -       100                   1            0.193            99.421
        101 -       104                   0            0.000            99.421
        105 -       108                   2            0.386            99.807
        109 -       112                   0            0.000            99.807
        113 -       114             -------1            0.193           100.000
                                        518

                         5.0      10.0      15.0      20.0      25.0
                 +---------+---------+---------+---------+---------+
                 I
                 I
                 IX
                 IXXX
                 IXXXXXXX
                 IXXXXXXXXXXXXXX
                 IXXXXXXXXXXXXXX
                 IXXXXXXXXXXXXXXXX
                 IXXXXXXXXXXXXXXXXXXXXXXXXXXXXXX
                 IXXXXXXXXXXXXXXXXXXXXXXXXXXXXXXXXXXXX
                 IXXXXXXXXXXXXXXXXXXXXXXXX
                 IXXXXXXXXXXXXXXXXXXXX
                 IXXXXXXXXXXXXXXXX
                 IXXXXXXXXX
                 IXX
                 IXX
                 IXX
                 IX
                 I
                 IX
                 I
                 I
                 IX
                 I
                 I
                 +---------+---------+---------+---------+---------+
                         5.0      10.0      15.0      20.0      25.0
```

Figure 9

```
VARIABLE:  TENS   NUMBER:   10     DESCRIPTION:  TENSILE              VARIABLE TYPE:  FIXED
THERE WERE  706 OBSERVATIONS, WHICH INCLUDED   134 CASES OF MISSING DATA SELECTED FROM A TOTAL  OF
                                                                                 706 OBSERVATIONS
SUM OF OBSERVATIONS =  1538885.             SUM OF OBSERVATIONS SQUARED =  0.4200112E+10
MEAN =  2690.358                            MEDIAN =  2661.000                  NUMBER OF OBSERVATIONS =
MAXIMUM =  3697                             MINIMUM =  1495                     MODE =  2660
STANDARD ERROR OF MEAN =  13.54925          STANDARD DEVIATION = 324.0510       RANGE =  2202
COEFFICIENT OF SKEWNESS =  0.3102679        COEFFICIENT OF VARIATION =  12.04490   VARIANCE =  105009.1
                                                                                KURTOSIS =  3.827942


                                                                   CUMULATIVE
      VALUE                          FREQUENCY       PERCENTAGE     PERCENTAGE

      1495 -     1583                       1          0.175           0.175
      1584 -     1672                       1          0.175           0.350
      1673 -     1761                       1          0.175           0.524
      1762 -     1850                       1          0.175           0.699
      1851 -     1939                       2          0.350           1.049
      1940 -     2028                       5          0.874           1.923
      2029 -     2117                       5          0.874           2.797
      2118 -     2206                      14          2.448           5.245
      2207 -     2295                      17          2.972           8.217
      2296 -     2384                      31          5.420          13.636
      2385 -     2473                      58         10.140          23.776
      2474 -     2562                      65         11.364          35.140
      2563 -     2651                      75         13.112          48.252
      2652 -     2740                      85         14.860          63.112
      2741 -     2829                      50          8.741          71.853
      2830 -     2918                      40          6.993          78.846
      2919 -     3007                      24          4.196          83.042
      3008 -     3096                      29          5.070          88.112
      3097 -     3185                      30          5.245          93.357
      3186 -     3274                      11          1.923          95.280
      3275 -     3363                      10          1.748          97.028
      3364 -     3452                       3          0.524          97.552
      3453 -     3541                       5          0.874          98.427
      3542 -     3630                       4          0.699          99.126
      3631 -     3697                       5          0.874         100.000
                                      -------
                                      572


                                    5.0       10.0      15.0      20.0      25.0
                          +---------+---------+---------+---------+---------+
                          I
                          I
                          I
                          I
                          IX
                          IXX
                          IXX
                          IXXXXX
                          IXXXXXX
                          IXXXXXXXXXXX
                          IXXXXXXXXXXXXXXXXXXXX
                          IXXXXXXXXXXXXXXXXXXXXXXX
                          IXXXXXXXXXXXXXXXXXXXXXXXXXX
                          IXXXXXXXXXXXXXXXXXXXXXXXXXXXXXX
                          IXXXXXXXXXXXXXXXXX
                          IXXXXXXXXXXXXXX
                          IXXXXXXXX
                          IXXXXXXXXXX
                          IXXXXXXXXXX
                          IXXXX
                          IXXX
                          IX
                          IXX
                          IX
                          IXX
                          +---------+---------+---------+---------+---------+
                                    5.0       10.0      15.0      20.0      25.0
```

Figure 10

```
VARIABLE:  ELONG   NUMBER:     12   DESCRIPTION:  ELONGATION         VARIABLE TYPE:  FIXED
THERE WERE  706 OBSERVATIONS, WHICH INCLUDED   133 CASES OF MISSING DATA SELECTED FROM A TOTAL  OF
                                                                                       706 OBSERVATIONS
SUM OF OBSERVATIONS =  281707.0              SUM OF OBSERVATIONS SQUARED =  0.1410076E+09
MEAN =  491.6353                             MEDIAN =  497.0000                      NUMBER OF OBSERVATIONS =
MAXIMUM =  670                               MINIMUM =  274                          MODE =  530
STANDARD ERROR OF MEAN =  2.767603           STANDARD DEVIATION = 66.24928           RANGE =  396
COEFFICIENT OF SKEWNESS =  -0.1577621        COEFFICIENT OF VARIATION =  13.47529    VARIANCE =  4388.966
                                                                                     KURTOSIS =  2.601573


                                                                     CUMULATIVE
       VALUE                         FREQUENCY       PERCENTAGE      PERCENTAGE

       274 -     289                         1            0.175           0.175
       290 -     305                         1            0.175           0.349
       306 -     321                         0            0.000           0.349
       322 -     337                         1            0.175           0.524
       338 -     353                         4            0.698           1.222
       354 -     369                        15            2.618           3.839
       370 -     385                        10            1.745           5.585
       386 -     401                        25            4.363           9.948
       402 -     417                        33            5.759          15.707
       418 -     433                        44            7.679          23.386
       434 -     449                        22            3.839          27.225
       450 -     465                        35            6.108          33.333
       466 -     481                        49            8.551          41.885
       482 -     497                        48            8.377          50.262
       498 -     513                        59           10.297          60.558
       514 -     529                        47            8.202          68.761
       530 -     545                        52            9.075          77.836
       546 -     561                        46            8.028          85.864
       562 -     577                        23            4.014          89.878
       578 -     593                        31            5.410          95.288
       594 -     609                         9            1.571          96.859
       610 -     625                         9            1.571          98.429
       626 -     641                         6            1.047          99.476
       642 -     657                         0            0.000          99.476
       658 -     670                   _______3            0.524         100.000
                                           573

                                 5.0       10.0      15.0      20.0      25.0
                        +---------+---------+---------+---------+---------+
                        I
                        I
                        I
                        I
                        IX
                        IXXXXX
                        IXXX
                        IXXXXXXXXX
                        IXXXXXXXXXXXX
                        IXXXXXXXXXXXXXXX
                        IXXXXXXXX
                        IXXXXXXXXXXXX
                        IXXXXXXXXXXXXXXXXX
                        IXXXXXXXXXXXXXXXXX
                        IXXXXXXXXXXXXXXXXXXXXX
                        IXXXXXXXXXXXXXXXX
                        IXXXXXXXXXXXXXXXXXX
                        IXXXXXXXXXXXXXXXX
                        IXXXXXXXX
                        IXXXXXXXXXXX
                        IXXX
                        IXXX
                        IXX
                        I
                        IX
                        +---------+---------+---------+---------+---------+
                                 5.0       10.0      15.0      20.0      25.0
```

Figure 11

```
VARIABLE:  DUR     NUMBER:  17     DESCRIPTION:  DUROMETER          VARIABLE TYPE:  FLOAT
THERE WERE   706 OBSERVATIONS, WHICH INCLUDED   276 CASES OF MISSING DATA SELECTED FROM A TOTAL  OF
                                                                                       706 OBSERVATIONS
SUM OF OBSERVATIONS =  26392.00              SUM OF OBSERVATIONS SQUARED =  1622522.
MEAN =  61.37674                             MEDIAN =  61.00000                     NUMBER OF OBSERVATIONS =
MAXIMUM =  69.00000                          MINIMUM =  50.00000                    MODE =  61.00000
STANDARD ERROR OF MEAN =  0.1202394          STANDARD DEVIATION =  2.493337         RANGE =  19.00000
COEFFICIENT OF SKEWNESS =  -0.4979397        COEFFICIENT OF VARIATION =  4.062348   VARIANCE =  6.216729
                                                                                    KURTOSIS =  5.129465


                                                              CUMULATIVE
     VALUE                     FREQUENCY     PERCENTAGE       PERCENTAGE

     50.00000                          2          0.465            0.465
     54.00000                          1          0.233            0.698
     55.00000                          9          2.093            2.791
     56.00000                          2          0.465            3.256
     57.00000                         13          3.023            6.279
     58.00000                         14          3.256            9.535
     59.00000                         28          6.512           16.047
     60.00000                         70         16.279           32.326
     61.00000                         96         22.326           54.651
     62.00000                         56         13.023           67.674
     63.00000                         63         14.651           82.326
     64.00000                         38          8.837           91.163
     65.00000                         24          5.581           96.744
     66.00000                          8          1.860           98.605
     67.00000                          2          0.465           99.070
     68.00000                          1          0.233           99.302
     69.00000                          3          0.698          100.000
                                 -------
                                     430


                           5.0       10.0      15.0      20.0      25.0
                  +---------+---------+---------+---------+---------+
                  IX
                  I
                  IXXXX
                  IX
                  IXXXXXX
                  IXXXXXXX
                  IXXXXXXXXXXXXX
                  IXXXXXXXXXXXXXXXXXXXXXXXXXXXXXXXX
                  IXXXXXXXXXXXXXXXXXXXXXXXXXXXXXXXXXXXXXXXXXXXX
                  IXXXXXXXXXXXXXXXXXXXXXXXXXX
                  IXXXXXXXXXXXXXXXXXXXXXXXXXXXXX
                  IXXXXXXXXXXXXXXXXX
                  IXXXXXXXXXXX
                  IXXXX
                  IX
                  I
                  IX
                  +---------+---------+---------+---------+---------+
                           5.0       10.0      15.0      20.0      25.0
```

Figure 12

```
VARIABLE:   SG     NUMBER:   18      DESCRIPTION:  TREAD SPECIFIC GRAV 1.()()  VARIABLE TYPE:        FLOAT
THERE WERE   706 OBSERVATIONS, WHICH INCLUDED   279 CASES OF MISSING DATA SELECTED FROM A TOTAL   OF
                                                                                   706 OBSERVATIONS
SUM OF OBSERVATIONS =  5376.000               SUM OF OBSERVATIONS SQUARED =  68168.00
MEAN =  12.59016                              MEDIAN =  13.00000                NUMBER OF OBSERVATIONS =
MAXIMUM =  16.00000                           MINIMUM =  8.000000               MODE =  12.00000
STANDARD ERROR OF MEAN =  0.5154423E-01       STANDARD DEVIATION =  1.065109    RANGE =  8.000000
COEFFICIENT OF SKEWNESS =  -0.2478130         COEFFICIENT OF VARIATION =  8.459850   VARIANCE [illegible]57
                                                                                KURTOSIS


                                                                 CUMULATIVE
         VALUE                      FREQUENCY     PERCENTAGE     PERCENTAGE

         8.000000                        1          0.234          0.234
         9.000000                        3          0.703          0.937
         10.00000                        7          1.639          2.576
         11.00000                       34          7.963         10.539
         12.00000                      161         37.705         48.244
         13.00000                      143         33.489         81.733
         14.00000                       65         15.222         96.956
         15.00000                       12          2.810         99.766
         16.00000                        1          0.234        100.000
                                    -------
                                       427



                                 10.0      20.0      30.0      40.0      50.0
                        +---------+---------+---------+---------+---------+
                        I
                        IX
                        IXX
                        IXXXXXXXX
                        IXXXXXXXXXXXXXXXXXXXXXXXXXXXXXXXXXXXXXX
                        IXXXXXXXXXXXXXXXXXXXXXXXXXXXXXXXXX
                        IXXXXXXXXXXXXXXX
                        IXXX
                        I
                        +---------+---------+---------+---------+---------+
                                 10.0      20.0      30.0      40.0      50.0
```

Figure 13

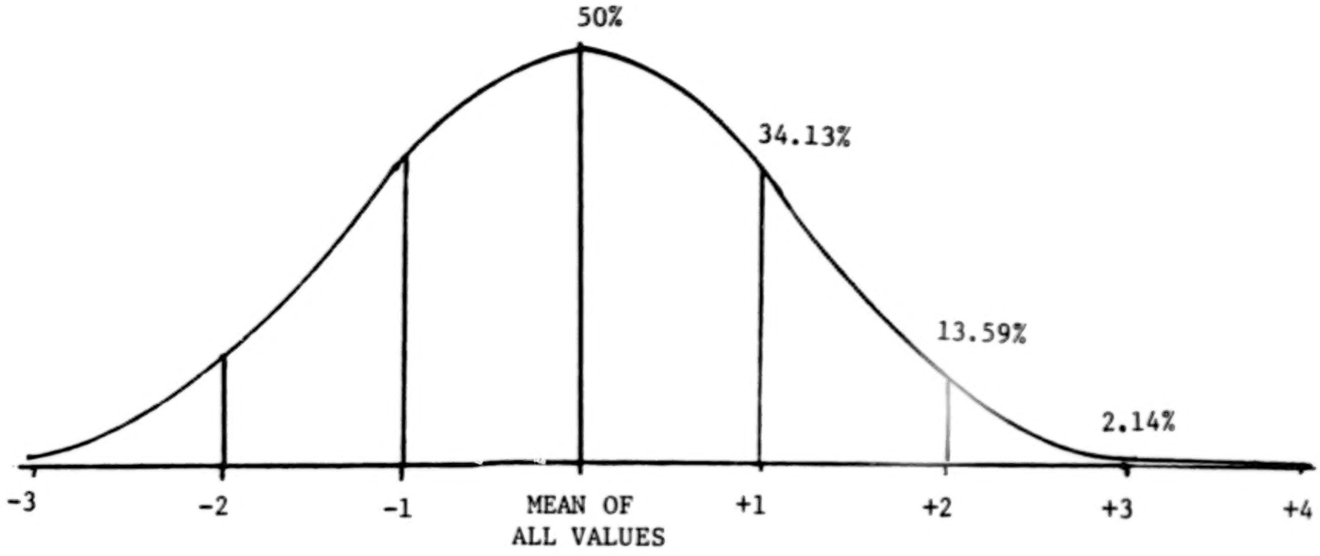
50%
34.13%
13.59%
2.14%
-3
-2
-1
MEAN OF
ALL VALUES
+1
+2
+3
+4

Figure 14

```
     PLOT OF VARIABLE:    1    (HORIZ.)   VS VARIABLE:    3    (VERT.)

              I---------+---------+---------+---------+---------+
 1.000        +                                      3B
              I                                     CA
              I                                  4CD
              I                                AC9
 0.8000       +                              3C3
              I                            2CA
              I                          1CB
              I                        2CC
 0.6000       +                      ACB
              I                     93
              I                  2CD3
              I                 CB
 0.4000       +               6D
              I             3D6
              I            79
              I          CC6
 0.2000       +       3DC1
              I      79
              I   6DC6
              I BD6
 0.1863E-07   +71
              I
              I
              I
-0.2000       +
              I---------+---------+---------+---------+---------+
           201.5               451.5               701.5
                     326.5               576.5               826.5
```

Figure 15

```
  PLOT OF VARIABLE:   VLOG1   (HORIZ.)  VS  VARIABLE:   VLOG3    (VERT.)

            I---------+---------+---------+---------+
  0.0000    +1  1                            YF
            I                               **
            I                             3*I
            I                            B*
 -0.4000    +                           I8
            I                          8E
            I                         BJ
            I                        IB
 -0.8000    +                       A
            I                      66
            I                    9B6
            I                   5
 -1.200     +                5562
            I              13
            I             12
            I           131
 -1.600     +
            I        112
            I
            I
 -2.000     +     1 1
            I
            I
            I
 -2.400     +
            I---------+---------+---------+---------+
     -0.8000E-01            1.520              3.120
                 0.7200              2.320
```

Figure 16

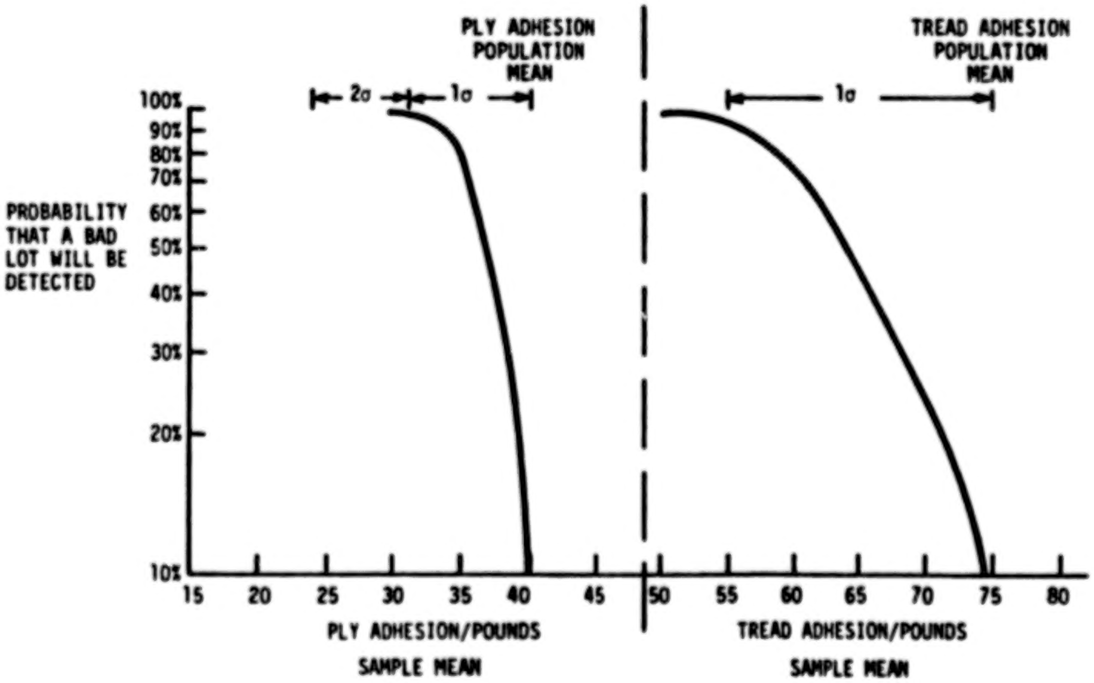

Figure 17

HEAT GENERATION IN AIRCRAFT TIRES

Samuel K. Clark
University of Michigan

ABSTRACT

A method has been developed for calculating the internal temperature distribution in an aircraft tire while free rolling under load. The method uses an approximate stress analysis of each point in the tire as it rolls through the contact patch. From this stress change, the mechanical work done on each volume element may be obtained and converted into a heat release rate through a knowledge of material characteristics. The tire cross-section is then considered as a body with internal heat generation, and the diffusion equation is solved numerically with appropriate boundary conditions of the wheel and runway surface. Comparison with data obtained with buried thermocouples in tires shows good agreement. The data presented in this paper were excerpted from reference 1.

The origin of aircraft tire heating lies in the hysteretic loss characteristics of polymeric materials used for both the nylon textile cord reinforcement and for the rubber components in an aircraft tire. Figure 1 shows a typical stress-strain curve between the two end points of the cyclic stress states associated with rolling a material element through the contact patch of the tire and out again.

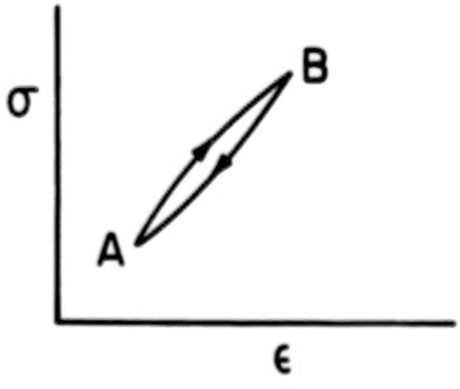

Figure 1

The stress excursion is presumed to occur between two points A and B located 180° apart on the rolling tire. One extreme is the upper point A where only inflation pressures act to produce an axisymmetric stress state of the tire. The other extreme point is the center of the contact patch, where again an axisymmetric solution is used to obtain the stress state in the tire deformed against a flat surface (fig. 2).

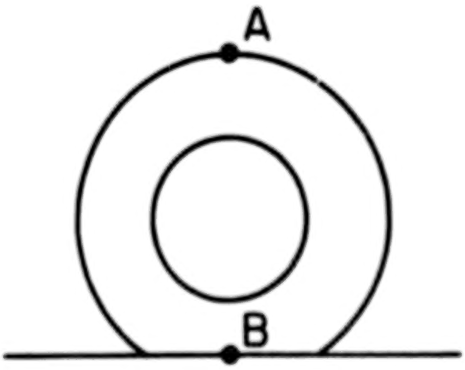

Figure 2

Figure 3 illustrates the assumed conditions in the vicinity of the contact patch of the tire. A total deflection Δ is presumed to take place between the outer surface of the tire crown and the ground. Inside this contact patch region the tire is presumed to be in complete contact with the flat runway surface.

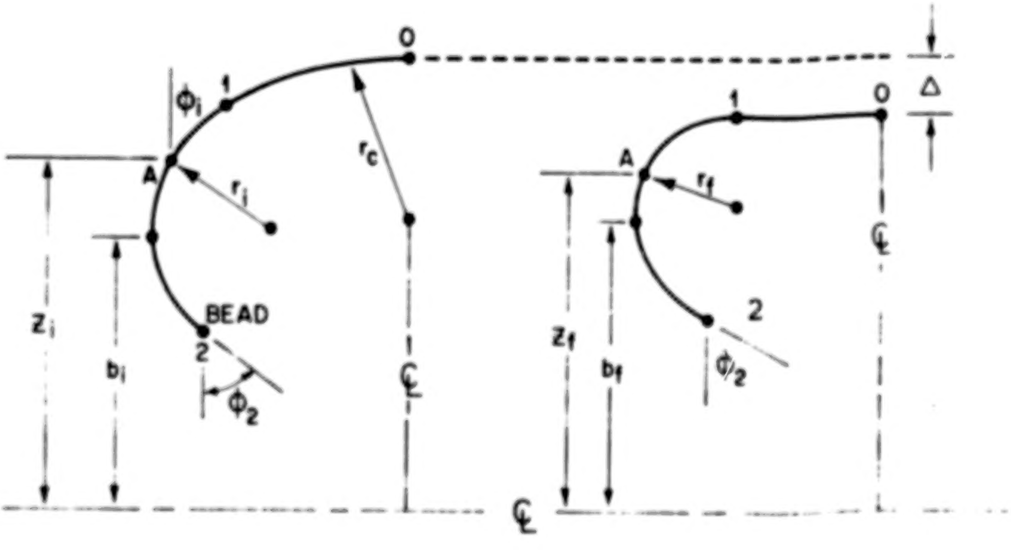
O
1
ϕ_i
A
r_i
r_c
BEAD
2
ϕ_2
z_i
b_i
℄
O
Δ
1
A
r_f
℄
2
z_f
b_f
$\phi/2$
℄

(a) Assumed geometry at point A of figure 2.

(b) Assumed geometry at point B of figure 2.

Figure 3

Figure 4 shows the assumed geometry of the tire at the two extreme conditions A and B illustrated in figures 2 and 3. In the case of axisymmetric inflation loads the geometric midline of the tire is represented by a torus as shown. For that portion of the tire in the center of the contact patch, the shape is considered to be flat in the contact region and made up of a single circular arc outside the contact region. The stress solutions are both obtained from axisymmetric considerations.

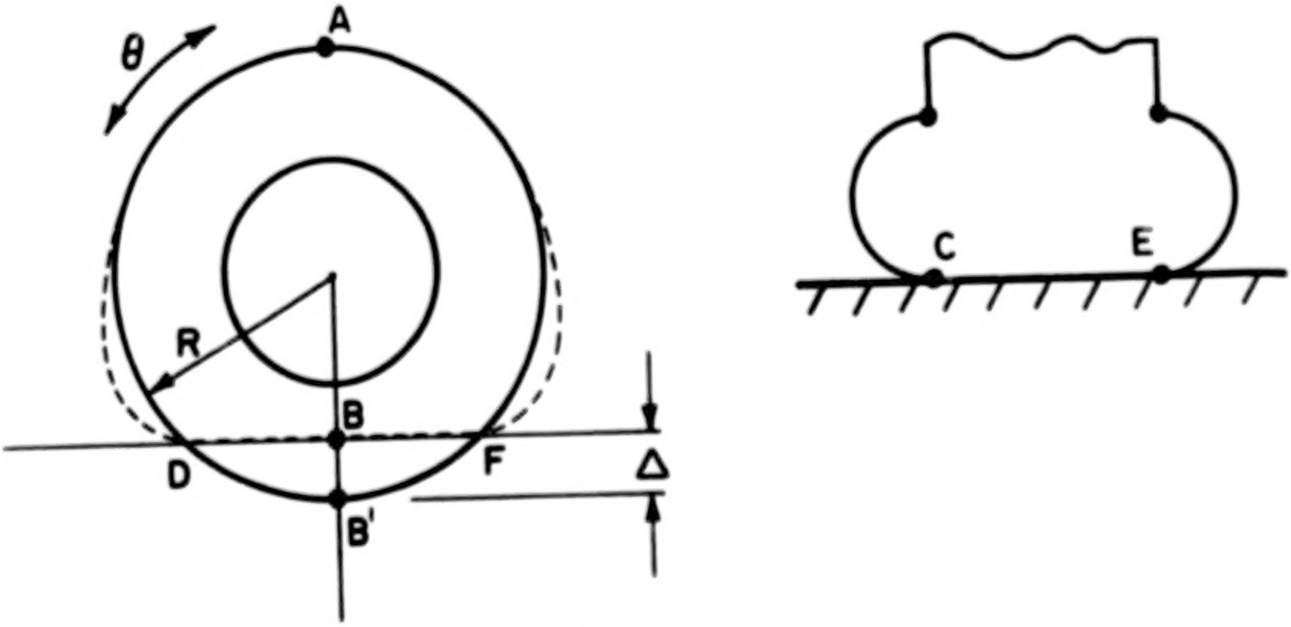

Figure 4

The tire is divided into five segments for purposes of both stress and thermal analysis (fig. 5). Segment I is that portion of the tire carcass lying in the contact patch. It has plane orthotropic elastic properties. Segment II is isotropic tread material in contact with the runway surface, and hence is acted upon by normal pressures as well as by membrane and bending strains. Segment III is that part of the side wall acted on by internal pressure, and also has orthotropic elastic properties. Segment IV is the sidewall cover of the tire and is considered to be isotropic in its material properties. Segment V is the bead region which is subject to a special description.

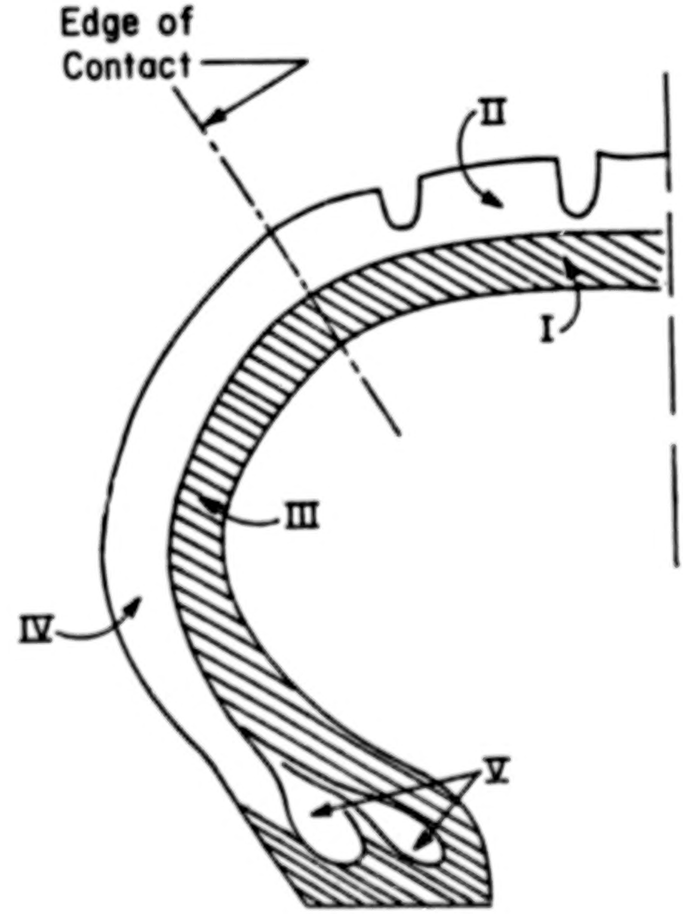

Figure 5

Figure 6 shows the method of splitting the tire cross section into various rectangular segments for purposes of thermal analysis. In general the decomposition process follows the natural boundary lines of the tire between the orthotropic and isotropic regions.

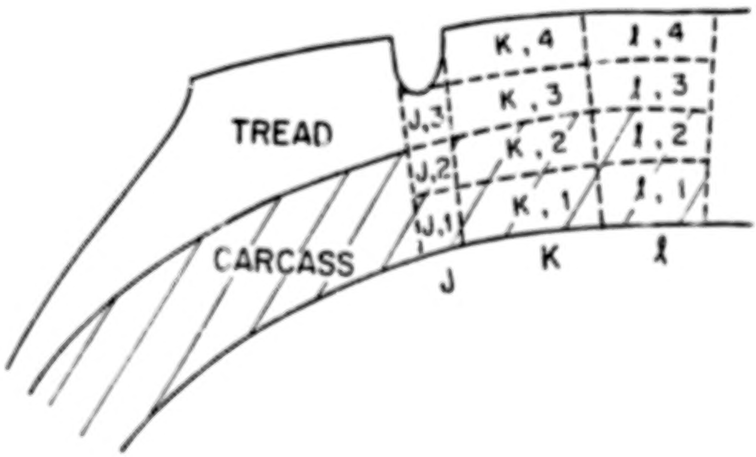
K , 4
ℓ , 4
J,3
K , 3
ℓ , 3
TREAD
J,2
K , 2
ℓ , 2
J,1
K , 1
ℓ , 1
CARCASS
J
K
ℓ

Figure 6

Figure 7 is the general heat diffusion equation which is being modeled on a discrete basis in the numerical calculation described here. However, the elements which are in contact with the outer surface or with the bead area of the tire have additional terms associated with either thermal conduction into the metallic wheel or convective heat transfer loss to the air.

$$K \nabla^2 \theta = \rho \frac{\partial \theta}{\partial t} - \overset{\circ}{q}$$

where

K = thermal conductivity

ρ = density

$\overset{\circ}{q}$ = heat generation rate

θ = temperature

Figure 7

The equation for convective heat transfer, temperature buildup and internal heat generation is discretized into the form shown in figure 8 for numerical calculation throughout the tire cross section. Note that due to the higher rotational speeds of the tire compared to thermal diffusion times, the temperature distribution is completely axisymmetric.

$$\begin{aligned}\frac{\Delta\theta}{\Delta t} = \dot{q} &+ \bar{\alpha}_{K-1,K,\ell}\,(\theta_{K-1,\ell}-\theta_{K,\ell})\\ &+ \bar{\alpha}_{K,K+1,\ell}\,(\theta_{K+1,\ell}-\theta_{K,\ell})\\ &+ \bar{\alpha}_{K,\ell-1,\ell}\,(\theta_{K,\ell-1}-\theta_{K,\ell})\\ &+ \bar{\alpha}_{K,\ell,\ell+1}\,(\theta_{K,\ell+1}-\theta_{K,\ell})\end{aligned}$$

with

$$\bar{\alpha}_{1,m,n} = \frac{KA}{d}$$

K = thermal conductivity

A = area of contact between subscripted elements

d = distance between centroids of subscripted elements

NOTATION FOR THERMAL ELEMENTS

	$K, \ell-1$	
$K-1, \ell$	K, ℓ	$K+1, \ell$
	$K, \ell+1$	

Figure 8

The strain energy density must be related to the hysteretic loss, which results in internal heat generation. Due to the lack of appropriate material constants, this is now being done on a provisional basis using the loss tangent tan δ, a quantity usually associated with uniaxial sinusoidal loading. Due to the linear relationship between rate of heat generation and frequency, the rate of heat generation is linearly proportional to aircraft velocity (fig. 9).

$$\dot{q} \cong 0.01 \frac{UV_0 \tan\delta}{r_0 - \Delta/3} \text{ cal/cm}^3\text{/sec}$$

where r_0 = outside radius of tire, in.

Δ = tire deflection, in.

V_0 = aircraft velocity, ft/sec

U = elastic energy, in.-lb/in.^{3}

Figure 9

In data shown in subsequent figures, calculations are carried out comparing predictions of this program with measured temperature rise data. These predictions are based on best estimates of material properties taken from the literature (ref. 2). These are given in figure 10.

MATERIAL CHARACTERISTICS OF

22 x 5.5 and 40 x 14 AIRCRAFT TIRES

Region[a]	Young's modulus of rubber, E, psi	Shear modulus of rubber, G, psi	[b] $\tan\delta_o$, psi	Cord angle, α, deg	Thermal conductivity, K, cal-cm/°C-cm^2-sec	Density, ρ, deg	Specific heat, C_p,
Tread (II)		335	0.15		5×10^{-4}	1.0	0.5
Carcass (I, III)	(c)		0.15	(d)	5×10^{-4}	1.0	0.5
Sidewall rubber (IV)		335	0.15			1.0	0.5
Bead (V)	15×10^6		0.03				

[a] See fig. 5.

[b] Values of $\tan\delta_o$ are given for 25°C. For higher temperatures, $\tan\delta$ is calculated by the approximate expression

$$\tan\delta = \tan\delta_o(e^{-.01\Delta\theta})$$

where $\Delta\theta$ is the temperature rise in °C above ambient.

[c] See reference 1. For shear modulus G of rubber use 335 psi.

[d] Calculated by cosine law using $\alpha = 35°$ crown angle.

Figure 10

Figure 11 represents a cross section of half of the 22 x 5.5 8 PR tire showing the elements used for temperature calculation as well as the thermocouple displacement used in the experimental program.

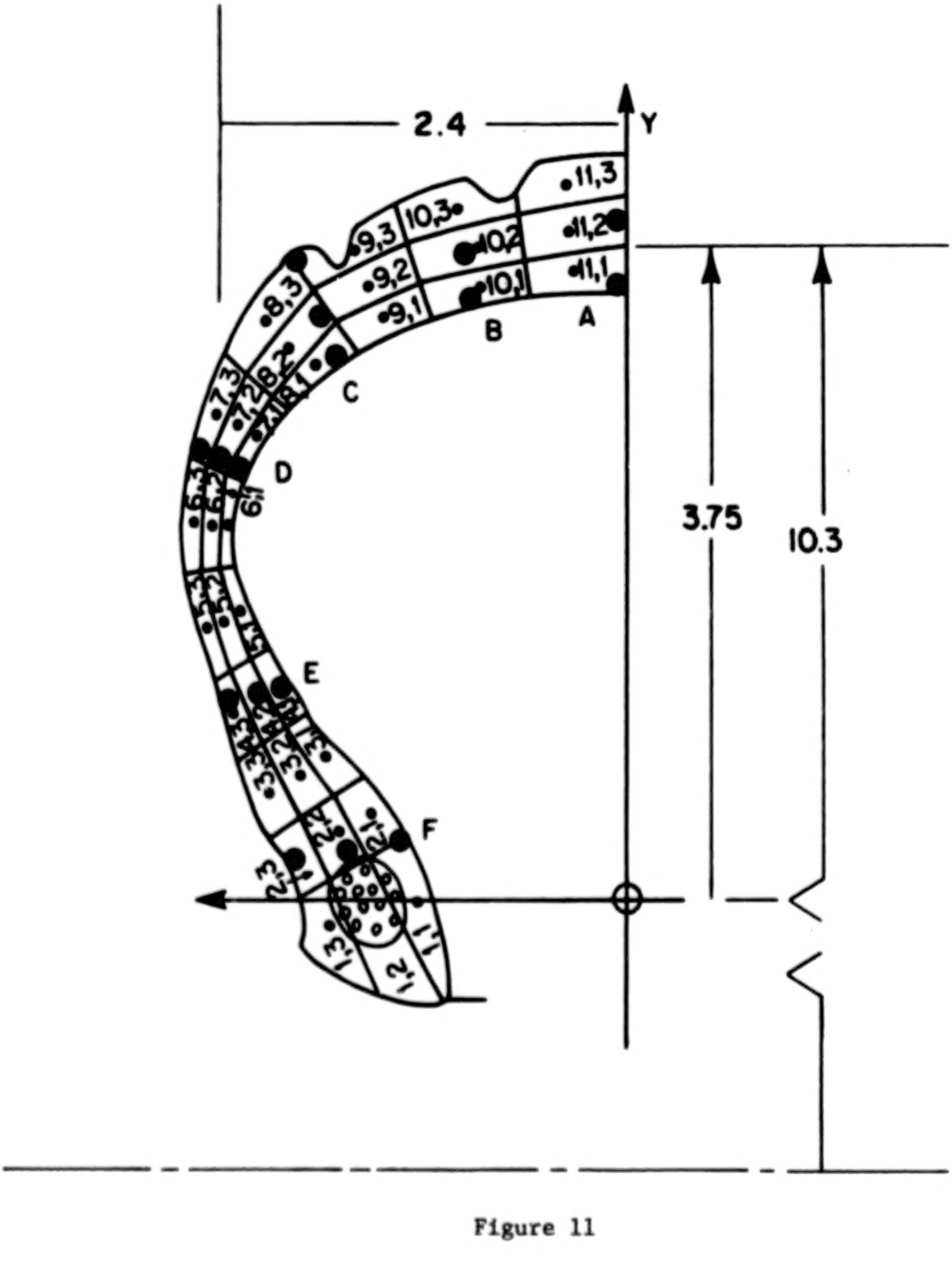
2.4
Y
11,3
11,2
11,1
10,3
10,2
10,1
9,3
9,2
9,1
8,3
8,2
8,1
7,3
7,2
7,1
6,3
6,2
6,1
5,3
5,2
5,1
3,3
3,2
3,1
2,3
2,2
2,1
1,3
1,2
1,1
A
B
C
D
E
F
3.75
10.3

Figure 11

Figure 12 shows comparison between temperature rise and time as measured by thermocouples, along with calculations for similar locations on the tire using the computer program previously described. Stations A through F correspond to those shown in figure 11.

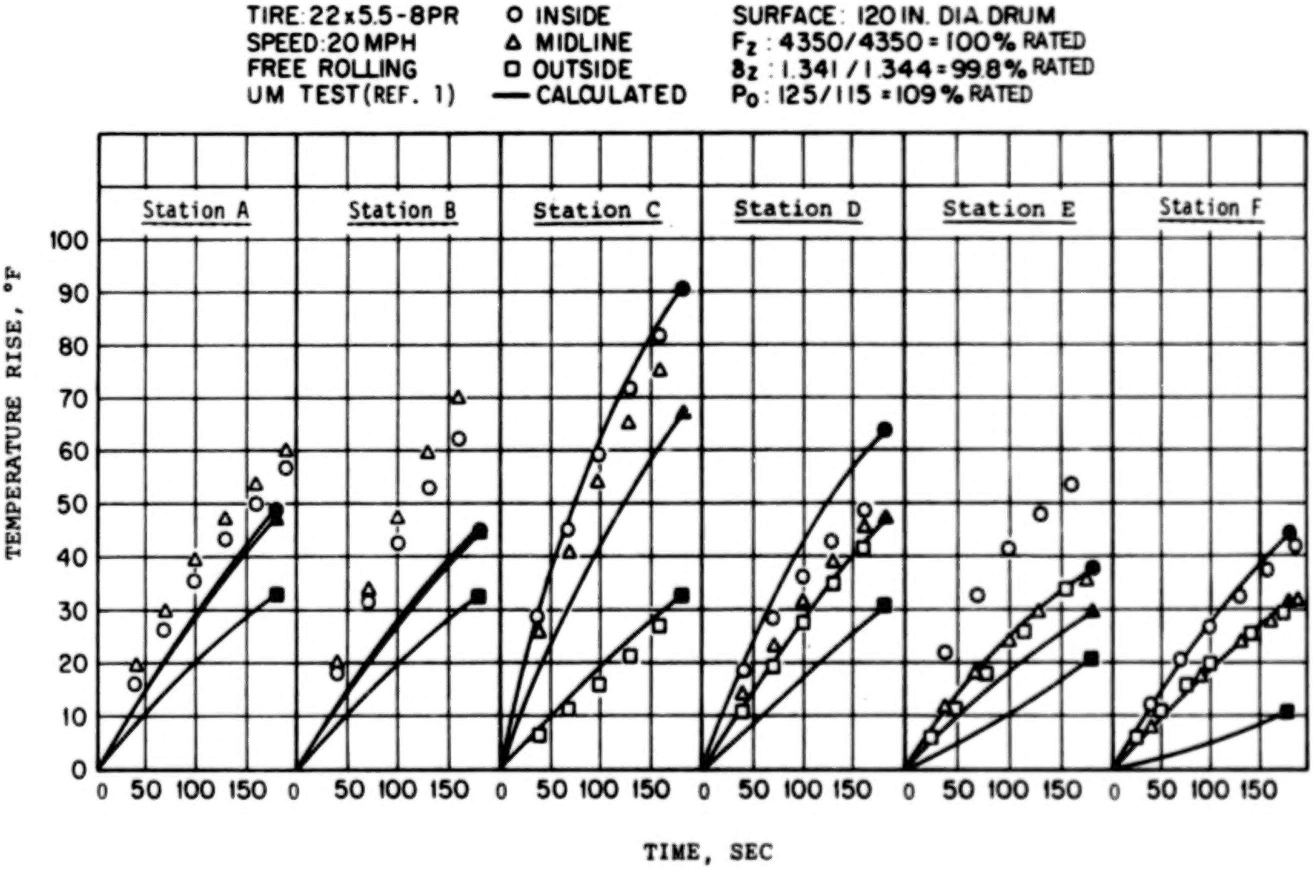

Figure 12

Figure 13 shows similar temperature vs. time information for a different form of this 22 x 5.5 tire. In this case the tire is a 12 PR tire and requires a different geometric description due to the thicker carcass. This in turn results in considerably higher temperatures being generated as this tire is run under rated load conditions for approximately 150 seconds. Again, measured data is compared with calculations from the computer program.

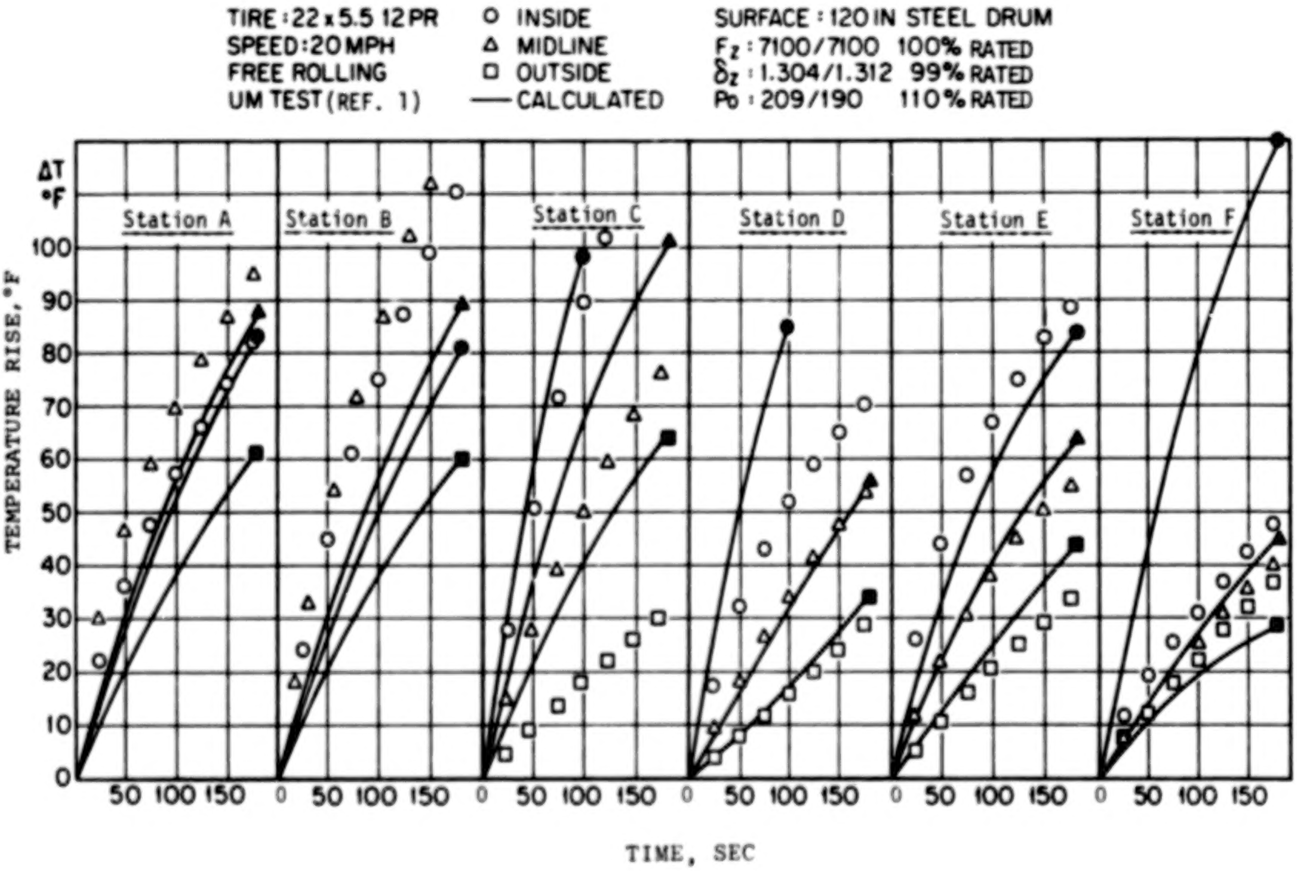

Figure 13

Figure 14 shows a cross section of a 40 x 14 28 PR tire used as a model of a large aircraft tire. This is a common commercial tire, and in this case a larger number of discrete sections is chosen for temperature calculation purposes. Again, thermocouple locations are shown by the black dots. Extensive experimental work has been done on this tire in order to compare it with the calculation.

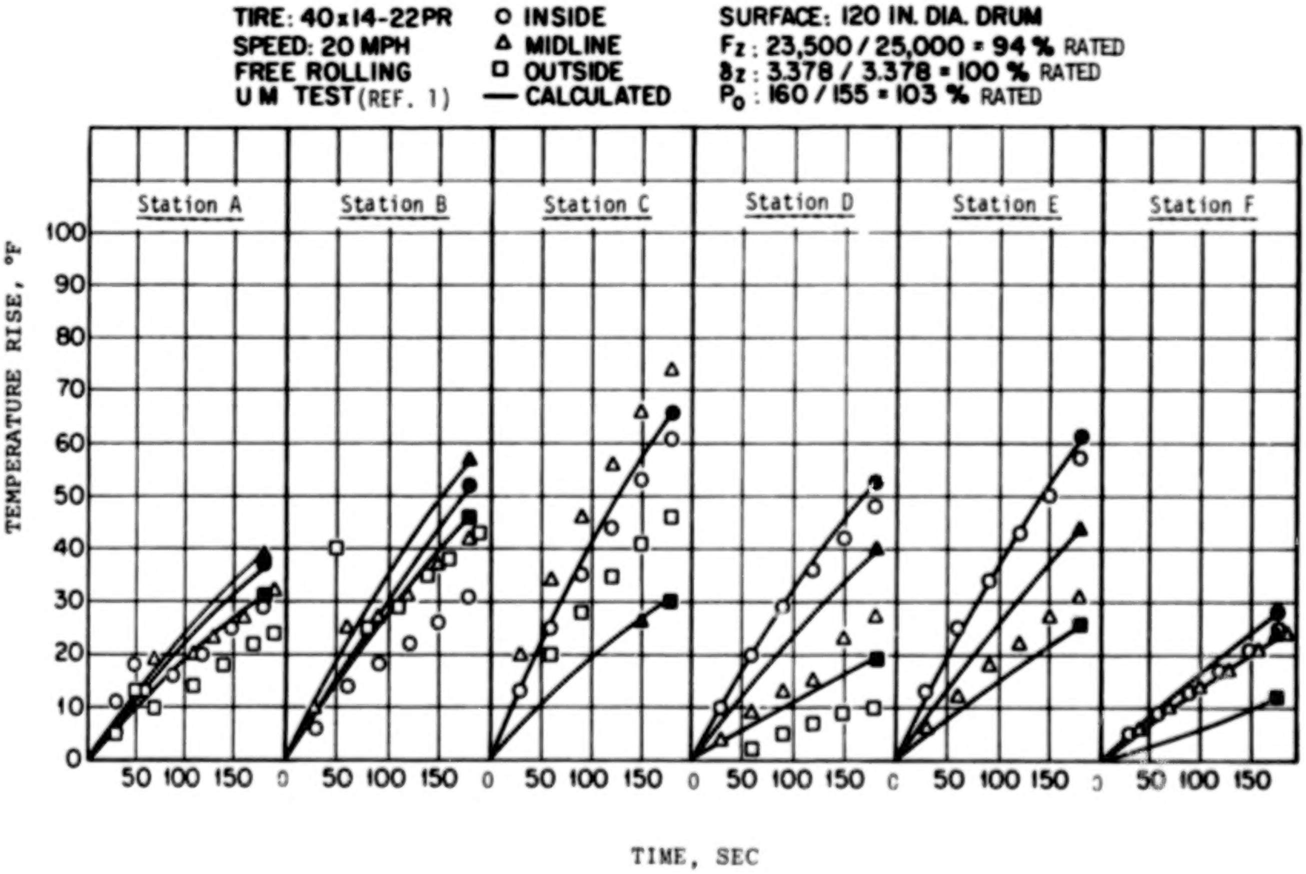

Figure 14

Figure 15 shows a comparison between a 22 ply rated version of the tire shown in figure 14 and calculations carried out using the program described previously. These calculations generally agree will with measured data.

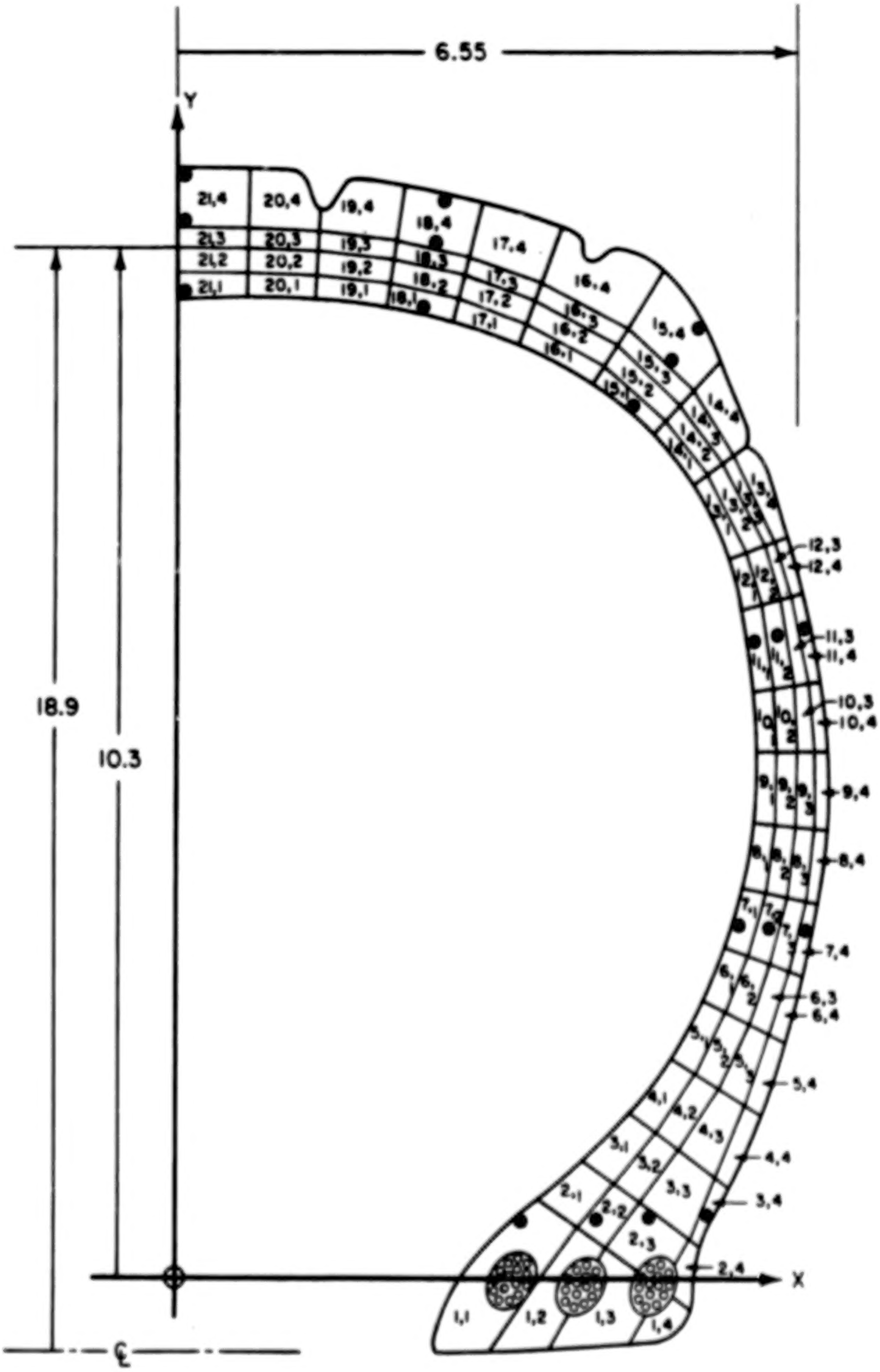
6.55
Y
X
18.9
10.3
℄
21,4
20,4
19,4
18,4
17,4
16,4
15,4
14,4
21,3
20,3
19,3
18,3
21,2
20,2
19,2
18,2
21,1
20,1
19,1
18,1
17,3
17,2
17,1
16,3
16,2
16,1
15,3
15,2
15,1
12,3
12,4
11,3
11,4
10,3
10,4
9,4
8,4
7,4
6,3
6,4
5,4
4,1
4,2
4,3
4,4
3,1
3,2
3,3
3,4
2,1
2,2
2,3
2,4
1,1
1,2
1,3
1,4

Dimensions in inches

Figure 15

Figure 16 shows temperature rise data up to approximately 150 seconds of running time under essentially rated conditions for the 28 ply rated version of this tire. In this case calculations agree well with experimental measurements, although here the thicker section tire also requires a separate geometric description.

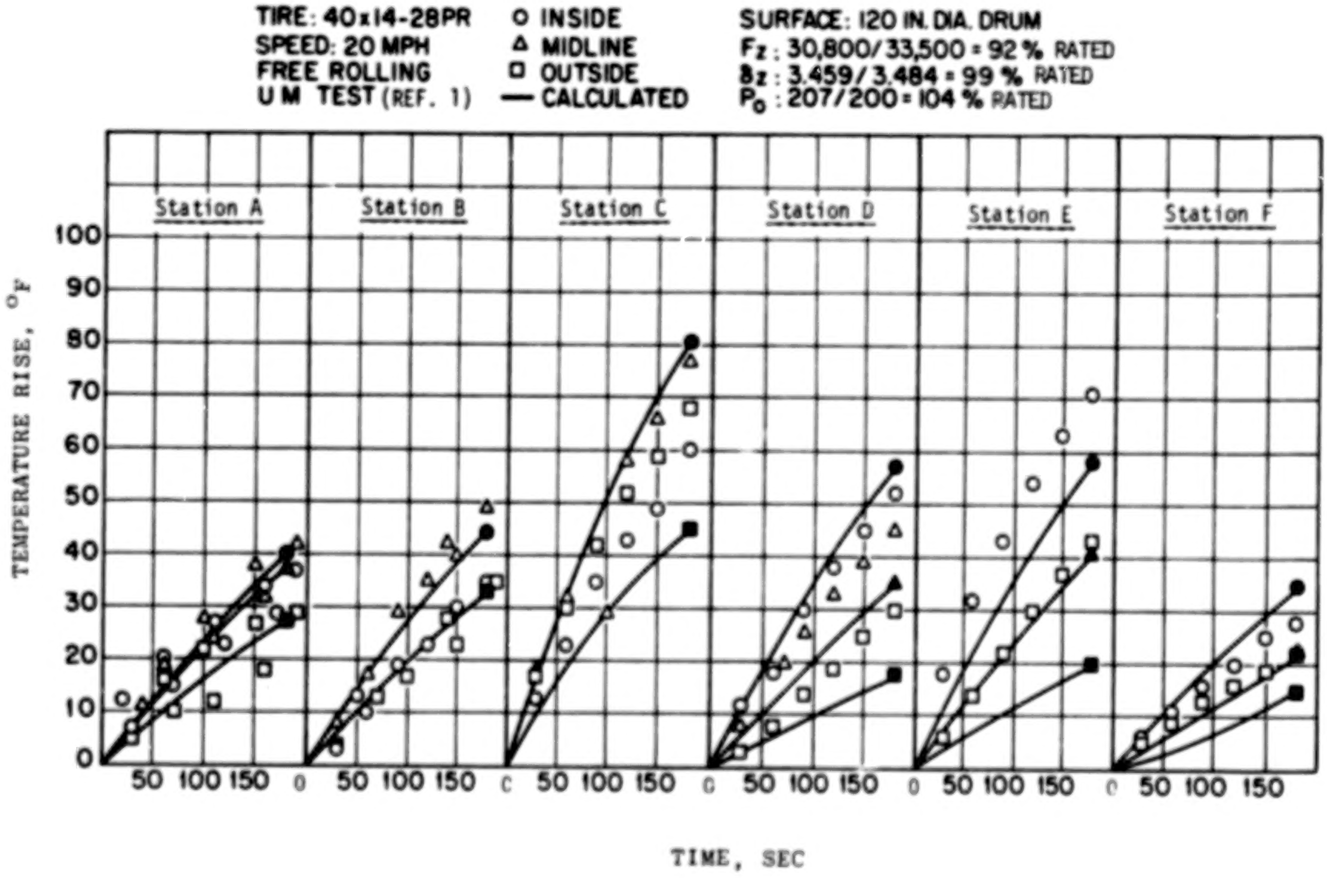

Figure 16

REFERENCE

1. Clark, Samuel K.; and Dodge, Richard N.: Heat Generation in Aircraft Tires Under Free Rolling Conditions. NASA CR-3629, 1982.

2. Clark, S. K. (ed.): Mechanics of Pneumatic Tires, NBS Monograph 122, National Bureau of Standards, 1981.

RESULTS FROM RECENT NASA TIRE THERMAL STUDIES

John L. McCarty
NASA Langley Research Center

ABSTRACT

This paper describes the testing technique and some results from an experimental study to determine tire temperature profiles to aid in defining the strength and fatigue limitations of the tire carcass structure. This effort is part of a program to explore analytically and through experiment the temperature distribution in an aircraft tire during free roll and braked and yawed rolling conditions. The analytical effort, together with a comparison with the experimental results, is discussed in the paper by Clark in this publication (ref. 1).

LOCATION OF THERMOCOUPLES IN TIRE THERMAL STUDY

Figure 1 shows the approximate locations of the eighteen thermocouples installed within the carcass of several tires to support the thermal study. As noted in the figure, the thermocouples were mounted on the inner and outer walls of the tires and along an approximate midline at six radial stations. Most of the thermocouple installation was accomplished by implanting the sensors in holes drilled into the tire carcasses after the carcasses had been buffed prior to retreading.

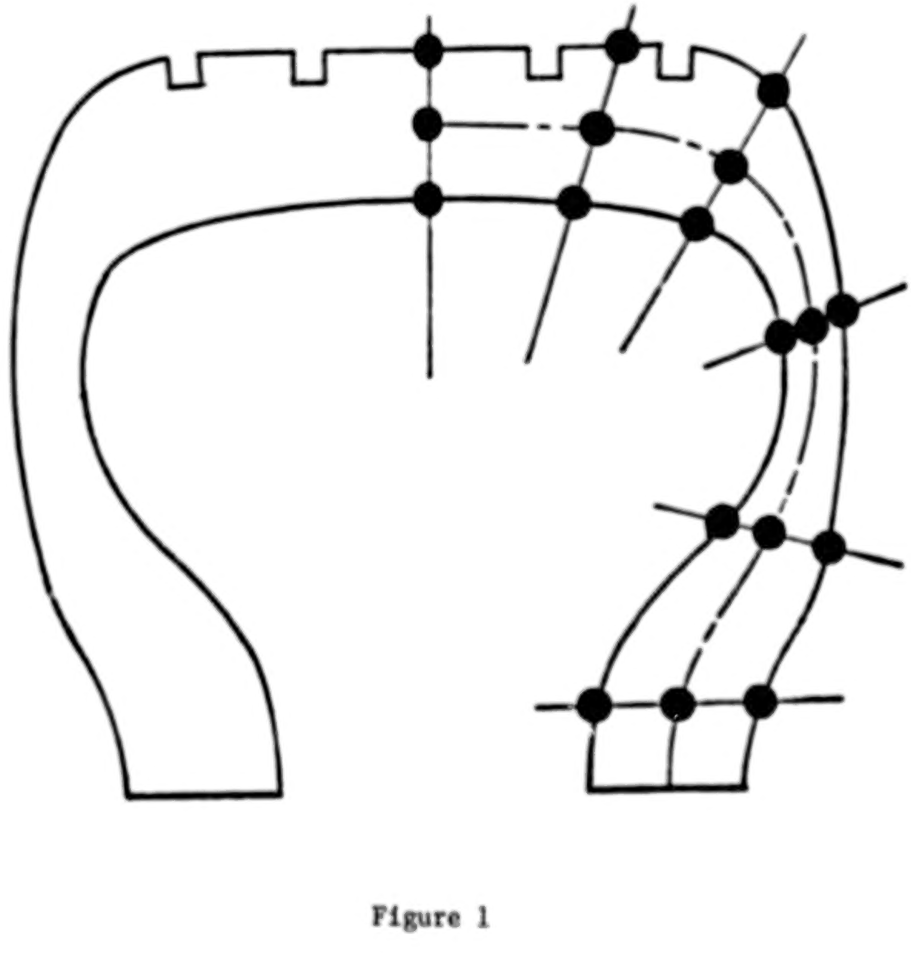

Figure 1

PHOTOGRAPH OF AN INSTRUMENTED TEST TIRE

Figure 2 is a photograph of a tire ready for testing, and shows how the outputs from the thermocouples were routed through a slip ring en route to a data logger located in the instrument section of the test vehicle pictured in figure 3. The tires for these tests were size 22 x 5.5, 12-ply rating, type VII aircraft tires.

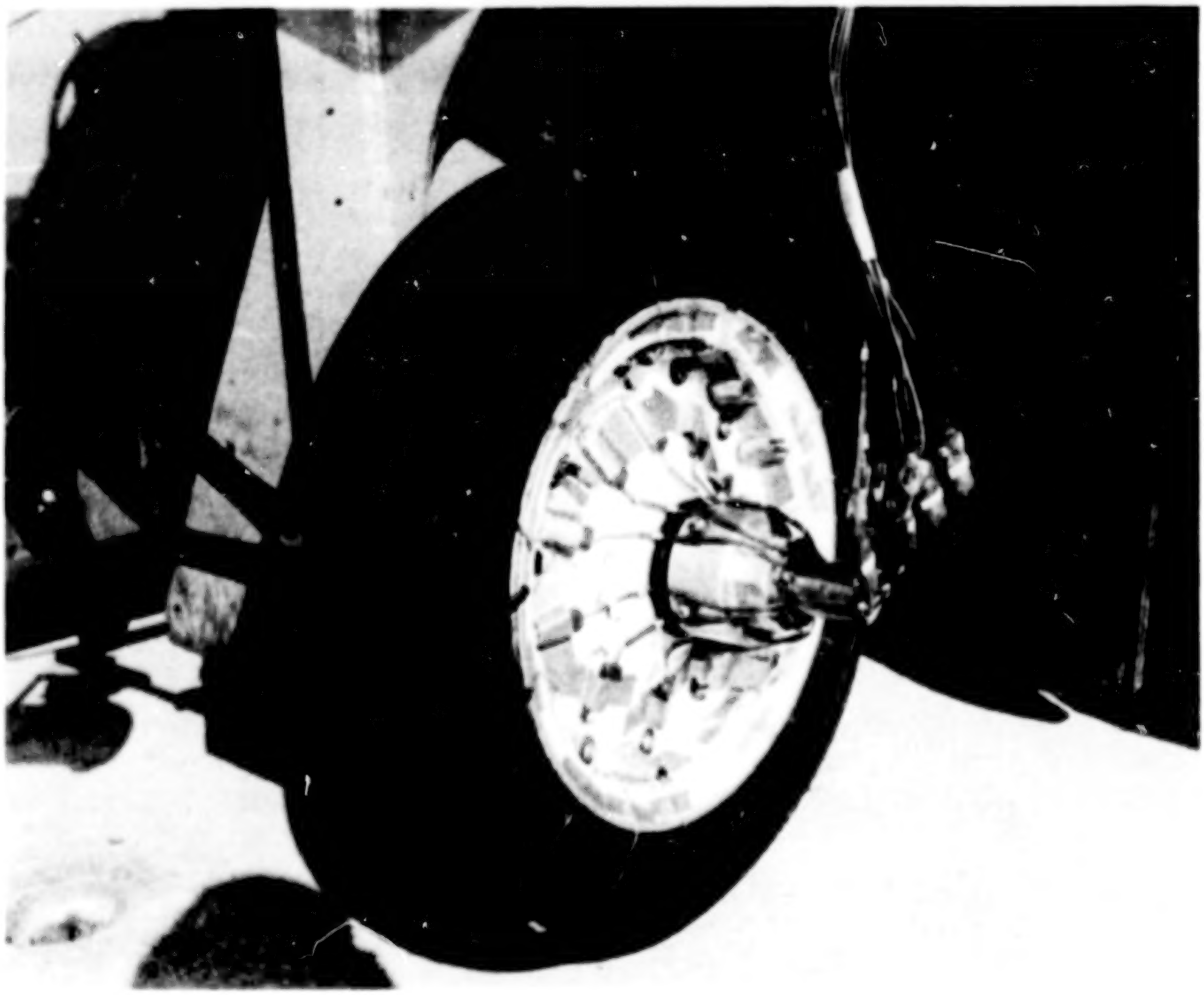

Figure 2

BEST DOCUMENT AVAILABLE

INSTRUMENTED TIRE TEST VEHICLE

Figure 3 is a photograph of the powered ground test vehicle used in this investigation. This vehicle consists of a truck which has been modified to accommodate a tire test fixture and supporting equipment. For the tests described here, the tires were vertically loaded to 4000 pounds and driven at 20 mph, except for one series where speeds were increased to 50 mph, over a known distance with temperature measurements recorded every 10 seconds. Data were taken with the tire free rolling, yawed rolling, and at fixed slip ratios to simulate braked-rolling conditions.

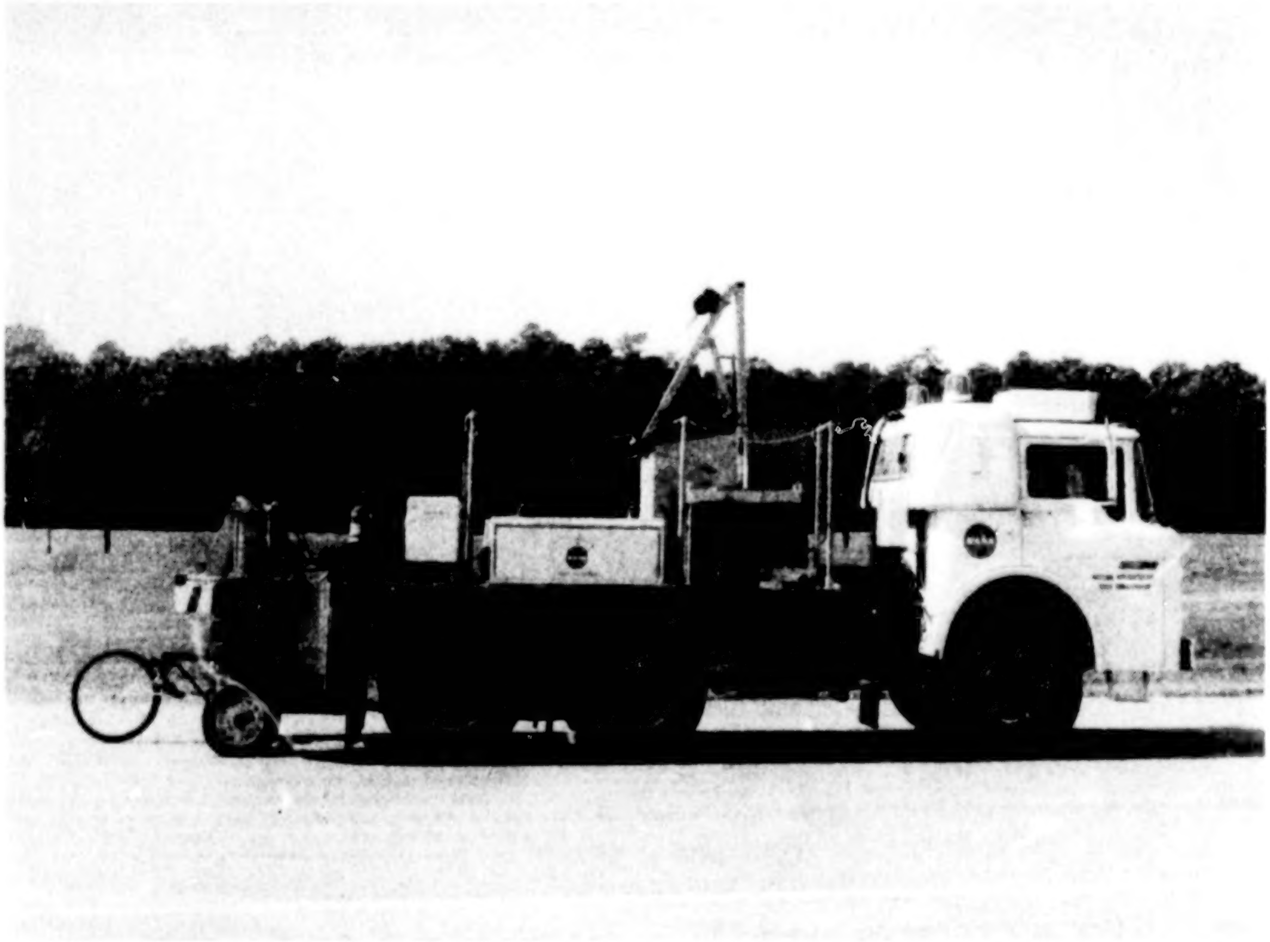

Figure 3

BEST DOCUMENT AVAILABLE

TYPICAL TEMPERATURES THROUGH THE TIRE CARCASS DURING FREE ROLLING

Figure 4 presents the time history of temperature buildup in six of the thermocouples as the tire in the free-rolling mode made two and a half passes of about 6500 feet each down an asphalt runway. As noted on the figure, the test tire was raised from the pavement surface following each pass while the test vehicle was being turned around for the return trip. The thermocouples were selected to illustrate the temperature rise through the tire carcass in the shoulder and bead areas. The figure clearly demonstrates that in both areas the rate of temperature buildup, and hence the magnitude of the temperature, is greatest along the interior wall, decreases through the carcass, and is lowest along the exterior wall. As would be expected because of tire flexure, the temperatures in the shoulder area are greater than the corresponding temperatures in the bead area.

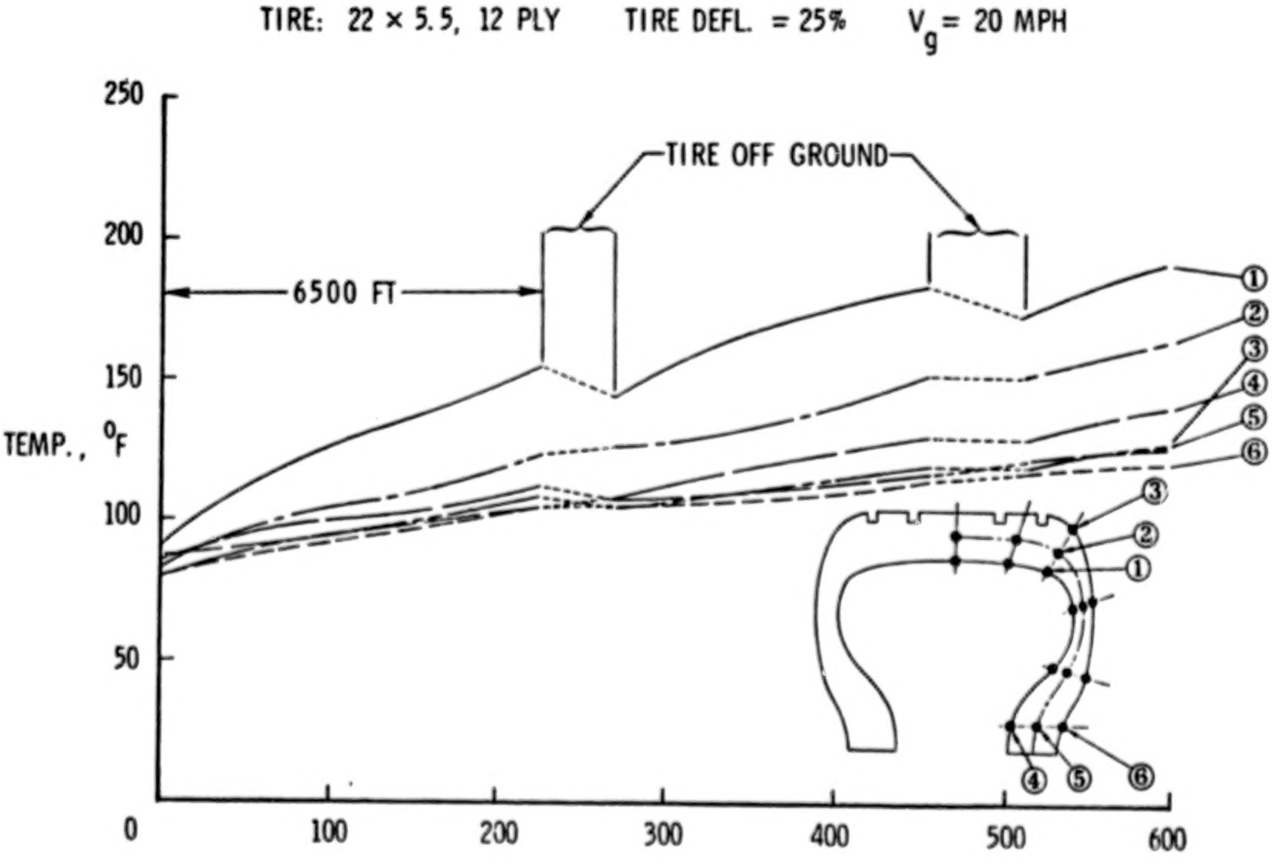

Figure 4

TYPICAL INTERIOR TIRE CARCASS TEMPERATURES DURING FREE ROLL

Temperature data from the six thermocouples installed along the tire internal wall are presented in figure 5 as a function of the free-roll distance. It is interesting to note that the maximum temperature was measured not in the center of the tread nor in the shoulder area, but between the two. The temperature in the bead area is again shown to be well below the other measured tire internal temperatures.

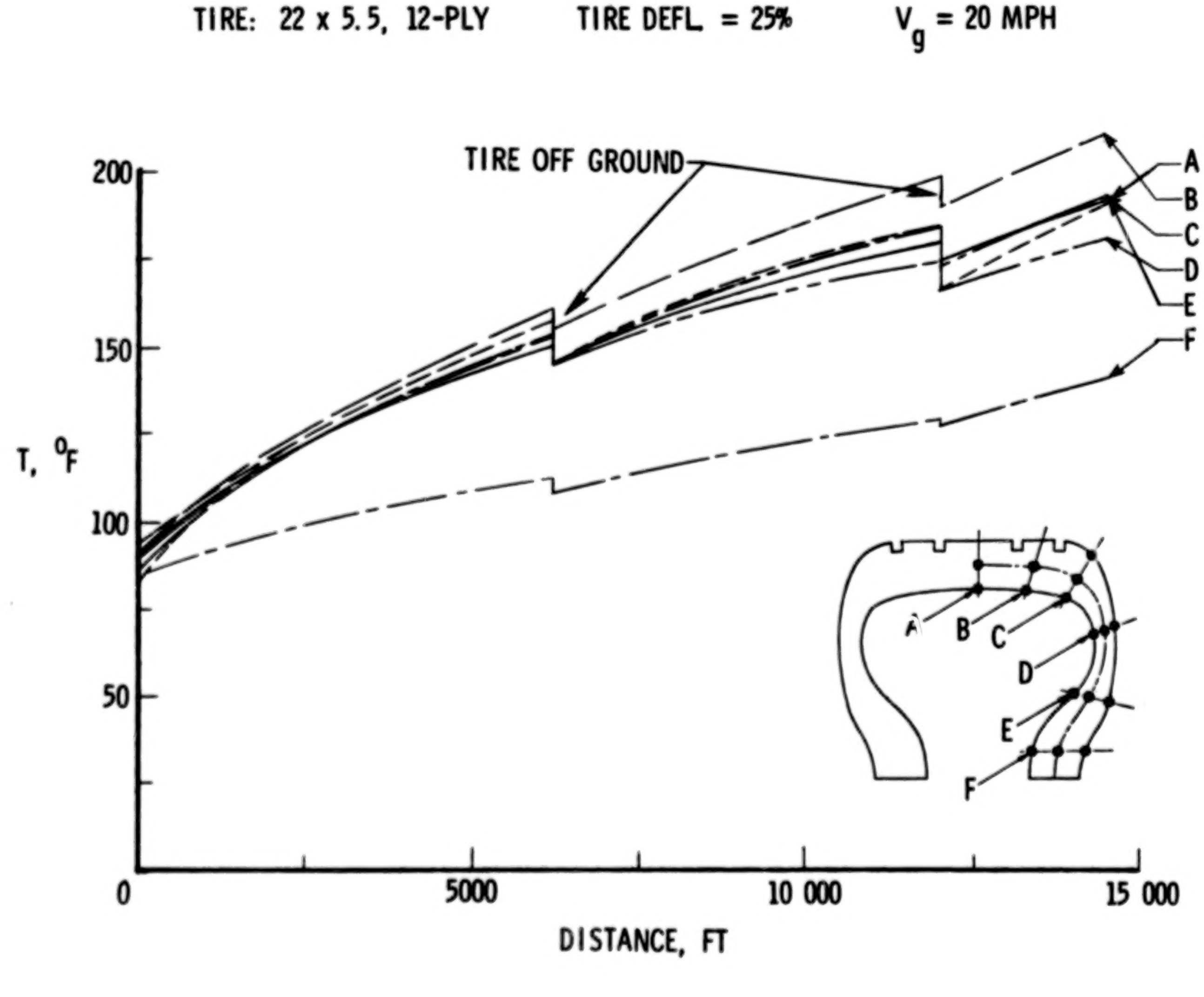

Figure 5

EFFECT OF TIRE DEFLECTION

Figure 6 illustrates the effect of tire deflection δ on the distribution of temperature within the tire carcass after the tire had free-rolled for a distance of 5000 feet. The different deflections in this case were obtained by changing the tire inflation pressure while maintaining the 4000-pound vertical loading. Although data are lacking in the tread region, similar tests on other tires showed little effect of tire deflection on temperatures in that area. However, the figure shows a pronounced effect on temperatures in the sidewall region. The higher temperatures associated with the greater deflections are attributed to the more severe sidewall flexing which increases with tire deflection. Similar trends were observed when the tire deflection was changed by varying the vertical load while maintaining a fixed inflation pressure.

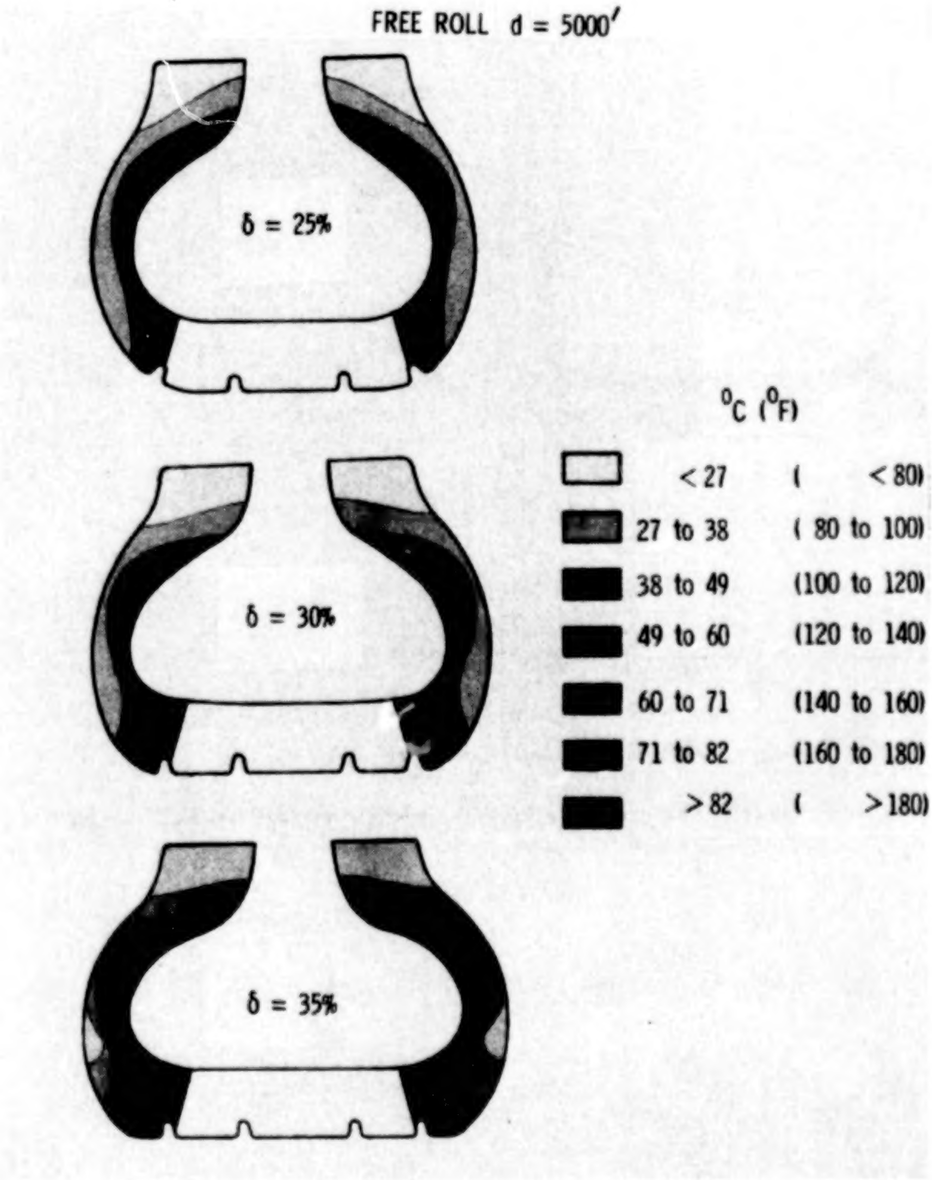
FREE ROLL d = 5000′
δ = 25%
δ = 30%
δ = 35%
°C (°F)
< 27 (< 80)
27 to 38 (80 to 100)
38 to 49 (100 to 120)
49 to 60 (120 to 140)
60 to 71 (140 to 160)
71 to 82 (160 to 180)
> 82 (> 180)

Figure 6

BEST DOCUMENT AVAILABLE

EFFECT OF YAW ANGLE

To examine the effect of yaw angle ψ on tire temperature distribution, a series of free-rolling tests was conducted where the tire was yawed to 3° and 6°. Because only one side of the tire was instrumented, two passes were required at each yaw angle with the tire yawed first in one direction (+3°, for example) and then in the other direction (-3°, for example) to complete the temperature picture. The results are illustrated in figure 7 which presents the tire temperature profiles after having traveled 7000 feet. The figure shows a considerable temperature build-up with yaw angle in the tread area and in the "downwind" sidewall of the tire with an accompanying cooling effect on the "upwind" side. The reduced temperature on the "upwind" side is apparently due to the stress relieving which occurs in the "upwind" sidewall when the shoulder area on that side is forced to roll partially into the footprint. Conversely, the greater tire distortion on the "downwind" side as the yaw angle is increased would account for those higher temperatures. The higher temperatures in the tread area can be explained by the increased scrubbing action in the tire footprint that is associated with increasing yaw angle.

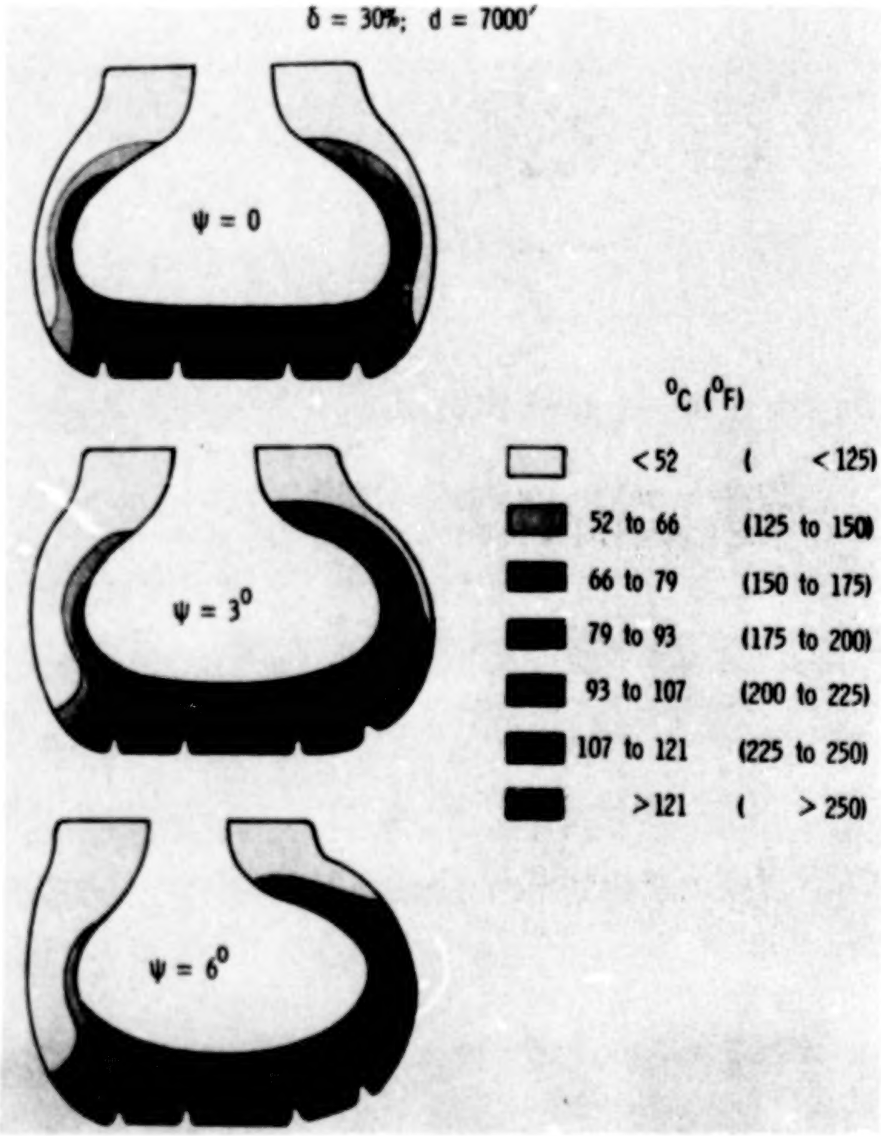

Figure 7

BEST DOCUMENT AVAILABLE

EFFECT OF BRAKING

Driving the test tire at fixed slip ratios provides a means for evaluating the effect of braking on the temperature buildup in the tire carcass. Figure 8 presents the temperature profiles after the tire had traveled 7000 feet first in free roll and subsequently at slip ratios of 5 and 10 percent. The figure shows that the influence of braking is essentially limited to the tread area. Minimal changes are noted in the temperature profiles of the sidewall regions.

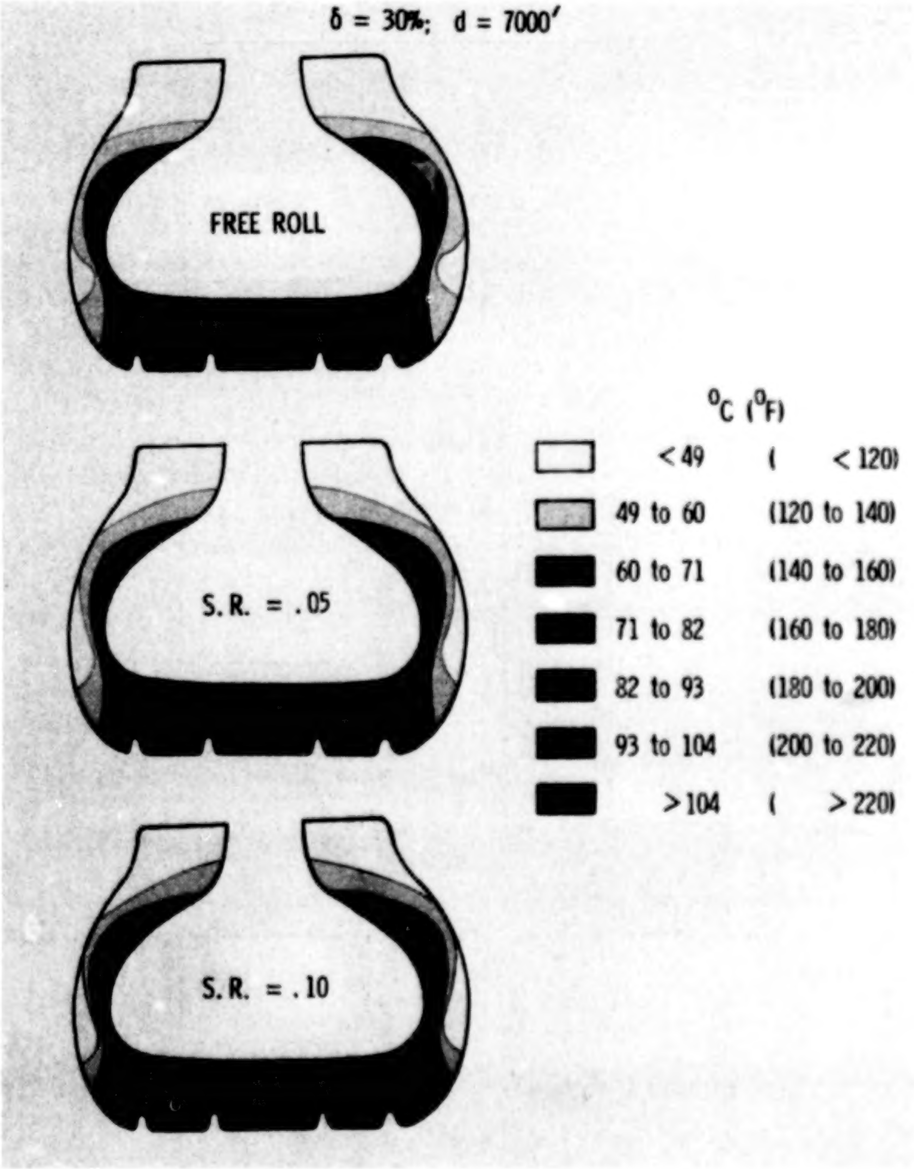
δ = 30%; d = 7000′
FREE ROLL
S.R. = .05
S.R. = .10
°C (°F)
< 49 (< 120)
49 to 60 (120 to 140)
60 to 71 (140 to 160)
71 to 82 (160 to 180)
82 to 93 (180 to 200)
93 to 104 (200 to 220)
> 104 (> 220)

Figure 8

BEST DOCUMENT AVAILABLE

EFFECT OF SPEED

Over the speed range of these tests, the influence of wheel speed on the tire temperature distribution is almost insignificant. As observed in figure 9, the sidewall temperature after free-rolling 7000 feet is essentially unaffected and only moderate increases can be seen in the tread temperature as the speed is increased. The rise in tread temperature at higher speeds is perhaps the result of the higher frequency squirming action which has been observed in the tire footprint.

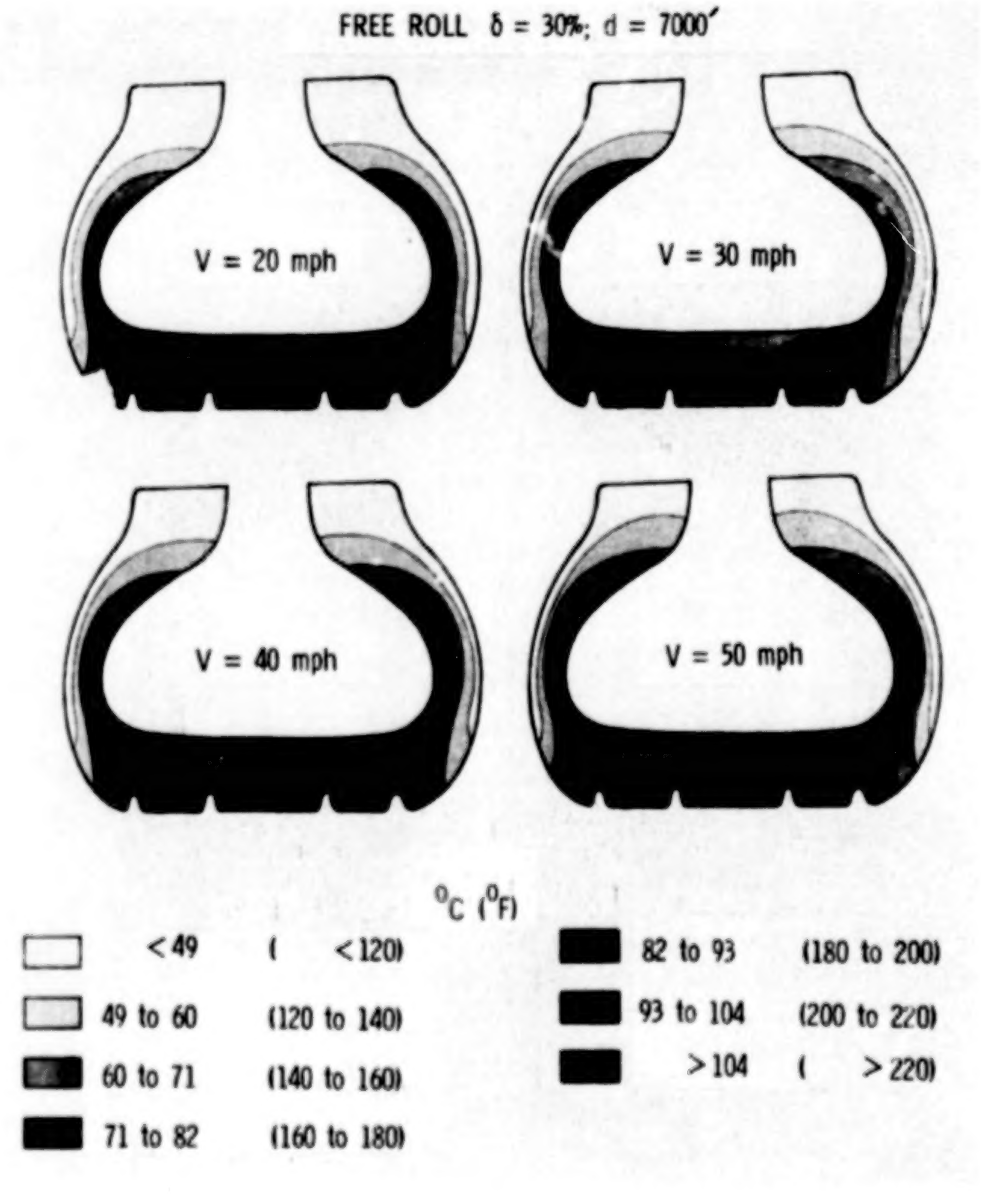

Figure 9

BEST DOCUMENT AVAILABLE

TIRE EQUILIBRIUM TEMPERATURES

The question arose during the course of this investigation as to whether the tire carcass would assume an equilibrium temperature profile if permitted to free roll for an indefinite period. To answer the question, many passes were made in both directions along a 7000-foot runway at 20 mph with a very brief turn-around time between passes to minimize any tire cooling. It became apparent after the tire had traveled approximately 65,000 feet that each thermocouple was approaching an equilibrium value. The final temperature profile, obtained after the tire had traveled in excess of 80,000 feet, is presented in figure 10 and shows temperatures approaching 300° F near the shoulder area. Note again that, particularly in the sidewall region, the temperatures along the inner wall are considerably greater than those near the outer surface. Also note that the centerline tread temperatures are somewhat lower than other temperatures in the tread.

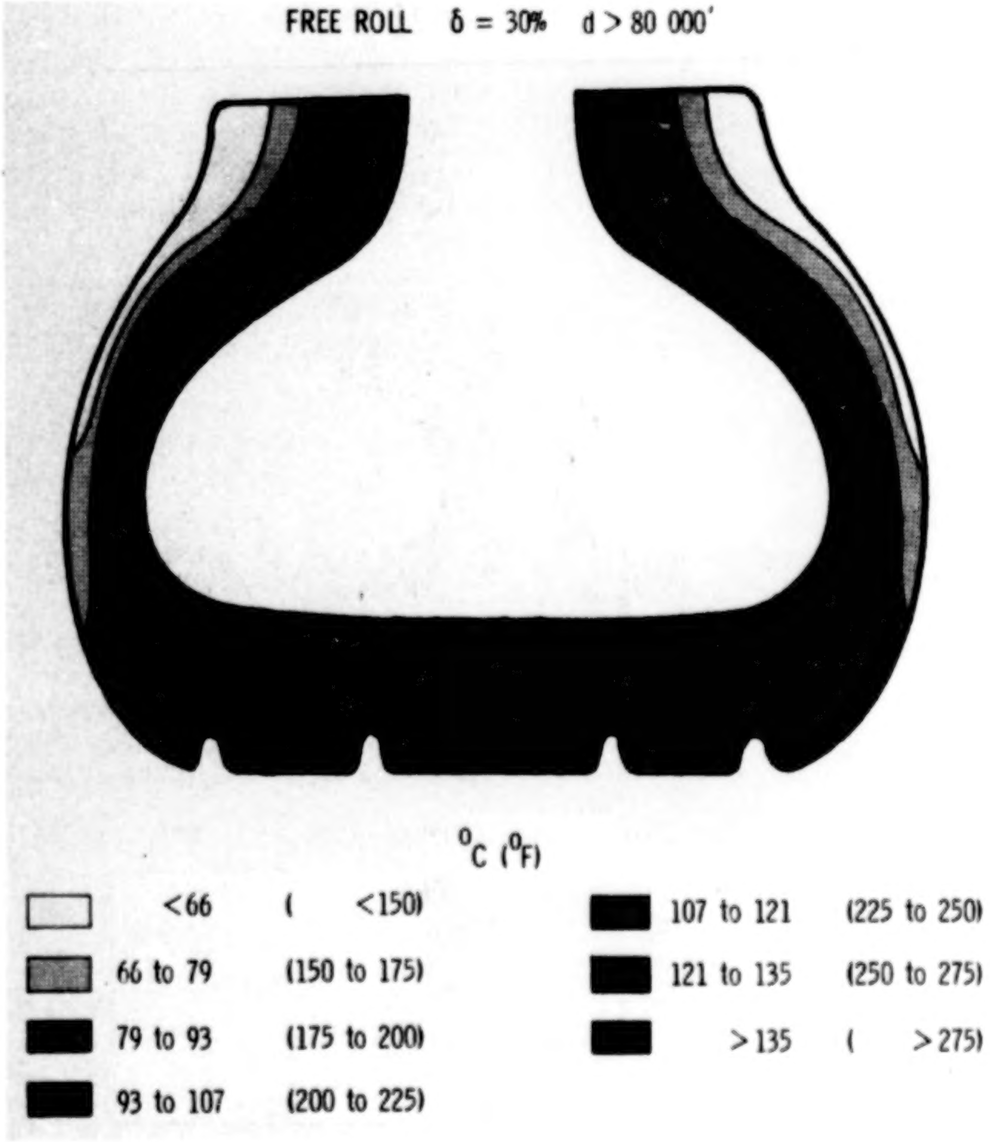
FREE ROLL δ = 30% d > 80 000'
°C (°F)
<66 (<150)
66 to 79 (150 to 175)
79 to 93 (175 to 200)
93 to 107 (200 to 225)
107 to 121 (225 to 250)
121 to 135 (250 to 275)
>135 (>275)

Figure 10

BEST DOCUMENT AVAILABLE

CONCLUDING COMMENTS

The results from a program to study tire temperature profiles to aid in defining the strength and fatigue limitations of an aircraft tire carcass structure suggest the following concluding comments.

- A testing technique has been developed for successfully measuring the thermal characteristics of a rolling tire.
- Tire shoulder and sidewall temperatures increase with increasing tire deflection due to either overload or underinflation.
- Tire tread and "downwind" sidewall temperatures increase with yaw angle.
- Large temperature increases are noted in the tread region during increased braking.
- Changes in ground speed (over the test range to 50 mph) produce insignificant effects on the temperature buildup in the tire carcass.

REFERENCE

1. Clark, Samuel K.: Heat Generation in Aircraft Tires. Tire Modeling, NASA CP-2264, 1983, pp. 193-210.

SUMMARY OF SESSION DISCUSSIONS

John A. Tanner

INTRODUCTION

General discussion periods were held at the end of each session to allow the participants to describe their own findings or to define problem areas in which they need help. In addition, a panel discussion was held among the session chairmen at the end of the workshop to review the status of tire modeling. These discussions identified two levels of tire modeling that were considered significant. One level was that required by the vehicle dynamicist who is concerned with the vehicle and tire combination and the response of the vehicle to braking and steering inputs, shimmy, and pavement roughness. The other level of modeling was that required by the tire designer who is concerned with detailed information on the stresses and strains associated with tire loading, carcass temperature profiles, and properties of the tire constituents. The following paragraphs will assess the status of tire modeling from the points of view of the vehicle dynamicist and the tire designer.

STATUS OF TIRE MODELING - VEHICLE DYNAMICIST POINT OF VIEW

The vehicle dynamicist is typically interested in the interaction between tire behavior and the performance of vehicular suspension systems or aircraft landing gear systems. For any simulation study, the dynamicist is generally seeking such tire response characteristics as surface interface friction, spring rates, hysteresis loss properties, and relaxation lengths. Ideally, these properties can only be obtained from experimental measurements, and this process may require considerable computer storage if the dynamicist is interested in simulations involving many different tire sizes or designs. However the use of semiempirical methods for predicting tire properties has met with some success. References 1 and 2 present examples for estimating mechanical properties of various aircraft tires.

The finite element method is generally considered to be too costly for this type of tire modeling, and the vehicle dynamicist typically resorts to much simpler models of the tire. The millions of well-behaved suspension systems and aircraft landing gear systems which provide good braking and cornering response and effectively eliminate shimmy and other potentially hazardous dynamic vibrations demonstrate the effectiveness of these simplified tire models.

From the point of view of the vehicle dynamicist, there is room for increased cooperation between the vehicle dynamicists in the automobile industry and the landing gear dynamicists in the aircraft industry. Although both groups of dynamicists work on similar tire problems, they tend to use different nomenclature. This fact suggests that the two groups generally do not communicate with each other or read each other's publications, and such a failure in communication can lead to a duplication of effort.

STATUS OF TIRE MODELING - TIRE DESIGNER POINT OF VIEW

The tire designer is interested in the load-carrying capability of the tire and hence requires a structural tire model for analytical studies. The development of reliable and cost effective structural tire models, however, is a formidable task. For example, the tire material properties are generally anisotropic and nonhomogeneous because of tire construction techniques. Such constituents as the nylon reinforcing cord and the rubber matrix tend to exhibit nonlinear elastic or viscoelastic behavior. Furthermore, typical loading conditions imposed upon the tire generally lead to large deformations and rotations and moderate strains. In addition, the material properties of the tire may be subject to temperature effects. The physics of tire loading and the thermal environment are not fully understood. All of these detrimental factors work in concert to complicate not only the modeling process but also the experimental techniques necessary to acquire corroborating data.

Current tire modeling studies usually employ large general purpose finite element codes such as ADINA, MARC, STAGS, and NASTRAN as the modeling tool. Unfortunately these codes are not designed to handle the array of technical problems associated with tire modeling, and early tire modeling efforts tended to produce results which were below expectation and thus led to some skepticism within the U.S. tire industry. Moreover, there is no communication among the tire modelers within the tire industry because of proprietary concerns, and this lack of communication can lead to a duplication of effort and the inability to apply a concerted effort to solve the problem.

The consensus of the workshop participants was that the development of finite element technology for tire design is a nonlinear structural mechanics problem that should be addressed vigorously, and this effort should be directed by an agency outside the tire industry. It was recommended that this effort include three tasks: (1) establish a family of benchmark tire modeling problems, (2) produce a data base of experimental measurements which characterize the tire response to these problems, and (3) develop a number of special purpose computer codes that will model this response.

REFERENCES

1. Smiley, Robert F.; and Horne, Walter B.: Mechanical Properties of Pneumatic Tires with Special Reference to Modern Aircraft Tires. NASA TR R-64, 1960.

2. Tanner, John A.; Stubbs, Sandy M.; and McCarty, John L.: Static and Yawed-Rolling Mechanical Properties of Two Type VII Aircraft Tires. NASA TP-1863, 1981.

BIBLIOGRAPHY

1. Akasaka, T.; and Kabe, K.: Deformation and Cord Tension of a Bias Tire in Contact with the Road. Tire Science and Technology, Vol. 5, No. 4, November 1977, pp. 171-201.

2. Andersen, Carl M.: Deep Anisotropic Shell Program for Tire Analysis. NASA CR-3483, Nov. 1981.

3. Andersen, G. E.: Prediction of the Natural Vibration Frequency for a Torus Shaped Air Spring and Mass System. M.S. Thesis, Department of Mechanical Engineering, University of Nebraska, 1975.

4. Anquez, L.; and Monthulet, A.: Freinage d'un Pneumatique (Braking of a Tire). La Recheche Aerospatiale, No. 1, 1981, pp. 13-31.

5. Avgerapoulos, G. N.; Janssen, M.; Potts, G. R.; and Walter, J. D.: Advances in Tire Composite Theory. ASTM Journal of Tire Science and Technology, Vol. 1, No. 2, May 1973, pp. 210-250.

6. Barson, C. W.; and Gough, V. E.: Measurement of Strain of Materials of Large Extensibility. British Journal of Applied Physics 13, 1963, 168-170.

7. Baumgarten, J. R.; and Andersen, G. E.: Analysis of Airspring Isolators. Proceedings of the 5th World Congress on ToMM, Vol. 1, ASME, New York, pp. 337-340.

8. Bergman, W.; and Clemett, H. R.: Tire Cornering Properties. Tire Science and Technology, Vol. 3, No. 3, Aug. 1975, pp. 135-163.

9. Bergman, W.: The Basic Nature of Vehicle Understeer-Oversteer. SAE Paper No. 957B, 1965.

10. Bergman, W.: Considerations in Determining Vehicle Handling Requirements. SAE Paper No. 69-0234, Jan. 1969.

11. Bernard, J. E.; Segel, L.; and Wild, R. E.: Tire Shear Force Generation During Combined Steering and Braking Maneuvers. SAE Paper No. 77-0852, 1977. (Previously presented at the Automotive Engineering Congress and Exposition, Feb. 23-27, 1976, Detroit).

12. Biderman, V. L.; Drozhzhin, P. K.; Pugin, V. A.; and Shchaveleva, V. F.: Experimental Investigation of Deformations in Elements of Pneumatic Tires (in Russian). Trans. Tire Research Inst. (NIIShP) 3, pp. 5-15, 1957 (State Scientific and Technical Publishing House, Moscow).

13. Biderman, V. L.: Deformation of Tyre Elements During Rolling. Revue Generale du Caoutchouc 36, 1959, pp. 1366-1371.

14. Biderman, V. L.; Pugin, V. A.; and Fil'ko, G. S.: Deformation and Stresses in the Cover Rubber of the Sidewall of a Radial Tyre. Soviet Rubber Technology 24 (7), 1965, pp. 18-20.

15. Black, R. J.: Comments on Synthesis of Tire Equations for Use in Shimmy and Other Dynamic Studies. AIAA Journal of Aircraft, April 1972.

16. Black, R. J.: Realistic Evaluation of Landing Gear Shimmy Stabilization by Test and Analysis. SAE Paper No. 76-0496, April 1976. (Also 1976 Trans. of the SAE, pp. 1695-1708.)

17. Bourcier de Carbon, C.: Etude Theorique Due Shimmy Des Roues D'Avion. Off. Nat. d'Etude et de Rech. Aer. 7, 1948. (Also published as Analytical Study of Shimmy of Airplane Wheels, NACA TM-1337, 1952.)

18. Browne, A. L.; and Whicker, D.: An Interactive Tire-Fluid Model for Dynamic Hydroplaning. Proc. ASTM Symposium on Frictional Interaction of Tires and Pavement, ASTM STP-793, 1983.

19. Browne, A. L.; and Arambages, A.: Modeling the Thermal State of Tires for Power Loss Calculations. SAE Paper No. 81-0163, February 1981.

20. Browne, A. L.; Whicker, D.; and Segalman, D. J.: A General Model for Power Loss in Pneumatic Tires. Engineering Mechanics Department, General Motors Research Laboratories, Warren, MI, 1980.

21. Browne, A.: Traction of Pneumatic Tires on Snow. The Physics of Tire Traction, Plenum Press, 1974, pp. 99-134.

22. Browne, A.; and Whicker, D.: Design of Tire Tread Elements for Optimum Thin Film Wet Traction. SAE Paper No. 77-0278, 1977.

23. Browne, A. L.: Predicting the Effect of Tire Tread Pattern Design on Thick Film Wet Traction. Tire Science and Technology, TSTCA, Vol. 5, No. 1, February 1977, pp. 6-28.

24. Bundorf, R. T.: The Influence of Vehicle Design Parameters on Characteristic Speed and Understeer. SAE Paper No. 67-0078, 1967.

25. Captain, K. M.; Wormley, D. N.; and Grande, E.: The Development and Comparative Evaluation of Analytical Tire Models for Dynamic Vehicle Simulation. Technical Report No. 11877, May 1974, TACOM, Mobility Systems Laboratory, U.S. Army Tank Automotive Command, Warren, MI.

26. Chakko, Mathew K.: Analysis and Computation of Energy Laws in Radial Tires. Presented at the 1st Conference on Tire Science and Technology, U. of Akron, Akron, OH, March 25-26, 1982.

27. Chakko, Mathew K.: Characterization of Energy Laws in Bending of Cords in Rubber Composites. Presented at the ACS Rubber Division Meeting, Chicago, IL, October 5-7, 1982.

28. Chomos, S. E.: Prediction of the Load-Deflection Characteristics of a Toroidal Air-Rubber Spring. M.S. Thesis, University of Nebraska, May 1979.

29. Clark, S. K.; and Staples, R. J.: Friction and Temperature Rise in Aircraft Tires. NASA CR-134666, March 1974.

30. Clark, S. K.; Dodge, R. N.; Lackey, J. I.; and Nybakken, G. H.: Structural Modeling of Aircraft Tires. J. Aircraft, Vol. 9, No. 2, pp. 162-167, February 1972.

31. Clark, S. K.: An Experimental Study of Pressure Distribution Curves Applicable to Pneumatic Tires. NASA CR-754, 1967.

32. Clark, S. K. (editor): Mechanics of Pneumatic Tires. NBS Monograph 122, National Bureau of Standards, 1981.

33. Clough, R. W.: Comparison of Three-Dimensional Finite Elements. Proc. Symposium on Application of Finite Element Methods in Civil Engineering, 1st, William H. Rowan and Robert M. Hackett, eds., Am. Soc. Civil Engineers, 1969,
34. pp. 1-26.

35. Collins, R. L.: Theories on the Mechanics of Tires and Their Application to Shimmy Analysis. AIAA Journal of Aircraft, April 1971, pp. 271-277.

36. Collins, R. L.; and Black, R. J.: Tire Parameters for Landing Gear Shimmy Studies. AIAA Journal of Aircraft, Vol. 6, No. 3, May-June, 1969, pp. 252-258.

37. Conant, F.; Potts, G. R.; and Sekula, P.: Dynamic Indoor Tire Testing and Fourier Transform Analysis. ASTM Journal of Tire Science and Technology, Vol. 4, No. 2, August 1976, pp. 66-85.

38. Conry, T. F.; and Seireg, A.: A Mathematical Programming Method for Design of Elastic Bodies in Contact. J. of Applied Mechanics, Trans. ASME, p. 387, June 1971.

39. Cooper, D. H.: Radial Stiffness of the Pneumatic Tyre. Trans. of the Institution of the Rubber Industry, Vol. 40, No. 1, 1964.

40. Cooper, D. H.: Distribution of Side Force and Side Slip in the Contact Area of the Pneumatic Tire. Kautschuk and Gummi 11 (10), Oct. 1958, 273-277.

41. Crisfield, M. A.: A First Incremental/Iterative Solution Procedure that Handles 'Snap-Through'. Computers and Structures, Vol. 13, pp. 55-62, 1981.

42. Csora, Thomas; and Potts, G. R.: Tire Vibration Studies - The State of the Art. Presented at the Winter Meeting of the Akron Rubber Group, Jan. 25, 1974. (Also ASTM J. Tire Science and Technology, Vol. 3, No. 3, Aug. 1975, pp. 196-210.) Cornell Univ., Buffalo, Jan. 1969.

43. Daughaday, H.; and Tung, C.: A Mathematical Analysis of Hydroplaning Phenomena. Cornell Aeronautical Laboratory Technical Report No. AG-2495-S-1, Buffalo, Jan. 1969.

44. Deak, Alexander L.: Stress Analysis of Aircraft Tires - Volume I. Analytical Formulations. Technical Report AFFDL-TR-76-11, Vol. 1, Air Force Flight Dynamics Laboratory, Feb. 1976.

45. Deak, A. L.; and Atluri, S.: The Stress Analysis of Loaded Rolling Aircraft Tires - Vol. 1 - Analytical Formulation. Technical Report AFFDL-TR-73-130, Air Force Flight Dynamics Laboratory, 1973.

46. DeEskinazi, J.; and Ridha, R. A.: Finite Element Analysis of Giant Earthmover Tires. Rubber Chemistry and Technology, Vol. 55, No. 4, September-October, 1982.

47. DeEskinazi, Jozef: A Finite-Element Model for the Stress Analysis of Pneumatic Tires in Contact with a Flat Surface. Ph.D. Thesis, Purdue Univ., 1976.

48. Dodge, R. N.; Larson, R. B.; Clark, S. K.; and Nybakken, G. H.: Testing Techniques for Determining Static Mechanical Properties of Pneumatic Tires. NASA CR-2412, June 1974.

49. Dodge, R. N.: Prediction of Pneumatic Tire Characteristics from a Cylindrical Shell Model. Report 02957-25-T, Office of Research Administration, the University of Michigan, Ann Arbor, MI, March 1966.

50. Dove, R. C.; and Adams, P. H.: Experimental Stress Analysis and Motion Measurement. Merrill: Columbus, Ohio, 1964.

51. Dugoff, H.; Fancher, P. S.; and Segel, L.: An Analysis of Tire Traction Properties and Their Influence on Vehicle Dynamic Performance. 1970 International Automobile Safety Conference Compendium, New York, Society of Automotive Engineers, 1970, pp. 341-366. (SAE Paper No. 70-0377.)

52. Dugoff, Howard; and Brown, B. J.: Measurement of Tire Shear Forces. SAE Paper No. 70-0092, 1970.

53. Dunham, R. S.; and Nickell, R. E.: Finite Element Analysis of Axisymmetric Solids with Arbitrary Loadings. Report No. 67-6, Department of Civil Engineering, University of California, Berkley, California, June 1967.

54. Ergatoudis, I.; Irons, B. M.; and Zienkiewicz, O. C.: Curved, Isoparametric, Quadrilateral Elements for Finite Element Analysis. International Journal of Solids and Structures, 4, 31-43, 1968.

55. Ervin, R. D.; Nisonger, R. L.; Mallikarjuarao, C.; and Gillespie, T. D.: The Yaw Stability of Tractor-Semitrailers During Cornering, Final Report. 3 volumes, Report No. UM-HSRI-79-21, Highway Safety Research Institute, Ann Arbor, 1979.

56. Ervin, R. D.; Nisonger, R. L.; and Mallikarjunarao, C.: Eliminating Yaw Instability in Tractor-Semitrailers During Cornering. HSRI Research Review, vol. 10, no. 1, July-Aug. 1979, pp. 1-17.

57. Fancher, P. S., Jr.; Dugoff, H.; and Ludema, K. C.: Eperimental Studies of Tire Shear Force Mechanics, Highway Safety Research Institute, Ann Arbor, July 1970.

58. Feng, W. W.; Tielking, J. T.; and Huang. P.: The Inflation and Contact Constraint of a Rectangular Mooney Membrane. ASME 75-APMW-6, ASME, 1975. (Also J. Appl. Mech., vol. 41, no. 4, Dec. 1974.)

59. Freitag, D. R.; and Green, A. J.: Distribution of Stress on an Unyielding Surface Beneath a Pneumatic Tire. Report No. MP4-469, U.S. Army Waterways Experiment Station, Vicksburg, MS, 1962.

60. Fromm, H.: Kurzer Bericht ueber die Geschichte der Theorie des Radflatterns. Ber. Lilienthal Ges. 140, 53, 1941. (Also published as Brief Report on the History of the Theory of Wheel Shimmy. Papers on Shimmy and Rolling Behavior of Landing Gear Presented at Stuttgart Conference, NACA TM-1365, Aug. 1954.)

61. Gallagher, R. H.; Padlag, J.; and Bijlaard, P. P.: Stress Analysis of Heated Complex Shapes. Journal of Aerospace Science, 32, 700-717, 1962.

62. Gassman, P. M.: Deflection and Contact Area of a Standing Torus. M.S. Thesis, Iowa State University, 1980.

63. Giles, C. G.; and Sabey, B. E.: The Effect of Pressure and Friction on Photographic Emulsions. British Journal of Applied Physics, Vol. 2, no. 6, 1951, p. 174.

64. Green, A. J.: Normal Stresses at the Tire-Soil Interface in Yielding Soils. Report No. MP4-629, U.S. Army Waterways Experiment Station, Vicksburg, MS, 1964.

65. Grossman, D. T.: F-15 Nose Landing Gear Shimmy, Taxi Test and Correlative Analyses. SAE Paper No. 80-1239, 1980.

66. Hegmon, R. R.: The Contribution of Deformation Losses to Rubber Friction. Rubber Chemistry and Technology, Vol. 42, 1969, pp. 1122-1135.

67. Hill, D. E.: Experimental Stress Analysis of an Inflated Toroidal Structure. M.S. Thesis, Dept. of Mechanical Engineering, Iowa State University, 1981.

68. Hill, D. E.; and Baumgarten, J. R.: Experimental Stress Analysis of a Thin-Walled Pressurized Torus Loaded by Contact with a Plane. Proceedings AIAA/ASME/ASCE/AHS 23rd Structures, Structural Dynamics, and Materials Conference, AIAA, 1982, pp. 369-373.

69. Hughes, T. J. R.; Taylor, R. L.; Sackman, J. L.; and Kanoknulchai, W.: Finite Element Method for a Class of Contact Impact Problems. Comp. Meth. in Appl. Mech. and Engineering, Vol. 8, p. 249, 1976.

70. Jankovich, E.: A Finite Element Method for the Analysis of Rubber Parts, Experimental and Analytical Assessment. Computers and Structures, vol. 14, no. 5-6, 1981, pp. 385-391.

71. Jankovich, E.; Eviard, G.; LeBlanc, F.; and Nottin, J. P.: Mixed Finite Element for Calculating Rubber Pieces Using Nonlinear Elasticity Laws, Experimental Verifications. Report No. FTD-ID(RS)T-1712-80, Air Force Systems Command, Wright Patterson Air Force Base, 1980.

72. Jankovich, E.: Non-Applicability of Linear Finite Element Programs to the Stress Analysis of Tires. NASA TM X-2637, September 1972, pp. 263-276.

73. Jankovich, E.: Finite Element Stress Analysis of Polymers at High Strains. NASA TM X-2893, September 1973, pp. 49-68.

74. Jankovich, E.: Stress Analysis as Applied to Polymers. Proc. INOVA Conference, Vol. 2 - New Energy, Ministére de l'Industrie, Paris, 1978.

75. Janssen, M. L.; and Walter, J. D.: Rubber Strain Measurings in Bias, Belted-Bias and Radial Ply Tires. J. Coated Fibrous Mater., vol. 1, Oct. 1971, p. 102.

76. Joy, T. J. P.; and Hartley, D. C.: Tire Characteristics as Applicable to Vehicle Stability Problems. Inst. Mech. Engrs., Proc. (Auto Div.), 1953-1954, pp. 113-122.

77. Kabe, K.; and Akasaka, T.: Deformation and Cord Tension of a Radial Tire in Contact with the Road.

78. Kaga, H.; Okamoto, K.; and Tozawa, Y.: Stress Analysis of a Tire Under Vertical Load by a Finite Element Method. Tire Science and Technology, Vol. 5, No. 2, June 1977, pp. 102-118.

79. Kalker, J. J.: On the Rolling Contact of Two Elastic Bodies in the Presence of Dry Friction. Department of Mechanical Engineering, Delft University of Technology, the Netherlands. WTHD No. 52, August 1973. (Also Ph.D. Thesis, Delft Univ., 1967.)

80. Kalnins, A.: Analysis of Shells of Revolution Subjected to Symmetrical and Non-Symmetrical Loads. Journal of Applied Mechanics, 31, 223, 1964.

81. Keller, H. B.: Practical Procedures in Path Following near Limit Point. In Computing Methods in Applied Sciences and Engineering (eds. Glowinski & Lions), North-Holland Publ, Inc., 1982.

82. Kern, W. F.: Strain Measurements on Tires by Means of Strain Gauges. Revue Generale du Caoutchouc 36, 1347-1365, 1959. (Also Kautschuk und Gummi 13, WT59-WT68, 1960.)

83. Klingbeil, W. W.: Theoretical Prediction of Test Variable Effects, Including Twin-Rolls, on Rolling Resistance. SAE Paper No. 80-0088, 1980.

84. Klingbeil, W. W.; Hong, S. W.; Kienle, R. N.; and Witt, H. W. H.: Theoretical and Experimental Analysis of Dual-Compound Tread Designs for Reduced Rolling Resistance. Paper No. 62, 122nd Meeting of the Rubber Division, American Chemical Society, Chicago, October 5-7, 1982.

85. Koch, J. B. C.: A Computer Model of Steady-State and Transient Traction Forces and Aligning Moment Developed by Pneumatic Tires. Report No. UM-HSRI-PF-75-2, Highway Safety Research Institute, Ann Arbor, Jan. 1975.

86. Koch, J. B. C.: Computer Simulation of Steady-State and Transient Tire Traction Performance. The Dynamics of Vehicles on Roads and on Railway Tracks, Proceedings of IUTAM Symposium, H. B. Pacejka, ed., Swets and Zeitlinger: Amsterdam, 1976, pp. 197-214.

87. Kraft, P.: Force Distribution in the Contact Surface Between Tire and Runway. Papers on Shimmy and Rolling Behavior of Landing Gear Presented at Stuttgart Conference, NACA TM-1365, Aug. 1954.

88. Langer, W.; and Potts, G. R.: Development of a Flat Surfaced Tire Test System. SAE Paper No. 80-0245, 1980.

89. Lauterbach, H. G.; and Ames, W. F.: Cord Stresses in Inflated Tires. Textile Research Journal 29, pp. 890- 29, 1959, pp. 890-900.

90. Le Tallec, P.; and Oden, J. T.: Existence and Characterization of Hydrostatic Pressure in Finite Deformations of Incompressible Elastic Bodies. Journal of Elasticity, Vol. 11, No. 4, pp. 341-357.

91. Li, Chin-Tsang; and Leonard, John W.: Finite Element Analysis of Inflatable Shells. Journal of the Engineering Mechanics Division, Proceedings of the American Society of Civil Engineering, Vol. 99, no. EM3, June 1973.

92. Lippman, S. A.; and Oblizajek, K. L.: The Distribution of Stress Between the Tread and the Road for Freely Rolling Tires. SAE Paper No. 74-0072, 1974.

93. Loo, Ming: A Mathematical Model of the Rolling Pneumatic Tire Under Load. Ph.D. Thesis, Univ. Michigan, 1980.

94. Loughborough, D. L.; Davies, J. M.; and Monfore, G. E.: The Measurements of Strains in Tires. Canadian J. of Research 28 (F), 1950, pp. 490-501. (Also Revue Generale du Caoutchouc 29, 1952, pp. 712-716.)

95. Lowrey, Richard D.: Optimization of Orthotropic Layered Shells of Revolution by the Finite Element Method. Presented at the 31st Annual Conference of the Society of Aeronautical Weight Engineers, Inc., Paper No. 939, May 22-25, 1972, Atlanta, GA.

96. Luchini, John Remo: Mathematical Model for Rubber Hysteresis. Ph.D. Dissertation, Univ. of Michigan, 1977.

97. Mack, M. J., Jr.: The Finite Element Analysis of an Inflated Toroidal Structure. M.S. Thesis, Dept. of Mechanical Engineering, Iowa State University, 1981.

98. Mack, M. J.; Gassman, P. M.; and Baumgarten, J. R.: The Analysis of a Thin-Walled Pressurized Torus Loaded by Contact with a Plane. Proceedings AIAA/ASME/ASCE/ASH 23rd Structures, Structural Dynamics, and Materials Conference, AIAA, pp. 181-187.

99. Markwick, A. H. D.; and Starks, H. J. H.: Stresses Between Tire and Road. J. Inst. Civil Engineers 16, 309 (1941).

100. Melosh, R. J.: Structural Analysis of Solids. Journal of the Structural Division, ASCE, 89, No. ST4, 205-224, 1963.

101. Mercier, J.; Fremau, J.; and Rocha, A.: Large Deformations and Stresses of a Thin, Highly Elastic, Toroidal Shell Under Internal Pressure. Int. J. Solids Structures, 1970, Vol. 6, pp. 1233-1241.

102. Nisonger, R. L.; and Ervin, R. D.: Measurement of Ride Vibrations on Semitrailers Incorporating Different Suspensions. Report No. UM-HSRI-79-57, Highway Safety Research Institute, Ann Arbor, 1979.

103. Nordeen, D. L.: Analysis of Tire Lateral Forces and Interpretation of Experimental Tire Data. SAE Paper No. 67-0173, 1967.

104. Oden, J. T.; and Pires, E. B.: Nonlocal and Nonlinear Friction Laws and Variational Principles for Contact Problems in Elasticity. Journal of Applied Mechanics, in press, 1983.

105. Oden, J. T.: Finite Elements of Nonlinear Continua. McGraw-Hill, New York, 1972.

106. Oden, J. T.; and Jacquotte, O.: Stability of RIP Methods for Stokesian Flows. TICOM Report 82-8, Texas Inst. for Computational Mechanics, Austin, 1982.

107. Oden, J. T.: Penalty Methods for Constrained Problems in Nonlinear Elasticity. IUTAM Symposium on Finite Elasticity, Martinum-Nijhoff Publishers, The Hague, pp. 281-300, 1982.

108. Oden, J. T.; and Pires, E. B.: Numerical Analysis of Certain Contact Problems in Elasticity with Non-Classical Friction Laws. Computers and Structures, in press, 1983.

109. Oguoma, O. N.: Analysis of the Contact Area of Toroidal Air Springs. M.S. Thesis, Iowa State University, 1980.

110. Pacejka, H. B.: Study of the Lateral Behaviour of an Automobile Moving Upon a Flat Level Road. Cornell Aeronautical Laboratory Report YC-857-F-23, 1958.

111. Pacejka, H. B.: Some Recent Investigations into Dynamics and Frictional Behavior of Pneumatic Tires. Proc. GM Symp. Physics of Tire Traction, eds. D. F. Hays and A. L. Browne, Plenum Press, New York, 1974, p. 257.

112. Pacejka, H. B.: The Wheel Shimmy Phenomenon. Ph.D. Dissertation, Tech. Univ. of Delft, The Netherlands, 1966.

113. Pacejka, H. B.: Dynamic Frequency Response of Pneumatic Tires to Lateral Motion Inputs. Proceedings of the 2nd Conference on Motor Vehicles and Motor Engineering, Vol. 1, Scientific Society of Mechanical Engineers, Budapest, 1971, pp. 43-52.

114. Pacejka, H. B.: Analysis of the Dynamic Response of a Rolling String-Type Tire Model to Lateral Wheel-Plane Vibrations. Vehicle System Dynamics, vol. 1, no. 1, May 1972, pp. 37-66.

115. Pacejka, H. B.; and Fancher, P. S.: Hybrid Simulation of Shear Force Development of a Tire Experiencing Longitudinal and Lateral Slip. XIV International Automobile Technical Congress of FISITA, Inst. of Mechanical Engineers, 1972, pp. 3.78-3.85.

116. Pacejka, H. B.; and Mital, N. K.: A Hybrid Computer Model of Tire Shear Force Generation (revised). Highway Safety Research Institute, Ann Arbor, 1972.

117. Padovan, J.: On Moving Thermal Contact Problems. AIAA J., vol. 15, 1977, p. 1811.

118. Padovan, J.; and Zeid, I.: On the Development of Traveling Load Finite Elements. Computers and Structures, vol. 12, no. 1, July 1980, pp. 77-83.

119. Padovan, J.: On Viscoelasticity and Standing Waves in Tires. Tire Science and Technology, Vol. 4, p. 233, 1976.

120. Padovan, J.: Circumferentially Traveling Radial Loads on Rings and Cylinders. Int. J. of Nonlinear Mechanics, Vol. 12, p. 241, 1977.

121. Padovan, J.; and Zeid, I.: On the Development of Rolling Contact Elements. The General Problem of Rolling Contact, vol. 40, A. L. Browne and N. T. Tsai, eds., ASME, 1980, pp. 1-17.

122. Padovan, J.; and Arechaga, T.: Formal Convergence Characteristics of Elliptically Constrained Incremental Newton-Raphson Algorithms. Int. J. Eng. Sci., vol. 20, no. 10, 1982, pp. 1077-1097.

123. Padovan, Joseph: Quasi-Analytical Finite Element Procedures for Axisymmetric Anisotropic Shells and Solids. Computers and Sciences, Vol. 4, pp. 467-483, 1974.

124. Parikh, Prashant D.: A Finite Element Analysis of the Static and Dynamic Behavior of the Automobile Tire. Ph.D. Dissertation, Texas Tech. Univ., Lubbock, 1977.

125. Patel, H. P.: Mathematical Analysis of Statically Loaded Pneumatic Tires. Ph.D. Thesis, North Carolina State University, Raleigh, 1975.

126. Patterson, R. G.: The Measurement of Cord Tensions in Tires. Rubber Chemistry and Technology 42, 812-822, 1969.

127. Pires, E. B.: Analysis of Nonclassical Friction Laws for Contact Problems in Elastostatics. Ph.D. Dissertation, University of Texas, Austin, 1982.

128. Potter, J. M.: Measurement of Strain on Curved Surfaces Using the Moire Method. M.S. Thesis, University of Illinois, 1968.

129. Pottinger, M. G.; Marshall, K. D.; and Arnold, G. A.: Effects of Test Speed and Surface Curvature on Cornering Properties of Tires. SAE Paper No. 76-0029, Feb. 1976.

130. Potts, G. R.; and Corsa, T. T.: Tire Vibration Studies. The State of the Art. Tire Sci. and Tech., vol. 3, no. 3, Aug. 1975, p. 135.

131. Potts, G. R.; Bell, C. A.; Charek, L.; and Roy, T.: Tire Vibrations. ASTM Journal of Tire Science and Technology, Vol. 5, No. 4, Nov. 1977, pp. 212-225.

132. Potts, G. R.: Trends and Techniques in Tire Rolling Resistance Testing. Presented at the ASTM F-9 Symposium on Tires, Akron, Ohio, May 1981.

133. Potts, G. R.: Tire Power Loss: The Effect of Heat Conduction Through the Wheel. Presented at the Symposium on Rolling Resistance, Rubber Division of the American Chemical Soc., Chicago, Oct. 5-8, 1982.

134. Potts, G. R.; and Walker, Hugh F.: Truck Vibrations - An Old Problem with a Modern Solution via Computer. Presented at the National Meeting of the American Astronautical Society, October 23-25, 1969, Las Cruces, New Mexico.

135. Potts, G. R.: Application of Holography to the Study of Tire Vibrations. ASTM Journal of Tire Science and Technology, Vol. 1, No. 3, August 1973, pp. 255-266.

136. Potts, G. R.; and Walker, Hugh F.: Nonlinear Truck Ride Analysis. ASME Paper 73-DET-119, 1973. (Also J. Eng. for Industry, vol. 96, no. 2, May 1974, pp. 597-602.

137. Pugin, V. A.: Electrical Strain Gages for Measuring Large Deformations. Soviet Rubber Technology 19 (1), 23-26, 1960.

138. Rheinboldt, W. C.: Numerical Analysis of Continuation Methods for Nonlinear Structural Problems. Computers and Structures, Vol. 13, pp. 103-113, 1981.

139. Ridha, R. A.: Analysis of Pressurized Composite Shells Deflected Against Rigid Flat Surfaces. Proceedings of the Symposium on Applications of Computer Methods in Engineering. Vol. 11, 1977, pp. 1075-0183.

140. Ridha, R. A.; Satyamurthy, K.; Hirschfelt, L. R.; and Holle, R. E.: Contact Loading of a Rubber Disk. First Meeting of the Tire Society, Akron, Ohio, March 25-26, 1982.

141. Ridha, R. A.: Analysis for Tire Mold Design. Tire Science and Technology Vol. 2, No. 3, August 1974, pp. 195-210.

142. Ridha, R. A.; and Clark, S. K.: Tire Stress and Deformation. In Mechanics of Pneumatic Tires, Ch. 7 (S. K. Clark, Ed.), U. S. Government Printing Office, Washington, DC, 1981.

143. Ridha, R. A.: Computation of Stresses, Strains, and Deformations of Tires. Rubber Chemistry and Technology, Vol. 53, No. 4, September-October, 1980, pp. 849-902.

144. Riks, E.: The Applications of Newton's Method to the Problems of Elastic Stability. J. Appl. Mech., Vol. 39, pp. 1060-1066, 1972.

145. Robbins, D. H.: The Contact of Certain Elastic Shells with Rigid Flat Surfaces. Report 05609-7-T (Office of Research Administration, The University of Michigan, Ann Arbor, MI, Sept. 1965).

146. Rogers, L. C.: Theoretical Tire Equations for Shimmy and Other Dynamic Studies. J. of Aircraft, Vol. 9, No. 8, Aug. 1972, p. 585.

147. Rogers, L. C.; and Brewer, H. K.: Synthesis of Tire Equations for Use in Shimmy and Other Dynamic Studies. J. of Aircraft, Vol. 8, No. 9, Sep. 1971, p. 689.

148. Sabey, B. E.; and Lupton, G. N.: Photography of the Real Contact Area of Tires During Motion. Report No. LR64, Road Research Laboratory, Harmondsworth, England, 1967.

149. Saito, Y.: A Study of Dynamic Steering Properties of Pneumatic Tires. Proc. 9th FISITA Intl. Auto. Tech. Congress, 1962, pp. 101-115.

150. Saleh, Hamdi Ahmed Elsaye: Development of Mathematical Models to Describe the Wear Process in Viscoelastic Materials. Ph.D. Thesis, North Carolina State Univ., Raleigh, 1979.

151. Sawyers, K. N.; and Rivlin, R. S.: Stability of a Thick Elastic Plate Under Thrust. Journal of Elasticity, 12, pp. 101-125, 1980.

152. Schapery, R. A.; and Tielking, J. T.: Investigation of Tire-Pavement Interaction During Maneuvering: Theory and Results. Report FHWA-RD-78-72, Federal Highway Administration, Washington, DC, June 1977.

153. Schapery, R. A.: Analytical Models for the Deformation and Adhesion Components of Rubber Friction. Tire Science and Technology, Vol. 6, No. 1, February 1978, pp. 3-47.

154. Schapery, R. A.: Analysis of Rubber Friction by the Fast Fourier Transform. Tire Science and Technology, Vol. 6, No. 2, May 1978, pp. 89-113.

155. Schippel, H. F.: Fabric Stresses in Pneumatic Tires. Industrial and Engineering Chemistry 15, 1121-1131, 1923.

156. Schuring, D. J.: Dynamic Response of Tires. Tire Science and Technology, TSTCA, Vol. 4, No. 2, May 1976, pp. 115-145.

157. Segalman, D.: Modeling Tire Energy Dissipation for Power Loss Calculations. SAE Paper No. 81-0162, Feb. 1981.

158. Segel, L.: Tire Traction on Dry Uncontaminated Surfaces. Proc. GM Symp. Physics of Tire Traction, D. F. Hays and A. L. Browne, eds., Plenum Press: NY, 1974, p. 65.

159. Segel, Leonard: Research in the Fundamentals of Automobile Control and Stability. SAE Paper No. 769, 1956.

160. Segel, L.: Lateral Mechanical Characteristics of Non-Stationary Pneumatic Tires. Cornell Aeronautical Laboratory, Inc. Report No. YD-1059-F-1, April 1956.

161. Segel, L.: Theoretical Prediction and Experimental Substantiation of the Response of the Automobile to Steering Control. Inst. Mech. Engrs, Proc. (Auto. Div.), No. 7, 1956-1957.

162. Segel, L.; and Wilson, R.: Requirements for Describing the Mechanics of Tires Used on Single-Track Vehicles. The Dynamics of Vehicles on Roads and on Railway Tracks, Proc. IUTAM Symp., H. B. Pacejka, ed., Swets and Zeitlinger: Amsterdam, 1976, pp. 173-186.

163. Segel, L.: Force and Moment Response of Pneumatic Tires to Lateral Motion Inputs. Trans. ASME, J. Engr. for Ind. 88B91, 1966.

164. Seitz, N.; and Hussmann, A. W.: Forces and Displacement in Contact Area of Free Rolling Tires. SAE Transactions, Vol. 80, Paper No. 71-0626, 1971.

165. Sims, D. F.; and Halpin, J. C.: Methods for Determining the Elastic and Viscoelastic Response of Composite Materials. Composite Materials: Testing and Design (Third Conference), ASTM Special Technical Publication 546, Philadelphia, PA, 1974, pp. 46-66.

166. Smiley, R. F.: Correlation, Evaluation, and Extension of Linearized Theories for Tire Motion and Wheel Shimmy. NACA TN-3632, June 1956.

167. Smiley, R. F.; and Horne, W. B.: Mechanical Properties of Pneumatic Tires With Special Reference to Modern Aircraft Tires. NACA TN-4110, 1958.

168. Smiley, Robert C.: Correlation, Evaluation, and Extension of Linearized Theories for Tire Motion and Wheel Shimmy. NACA TN-1299, 1957.

169. Tabaddor, F.: Review of Fatigue in Rubber and Rubber Composites. Paper No. 21, American Chem. Soc., Rubber Div., 1982.

170. Tabaddor, Farhad; and Chen, C. H.: Reinforced Composite Material with Curved Fibers. Journal of Spacecraft and Rockets, Vol. 8, No. 3, March 1971, p. 301.

171. Tabaddor, Farhad: A Note on Effective Moduli of Composite Materials. Journal of Applied Mechanics, June 1972.

172. Tabaddor, Farhad: Constitutive Equations for Bi-Modulus Elastic Materials. Presented at the Third Canadian Congress of Applied Mechanics, Calgary, Alberta, Canada, May 1971. (Also AIAA J., April 1972.)

173. Tabaddor, Farhad: Large Deformations of Extensible Cord-Reinforced Materials. International Conference on Variational Methods in Engineering, September 25-29, Southhampton, England, March 1973.

174. Tabaddor, Farhad; and Chen, C. H.: On the Effective Moduli of Layered Composites. Journal of Spacecraft and Rockets, April 1974.

175. Tabaddor, Farhad: Large Deformations of Cord-Reinforced Multilayered Shells. Presented before the 15th Midwestern Mechanics Conference, University of Illinois, Chicago, March 1976.

176. Tabaddor, Farhad: Two-Dimensional Finite Element Analysis of Bi-Modulus Materials. Second International Conference on Computational Methods in Nonlinear Mechanics, Univ. of Texas, Austin, March 26-29, 1979. (Also J. Fibre Sci. and Techn., vol. 14, 1981.)

177. Tabaddor, Farhad: Finite Element Analysis of Hyperelastic Structures. Research in Nonlinear Structural and Solid Mechanics, NASA CP-2147, 1980.

178. Tabaddor, Farhad; and Stafford, J. R.: Nonlinear Vibration of Cord-Reinforced Composite Shells. Computers and Structures, June 1981.

179. Tabaddor, F.; and Clark, S. K.: Linear and Nonlinear Viscoelastic Constitutive Relations of Cord Reinforced Elastomers. International Conference on Constitutive Laws for Engineering Materials, Tucson, Jan. 10-14, 1982.

180. Tielking, J. T.: Analytical Tire Model. Phase I: The Statically Loaded Toroidal Membrane, Final Report. Report No. UM-HSRI-PF-75-7, Highway Safety Research Institute, Ann Arbor, 1975.

181. Tielking, J. T.; and Mital, N. K.: A Comparative Evaluation of Five Tire Traction Models. Report UM-HSRI-PF-74-2, Highway Safety Research Institute, University of Michigan, Ann Arbor, January 1974.

182. Tielking, J. T.; Fancher, P. S.; and Wild, R. E.: Mechanical Properties of Truck Tires. SAE Paper No. 73-0183, 1973.

183. Tielking, J. T.: Plane Vibration Characteristics of a Pneumatic Tire Model. SAE Paper No. 65-0492, 1965.

184. Tielking, J. T.; and Schapery, R. A.: Calculation of Tire-Pavement Shear Forces. The General Problem of Rolling Contact, vol. 40, A. L. Browne and N. T. Tsai, eds., ASME, 1980.

185. Tielking, J. T.; and Schapery, R. A.: An Analytical Model for Tire Power Loss Calculations. SAE Conference Proceedings P-74, R&D Planning Workshop on Tire Rolling Losses and Fuel Economy, Transportation Systems Center (DOT), Cambridge, MA, October 1977, pp. 95-101.

186. Tielking, J. T.; McIvor, I. K.; and Clark, S. K.: A Modified Linear Membrane Theory for the Pressurized Toroid. ASME Paper No. 70-WA/APM-49, 1969.

187. Tielking, J. T.; and Feng, W. W.: The Application of the Minimum Potential Energy Principle to Nonlinear Axisymmetric Membrane Problems. ASME Paper No. 74-WA/APM-6, 1974. (Also J. Appl Mech., vol. 41, no. 2, June 1974, pp. 491-496.

188. Tielking, J. T.; and Shih, M. H.: HSRI Digial Computer Programs for Semi-Empirical Tire Models. Report No. UM-HSRI-PF-74-11, Highway Safety Research Institute, Ann Arbor, 1974.

189. Tielking, J. T.; Martin, R. E.; and Schapery, R. A.: A Note on Tire Carcass Mechanical Properties. Tire Science and Technology, vol. 6, no. 4, November 1978, pp. 248-262.

190. Tielking, J. T.; and Schapery, R. A.: A Method for Toroidal Shell Contact Analysis. Texas A&M University Report MM-9045-80-2, January 1980.

191. Tielking, J. T.; and Schapery, R. A.: A Method for Shell Contact Analysis. Computer Methods in Applied Mechanics and Engineering, vol. 26, no. 2, pp. 181-195, May 1981.

192. Tielking, J. T.: General Deformations of Membrane Structures. Kautschuk und Gummi (Journal of the German Rubber Society), vol. 30, no. 11, pp. 814-822, November 1977.

193. Tielking, J. T.; and Schapery, R. A.: Energy Loss in an Analytical Membrane Tire Model. Tire Science and Technology, vol. 5, no. 3, pp. 136-151, August 1977.

194. Tielking, J. T.; Clark, S. K.; and McIvor, I. K.: A Modified Linear Membrane Theory for the Pressurized Toroid. Journal of Applied Mechanics, vol. 38, no. 2, pp. 418-422, June 1971.

195. Tielking, J. T.: Plane Vibration Characteristics of a Pneumatic Tire Model. SAE Paper No. 65-0492, 1965.

196. Tret'yakov, O. B.; and Novopol'skii, V. I.: Distribution of Contact Stresses Over the Projections of Tread Patterns. Soviet Rubber Technology, vol. 28, no. 8, August 1969, pp. 40-43.

197. Turner, M. J.; Clough, R. W.; Martin, H. C.; and Topp, L. J.: Stiffness and Deflection Analysis of Complex Structures. Journal of Aeronautical Sciences 23, 805-823, 1956.

198. Vermeulen, P. J.; and Johnson, K. L.: Contact of Nonspherical Elastic Bodies Transmitting Tangential Forces. J. Appl. Mech. 31 (2), June 1964, p. 338.

199. Vincent, Ronald James: Longitudinal Transient Behavior of a Rolling Tire: A Discretized Tire Tread Model. Ph.D. Thesis, Cornell Univ., 1976.

200. Von Schlippe, B.; and Dietrich, R.: Shimmying of a Pneumatic Wheel. Papers on Shimmy and Rolling Behavior of Landing Gear Presented at Stuttgart Conference, NACA TM-1365, Aug. 1954, p. 125.

201. Von Schlippe, B.; and Dietrich, R.: Zur Mechanik des Luftreifens. R. Oldenbourg: Munich and Berlin, 1942.

202. Walter, J. D.: A Wirecord Tension Transducer. Textile Research Journal 39, 191-196 (1969).

203. Walter, J. D.; and Conant, F. S.: Energy Losses in Tires. Tire Science and Technology, vol. 2, no. 4, November 1974, pp. 235-260.

204. Walter, J. D.: Centrifugal Effects in Inflated, Rotating Bias Ply Tires. Textile Research Journal 46, 1-7, 1970.

205. Walter, J. D.; and Hall, G. L.: Cord Load Characteristics in Bias and Belted-Bias Tires. SAE Paper No. 69-0522, 1969.

206. Weickert, B.: Methods for Measuring Static Strains in Automobile Tires. Textile Research Journal 32, 705-710, (1962).

207. Wempner, G. A.: Discrete Approximations Related to Nonlinear Theories of Solids. Int. J. Solids Structures, vol. 7, pp. 1581-1599, 1971.

208. Whicker, D.; and Rhode, S. M.: Modeling Tire Deformations for Power Loss Calculations. SAE Paper 81-0161, Feb. 1981.

209. Whicker, D.; Browne, A. L.; and Segalman, D. J.: The Structure and Use of the GMR Combined Thermo-Mechanical Tire Power Loss Model. SAE Paper No. 81-0164, Feb. 1981.

210. Whicker, D.; Browne, A. L.; Segalman, D. J.; and Wickliffe, L. E.: A Thermomechanical Approach to Tire Power Loss Modeling. GM Research Publication GMR-3310, 1980.

211. Wilson, E. L.: Structural Analysis of Axisymmetric Solids. AIAA Journal 3, 2269-2274, 1965.

212. Yandell, W. O.: A New Theory of Hysteretic Sliding Friction. Wear, vol. 17, 1971, pp. 229-244.

213. Zeid, Ibrahim F.: Large and Small Deformation Finite Element Analysis of Rolling Contact. Ph.D. Thesis, Univ. of Akron, 1981.

214. Zienkiewicz, O. C.; Irons, B. M.; Ergatoudis, J.; Ahmed, S.; and Scott, F. C.: Isoparametric and Associated Element Families for Two- and Three-Dimensional Analysis, Finite Element Methods in Stress Analysis. TAPIR, Technical University of Norway, Trondheim, 1969, Chapter 13.

215. Zorowski, C. E.; and O'Neil, E. W.: Measurement of Pneumatic Tire Contact Pressure for Static Loading. Report to the Office of Vehicle Systems Research, North Carolina State University, Raleigh, 1969.

☆U.S. GOVERNMENT PRINTING OFFICE: 1983 639 008 31

1. Report No.
NASA CP-2264

2. Government Accession No.

3. Recipient's Catalog No.

4. Title and Subtitle
TIRE MODELING

5. Report Date
March 1983

6. Performing Organization Code
505-45-23-01

7. Author(s)
John A. Tanner, Compiler

8. Performing Organization Report No.
L-15578

9. Performing Organization Name and Address
NASA Langley Research Center
Hampton, VA 23665

10. Work Unit No.

11. Contract or Grant No.

12. Sponsoring Agency Name and Address
National Aeronautics and Space Administration
Washington, DC 20546

13. Type of Report and Period Covered
Conference Publication

14. Sponsoring Agency Code

15. Supplementary Notes

16. Abstract

This report is a compilation of papers presented at the NASA Tire Modeling Workshop held at Langley Research Center, September 7-9, 1982. The papers included in the report cover the topics of finite element developments, applications to the dynamic problems, solution techniques for tire contact problems, experimental data, and tire thermal studies. A summary of session discussions is also included.

17. Key Words (Suggested by Author(s))
Automobile Tires
Aircraft Tires
Finite Element Techniques
Tire Mechanical Properties

18. Distribution Statement
Unclassified-Unlimited

Subject Category 39

19. Security Classif. (of this report)	20. Security Classif. (of this page)	21. No. of Pages	22. Price
Unclassified	Unclassified	248	A11

N-305

For sale by the National Technical Information Service, Springfield, Virginia 22161

240